Chem Soc Rev

REVIEW ARTICLE

View Article Online
View Journal | View Issue

Cite this: *Chem. Soc. Rev.*, 2015, **44**, 7262

Probing zeolites by vibrational spectroscopies

Silvia Bordiga,[a] Carlo Lamberti,*[bc] Francesca Bonino,[a] Arnaud Travert[d] and Frédéric Thibault-Starzyk[d]

Received 17th May 2015

DOI: 10.1039/c5cs00396b

www.rsc.org/chemsocrev

This review addresses the most relevant aspects of vibrational spectroscopies (IR, Raman and INS) applied to zeolites and zeotype materials. Surface Brønsted and Lewis acidity and surface basicity are treated in detail. The role of probe molecules and the relevance of tuning both the proton affinity and the steric hindrance of the probe to fully understand and map the complex site population present inside microporous materials are critically discussed. A detailed description of the methods needed to precisely determine the IR absorption coefficients is given, making IR a quantitative technique. The thermodynamic parameters of the adsorption process that can be extracted from a variable-temperature IR study are described. Finally, cutting-edge space- and time-resolved experiments are reviewed. All aspects are discussed by reporting relevant examples. When available, the theoretical literature related to the reviewed experimental results is reported to support the interpretation of the vibrational spectra on an atomic level.

[a] *Department of Chemistry, NIS and INSTM Reference Centers, University of Torino, Via Quarello 15, I-10135 Torino, Italy*
[b] *Southern Federal University, Zorge Street 5, 344090 Rostov-on-Don, Russia*
[c] *Department of Chemistry, CrisDi Centre for Crystallography, University of Torino, Via Giuria 7, I-10125 Torino, Italy. E-mail: carlo.lamberti@unito.it; Tel: +39 0116707841*
[d] *Laboratoire Catalyse et Spectrochimie, ENSICAEN – Université de Caen Normandie – CNRS, 6 Boulevard du Maréchal Juin, 14050 Caen Cedex, France*

1. Introduction

Vibrational spectroscopies have played a large role in the characterization of zeolites and zeotype materials.[1–34] The insertion of heteroatoms (Ti, Ge, Sn, Zr, Fe, Ga, and In), which are isomorphically substituted at T centers, perturbs the [TO_4]

Silvia Bordiga

Prof. Silvia Bordiga received her PhD in Chemistry in 1993 and since 2001 has been associate professor at the Department of Chemistry. The research focus of Silvia Bordiga is fundamental studies of materials with relevant interest in key technologies. The core part of her work consists of the characterization of the physical-chemical properties of nanostructured materials with large surface areas (oxides, zeolites, MOFs, and porous polymers) used as heterogeneous catalysts, photocatalysts, and materials for adsorption, separation and storage, with a multi-technique approach. The studies are mainly related to characterization through vibrational and electronic spectroscopies in absorbance (IR and UV-Vis-NIR), scattering (DRIFT and Raman), and emission (luminescence). Starting from January 2012, she got a 3 + 2 years contract as 20% full professor (Professor II) in the Chemistry Department at Oslo University. She has published more than 300 papers that have received more than 18 000 citations, resulting in an h-index of 78 (ISI WoS data).

Carlo Lamberti

Prof. Carlo Lamberti was born in 1964 and received a degree in Physics in 1988; He obtained PhD in solid-state physics in 1993. He is associate professor in Physical Chemistry at the University of Turin since 2006. His research activities are focused on the multi-technique characterization of nanostructured materials with synchrotron radiation techniques. He has edited 4 books and authored and coauthored more than 300 research papers, 14 review articles, and 15 book chapters, which have received more than 13 000 citations (h-index 64, ISI WoS data). He is the Italian coordinator of the European Master in Materials Sciences program MaMaSELF (http://etudes.univ-rennes1.fr/mamaself) between Turin, Rennes-1, Montpellier-2, LMU and TUM universities. He is the PI of the Mega-grant of the Russian Federation Government to support scientific research at Southern Federal University, No. 14.Y26.31.0001.

framework modes and can be directly detected by IR and Raman, whereas for the studies dealing with mesoporous materials, approaches using probe molecules have given great potential to vibrational spectroscopies. The variety of usable probe molecules (CO, NO, CO_2, N_2, H_2, O_2, NH_3, CCl_3H, CF_3H, Py, benzene, and substituted benzenes, *etc.*) provides a large range of chemical reactivity and steric hindrance, significantly increasing the number of potential experiments that can be performed on microporous materials.

As is the case with all catalysts, zeolites also require special *in situ* and *operando*[35] conditions to be properly characterized. Consequently, several specific catalytic cells have been developed to allow IR and Raman experiments under relevant conditions.[14,36–44]

Table 1 Bibliometric data reporting the number of studies published in the 1996–May 2015 time interval using the keywords (zeolite OR zeolites OR zeotype OR zeotypes) with (IR OR FTIR OR Infrared OR "infra-red") or (Raman) or (INS OR "inelastic neutron scattering") or (EEL OR EELS OR "electron energy loss"). ISI Web of Science database

Technique	N. of papers
Infrared	10 133
Raman	1396
INS	129
EELS[a]	43

[a] The number of 43 papers obtained from this bibliographic research is actually overestimated, as several deal with electron energy loss in the 0.1–2 keV range obtained inside TEM instruments and providing XANES-like spectra.

For the characterization of zeolite and zeotype materials, among the different vibrational techniques, such as infrared (IR), Raman, inelastic neutron scattering (INS) and electron energy loss spectroscopy (EELS), to date, the most used is IR, followed by Raman spectroscopy, INS and EELS. However, the difference between the number of studies published on IR and those published on Raman and INS is one and two orders of magnitude, respectively, as shown in Table 1. Therefore, the large majority of the examples reviewed in this study refer to IR studies. Few concern Raman studies and one relates to INS, whereas EELS has been overlooked owing to its need to operate under ultrahigh vacuum conditions that are far away from the operating medium of the catalysts.

The relatively low number of studies published on INS is obviously justified by the relatively high difficulty of access to neutron facilities. On the other hand, Raman spectroscopy has to face several severe experimental difficulties such as follows: (i) the low quantum efficiency of the Raman phenomenon, which is a photon-in-photon-out process; (ii) the risk of

Francesca Bonino

Francesca Bonino was born in 1976. She received her PhD in Materials Science and Technology in 2003 at the University of Turin. She has been Assistant Professor since 2011 at the Department of Chemistry of the University of Turin. Her research interests are devoted to the spectroscopic characterization of nanostructured materials with large surface area, mainly zeolites and MOFs used as heterogeneous catalysts and materials for adsorption, separation and storage. She is the author of more than 70 papers listed in the ISI database (h-index 32) and she has received more than 3000 citations.

Arnaud Travert

Arnaud Travert is Associate Professor at the University of Caen–Normandy, and member of the Laboratoire Catalyse et Spectrochimie. He obtained his PhD in Caen in 2000 on the characterization of the acidity of sulfided catalysts by IR spectroscopy. He then joined the group of Rutger van Santen (TU Eindhoven, NL) for a postdoctoral study on the modelling of hydrogen activation by sulfided phases for hydrotreatment. Back in Caen, he studied hydrotreatment and desulfidation in FCC. In 2009, he spent a sabbatical at the Grace Davison Research Center (Columbia, MD, USA). His present interests are biomass conversion, 2nd generation biofuels, and the design of new operando IR methodologies for the quantification and determination of the thermodynamics and reaction kinetics of adsorbed probe molecules or reactants under reaction conditions.

Frédéric Thibault-Starzyk

Frédéric Thibault-Starzyk was born in Saint-Lo (France) in 1965. He received his PhD in synthetic organic chemistry in 1992 in Caen. After a post-doctorate with Pierre Jacobs in Leuven (BE), he entered CNRS in 1995 at the Catalysis and Spectrochemistry Laboratory (Caen, France), and has now been director of the laboratory since 2011. In 2003–4, he was a fellow at Churchill College, University of Cambridge, with David King. He was president of the French Zeolite Group (2009–2014). His research interests are in heterogeneous catalysis and infrared spectroscopy, including operando spectroscopy, time-resolved measurements, and new spectroscopic approaches for the characterisation of solids and zeolites.

radiation damage effects due to the relatively high power delivered per sample unit area by the laser source; (iii) the high fluorescence background usually emitted by zeolites after thermal activation; (iv) the high black-body radiation background emitted by the sample when performing high-temperature experiments under *in situ* or *operando* conditions. Although severe, all these difficulties can be overcome, at least partially, by appropriate instrumental conditions as detailed below and high-quality results can be obtained by Raman spectroscopy.

The intrinsically low intensity of Raman spectra can be in part overcome by the use of more powerful laser sources; however, this is not always a viable solution because of the collateral risk of radiation damage effects. The use of Fourier transform Raman spectrometers working with a near-IR (NIR) laser source or the use of multi-channel strip detectors in dispersive geometries that allow simultaneous collection of a significant fraction of the spectrum is more efficient. Obviously, FT-Raman cannot be used in *operando* conditions at high temperatures because of the huge background in NIR coming from black-body radiation. Alternatively, enhancement phenomena could be exploited. This is the case with resonant Raman,[20,30,31,45–49] where the use of a laser with an appropriate wavelength (λ), which is able to match a particular charge transfer transition, allows the enhancement of the Raman modes related to the species subjected to that CT by some orders of magnitude (see Section 3.3.2). The availability of several Raman sources of different wavelengths or of a tunable laser is required to cover the large number of possible cases. Alternatively, when dealing with metal nanoparticles embedded in zeolite cages,[50–53] it is possible to perform surface-enhanced Raman spectroscopy (SERS) experiments.[49,54,55] SERS is a surface-sensitive technique that enhances Raman scattering by molecules adsorbed on metal surfaces. The enhancement factor can be as much as 10^{10}, which means that the technique may potentially detect single molecules as well.[56] The drawback of SERS is that it requires a very particular class of materials. The aforementioned two methods allowing the enhancement of the intensity of Raman spectra have an additional advantage of providing a microscopic resolution to the experiment (see Section 8). This is the case with stimulated Raman scattering (SRS) microscopy (see Section 8.3). SRS allows the sensitivity of Raman to be increased by several orders of magnitude by combining two picosecond lasers (Stokes and pump lasers) for obtaining non-linear spectroscopy,[57–59] reaching a spatial resolution better than 1 μm.[60] SRS overcomes the speed limitation of confocal Raman microscopy, while avoiding the non-resonant background problem of coherent anti-Stokes Raman scattering (CARS) microscopy.[59,61,62] Finally, tip-enhanced Raman spectroscopy (TERS)[49,55,63,64] is a promising scanning probe microscopy technique that combines the chemical/structural characterization capability of Raman spectroscopy with the spatial resolution of atomic force microscopy (AFM). It is one of the few techniques that provide chemical and structural information in ambient conditions at high spatial resolution, as low as 30 nm. To the best of our knowledge, TERS has not been applied to the investigation of zeolitic materials to date but clearly represents an attractive method for future investigations.

The risk of radiation damage by the laser beam can be overcome by the use of appropriate *operando* experimental cells that mimic a fluidized-bed reactor, where the catalyst particles move continuously inside the beam,[38,44] as discussed in Section 9.2.5. Finally, the problems related to the background generated by fluorescence centers or by black-body radiation in high-temperature experiments can be overcome by the use of UV and far-UV lasers.[20,30,31,65]

On the other hand, Raman spectroscopy exhibits some relevant advantages with respect to IR, which make it the vibrational technique of choice in some specific applications relevant to the zeolite class of materials. This is the case with *in situ* or *operando* experiments that are performed in the liquid phase using water as solvent. The huge IR absorption coefficient of H-bonded water molecules in the liquid phase obscures the infrared spectrum in the 4000–1000 cm^{-1} region, whereas Raman spectra are almost unaffected by the presence of the liquid phase, because H_2O molecule is a very poor Raman scatterer. Raman spectroscopy is better suited to investigate the zeolite framework stretching region of 1200–700 cm^{-1}, which is only partially inaccessible to IR spectroscopy owing to the fact that the 1200–1000 cm^{-1} interval is obscured by the asymmetric stretching of [TO_4] units, as discussed in Section 3.3. Finally, Raman spectroscopy is more appropriate for investigating zeolite deactivation processes due to the formation of coke inside the pores (see Section 9.2.5), because the black nature of such carbonaceous species totally absorbs mid-IR radiation. All these aspects are discussed in this review using relevant examples.

In summary, this complex analysis of the advantages and disadvantages of the three main vibrational techniques (IR, Raman and INS) considerably explains the important difference in terms of published studies, which has shown in Table 1.

Coming to the content of this review, we start by discussing in great detail how vibrational spectroscopies have shed light on the aspects of zeolite acidity and basicity. Brønsted and Lewis acidities are discussed in Sections 2 and 3, respectively, whereas Section 4 is devoted to basicity, where we underline how distinguishing between surface Lewis and Brønsted bases is misleading and should be avoided. Section 5 illustrates how IR spectroscopy, using probe molecules of different steric hindrance, can discriminate among different sites hosted in crystalline nanoporous materials. The relevant problem of making IR a quantitative technique is addressed in Section 6, where the accurate determination of the molar absorption coefficient ε is discussed. In Section 7, we review IR experiments performed at various temperatures, showing how it is possible to extract accurate thermodynamic quantities, such as the entropy and enthalpy of adsorption, which are site-specific and not averaged values, contrary to those obtained with standard calorimetric approaches. Finally, in Sections 8 and 9 we address the cutting-edge topics of space- and time-resolved experiments with resolutions as low as μm and μs, respectively.

It is worth stressing that this review focuses on the experimental aspects of vibrational spectroscopies applied to zeolites. This choice reflects the competencies of the authors and the fact that this themed issue of the journal already has an authoritative review that focuses on highlighting the advances

in theory and their application within the field of zeolite chemistry.[66] Notwithstanding this limitation, we are fully aware that the contribution of theoretical calculations to the field is tremendous and that in several cases it has been essential for the correct interpretation of the experimental results. For this reason, if at any time the specific reviewed experimental example was complemented by a parallel *ab initio* calculation, the corresponding study was mentioned and quoted. Indeed, the quoted literature reports several contributions from highly reputed theoretical colleagues such as Bagus, Catlow, Civalleri, Damin, Doll, Ferrari, Garrone, Nachtigall, Nachtigallova, Pacchioni, Pelmenschikov, Ranghino, Ricchiardi, Sauer, Ugliengo, Valenzano, van Santen, *etc.*

This review has been written in a modular way; thus, each section is self-consistent and independent and can be read separately from the remaining text. However, several cross-references among different sections have been created to obtain a homogeneous text that aims to go beyond the topic of each single section.

2. Brønsted acidity in zeolites

2.1. General considerations

The protonic forms of zeolites are active catalysts in a large variety of reactions[67–69] such as hydrocarbon cracking,[70–73] alkylation of aromatic hydrocarbons,[74–76] alkane hydroisomerization,[77–80] conversions of methanol to hydrocarbons,[81–91] olefins,[82,88,92–97] or gasoline,[88,98,99] and of other oxygen compounds.[100] To optimize such reactions, an accurate determination of the acidic strength of Brønsted sites is required.

Besides theoretical approaches,[66,101–113] several experimental methods have been developed to measure the acidic strength in solids in general and in zeolites in particular. Among these, we mention titration methods,[114–116] calorimetric measurements,[115,117–119] temperature-programmed desorption (TPD) of basic molecules (like ammonia),[120] and on the spectroscopic side, ^{1}H[107,110,113,121–129] and ^{17}O[130,131] solid-state NMR and IR.[18,99,120,123,125–128,132–163]

IR spectroscopy allows to evaluate the strength of the O–H bond by the direct measurement of ν(OH) stretching frequency: the higher is ν(OH), the stronger is the O–H bond, the less prone is the Al–O–H zeolitic site to release H^+ to an adsorbed base B, and consequently the lower is the Brønsted acidic strength of the site. This simple concept is clearly shown in Fig. 1, where the IR spectra of several activated zeolites are displayed in the O–H stretching region. Thermal activation *in vacuo* at a high temperature is a mandatory pre-treatment to remove all molecules (mainly water) adsorbed in the zeolitic channels, which would otherwise perturb O–H stretching, because of the following reasons. At high frequencies, all the zeolites exhibit a peak that has a sharp maximum in a very narrow interval (3747–3744 cm^{-1}), independent of the zeolite topology and Si/Al ratio. This band tails off differently on the low-frequency side, depending on the different materials and reflects the presence of an internal silanol generated by one or more Si vacancies.[46,166–171] In Al-free silicalite-1 (top spectrum in Fig. 1), this silanol band is the only spectroscopic feature in

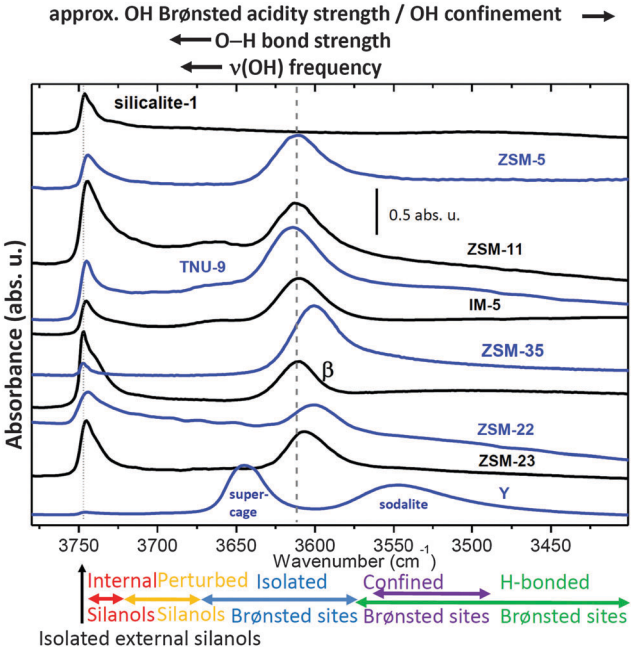

Fig. 1 IR spectra of activated protonic zeolites. From top to bottom: Al-free silicalite-1 (MFI, ∞), ZSM-5 (MFI, 18), ZSM-11 (MEL, 20), TNU-9 (TUN, 20), IM-5 (IMF, 16), ZSM-35 (FER, 15), β (BEA, 18), ZSM-22 (TON, 30), ZSM-23 (MTT, 23), and Y (FAU, 3). The zeolite topology[164,165] and Si/Al ratio are shown in the parentheses. All the spectra have been obtained after the thermal activation of the zeolites *in vacuo* to remove all molecules (mainly water) adsorbed in the zeolitic channels, which would otherwise perturb O–H stretching. The spectral regions corresponding to isolated, internal and perturbed silanols and isolated, H-bonded and confined Brønsted sites are roughly defined at the bottom using colored arrows. The intervals of these regions are only qualitative. The dotted and dashed vertical lines represent the position of isolated silanols and Brønsted sites in H-ZSM-5 zeolite. Previously unpublished figure.

the whole ν(OH) stretching region owing to the absence of Brønsted sites. Moreover, in this case, the low-frequency tail reflects the presence of internal silanol nests. The high frequency of the silanol bands reflects the almost negligible acidic strength of the silanols. Moving to a lower frequency, the 3650–3600 cm^{-1} interval is the region of isolated (unperturbed) Brønsted sites. The ν(OH) mode of Brønsted sites hosted in the supercage of zeolite Y occurs at 3645 cm^{-1} (the literature often refers to this band as the high-frequency (HF) band of zeolite Y). The Brønsted sites of all other zeolites illustrated in Fig. 1 are stronger, falling in the 3615–3600 cm^{-1} interval. Unfortunately, in this case, the absolute value of the ν(OH) mode cannot be used to establish a reliable scale for the strength of Brønsted acidity. In fact, the exact position of the band is slightly perturbed by very weak Si–O–H···O adducts with adjacent oxygen atoms of the framework. This fact is evident in the case of Brønsted sites hosted in the sodalite cage of zeolite Y, which absorb at 3545 cm^{-1} (the literature often refers to this band as the low-frequency (LF) band of zeolite Y), where owing to the small size of the sodalite cage, hydrogen bonding with the framework oxygen is quite strong. Section 5.1 gives a detailed description of the IR spectrum of H-Y zeolite, and, in particular, Fig. 20 schematically illustrates the structure of

zeolite Y. HF and LF bands are also present in H-mordenite, although characterized by a much smaller difference in the corresponding $\tilde{\nu}$(OH), as discussed in Sections 5.4.1 and 6.2, together with Fig. 22 and 26. For these reasons, a reliable infrared scale for the strength of acidity can only be obtained with the use of probe molecules by carefully monitoring all the perturbations of vibrational features induced by the adsorption of the probe on the Brønsted site, as discussed in the subsequent section.

Finally, it is worth noting that the relative ratio between the intensities of the IR bands associated with Brønsted sites and external silanols is related to two factors: the Si/Al ratio of the zeolite and the average crystal size. When two different families of Brønsted sites are present, such as the HF and LF components in H-Y or H-mordenite zeolites mentioned above, the relative intensity of the two bands does not immediately reflect the relative populations of the two sites because the molar absorption coefficient ε of ν(OH) mode is strongly increased in the case of H-bonding that occurs in Brønsted groups confined in the sodalite cage of zeolite Y or in the side pocket of mordenite zeolites. These aspects will be discussed in detail in Section 6.

2.2. Brønsted acidity in zeolites investigated by probe molecules of different proton affinity: spectroscopic scale of acidity

Vibrational spectroscopy has definitely played a major role in elucidating the interaction mechanisms and structure of the adsorbed species. The classical IR spectroscopic method of studying the acidity of Brønsted sites in zeolites is to measure the perturbation of the vibrational modes of OH sites upon interaction with bases. This method is based on the experimental observation that the formation of ZH···B adducts between a Brønsted acid ZH of the zeolitic framework and a base B *via* the acid–base reaction (see eqn (1) and Scheme 1) is accompanied by a downward shift in the ν(OH) stretching frequency, which is proportional to the adsorption enthalpy.

$$ZH + B \rightarrow ZH\cdots B \quad (1)$$

This perturbation effect is not only documented for a number of hydrogen-bonded compounds in the crystalline state[172] and for homogeneous systems in solutions[173] but also for heterogeneous systems like those encountered in zeolite channels[137,145,174] and on the surface of oxides.[175,176] In particular, one of the key questions associated with the activity of Brønsted groups present in zeolite channels is related to the estimation of their acid strength and its comparison with that of the most common mineral acids and superacids.[136] To illustrate the results obtained by the application of vibrational spectroscopy in a systematic way, we have chosen zeolite β as a prototype system and we will follow, using IR spectroscopy, the perturbation induced in ν(OH) stretching frequency by B molecules characterized by a proton affinity (PA) ranging over a very broad interval: N_2 (PA = 118.2 kcal mol^{-1}), CO (PA = 141.9 kcal mol^{-1}), C_2H_4 (PA = 162.6 kcal mol^{-1}), C_3H_6 (PA = 179.5 kcal mol^{-1}), H_2O (PA = 166.5 kcal mol^{-1}), CH_3CN (PA = 188.6 kcal mol^{-1}), CH_3OH (PA = 181.9 kcal mol^{-1}), $(CH_3)_2O$ (PA = 192.1 kcal mol^{-1}), tetrahydrofuran (THF, PA = 196 kcal mol^{-1}) and pyridine (Py, PA = 204 kcal mol^{-1}).[145,151] All these molecules exhibit basic character, which increases along the sequence, and when appropriate temperature and pressure conditions are adopted, they can form hydrogen-bonded adducts with Brønsted groups, as shown in Scheme 1.

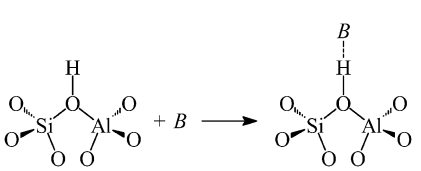

Scheme 1 Formation of ZH···B adducts between a Brønsted acid ZH hosted inside a zeolite channel, Z≡[(−O)$_3$−Si]−O−[Al−(O−)$_3$], and a base B *via* a classical acid–base reaction. Previously unpublished scheme.

The spectroscopy of homogeneous ZH···B systems comprising an acid ZH and a base B can be outlined by briefly describing six representative situations: (i) isolated ZH; (ii) ZH interacting with B through a weak H-bond; (iii) ZH interacting with B through a H-bond of medium-high strength; (iv) ZH interacting with B through a strong H-bond; (v) ZH interacting with B through a very strong H-bond; and (vi) $Z^-\cdots H{-}B^+$ hydrogen-bonded ionic pairs, corresponding to proton transfer. Fig. 2a hereafter shows the experimental ν(OH) or ν(BH) spectra, while the corresponding potential energy profiles experienced by the proton and the model OH (BH) vibrational spectra are shown in Fig. 2c and b, respectively.

The complex spectral features illustrated in Fig. 2 are described in the following in the order of increasing proton affinity of the adsorbed base B. Because Z is not a single atom but represents a zeolitic framework (see Scheme 1), the unperturbed ZH oscillator is characterized by three vibrational modes: stretching ν and bending modes δ and γ (in and out of the plane) (see Fig. 2(b)i). The proton potential energy of unperturbed AH is typical of an anharmonic oscillator; the shape of the function being that of a curve with a single minimum, see Fig. 2(c)i.

Upon interaction with a weak base B, ν(AH) stretching undergoes a negative shift ($\Delta\tilde{\nu}$), which occurs in the 0–400 cm^{-1} interval, as well as a proportional increase in integrated intensity (I) and full width at half maximum (FWHM). At the same time, the bending modes δ and γ shift to higher frequencies. This is schematically represented in Fig. 2(b)ii and ii′ and lead to the top red spectra in Fig. 2(a). It can be easily verified that, in first approximation, FWHM is empirically proportional to the red shift of the band $|\Delta\tilde{\nu}(\mathrm{OH})|$ with a proportionality factor close to three-quarters:

$$\mathrm{FWHM} = \sim -3/4\Delta\tilde{\nu}(\mathrm{OH}) \quad (2)$$

$\Delta\tilde{\nu}$(OH), I and FWHM are proportional to the enthalpy of formation of the H-bond.[173] The increase in integrated intensity and FWHM is due to anharmonic coupling between the ν(OH) mode and the low-frequency external mode ν(Z···B), which is in turn coupled with thermal bath fluctuations.[179] Because of this anharmonic coupling, the ν(ZH···B) mode can be better described as a continuum. Upon formation of a weak hydrogen bond, the proton potential becomes more anharmonic and the

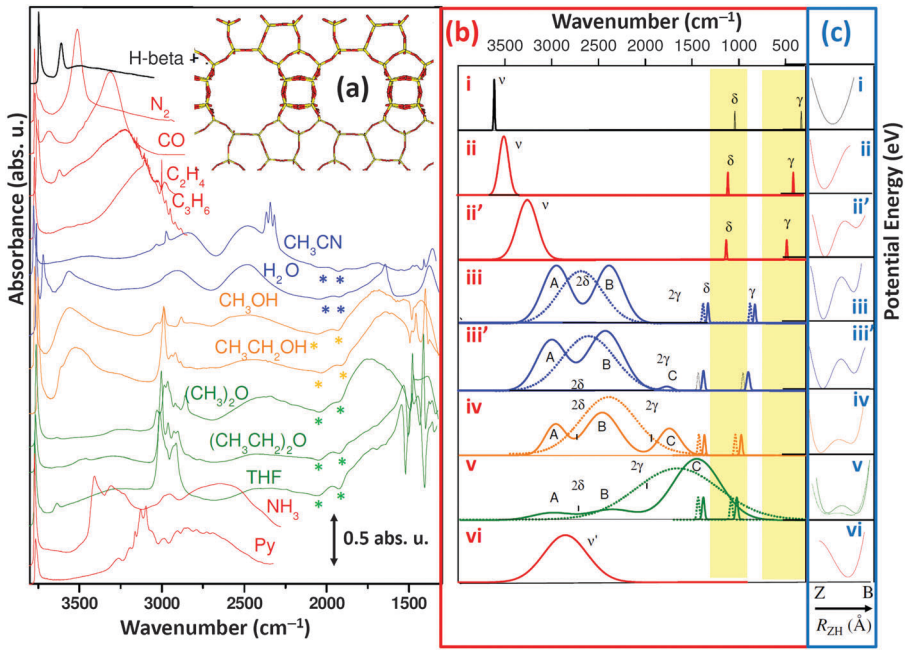

Fig. 2 Part (a): Experimental IR spectra of unperturbed H-β (black top curve) and H-β/B 1 : 1. The spectra have been displayed from top to bottom according to the proton affinity of the bases B and classified in classes identified by the line color: N_2, CO, C_2H_4, C_3H_6 (top red spectra), CH_3CN, H_2O (blue spectra), CH_3OH, CH_3CH_2OH (orange spectra), $(CH_3)_2O$, $(CH_3CH_2)_2O$, THF (green spectra) and NH_3 and Py (bottom red spectra). The asterisks indicate "false" bands due to the effects of the adsorption of bases on the zeolite skeletal modes, as discussed in ref. 177. The top right corner shows a stick representation of β zeolite (BEA topology[165]) viewed from the [010] direction: Si or Al (yellow) and O (red). Part (b), frames (i–vi): qualitative representations of the IR spectra of unperturbed and weak, medium, and strong Z–H···B or $Z^-\cdots H–B^+$ H-bonded complexes. Frames (iii–v): dotted curves correspond to hypothetical spectra without Fermi resonance. Full curves correspond to actual spectra affected by Fermi resonance. The half-width of the bending modes is assumed somewhat arbitrarily to slightly increase upon an increase in the hydrogen bond strength. The yellow areas correspond to regions obscured by the skeletal modes of the zeolite framework. Part (c), frames (i–vi): schematic representation of the correlated evolution of the proton potential energy as a function of the Z–H distance in Z–H···B or $Z^-\cdots H–B^+$, according to ref. 178. The separation barriers in (v) and (vi) can be very low and a potential curve characterized by an asymmetric single flat minimum could be used instead. Adapted and used by permission of the American Chemical Society (copyright 1997) from ref. 145.

equilibrium R_{ZH} distance increases, as illustrated in Fig. 2(c)ii and ii′.

Upon the formation of AH···B adducts, characterized by hydrogen bonds of medium strength, $|\Delta\tilde{\nu}|$ gradually increases to 1000 cm^{-1}, with a parallel increase in I and FWHM, as represented by the dotted curves in Fig. 2(b)iii and (b)iii′. However, the spectroscopy of H-bonded systems of medium strength is not as simple as illustrated by the dotted curves, because the shape of the bands is extensively modified by Fermi resonance effects with 2δ and 2γ overtones.[180–182] Fermi resonance occurs between two very close vibrational levels of proper symmetry; as a consequence, the two original modes mix together and lead to two different bands, each of which being a mixture of the original modes.[145,183] According to a simplified approach,[184] Fermi resonance between the ν(ZH···B) and 2δ and 2γ modes of the ZH···B adduct in medium-strength hydrogen-bonded systems modifies the profile of the ν(OH) mode with the appearance of up to three components named A, B, and C in Fig. 2(b)iii, iii′, iv and v. The simplest case occurs when the maximum of the ν(ZH···B) mode band coincides with the 2δ band; the 2γ band being outside the unperturbed envelope of the ν(OH) mode (dotted curves in Fig. 2(b)), as illustrated in Fig. 2(b)iii. In this case, the observed ν(ZH···B) band is split into two bands of equal intensity (A and B), whereas the C band is not observed. By increasing the hydrogen bond strength, the 2δ frequency becomes higher than the maximum of the ν(ZH···B) band (which exhibits a progressive red shift) and the 2γ frequency decreases in its low-frequency tail. Here, both 2δ and 2γ overtones become incorporated in a further broadened ν(ZH···B) continuum. As a consequence, the C band starts appearing on the extreme low-frequency side with very low (Fig. 2(b)iii′) or low (Fig. 2(b)iv) intensity. The relative intensity of the observed A, B and C bands changes gradually from $I_A \cong I_B \gg I_C$ to $I_A < I_B \cong I_C$ with an increase in the strength of the hydrogen bond (from medium to strong) and an increase in R_{ZH} (decrease in the R_{HB} distance) in the ZH···B complex. The corresponding potential energy profiles are illustrated in Fig. 2(c)iii′ and iv. Bands of this type are well known in the literature and are usually considered to correspond to proton potential functions that consist of an asymmetric double minimum, with a gap in energy between the two minima decreasing as the strength of the H-bond increases.[185] The present description is only qualitative, because the real shape of the potential curve for hydrogen bonds corresponding to shifts $\Delta\nu$(OH) = −1000 cm^{-1} is not well established.[186] Parallel to the increase in hydrogen bond strength, the tunneling probability also increases and

clear localization of the proton becomes increasingly difficult due to its fast fluctuation between the two limit structures under the effect of external perturbations; the system consequently evolves progressively towards more polar forms.

For very strong H-bonds, the interaction energy between ZH and B reaches its maximum value and correspondingly $\Delta\nu$(OH) reaches its maximum (from -2000 to -2500 cm^{-1}), whereas the R_{ZB} distance reaches its minimum, as shown in Fig. 2(c)v. Under these circumstances, the potential function of the proton is characterized by a symmetric double-minimum curve with a very low gap in energy between the two minima or by a single broad, flat minimum,[185] as shown in Fig. 2(c)v, where A and B components nearly completely disappear and only the C component remains as the dominant feature. This C band (also named band "D" by some authors) is a very intense broad band extending towards low frequencies, as shown in Fig. 2(b)v. This absorption is generally modulated by a large variety of narrow Evans windows caused by direct resonant interaction with the δ (and perhaps γ) mode and with the internal modes of the A and B moieties.

When the proton affinity of B approaches 200 kcal mol^{-1} (as for NH_3 and Py), the H-bonding interaction between ZH and B can be followed by a proton transfer reaction leading to the formation of the anion Z^- and a protonated HB^+ hydrogen-bonded pair. The probability that protonation can really occur does not depend only on the strength of the H-bond (and therefore on the proton affinity of the reactants), but also on the stabilization of the ionic pairs; this stabilization is due, in homogeneous conditions, to solvent effects[118,119] and, in heterogeneous conditions, to interaction with the surfaces.[145,148] Remembering the elementary concept that the stronger the base B, the weaker is the hydrogen bond in the $Z^-\cdots HB^+$ pair, the IR spectrum of the pair becomes similar again to that of hydrogen-bonded systems of medium strength, as shown in Fig. 2(b)vi. The frequency of $\nu(BH^+\cdots Z^-)$ band increases, whereas $\Delta\tilde{\nu}$(BH), I and FWHM decrease. As observed in Fig. 2(b)vi, no attempt has been made to localize δ and γ modes because they are heavily mixed with internal modes of BH^+ (ring modes in the case of PyH^+).[138]

After this general introduction, we discuss in some detail the cases of N_2, CO and CD_3CN probes, as shown in parts (a)–(c) of Fig. 3, respectively. Starting from molecules with lower PA, parts (a) and (b) of Fig. 3 illustrate the modifications induced by hydrogen-bonding perturbations on the ν(OH) stretching mode of the Brønsted groups of β zeolite as a function of the pressure of N_2 and CO, respectively (the same probes were used by Wakabayashi *et al.* on H-ZSM-5[187]). From the spectra, it can be clearly inferred that upon the addition of base B, the intensity of the ν(OH) mode of unperturbed groups (band at 3614 cm^{-1}) gradually declines, whereas that of the ν(OH$\cdots$B) vibration (shifted to lower frequency) simultaneously increases. The clear isosbestic points observed in both spectra confirm that the 1 : 1 process illustrated in Scheme 1 really occurs in a stoichiometric way. Other important observations are as follows: (i) the negative shift $\Delta\tilde{\nu}$(OH) increases on passing from N_2 ($\Delta\tilde{\nu} = -126$ cm^{-1}) to CO ($\Delta\tilde{\nu} = -319$ cm^{-1}), *i.e.* with increasing proton affinity of the base and (ii) the full width at half maximum

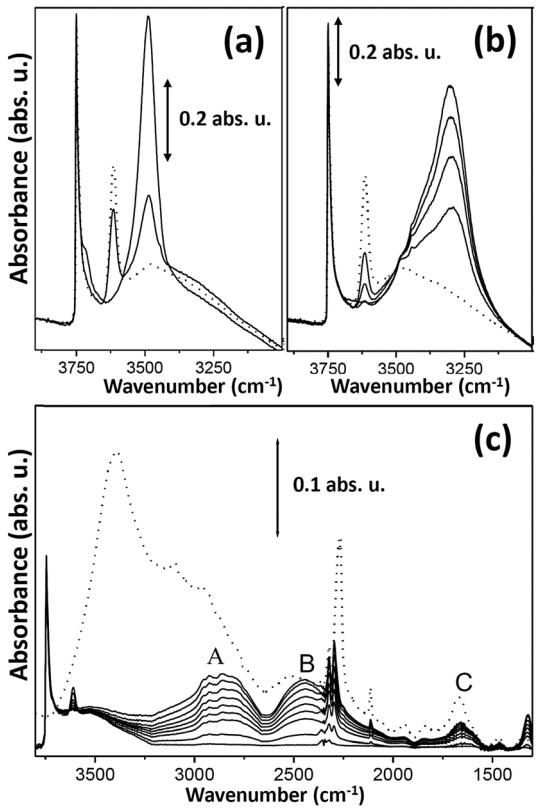

Fig. 3 Part (a): IR spectra in the O–H stretching region of increasing equilibrium pressures (up to 133 Pa) of N_2 (PA = 118.2 kcal mol^{-1}) adsorbed at liquid nitrogen temperature on activated H-β zeolite. Part (b): Similar to part (a) for CO dosage (up to 1000 Pa, PA = 141.9 kcal mol^{-1}). In parts (a) and (b) the dotted-line spectrum is that recorded before gas dosage. Part (c): IR spectra of increasing equilibrium pressures of CD_3CN adsorbed on H-β zeolite. The solid-line spectra refer to CD_3CN equilibrium pressures in the $0-10^{-1}$ Torr interval (1 Torr = 133.3 Pa), whereas the dotted-line spectrum refers to a much higher pressure (30 Torr). Labels A, B and C denote the three components due to Fermi resonance effects (see text). Parts (a) and (b) adapted by permission of the American Chemical Society (copyright 1997) from ref. 145. Part (c) adapted by permission of Elsevier (copyright 2002) from ref. 151.

(FWHM) of the ν(OH) mode increases on passing from unperturbed Brønsted groups (FWHM $\approx$ 20 cm^{-1}) to N_2 (FWHM $\approx$ 85 cm^{-1}) and CO (FWHM $\approx$ 220 cm^{-1}) adducts, in fair agreement with the empirical correlation reported in eqn (2). The observations illustrated in Fig. 3a and b are typical of those expected from the presence of linear hydrogen bonds[173,188] and are a clear demonstration of the formation of 1 : 1 adducts. In accordance with the immense literature on the IR spectroscopy of hydrogen-bonded systems, the shift to a lower frequency and the increase in bandwidth are due to the decrease in the force constant induced by the polarization of the O–H bond and by coupling of the ν(OH) mode with the ν(O$\cdots$B) modes of the adducts, which consequently can be better expressed as ν(OH$\cdots$B) $\pm$ ν(O$\cdots$B).[151]

The formation of hydrogen-bonded adducts is also accompanied by a perturbation of the internal modes of the base, resulting in $\Delta\tilde{\nu}$(NN) = +6 cm^{-1} and $\Delta\tilde{\nu}$(CO) = +34 cm^{-1} for N_2 and CO probes, respectively; we refer to the original paper for more details.[145]

At the highest coverages (not reported in Fig. 3b), the silanols located on the external surfaces of the microcrystals or at internal defects also form hydrogen-bonded adducts with CO.[145] The shift induced in the ν(OH) stretching frequency of the silanols is definitely smaller ($\Delta\tilde{\nu}$(OH) = −90 cm^{-1}) than that observed for Brønsted sites; this is simply a consequence of the fact that the shift in the ν(OH) mode of acid centers caused by interaction with a given base is related to the acid strength of the group itself. In other words, this different response simply reflects the fact that the OH groups of the structural Brønsted sites are much stronger acids than the OH groups of the silanols. This observation can be supported by a large amount of experimental observations obtained with different bases and different zeolites (see Fig. 5), thus proving its general validity. This general correlation, which is the extension to heterogeneous systems of the Bellamy–Hallam–Williams (BHW) relation extensively documented for homogeneous phases,[189–195] will form the basis of the spectroscopic method for the acid strength evaluation of the surface acidic sites on oxides[196] and of the Brønsted groups of zeolitic systems.[145,148,197]

In this review article, it is not possible to continue in the same detailed way with the description of the spectra obtained with molecules such as ethene, propene, and acetylene, which come immediately after N_2 and CO in the PA scale (Fig. 2). Therefore, we move to acetonitrile (PA = 188.6 kcal mol^{-1}). The reasons for this choice are twofold: (i) the acetonitrile probe (CH_3CN and CD_3CN) has been studied extensively with a great variety of zeolites[137,146,151,177,186,197–202] and (ii) the acetonitrile–zeolite complex is characterized by a complex spectroscopy generated by Fermi resonance effects.[145,186] Because these effects are dominant in the spectra of the adducts of structural Brønsted sites with bases of medium-strong PA, their detailed illustration for acetonitrile complexes can be useful for the comprehension of a great variety of experiments that involve different and stronger bases. The spectra with increasing doses of deuterated acetonitrile adsorbed on β zeolite[201] are illustrated in Fig. 3c, where we observe a progressive decrease in structural Brønsted groups because of the formation of hydrogen-bonded adducts (full-line spectra in Fig. 3c); at the highest coverages, the band due to the silanol groups also decreases (dotted-line spectrum). However, upon interaction with the nitrile molecule the silanol band appears as a broad peak shifted to a lower frequency ($\Delta\tilde{\nu}$(OH) = −345 cm^{-1}; FWHM = 260 cm^{-1}); two absorptions with apparent maxima at 2856 and 2452 cm^{-1} (previously named as A and B) originate from the structural Brønsted peak (instead of the single one expected without considering Fermi resonances). Other relevant features of the spectra illustrated in Fig. 2 are as follows: (i) the ν(CN) modes of the structural Brønsted groups and weaker silanols are found at 2297 and 2275 cm^{-1}, respectively (*i.e.* at frequencies higher than those of the free molecule) and (ii) a novel band at 1325 cm^{-1} appears with increasing coverage, which is ascribed to the δ mode of the Brønsted-acetonitrile group. The last result demonstrates that the interaction has become sufficiently strong to shift the δ mode into a frequency range that is not dominated by the framework vibrations (a fact that makes it observable). The observation of the precise position of the δ mode gives us the key for the explanation of the presence of the A–B doublet. In fact, as the minimum separating the A and B partners is observed at a frequency corresponding to twice that of the δ mode, it can be readily inferred that it corresponds to the Evans window generated by a Fermi resonance effect between the ν(OH···B) ± ν(O···B) mode centered at 2680 cm^{-1} (FWHM = 750 cm^{-1}) and the 2δ overtone. In Fig. 3c, a band at 1680 cm^{-1} (labeled with the symbol C) is clearly evident as well. A similar band is observed for acetonitrile on H-ZSM-5 and H-MOR.[177]

Once the strong Brønsted groups have been fully consumed, further addition of B leads to the progressive consumption of the silanols (which, as discussed above, are Brønsted sites of weaker acidity) and also leads to the formation of liquid-like species in the channels. From the previous considerations, it is evident that by investigating the whole spectroscopic isotherms, it is possible to determine the effect of the same base on two Brønsted sites of different strengths present in the same solid and characterized by a very similar environment. This is true not only for the simplest bases such as N_2 and CO, but also for other bases such as C_2H_2, C_2H_4, C_3H_6, H_2O, CH_3CN, CH_3OH, CH_3CH_2OH, $(CH_3)_2O$, $(CH_3CH_2)_2O$ and THF. The $\Delta\tilde{\nu}$(OH) shifts obtained by the interaction of these bases with the silanols on the external surfaces of β zeolite are identical to those found with silica and silicalite upon interaction with the same bases.[133,139,178,183,184,196,203,204] The $\Delta\tilde{\nu}$(OH) values of the stretching band of the strong Brønsted groups are reported *vs.* the analogous shift observed with silanols in the BHW plot of Fig. 4.

This type of plot is suggested by the well-known fact that in solution it is possible to study the properties of an acid solute X−H by directly comparing $\Delta\tilde{\nu}$(XH) caused by the formation of a 1 : 1 XH···B adduct with the shift in frequency caused by the same base on a second different solute X′−H (for instance, pyrrole used as a standard). This has been verified in a variety of solvents.[189–193,195] For each solute and for hydrogen bonds of weak–medium strength, linear relationships are constantly observed, and the relative slopes of the straight lines obtained for different X−H systems have been correlated with the pK_a values of the solutes in aqueous solutions. From Fig. 4, it clearly emerges that a linear relationship exists between the $\Delta\tilde{\nu}_{\text{Brønsted}}$(OH) shifts of the stretching mode of the strong Brønsted sites of H-β (pink ◆ symbols), H-ZSM-5 (orange ● symbols), H-MOR (red ■ symbols), and H-Y (black ▲ symbols) zeolites and $\Delta\tilde{\nu}_{\text{Silanols}}$(OH) of silanols (used as standards)[139,145,151] and that the slope of the straight line is a characteristic parameter of each zeolite, as shown in Table 2. The universal validity of this correlation is also proved by the fact that the shifts in $\Delta\tilde{\nu}_{\text{Silanols}}$(OH) of the silanol stretching modes are also linearly correlated with the shifts obtained for HF interacting with the same bases in an argon matrix[205–210] (blue * symbols in Fig. 4), which is not obvious because of the different "solvents" (zeolite framework *vs.* argon).

It is worth noting that the linear correlation illustrated in Fig. 4 holds only when $\Delta\tilde{\nu}_{\text{Brønsted}}$(OH) of strong Brønsted site stretching modes is not greater than 1000 cm^{-1}. For $\Delta\tilde{\nu}_{\text{Brønsted}}$(OH) > 1000 cm^{-1}, the linear correlation is lost because we are comparing strong hydrogen bonds

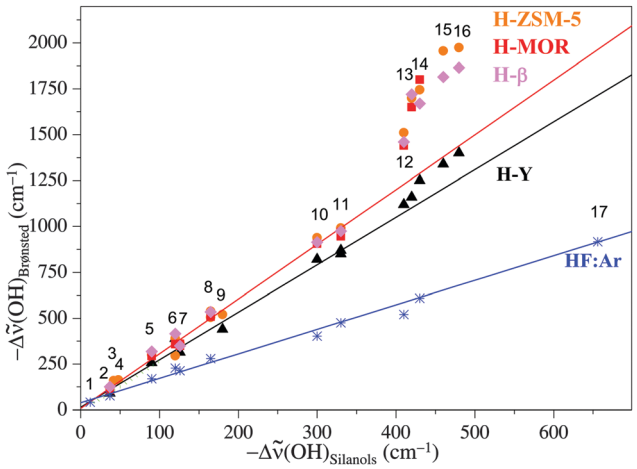

Fig. 4 BHW plot of $\Delta\tilde{\nu}_{Brønsted}$(OH) observed for the Brønsted sites inside H-ZSM-5 (orange ● symbol),[179] H-MOR (red ■ symbol),[179] H-β (pink ◆ symbol),[145] and H-Y (black ▲ symbol)[179] zeolites upon the formation of 1 : 1 hydrogen-bonded complexes with different bases *vs.* $\Delta\tilde{\nu}_{Silanols}$(OH) of the silanol groups in 1 : 1 hydrogen-bonded complexes with the same bases. The different bases are labelled with the numbers: (1) O_2; (2) N_2; (3) N_2O; (4) CO_2; (5) CO; (6) C_4H_4S, C_2H_2; (7) C_2H_4, C_6H_6, C_4H_6; (8) C_4H_4O, C_3H_6; (9) HC_2CH_3; (10) H_2O; (11) CH_3CN, $(CH_3)_2CO$; (12) CH_3OH; (13) CH_3CH_2OH; (14) $(CH_3)_2O$; (15) $(CH_3CH_2)_2O$; (16) THF; and (17) NH_3. The blue * symbols represent the experimental data of HF in cryogenic Ar matrices.[205–210] For each family of data, a straight line with the same color represents the best linear fit of the experimental points in the $\Delta\tilde{\nu}_{Brønsted}$(OH) < 1000 cm^{-1} interval.[145,179] The data for H-ZSM-5, H-MOR and H-β have been fitted with a single line, being virtually indistinguishable within the experimental errors. See Table 2 for the quantitative results of the fits. Adapted by permission of the American Chemical Society (copyright 1997) from ref. 145.

(associated with proton potentials characterized by two minima separated by a low or negligible energy barrier, see bottom parts of Fig. 2) with medium–strength hydrogen bonds in SiOH···B adducts (where the potentials present a single minimum). There is another potential case where the linear correlation foreseen by the BHW relationship will fail to hold in zeolites or in microporous materials in general. Indeed, the BHW relationship holds only if the base B is free to optimize its orientation to maximize hydrogen-bonding interactions with the acidic site. This may not be fully possible if the molecule B is quite large and if the zeolite pores are quite narrow, as documented by the work of Onida *et al.*,[211] which is reviewed in detail in Section 5.4.3.

From the data summarized in Fig. 3 and Table 2, it emerges that the shifts in $\Delta\tilde{\nu}_{Brønsted}$(OH) are practically identical for H-MOR, H-β and H-ZSM-5; this means that the slopes of the straight lines corresponding to these zeolites are identical (within the range of experimental error) and hence the acidic character of the Brønsted sites of all these zeolites is nearly equal. This is the reason why Pazé *et al.*[145] decided to report a single linear fit for these three datasets joined together (2.93 ± 0.05, see fourth row in Table 2). Conversely, the acidity of these three solids is appreciably greater than that of H-Y (2.59 ± 0.12 in Table 2), in particular for H-ZSM-5 and H-MOR, and much greater than HF in Ar matrix (1.30 ± 0.04). The fact worth noting is that the intercept value is always very small (on an ordinate scale that goes up to 2000 cm^{-1}), approaching the ideal 0 cm^{-1} that is theoretically expected for a null perturbation.

Table 2 Summary of the best linear fits produced for the $\Delta\tilde{\nu}_{Brønsted}$(OH) *vs.* $\Delta\tilde{\nu}_{Silanols}$(OH) data reported in Fig. 4 for different zeolites. As the slopes for H-ZSM-5, H-MOR and H-β zeolites are within comparable margins of error, a best linear fit has also been reported for these three datasets joined together (fourth row). Previously unpublished table analyzing data reported in ref. 145, 179 and 205–210

System	Slope	Intercept (cm^{-1})	R^2
H-ZSM-5	2.98 ± 0.09	8 ± 16	0.9887
H-MOR	2.91 ± 0.07	8 ± 13	0.9959
H-β	2.89 ± 0.12	36 ± 23	0.9897
⟨H-ZSM-5, H-MOR, H-β⟩	2.93 ± 0.05	15 ± 10	0.9908
H-Y	2.59 ± 0.12	14 ± 26	0.9849
HF:Ar	1.30 ± 0.04	39 ± 11	0.9904

It has been established that, in heterogeneous systems, the ratio of frequency shift of the strong Brønsted groups and that of the SiOH groups (used as standard) measured in the same conditions is correlated with the proton affinities given by the following empirical relation:[145,151,174,177,197]

$$PA_{Brnsted} = PA_{Silanols} - A \log\left[\frac{\Delta\tilde{\nu}_{Brnsted}}{\Delta\tilde{\nu}_{Silanols}}\right] \quad (3)$$

where $PA_{Silanols}$ = 1390 kJ mol^{-1} and A = 442.5 kJ mol^{-1}. It is evident that this equation affords a means of measuring the proton affinity of the Brønsted sites of any zeolite. The most important conclusion that can be derived is that the $\Delta\tilde{\nu}_{Brønsted}(OH)/\Delta\tilde{\nu}_{Silanols}(OH)$ ratio is independent of the base B used to probe the zeolite.

2.3. From H-bonds to the protonation of acetonitrile: exploring superacidity

Zeolites have often been described as solid solvents. They can stabilize dissociated ionic species and play the same solvating role as water. This aspect of zeolites opens the way to a new part of the acidity scale. Acidity in a mixture is limited by the dissociation of the solvent in which a reaction is observed. This is what defines the pH scale in water. It was therefore proposed that, in the absence of water, zeolites could enable the use of stronger acids, without the usual limit in strength imposed by water. A strongly acidic zeolite could even contain so-called superacidic sites in itself, and it has long been an important objective to detect and measure such sites. It should be noted that superacidity, by definition, disappears in the presence of water (the system would then revert to the pH scale between 1 and 14, as defined in water). The Hammett acidity scale H_0 is used to monitor acidity outside the pH scale and the scale is, in this way, extended to negative values. For an acid BH^+ that will dissociate into B and H^+ with an equilibrium constant K_a, the Hammett acidity function H_0 is defined as follows:

$$H_0 = pK_a + \log\left(\frac{[B]}{[BH^+]}\right) \quad (4)$$

Concentrated anhydrous sulphuric acid has been defined as the limit of superacidity with a Hammett constant of $H_0 = -12$. Adding SO_3 to concentrated sulphuric acid yields a superacid

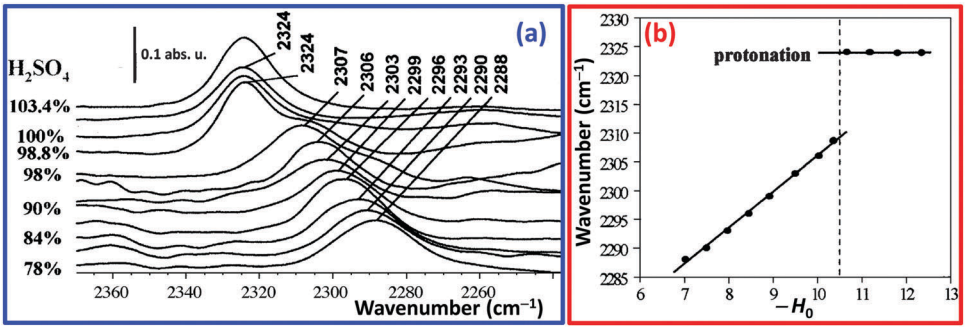

Fig. 5 Part (a): ν(C≡N) frequency of CD_3CN in solutions with various H_2SO_4 concentrations. Part (b): Variation in ν(C≡N) of the spectra reported in part (a) with H_0. Adapted by permission of the Royal Society of Chemistry (copyright 1999) from ref. 212.

solution known as oleum. A [SO_3–H_2SO_4] pair is formed (at higher SO_3 concentrations, polysulphuric acids are obtained: $H_2S_3O_{10}$, $H_2S_4O_{13}$, *etc.*). SO_3 is a strong Lewis acid that enhances the Brønsted acidity of H_2SO_4 by withdrawing its electrons. The same happens in "magic acid" HSO_3F–SbF_5 or in some hydrotreated or steamed zeolites. The least trace of water dissociates the complex and destroys superacidity (quantitatively), and any superacidity can only be studied in perfectly anhydrous conditions, which are very hard to obtain with zeolites. Superacidity can be measured by protonation of very weakly basic probe molecules, for example, some nitriles.

Anquetil *et al.*[212] showed that acetonitrile is protonated in solution at $H_0 = -10.6$, as shown in Fig. 4. When the acid strength of the solution increases, the ν(CN) vibration band at 2300 cm^{-1} (for H-bonds in moderately acid solutions) shifts towards higher frequencies and suddenly disappears when protonation takes place. A new ν(CN) vibration band appears at 2324 cm^{-1}. This very specific spectroscopic feature is a good way to detect protonation and measure the strength of an acidic medium.

The acid strength at which a nitrile is protonated can be tuned by substitution with halogen. Halogenated acetonitrile is less basic, and the threshold for protonation shifts to stronger acidity. Chloroacetonitrile is protonated at $H_0 = -12.4$, bromoacetonitrile at −12.6, and dichloroacetonitrile is only protonated at $H_0 = -13.2$, which leads to a powerful scale for measuring superacidity in solids. The authors have applied this technique to zeolites (which did not reach the level of superacidity) and sulphated zirconia, for which protonation was measured at $H_0 = -13$, thus revealing itself as a superacid.[212]

This shows that although some zeolites are very strong acids, those tested in that study (including the so-called "superacidic" steamed Y zeolite) did not reach the threshold of superacidity. Only some solids like sulfated zirconia[213–216] and the perfluorosulfonic membrane Nafion[136,138,139,177,217,218] were found to be superacidic.

2.4. INS and *ab initio* (MP2) study of the possible protonation of H_2O in H-ZSM-5

The groups of Jobic and Sauer investigated the adsorption of water at different concentrations in H-ZSM-5 using a combination of inelastic neutron scattering (INS) and DFT.[219] The study aimed to determine whether the acidic sites in H-ZSM-5 are sufficiently strong to protonate water.

$$Z^-OH^+ + H_2O \rightarrow Z^-OH^+\cdots H_2O \rightleftharpoons ZO^-\cdots H_3O^+ \qquad (5)$$

As discussed in depth in Section 2.2, the relevance of evaluating the correct acid strength of a given site hosted on the internal or external surfaces of a mesoporous material is of high significance. It is consequently important to determine whether reaction (5) is fully displaced to the right. Section 2.2 and Fig. 2 have shown how elegant, but complex, is the IR spectroscopy of strong and very strong H-bonded complexes in zeolites. INS represents an interesting alternative method to address this problem. This technique is particularly sensitive to vibrational modes involving motions of hydrogen because of the large incoherent cross-section and low mass of the proton.[220,221] In fact, the incoherent cross-sections of the most abundant nuclei present in zeolitic frameworks are as follows: Si (0.004 barn, 1 barn = 1 × 10^{-24} cm^2), Al (0.0082 barn), O (0.0008 barn), P (0.005 barn), B (1.7 barn), Ti (2.87 barn), Fe (0.4 barn), Ga (0.16 barn), Ge (0.18 barn), and Sn (0.022 barn), as compared to that of hydrogen (82.02 barn). Furthermore, vibrational frequencies below 800 cm^{-1} are more easily observed with INS than with IR. Another important feature is that INS intensities are directly related to atomic displacements, which can be computed from empirical force fields or from *ab initio* quantum chemical methods.[219,221] Excellent agreement can be obtained between experimental INS spectra and simulated spectra using theoretical frequencies and atomic displacements as inputs.[222] Because the atomic displacements of water molecules adsorbed on Brønsted sites in zeolites were calculated for the two possible water structures by Krossner and Sauer,[223] in a subsequent study in collaboration with Jobic, the INS spectra of water in interaction with an acid site were simulated and compared with experimental data, as shown in Fig. 6.

The authors were able to conclude that simulations of INS spectra based on *ab initio* MP2 calculations show that a water molecule is attached to an acid site *via* two hydrogen bonds and that the protonated species are not observed; thus, in H-ZSM-5, reaction (5) stops at the middle term.

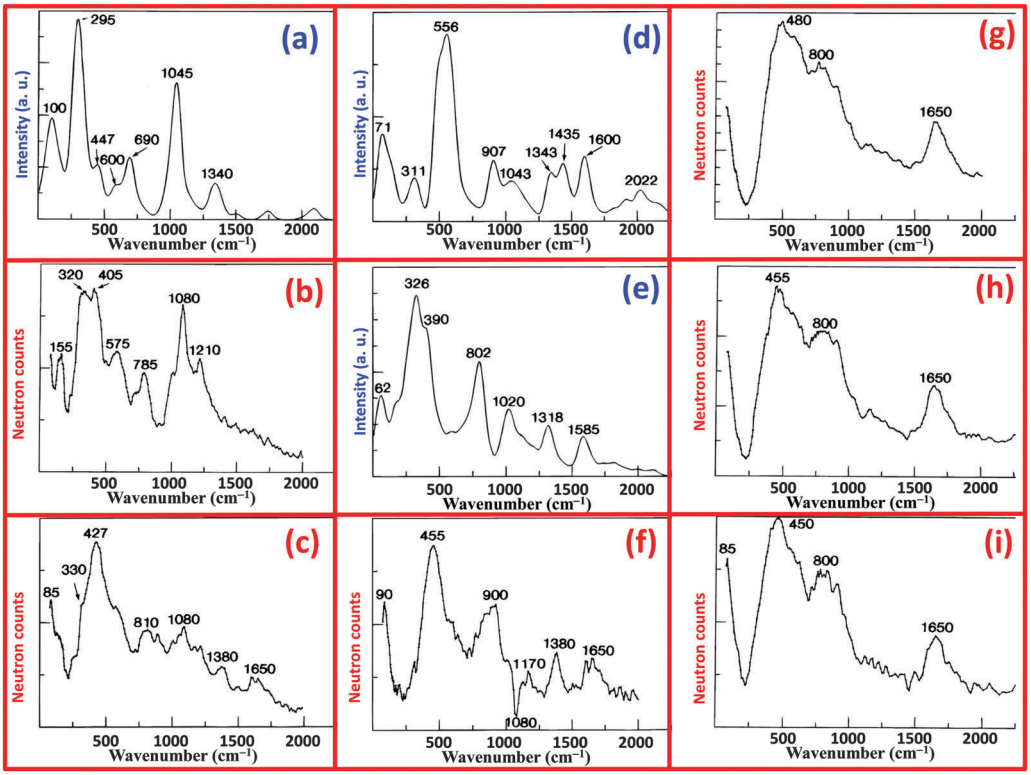

Fig. 6 Part (a): Calculated INS spectrum of dehydrated H-ZSM-5. Part (b): Experimental INS spectrum of dehydrated H-ZSM-5. Part (c): INS of H_2O adsorbed on H-ZSM-5 (loading θ_1: 3.5 molecules per unit cell). Part (d): Simulated INS spectrum for a hydroxonium ion (H_3O^+). Part (e): Simulated INS spectrum for a water molecule hydrogen-bonded to a bridging hydroxyl group. Part (f): Difference spectrum between the experimental INS spectra shown in parts (c) and (b). Parts (g), (h) and (i): Experimental INS spectra of water adsorbed at 35, 10.2 and 6.2 molecules per unit cell, respectively. Adapted by permission of the American Chemical Society (copyright 1996) from ref. 219.

3. Lewis acidity in zeolites

Lewis acid centers (*i.e.* electron acceptor centers) in zeolites can be of three main types: (i) charge-balancing extraframework cations,[204,224–231] discussed in Section 3.1; (ii) extraframework aluminum species Al^{3+},[113,204,232–244] reviewed in Section 3.2; and (iii) heteroatoms substituted at framework T positions,[21,22,245–257] described in Section 3.3. Sections 3.1–3.3 are devoted to the discussion on how IR spectroscopy is able to characterize charge-balancing cations, extraframework aluminum species and heteroatoms in zeolitic frameworks, respectively.

3.1. Charge-balancing extraframework cations

3.1.1 Alkaline and alkaline-earth cations. CO molecule has been the most widely used probe for characterizing cationic sites in zeolites. In the case of adsorption on alkaline and alkaline-earth cations, the interaction is of purely electrostatic origin because the absence of metal d-electrons prevents the presence of σ-(M^{n+} ← CO) and π-(M^{n+} → CO) components. The electric field created by the positive charge of the non-d cation, which is partially compensated by the first-shell negatively charged oxygen atoms, causes a polarization of the CO molecule, which depends on the local electric field strength of the site, *i.e.* mainly on the charge density of the cation that is modulated by the neighboring anions.[29,226,228–230,258–260] The spectroscopic evidence for the polarization of the CO molecule is an upward shift (blue shift) in the stretching frequency of C–O bond with respect to the $\tilde{\nu}_0$(CO) of the gas (2143 cm^{-1}),[261] owing to an increase in the force constant of the C–O bond and a decrease in the bond length.[29,262–266]

The closed-shell configuration of all alkali metal cations M^+ makes them ideal probing sites for a purely electrostatic interaction. In such a case, the perturbation of the C–O stretching frequency (Fig. 7), $\Delta\tilde{\nu}$(CO), is proportional to the local electric field strength ($||\boldsymbol{E}||$), according to the Stark effect:[230]

$$\Delta\tilde{\nu}(\mathrm{CO}) \propto ||\boldsymbol{E}|| = (1/4\pi\varepsilon_0)(q_{\mathrm{site}}/d_{\mathrm{M-CO}}{}^2) - ||\boldsymbol{E}_z|| \qquad (6)$$

where ε_0 is the permittivity of a vacuum ($\varepsilon_0 = 8.854 \times 10^{-12}$ C^2 m^{-2} N^{-1}, *i.e.* $1/4\pi\varepsilon_0 = 8.9876 \times 10^9$ N m^2 C^{-2}), q_{site} is the formal charge of an M^+ site (which is lower than $|e|$ because of the contribution of the negatively charged framework oxygen atoms, see the inset in Fig. 8a), $-||\boldsymbol{E}_z||$ is the contribution of the zeolitic environment and $d_{\mathrm{M-CO}}$ is the distance between the nucleus of the cation and the barycenter of CO ($d_{\mathrm{M-CO}} = R_{\mathrm{M}} + R_{\mathrm{CO}}$, where R_{M} is the cationic radius[269] and R_{CO} is the semi-major axis of CO along the C–O direction ($R_{\mathrm{CO}} = 2.1$ Å),[270] see inset in Fig. 8a). This fact is clearly evident in the spectra illustrated in Fig. 7, which shows the IR spectra collected at a liquid-nitrogen temperature on M-ZSM-5, part (a), and M-MOR, part (b) (M = Cs, Rb, K and Na), where $\Delta\tilde{\nu}$(CO) of the main band

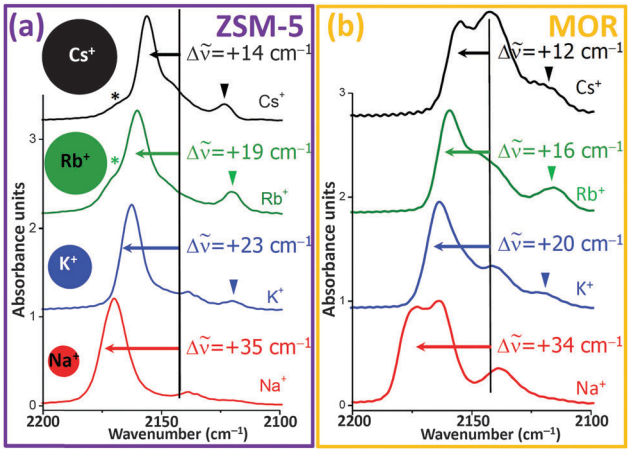

Fig. 7 Part (a): IR spectra of CO adsorbed on M^+-ZSM-5 at 77 K at an equilibrium pressure of *ca.* 102 Pa (M = Cs, Rb, K and Na). The main band is due to $M^+\cdots$CO adducts. The shoulder present on the left side of the main band of Rb and Cs (indicated with *) is due to a small fraction of sodium that is still present after the ion-exchange procedure.[228] On the left-hand side the different sizes of the cations are schematically represented. Part (b): Similar to part (a) for M^+-MOR. All the spectra are background-subtracted. In both parts, the vertical black line represents the C–O stretching frequency of the unperturbed molecule in the gas phase $\tilde{\nu}_0$(CO) = 2143 cm^{-1}, whereas the horizontal arrows give a qualitative idea of the blue shift $\Delta\tilde{\nu}$(CO) undergone by the CO molecule upon adsorption on the cationic sites. The broad band around 2138 cm^{-1} is due to liquid-like CO physisorbed in the channels,[226,227,267,268] whereas the band at lower wavenumbers, indicated by a triangle in the cases of Cs, Rb and K (not visible for Na) is due to minority $M^+\cdots$OC adducts. Previously unpublished figure reporting spectra from published data in ref. 228 and 229.

follows the order Na > K > Rb > Cs. On quantitative grounds, a linear correlation between $\Delta\tilde{\nu}$(CO) and $d_{M-CO}{}^{-2}$ is clearly visible from the data reported as full symbols in Fig. 8. Part (a) refers to the M-ZSM-5 and M-MOR spectra illustrated in Fig. 7, whereas part (b) refers to other zeolitic frameworks (ferrierite, β, and Y).

The model reported in eqn (6) was derived by Lamberti *et al.*,[230] who used the experimental $\Delta\tilde{\nu}$(CO) values measured by FTIR on Na^+-, K^+-, Rb^+- and Cs^+-exchanged ZSM-5 and MOR zeolites to determine the local positive electric field strength at the cation site $||\boldsymbol{E}||$ (2–6 V nm^{-1}), the effective charge on the cation site (q_{site} = +0.65–0.75 $|e|$) and the negative contribution from the negatively charged zeolitic framework $-||\boldsymbol{E}_z||$ (−4.2 and −4.7 V nm^{-1} for ZSM-5 and MOR, respectively). From eqn (6), the slope of the line resulting from the best linear fit of the points obtained for the different cationic forms of a given zeolitic framework is directly proportional to q_{site}, *i.e.* to the average charge of the first-shell oxygen atoms. This means that the slopes of the lines illustrated in Fig. 8 are an indirect measure of the basicity of the zeolitic framework (see Section 4). From the data reported in Fig. 8, the following scale of framework basicity emerges: Y ≫ MOR ∼ ZSM-5 ∼ FER ∼ β. Fig. 8a also contains the data collected for Li-ZSM-5 and Li-MOR, where the local electric field is as high as 8.2 V nm^{-1}. It is worth noting the large values of the local electric field probed by CO, as 1 V nm^{-1} = 10^9 V m^{-1}. The presence of a simple electrostatic interaction was observed already in the late 1970s by Hauge *et al.*, who monitored $\Delta\tilde{\nu}$(CO) of carbon monoxide in interactions with different alkali metal fluoride molecules isolated in cryogenic argon matrices.[271] They found that a positive $\Delta\tilde{\nu}$(CO) roughly increased upon a decrease in the cationic radius (R_M), which is a clear evidence that the $M^+\cdots$CO interaction is of purely electrostatic origin.

The simple electrostatic model summarized here[230] has successively been significantly improved by Ferrari *et al.* by a more sophisticated *ab initio* approach with bare cations[272] and fragments that mimic zeolite sites.[273] These two successive studies confirmed the electrostatic nature of the interaction. In this regard, the theoretical works of Larin *et al.*[259,260] are also worth mentioning together with the subsequent and more refined works of Nachtigall *et al.*[274–281]

Other minor spectroscopic features are present in the spectra shown in Fig. 7. The broad band around 2138 cm^{-1}, which is just below the vertical black line of the unperturbed CO molecule in the gas phase ($\tilde{\nu}_0$(CO) = 2143 cm^{-1}), is due to liquid-like CO molecules inside the zeolitic channels,[226,227,267,268] whereas the band at lower wavenumbers observed for the Cs, Rb and Na forms of both ZSM-5 and MOR frameworks is due to minority $M^+\cdots$OC adducts,[288] which is discussed in details in Section 7.2.3, which refers to variable-temperature IR experiments; in particular, see Fig. 32 and Table 9. This band is not observed at 77 K with Na-exchanged zeolites and is formed only at higher temperatures. Moreover, for $M^+\cdots$OC adducts, the interaction is of electrostatic origin and is governed by eqn (6); the only difference with respect to the dominant $M^+\cdots$CO adducts is that, as the dipole of the CO molecule is inverted, the Stark effect generated by the local electric field at the cationic site has the opposite effect and results in weakening of the C–O bond with a consequent red shift of the ν(CO) mode. Again, the size of the perturbation (and therefore of the red shift) is proportional to the local electric field; thus, a linear correlation between $\Delta\tilde{\nu}$(CO) and $(d_{M-CO})^{-2}$ is also observed for this family of bands; however, they have a negative slope; compare the continuous lines with the dotted segments in Fig. 8.

3.1.2. Transition metal cations: the copper case. Cation-exchanged zeolites with transition metal cations represent a large class of materials that play an important role in catalysis. Vibrational spectroscopies, in particular IR, have been very informative in determining the coordination and oxidation state of the extraframework cations. Herein, we have used copper-exchanged zeolites as a case study to discuss in detail the potential of IR spectroscopy, whereas other relevant charge-balancing transition metal cations, such as chromium,[289] manganese,[290–293] iron,[21,249–251,294–305] cobalt,[293,306–313] nickel,[293,314] zinc,[315–323] molybdenum,[324,325] palladium,[326–331] silver,[53,266,332–339] iridium,[340] cadmium,[289] platinum,[341–343] and gold,[344–351] are briefly mentioned. In the cases of tri- and tetravalent cations (Fe, Co, Zn, and Mo), IR spectroscopy is critical for discriminating between framework insertions (isomorphic substitutions at T sites, see Section 3.3) and extraframework charge-balancing cationic positions. In the case of noble metals (Pd, Ag, Ir, Pt and Au), IR spectroscopy is of great help for discriminating between isolated charged counter-ions and clustered reduced nanoparticles and for following their

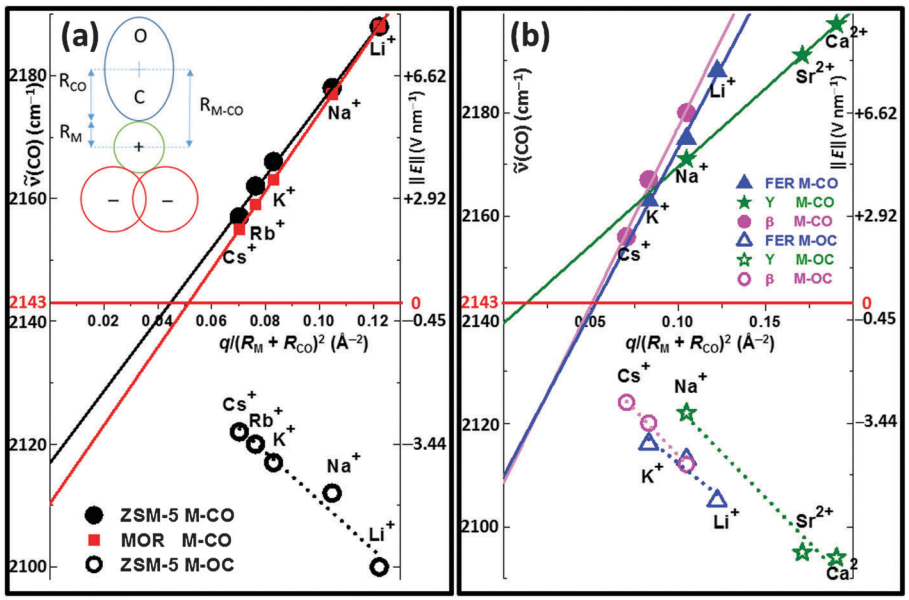

Fig. 8 Part (a): Left ordinate axis: $\tilde{\nu}$(CO) stretching frequency *vs.* $d_{M-CO}^{-2} = (R_M + R_{CO})^{-2}$ for alkali-metal-exchanged ZSM-5 (black circles, corresponding to the spectra shown in Fig. 7a) and mordenite (red squares, corresponding to the spectra shown in Fig. 7b). Full symbols refer to $M^+\cdots CO$ adducts (blue-shifted main IR band); open symbols refer to $M^+\cdots OC$ adducts (red-shifted minor IR band). The abscissa axis has been located at $\tilde{\nu}$(CO) = 2143 cm^{-1}, corresponding to $\Delta\tilde{\nu}$(CO) = 0 cm^{-1} and $||\boldsymbol{E}||$ = 0 V nm^{-1}. Right axis: determination of the local electric field strength probed by CO from $\Delta\tilde{\nu}$(CO) according to the Stark effect quantified by Pacchioni *et al.*[282] The dotted and dashed curves indicate the best linear fits of the two datasets; the corresponding intercepts with the ordinate axis ($R_M \rightarrow +\infty$ limit) provides the magnitude of the negative electric field E_z generated by the negatively charged zeolite cavities, see eqn (6). The inset illustrates a scheme of the cation site geometry showing the relationships between the geometrical quantities used in eqn (6). Part (b): Similar to part (a) for ferrierite (blue triangles), Y (green stars) and β (pink circles) zeolites. Parts (a) and (b) have been plotted on different scales; thus, a direct comparison between the slopes of the lines in the two parts is not possible. The inset in part (a) has been adapted with permission from ref. 230, copyright American Institute of Physics, 1995. The remaining parts are previously unpublished graphical material summarizing data from ref. 228, 229, 283–287.

evolution along different thermal, reductive, and oxidative treatments. In the quoted studies from the groups of Gates and Lamberti, IR characterization was often complemented by a parallel EXAFS and XANES study. The remaining part of this subsection is devoted to Cu-exchanged zeolites. This choice has been dictated by the huge experimental and theoretical study carried out over the last decades on Cu-exchanged zeolites,[23,29,161,162,266,352–365] mainly because of their use as efficient catalysts for the selective catalytic reduction (SCR) of NO_x by ammonia (NH_3-SCR),[364,366–374] as discussed in Section 9.1.3.

In this context, we want to stress that the choice of an appropriate probe molecule is a crucial point in FTIR spectroscopy. Different probe molecules may be able to reveal different aspects of the investigated surface, and often the combined use of markedly different probes is the key for reaching a comprehensive understanding of the surface.[23,29] In this section, we will show how the combined use of CO, N_2, and NO probes to characterize Cu-exchanged zeolites ZSM-5, MOR, β, Y, and SSZ-13 has been largely informative.[161,375–386] The use of a weakly interacting probe such as N_2 allows the perturbation induced by the probe to be minimized and thus enables better discrimination between similar adsorption sites. The use of CO allows selectivity towards Cu^+ sites, whereas NO can probe both Cu^+ and Cu^{2+} sites. Experiments performed at liquid-nitrogen temperature allow to detect the surface sites, which are characterized by a weak interaction with the probe not visible in room temperature (RT) experiments. This is relevant for N_2, whereas a low-temperature experimental set-up is essential for NO, which is reactive at RT and therefore does not act solely as a probe.[378,385,386]

In the presence of an acceptor of electron pairs, such as a transition metal cation possessing empty orbitals of suitable energy (and thus acting as a Lewis acidic center), the C-end lone pair of CO is transferred to the metal cation, giving rise to a σ-coordination ($M^{n+} \leftarrow CO$). In this case as well, the interaction between CO and the metal cation causes the $\Delta\tilde{\nu}$(CO) stretching frequency to shift towards a value higher than that of the gas, similar to the case for the electrostatic interaction discussed in Section 3.1.1. It is generally accepted that the higher the blue shift, the stronger is the interaction, according to the Lewis acidic strength of the metal site.[29,262–266,387] Moreover, in the case of transition metal cations possessing partially filled d orbitals, significant $M^{n+} \rightarrow CO$ π-donation can occur from the orbitals of the d-block metal back to the orbitals of the CO molecule. The increase in electron density in the antibonding orbitals of the CO molecule causes the force constant of the C–O bond to decrease, the C–O bond length to increase and therefore $\Delta\tilde{\nu}$(CO) to be red-shifted with respect to that of the gas. The strength of the bond between CO and d-block metal cations, as well as the $\Delta\tilde{\nu}_{CO}$ stretching frequency, is not expected in such a case to be simply correlated. In fact, as far as the strength of the carbonyl bond increases, as a consequence of the synergistic effect of the σ-($M^{n+} \leftarrow CO$) and π-($M^{n+} \rightarrow CO$) components, the

resulting $\Delta\tilde{\nu}$(CO) is located at a spectral position that is a compromise between blue and red shifting interactions.[29,262–266,337,388–392]

Cu-exchanged zeolites are usually prepared *via* liquid-phase exchange from cupric salts, resulting in the introduction of divalent cations into the framework.[393] Since the late 1980s they have been widely investigated because of their catalytic activity in the direct decomposition of NO.[369,393–400] Upon thermal activation, cupric ions are reduced to cuprous species, resulting in Cu^+-zeolites.[363,383,384,386,401–403]

CO probe has been used to confirm the high coordinative unsaturation of Cu^+ cations hosted in zeolites. Indeed, depending on CO equilibrium pressure (P_{CO}) and temperature, carbonyl complexes of high structural and spectroscopic quality have been formed at Cu^+ sites. At room temperature, relatively stable adducts such as monocarbonyl $[Cu(CO)]^+$ and dicarbonyl $[Cu(CO)_2]^+$ complexes are observed[266,375,376,378–386,388,404–406] (see Fig. 9a and b), which evolve into tricarbonyl $[Cu(CO)_3]^+$ species when the system is cooled to liquid-nitrogen temperature,[266,376,378–386,404,405] see Fig. 9c. The occurrence of a $Cu^+\cdots(CO) \rightarrow Cu^+\cdots(CO)_2$ transformation has been proved using Cu K-edge EXAFS spectroscopy,[407] and two-dimensional correlation spectroscopy (2D-COS).[266] The latter is a mathematical method for analyzing a series of spectra collected on a system subjected to a perturbation (such as a gradient in pressure or temperature). It is used to assess statistical relationships between different spectroscopic features that change during a dynamic variation for extracting valuable information, which can otherwise be difficult to obtain.[408–417]

IR spectroscopy of CO dosed at increasing P_{CO} onto Cu^+-zeolites is reported in Fig. 9a–c for β, SSZ-13, Y, ZSM-5, and mordenite hosting frameworks. At a low P_{CO} (Fig. 9a), a single band is observed for the monocarbonyl complex in ZSM-5, β, SSZ-13 and mordenite zeolites. Conversely, in Y zeolite, two different $Cu^+\cdots CO$ adducts are observed characterized by $\tilde{\nu}$(CO) = 2160 and 2144 cm^{-1}, which are formed at two different cationic sites, labeled as **II** and **II***, respectively (see Fig. 9e).[384] This IR evidence is supported by the Rietveld refinement of X-ray Powder Diffraction (XRPD) data collected at the European Synchrotron Radiation Facility (ESRF), where two different cationic sites were determined in the supercage.[384] By increasing P_{CO} (Fig. 9b), the formation of $Cu^+\cdots(CO)_2$ adducts is observed for all the samples, as proved by the splitting of the monocarbonyl band into two bands due to the $\nu_{asym}(CO)_2$ and $\nu_{sym}(CO)_2$ modes of the complex.[161,378,379,384,404,407] The fact that both bands are IR-active indicates that the intrazeolitic $Cu^+\cdots(CO)_2$ adducts have C_{2v} symmetry (or lower), whereas their homogeneous counterparts are linear ($D_{\infty h}$).[418] A further increase in P_{CO} (Fig. 9c) for ZSM-5, β and Y zeolites causes a nearly total $Cu^+\cdots(CO)_2 \rightarrow Cu^+\cdots(CO)_3$ transformation, as indicated by the appearance of a new triplet of IR-active bands. This triplet is indicative of a symmetry lower than C_{3v}, unlike the homogeneous counterparts, which form planar adducts of D_{3h} symmetry.[418]

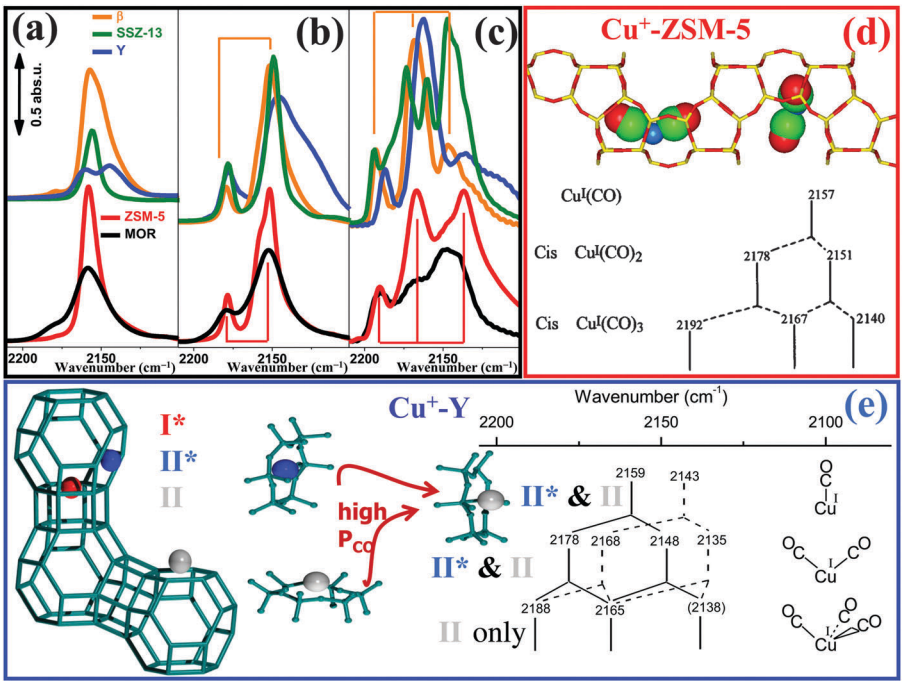

Fig. 9 IR spectra of CO dosed at liquid-nitrogen temperature onto Cu^+-β (orange curves), H^+-Cu^+-SSZ-13 (green curves), Cu^+-Y (blue curves) Cu^+-ZSM-5 (red curves), and Cu^+-MOR (black curves) zeolites. Parts (a), (b) and (c) show low, medium and high P_{CO} spectra, respectively, approximately corresponding to mono-, di- and tri-carbonyl complexes. Part (d): schematic representation of a fraction of the ZSM-5 framework with two equivalent Cu^+ sites forming a di-carbonyl complex (top, corresponding to the situation indicated by the red spectrum in part b) and evolution of the C–O stretching frequencies along the $Cu^+\cdots(CO) \rightarrow Cu^+\cdots(CO)_2 \rightarrow Cu^+\cdots(CO)_3$ pathway driven by an increase in P_{CO}. Part (e): Schematic representation of a fraction of the Y zeolite framework with three inequivalent Cu^+ sites (**I***, **II*** and **II**, left) as determined by XRPD,[384] the P_{CO}-induced **II*** → **II** migration (center), and the evolution of the C–O stretching frequencies along the $Cu^+\cdots(CO) \rightarrow Cu^+\cdots(CO)_2 \rightarrow Cu^+\cdots(CO)_3$ pathway driven by an increase in P_{CO}. Site **I*** is not accessible by CO. See Table 3 for the exact frequencies of mono-, di- and tricarbonyl components formed inside Y and other zeolites. Previously unpublished figure reporting spectra published in ref. 161, 378, 379 and 384 (parts a–c) and adapting schemes published in ref. 29 and 407 (part d) and ref. 29 and 384 (part e).

In Cu^+-SSZ-13, a significant fraction of $Cu^+\cdots(CO)_2$ complexes is still present.[161]

As far as mordenite is concerned, the presence of cations in the less accessible side pocket sites implies the simultaneous presence of mono-, di- and tri-carbonyl adducts even at a higher P_{CO},[379] resulting in a broader and rather unresolved IR spectrum (black curve in Fig. 9c). For Y zeolite, it is worth noting that, in spite of the presence of two cationic sites in the supercage, the IR spectrum obtained at high P_{CO} indicates the presence of only one family of $Cu^+\cdots(CO)_3$ adducts. This relevant fact is explained in terms of the high solvation power of CO molecules, which are able to extract Cu^+ cations from the more shielded position (site **II***) to more exposed cationic positions (site **II**), as proved by both EXAFS and XRPD,[384] as shown Fig. 9e. The set of spectra collected for Cu^+-Y represents a clear example of adsorption-induced effects on cation displacement. A similar solvation effect promoted by the adsorption of CO has been observed for Cu^+-ZSM-5,[404,407] Ni^{2+}/SiO_2,[419,420] and Cr^{2+}/SiO_2.[421] The experiments reported in Fig. 9a–c indicate that ZSM-5 and β zeolites are more suitable for the formation of well-defined $Cu^+\cdots(CO)_n$ (n = 1, 2, 3) complexes than Y or MOR zeolite, and are indicative of how IR spectroscopy of adsorbed probe molecules is able to discriminate different surface sites. In the case of H^+-Cu^+-SSZ-13 (green curves in Fig. 9c),[161] the situation is more complex because at high P_{CO}, ZOH$\cdots$CO adducts are also observed at both Brønsted sites (2173 cm^{-1}) and external silanols (2160 cm^{-1}), together with the liquid-like component (2138 cm^{-1}).[226,227,267,268]

The exact frequencies of mono-, di- and tri-carbonyl components reported to be formed inside Cu-exchanged zeolites, as shown in Fig. 9a and discussed above, and inside other zeolites are given in Table 3.

N_2 molecule interacting with cuprous ions inside zeolites leads to a ν(NN) band in the 2300–2290 cm^{-1} region,[377,378,428] which is significantly downshifted with respect to the (Raman active) gas-phase value of 2321 cm^{-1}. This bathochromic shift could be explained in terms of chemical interactions involving molecular orbitals (MO) of the probe molecule and a suitable d-orbital of the metal cation.[29] For dinitrogen, the corresponding MOs are $3\sigma_g$, which act as electron donors, while the empty $1\pi_g$ acts as an electron acceptor. Both σ-donor and π-acceptor interactions weaken the N≡N bond, thus explaining the observed bathochromic shift in the $Cu^+\cdots N_2$ adducts.[29] The interaction of N_2 with Cu^{2+} and H^+ is considerably weaker.

The IR spectra of N_2 adsorbed on vacuum-activated Cu-SSZ-13 are illustrated in Fig. 10a. A predominant band centered at 2293 cm^{-1} is observed starting from low coverages. This component increases in intensity upon increasing coverage without shifting, while a second component centered around 2300 cm^{-1} is progressively developed. Both components are assigned to $Cu^+\cdots N_2$ stable complexes.[161,377,378,428] The presence of two components in the spectrum of Cu-SSZ-13 implies the presence of two significantly different (in terms of the local environment of the cation) Cu^+ sites, which supports the conclusions proposed by Dedecek *et al.*[429] and Szanyi *et al.*[425,430] As expected, the Cu^+ sites that are involved behave as isolated adsorption sites for N_2, because of the invariance in the corresponding IR band upon changes in pressure.[29]

A single and symmetric band centered at 2296 cm^{-1} is observed for vacuum-activated Cu-ZSM-5 (Fig. 10b). Moreover, in this case, the frequency of the band is coverage-independent. This frequency is almost equivalent to that found for Cu^+-ZSM-5 prepared by gas-phase exchange with CuCl,[378] as shown in Table 4. This implies that, if present, different Cu^+ cationic sites in ZSM-5 are characterized by very similar local environments that cannot be discriminated by N_2 adsorption. The spectra of N_2 adsorbed on Cu-β (Fig. 10c) are dominated by a coverage-independent component at 2293 cm^{-1}. A second component, which is less intense and resolved than in the case of Cu-SSZ-13, develops at higher coverages around 2300 cm^{-1}.

The fact that the bathochromic shift in the main component is larger for Cu-SSZ-13 and Cu-β than for Cu-ZSM-5 implies that

Table 3 C–O and $\nu_a(CO)_m$ (m = 1, 2, 3) stretching frequencies of carbonyl adducts on Cu^+-zeolites and supported Cu_2O. When needed, label "a" (a = l, m, h) refers to low, medium and high frequency components of the adduct. For Cu_2O/SiO_2 and bulk Cu_2O samples, an interval of frequencies is reported for ν(CO), $\nu_l(CO)_2$ and $\nu_h(CO)_2$ because the position of the frequency of the band was pressure-dependent.[422] sh = shoulder; N.F. = not formed; N.D. = not detected (because experiments were performed at RT). New table, updating tables previously published in ref. 161 and 423 and reporting data published in the references quoted in the last column

Sample		$\tilde{\nu}$(CO) (cm^{-1})	$\tilde{\nu}_l(CO)_2$ (cm^{-1})	$\tilde{\nu}_h(CO)_2$ (cm^{-1})	$\tilde{\nu}_l(CO)_3$ (cm^{-1})	$\tilde{\nu}_m(CO)_3$ (cm^{-1})	$\tilde{\nu}_h(CO)_3$ (cm^{-1})	Ref.
H-Cu-SSZ-13[a]		2155	2150	2178	2134 (sh)	2169 (sh)	2194	161
Cu-ZSM-5[a]		2158	2150	2178	2134 (sh)	2166 (sh)	2192	161
Cu-β[a]		2158, 2153	2152	2180	2134 (sh)	2168 (sh)	2193	161
Cu-ZSM-5[b]		2157	2151	2178	2138	2167	2192	378
Cu-β[b]		2157	2152	2180	2146	2167	2193	424
Cu-SSZ-13		2154	2151	2178	N.D.	N.D.	N.D.	425
Cu-MOR[b]		2159	2152	2180	2146	2167	2193	379
Cu-FER[b]		2157	2149	2178	2135 (sh)	2170	2191	426
Cu-Y[b]	Site II	2159	2148	2178	2138	2165	2188	384
	Site II*		2143	2135	2168			
Na-Cu-ETS-10(B)		≅2155	≅2150	≅2180	≅2135	2162	2191	423
Cu^+-MCM-41		2159	2152	2180	2138	2171	2194	427
Cu_2O/SiO_2		2132–2127	2127–2120	2162–2154	N.F.	N.F.	N.F.	422
Cu_2O unsupported		2127–2121	2121–2113	2158–2145	N.F.	N.F.	N.F.	422

[a] Cu-zeolites prepared *via* standard liquid-phase cation exchange with cupric salts and subjected to reduction by thermal activation *in vacuo*. [b] Cu-zeolites prepared *via* stoichiometric gas-phase exchange with CuCl, resulting in the atomic ratio of Cu/Al = 1.

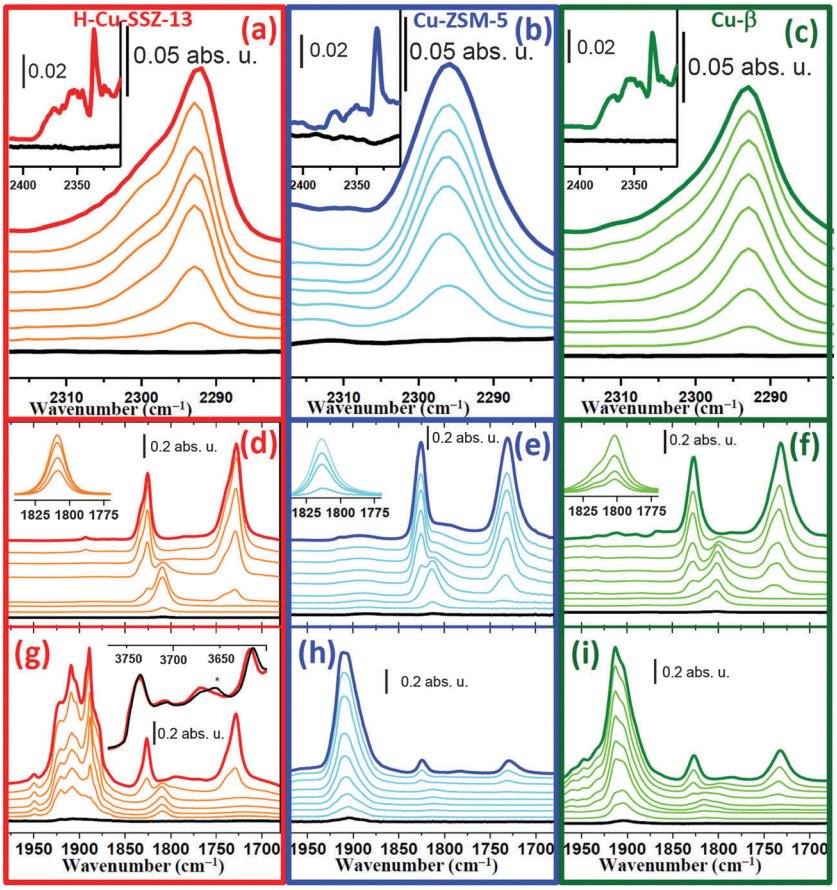

Fig. 10 Part (a): IR spectra of N_2 dosed at liquid-nitrogen temperature (~100 K) onto vacuum-activated H-Cu-SSZ-13 zeolite. The bold black spectrum is the background collected before N_2 dosage, whereas orange spectra present increasing equilibrium pressures of N_2 from 10^{-2} to 5 Torr (bold red curve). The main part refers to the ν(N–N) stretching region of $Cu^+\cdots N_2$ adducts, whereas the inset shows the region related to adducts formed at Brønsted sites ($ZOH^+\cdots N_2$) and extraframework species ($Al^{3+}\cdots N_2$). Part (b): Similar to part (a) for Cu-ZSM-5 zeolite. Part (c): Similar to part (a) for Cu-β zeolite. Part (d): IR spectra of NO dosed at liquid-nitrogen temperature (~100 K) on vacuum-activated H-Cu-SSZ-13 zeolite at increasing equilibrium pressures (from 7×10^{-2} to 7×10^{-1} Torr, bold red curve). The spectra in the main part show the evolution of $Cu^+\cdots NO \rightarrow Cu^+\cdots(NO)_2$; the inset shows low-coverage spectra corresponding to $Cu^+\cdots NO$ complexes. Part (e): Similar to part (d) for Cu-ZSM-5 zeolite. Part (f): Similar to part (d) for Cu-β zeolite. Part (g) similar to part (a) for O_2-activated zeolites showing $Cu^{2+}\cdots NO$ and residual $Cu^+\cdots(NO)_2$ adducts. The inset in Part (g) shows the corresponding bands in the ν(OH) region, confirming the decrease in the 3650 cm^{-1} band (see *) upon the formation of NO adducts with dehydrated $[Cu–OH]^+$ species. Part (h): Similar to part (g) for Cu-ZSM-5 zeolite. Part (i): Similar to Part (g) for Cu-β zeolite. Previously unpublished figure adapting spectra published in ref. 161.

the dominant Cu^+ sites in SSZ-13 and β are able to perform more efficient σ-donation and/or π-back-donation processes with the MO of the N_2 molecule. This could be associated with a larger space in the vicinity of the cation or a more effective ionicity of the cation in the cases of Cu-SSZ-13 and Cu-β.[161]

In both Cu-SSZ-13 and Cu-β samples, the less abundant Cu^+ sites, which are responsible for the shoulder around 2300 cm^{-1}, interact with N_2 in a similar way to the Cu^+ cations hosted in the MOR framework,[428] as shown in Table 4. The absence of any peak around 2283 cm^{-1} confirms that no undesired additional Cu_2O phase[423] is present in the three samples.

We will conclude this section by discussing the interaction of NO with both Cu^+ and Cu^{2+} sites in zeolites. The main difference between CO and NO is that the additional electron in NO occupies the π*-orbital. This causes greater sensitivity for NO to the electronic state of the cation during the formation of $M\cdots NO$ bond than for CO, because even slight alterations in electron density in this orbital noticeably change the frequency of the NO stretching vibration, $\tilde{\nu}$(NO). NO is currently used to determine the oxidation state of copper cations in zeolites, due to its ability to form stable nitrosyl adducts with both Cu^{2+} and Cu^+ cations.[29,161,375,376,378,385,386,431]

At room temperature, the coordination of NO to Cu^+ sites and formation of nitrosyls are combined with a decomposition reaction, with the initial formation of N_2O and $Cu^{2+}(NO)(NO_2)$ adducts.[376,378,385] For this reason, to suppress NO decomposition, NO must be dosed at liquid-nitrogen temperature to be used as a probe molecule on copper sites.

Fig. 10 illustrates NO adsorption experiments on vacuum- (parts d–f) and O_2-activated (parts g–i) samples. Starting from low coverages of NO, vacuum-activated Cu-SSZ-13 (Fig. 10d) exhibits a band centered at 1810 cm^{-1} due to the interaction between NO and isolated Cu^+, leading to the formation of $Cu^+\cdots NO$ mononitrosyl complexes.[29,161,376,378,385,386] The first dosages of NO on the sample are illustrated in the inset of this figure, which clearly show a symmetric and well-defined band.

Table 4 $\tilde{\nu}$(NN) stretching frequencies of dinitrogen adducts formed at Cu^+ sites in Cu-exchanged zeolites and zeotypes and on supported Cu_2O. sh = shoulder. New table, updating tables previously published in ref. 161 and 423 and reporting data published in the references quoted in the last column

Sample	$\tilde{\nu}$(NN) (cm^{-1})	Ref.
Cu-SSZ-13[a]	2293, 2300 (sh)	161
Cu-ZSM-5[a]	2296	161
Cu-β[a]	2293, 2300 (sh)	161
Na-Cu-ETS-10[a]	2281	423
Na-Cu-ETS-10[a,c]	2285	423
Cu-MOR[a]	2299	428
Cu-ZSM-5[b]	2295	378
Cu_2O/SiO_2	2283	423

[a] Cu-zeolites prepared *via* standard liquid-phase cation exchange with cupric salts and subjected to reduction by thermal activation *in vacuo*. [b] Cu-zeolites prepared *via* stoichiometric gas-phase exchange with CuCl, resulting in the atomic ratio of Cu/Al = 1. [c] Sample obtained after a second ion-exchange process.[423]

By increasing the coverage of NO, the 1810 cm^{-1} band evolves into two main components at 1826 cm^{-1} (with a shoulder at 1833 cm^{-1}) and 1728 cm^{-1} (with a shoulder at 1742 cm^{-1}), which are ascribed as symmetric and asymmetric stretching of $Cu^+(NO)_2$ dinitrosyl complexes, respectively.[29,161,376,378,385,386] A single NO molecule is able to form similar $Cu^+\cdots NO$ adducts at two slightly different Cu^+ sites (already detected by adsorption of N_2, see Fig. 10a); however, when a second NO molecule is inserted, the $Cu^+\cdots(NO)_2$ complexes are able to probe a larger space around the Cu^+ sites, and therefore they can better discriminate among them. The absence of any significant band in the 1950–1870 cm^{-1} range, where $Cu^{2+}\cdots(NO)$ complexes are expected, implies that nearly all cupric ions in accessible positions have been reduced to cuprous ions during thermal activation. This is in line with what has already been observed for other Cu^{2+}-exchanged zeolitic systems.[383,386] Vacuum-activated Cu-ZSM-5 (Fig. 10e) and Cu-β (Fig. 10f) exhibit approximately the same trend as Cu-SSZ-13, and the corresponding frequencies of mono- and di-nitrosyl complexes are reported in Table 5. In Cu-ZSM-5, the shape of the mononitrosyl band at 1813 cm^{-1} has a significant tail on the low-frequency side, which suggests some site heterogeneity, whereas for Cu-β, two components are observed at 1802 cm^{-1} and 1815 cm^{-1} (shoulder). In both the cases, we observe total conversion of mononitrosyl into dinitrosyl complexes upon an increase in P_{NO}. The exact frequencies of the observed nitrosyl complexes are reported in Table 5, together with literature data reported for comparison.

Despite the presence of oxygen during thermal treatment, a non-negligible amount of Cu^+ was detected on the O_2-activated samples (Fig. 10 parts g–i). Both the shape and position of the bands for $Cu^+\cdots(NO)_n$ (n = 1, 2) complexes with O_2-activated samples are approximately equal to those observed with vacuum-activated samples, which implies that the location and distribution of Cu^+ are not affected by the presence of oxygen during thermal treatment. Finally, the complexity of the absorption features of $Cu^{2+}(NO)$ adducts (which is particularly relevant for Cu-SSZ-13) clearly suggests the presence of different Cu^{2+} cationic sites, see Table 6, where the stretching frequencies of mono- and di-nitrosyl adducts formed on cupric cations inside Cu-SSZ-13 and other zeolites is summarized.

This section was devoted to the use of probe molecules to characterize Cu sites in Cu-exchanged zeolites by IR. As detailed hereafter in Sections 9.1.2, 9.1.3 and 9.3.1, IR also played a relevant role in determining the reactivity of Cu-zeolites.[162,363,364,378,385,386,435,436]

3.1.3. Post-transition metal and lanthanide cations. Besides the standard cation-exchange procedure, which directly introduces post-transition metal cations into extraframework cationic positions inside zeolite pores, several post-transition metals have been successfully introduced into the zeolitic framework *via* isomorphic substitution at tetrahedral Si sites, as discussed in Section 3.3. Similar to the case of iron,[21,249–251,294–305] severe thermal treatment can lead to the migration of a fraction of post-transition metal ions from framework into extraframework positions, similar to those occupied *via* conventional cation exchange. For both gallium[437–445] and indium,[439,440] IR spectroscopy has been the technique of choice to discriminate the framework M(III) species, which lead to Brønsted acidity,

Table 5 ν(N–O) stretching frequencies of mono- and di-nitrosyl adducts at Cu^+ sites in zeolites and supported Cu_2O. N.O. = not observed. Table reproduced with permission from ref. 161, copyright Royal Society of Chemistry

Sample (site)	$\tilde{\nu}$(NO) (cm^{-1})	$\tilde{\nu}_{sym}(NO)_2$ (cm^{-1})	$\tilde{\nu}_{asym}(NO)_2$ (cm^{-1})	Ref.
Cu-SSZ-13 (A)	1809	1826	1728	161
Cu-SSZ-13 (B)	1809	1833 (sh)	1742 (sh)	161
Cu-SSZ-13[a]	1810, 1785 (sh)	N.O.	N.O.	425
Cu-ZSM-5	1813	1730	1825	161
Cu-ZSM-5[b]	1812	1734	1827	378
Cu-β	1802, 1815 (sh)	1828	1734, 1743 (sh)	161
Cu-β[a]	1810	N.O.	N.O.	432
Cu-β[b]	1811	1730	1826	424
Cu-MOR[b] (main channel)	1813	1730	1828	23
Cu-MOR[b] (side pocket)	1813	1785	1870	23
Cu-Y[b] (II)	1814	1728	1824	384
Cu-Y[b] site (II*)	1788	N.O.	N.O.	384
Cu_2O/SiO_2	1775	1709	1811	423

[a] Experiment performed at room temperature, thus under conditions of NO decomposition. [b] Cu-zeolites prepared *via* stoichiometric gas-phase exchange with CuCl, resulting in an atomic ratio of Cu/Al = 1.

Table 6 ν(N–O) stretching frequencies of mononitrosyl adducts at Cu^{2+} sites in zeolites and supported CuO. w = weak; m = medium; s = strong; and sh = shoulder. Table reproduced with permission from ref. 161, copyright Royal Society of Chemistry

Sample (site)	$\tilde{\nu}$(NO) (cm^{-1})	Ref.
Cu-SSZ-13	1950^{w}, 1921^{m}, 1909^{m}, 1904^{m}, 1890^{s}	161
Cu-SSZ-13[a] (I)	1920–1880	425
Cu-SSZ-13[a] (II)	1948, 1930	425
Cu-ZSM-5	1912, 1905, 1895 (sh)	161
Cu-ZSM-5[a]	1921, 1912, 1906, 1895	433
Cu-ZSM-5[b]	1890	378
Cu-β	1912, 1903, 1895 (sh)	161
Cu-β[a]	1896	432
Cu-MOR[a]	1960, 1938, 1921, 1909^{s}, 1895	433
Cu-Y[b] (II)	1955	384
Cu-Y[b] (II*)	1923	384
CuO	1865, 1855	434

[a] Experiment performed at room temperature, thus under conditions of NO decomposition. [b] Cu-zeolites prepared *via* stoichiometric gas-phase exchange with CuCl, resulting in an atomic ratio of Cu/Al = 1.

and extraframework M(III) species, which lead to Lewis acidity, and to monitor their relative evolution during different activation/reaction treatments. IR spectroscopy is also informative in the characterization of cation exchange with lead(II)[289] and post-synthetic modification with tin precursors.[446,447]

We finish this brief summary of the periodic table of the elements by considering lanthanide cations. Their insertion as charge-balancing cations inside zeolitic frameworks, besides some catalytic applications,[448–454] results in remarkable luminescence properties.[455–464] In addition, the local environment, accessibility and reactivity of lanthanide charge-balancing cations have been widely investigated by vibrational spectroscopies. Without entering into details, we report some relevant bibliography for the different cations as follows: lanthanum,[448–453,465–472] cerium,[449,454,472–477] praseodymium,[449,472] neodymium,[449,465,467,468,470,472,478] samarium,[449,467,468,472,475,476,479] europium,[449,458,472,480–484] gadolinium,[449,467,468,481,484] terbium,[458,481,483,485] dysprosium,[467,468] holmium,[476] erbium,[486] and ytterbium.[465,470,487]

3.1.4. Correlation among different probes and different cationic sites. As thoroughly discussed in Section 3.1.2, the use of different probes, such as CO (Fig. 9), N_2 (Fig. 10a–c) and NO (Fig. 10d–i), provides a fundamental understanding of the nature and coordination of adsorbing sites.

We start this comparison by considering H_2 and CO probes. For electrostatic-type interactions, when a comparison is made with spectroscopic data concerning adsorption at the same sites, it is found that the shifts in the $\Delta\tilde{\nu}$(CO) and $\Delta\tilde{\nu}$(HH) frequencies are linearly correlated and that the bathochromic shift in the ν(HH) mode is basically twice the hypsochromic shift in ν(CO):[29,304]

$$\Delta\tilde{\nu}(\mathrm{HH}) \approx -2\Delta\tilde{\nu}(\mathrm{CO}) \quad (7)$$

The validity of the empirical relationship (7) can be appreciated from the data shown in Fig. 11a. The larger sensitivity of $\Delta\tilde{\nu}$(HH) as compared to $\Delta\tilde{\nu}$(CO) is mainly due to the fact that a single H–H bond is more affected than a triple C≡O bond by local effects (such as structure and the number of ligands in the coordination sphere) which possibly influences the physico-chemical properties of the adsorbing centers.[18,29] The data illustrated in Fig. 11a clearly show that this relationship has been verified for a number of systems, including SiO_2, acidic and exchanged zeolites, and oxides. The gray shaded region

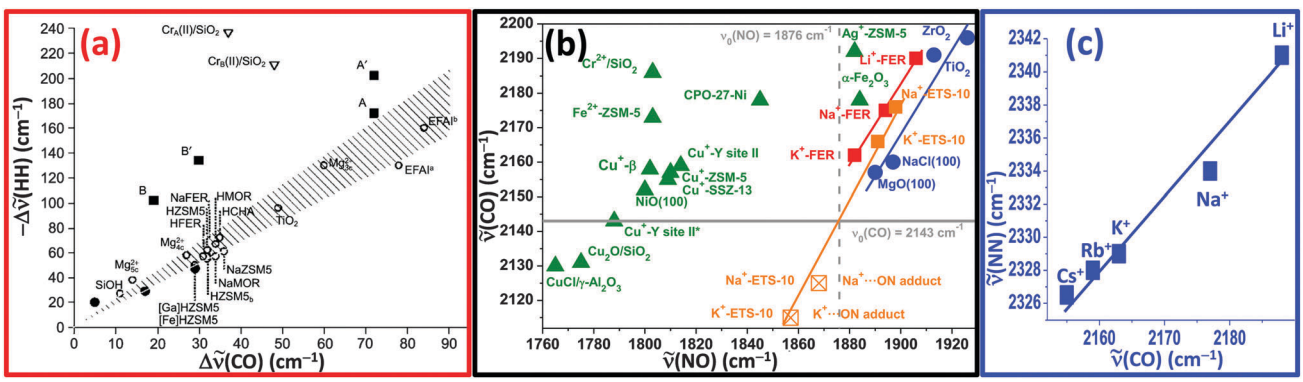

Fig. 11 General comparison between different probes used to characterize the same sites. Part (a): Plot of the shifts $-\Delta\tilde{\nu}$(HH) for H_2 adsorbed on the Lewis or Brønsted acid sites of zeolitic and oxide materials *vs.* the corresponding shifts observed for CO: $\Delta\tilde{\nu}$(CO). Circled data are obtained from a study by Zecchina *et al.*[18] Triangles refer to the Cr^{2+}/SiO_2 system (Phillips catalyst).[489] Data concerning Fe-Sil Lewis acid sites are represented by filled squares ($\Delta\tilde{\nu}$(HH), values are obtained from a study by Berlier *et al.*;[304] $\Delta\tilde{\nu}$(CO) values are obtained from a study by Berlier *et al.*;[249]) A and A′ refer to Fe^{3+} centres, whereas B and B′ refer to Fe^{2+} centres; those concerning Brønsted sites are represented by filled circles. The gray dashed region corresponds to nearly pure electrostatic interactions between H_2 (or CO) and the adsorbing site. Adapted with permission from ref. 249, copyright Elsevier 2006. Part (b): $\tilde{\nu}$(CO) *vs.* $\tilde{\nu}$ (NO) for monomeric CO and NO complexes formed on Li^+-, Na^+-, and K^+-ferrierite (red squares); Na^+- and K^+-ETS-10 (orange squares); TiO_2, ZrO_2, NaCl and MgO (blue circles) and α-Fe_2O_3, NiO, Cu^+-ZSM-5, Ag^+-ZSM-5, CPO-27-Ni, Cu_2O/SiO_2, CuCl/γ-Al_2O_3, Cr^{2+}/SiO_2 and Fe^{2+}-ZSM-5 (green triangles). In the cases of Cr^{2+}/SiO_2, Fe^{2+}-ZSM-5 and CuCl/γ-Al_2O_3, where only dinitrosyl adducts were observed, the frequency of the barycenter has been reported. For systems undergoing a coverage-dependent shift, the frequency at the $\theta \rightarrow 0$ limit has been reported. Data concerning MgO and NaCl are inferred from the published data by assuming that the $\tilde{\nu}$(NO) frequencies of the monomers coincide with the highest-frequency mode of the adsorbed dimers. Part (c): correlation between $\tilde{\nu}$(NN) and $\tilde{\nu}$(CO) observed in alkali-metal-exchanged MOR; previously unpublished graphic, reporting data from ref. 204 and 229. Adapted and used with permission from ref. 29, copyright Royal Society of Chemistry, 2010.

corresponds to interaction mechanisms between H_2 (or CO) and the adsorbing sites that are dominated by electrostatic forces. On the contrary, it is worth noting the large deviation of the points corresponding to Cr^{2+} species grafted on silica,[488] a system where covalent contributions play a certain role in both $Cr^{2+}\cdots CO$ and $Cr^{2+}\cdots H_2$ interactions.[489]

A comparison between CO and NO probes used on the same sites is shown in Fig. 11b. Investigated systems are as follows: Li^+-, Na^+- and K^+-FER,[490] Na^+- and K^+-ETS-10,[382] Cu^+-ZSM-5,[378,385] Cu^+-Y,[384] Cu^+-β,[161] Cu^+-SSZ-13,[161] Ag^+-ZSM-5,[334,335] and Fe^{2+}-ZSM-5,[249] and, for comparison, TiO_2,[491] ZrO_2,[491] MgO,[39] NiO,[492] α-Fe_2O_3,[21] Cu_2O/SiO_2,[423] NaCl,[493] $CuCl/\gamma$-Al_2O_3,[431] Cr^{2+}/SiO_2,[488] and CPO-27-Ni.[494,495]

A linear dependence has been obtained for $\tilde{\nu}$(CO) *vs.* $\tilde{\nu}$(NO) data collected for alkali-metal-exchanged ferrierite (red squares in Fig. 11b), where the interaction is purely electrostatic and the anionic environment is exactly the same for the three investigated cations (see the discussion in Section 3.1.1). The same is true for Na^+- and K^+-exchanged ETS-10 ($M^+\cdots NO$ and $M^+\cdots ON$ linkage isomers, filled and open orange squares, respectively, in Fig. 11b) and for the $\tilde{\nu}$(NN) *vs.* $\tilde{\nu}$(CO) relation obtained with Li^+-, Na^+-, K^+-, Rb^+- and Cs^+-exchanged mordenite,[204,229] as shown in Fig. 11c.

An acceptable linear dependence between $\tilde{\nu}$(CO) and $\tilde{\nu}$(NO) has also been obtained for non-d and d^0 metal oxides (blue circles in Fig. 11b); the lower accuracy of the linear fit is due to the different anionic environments of the investigated samples. In any case, it is evident that the overall red, orange and blue sets of data are well correlated, which proves that all these interactions are mainly dominated by electrostatic interactions and that the two molecules respond in the same way to the Stark effect induced by the same cationic sites.

When d-metals are considered (green triangles), any attempt to rationalize $\tilde{\nu}$(CO) *vs.* $\tilde{\nu}$(NO) fails, which proves that the extent of π-back donation is significantly different for CO and NO probes.[29]

It is in particular worth noting that, with the sole exceptions of Cu_2O/SiO_2 and $CuCl/\gamma$-Al_2O_3, for all the remaining d-systems that were investigated, $\tilde{\nu}$(CO) is blue-shifted, which indicates dominant electrostatic and σ-donation interactions, whereas $\tilde{\nu}$(NO) is significantly red-shifted (only Ag^+-ZSM-5 and α-Fe_2O_3 making exceptions), which reveals the major role played by π-back donation interaction.

3.2. Extraframework Al^{3+} species

Extraframework Al^{3+} species are usually formed upon thermal activation of zeolites.[496–498] In some cases, such as ultrastable Y zeolite (H-USY), a partial dealumination process is carried out to activate the zeolite under steam conditions,[240,499–501] as discussed in Section 5.1.

The absence of d-electrons implies that the interaction of extraframework Al^{3+} species with probes is mostly electrostatic and the high charge/radius ratio implies that we are dealing with strong Lewis acid centers. CO molecule probes extraframework Al^{3+} species to form $Al^{3+}\cdots CO$ adducts, which are characterized by a very high $\tilde{\nu}$(CO) stretching frequency.[502,503] Fig. 12a shows the interaction at liquid-nitrogen temperature of CO with H-MOR, which exhibits a fraction of extraframework Al^{3+} species. The weak band at 2225 cm^{-1} is due to $Al^{3+}\cdots CO$ adducts; the main band at 2173 cm^{-1} is due to the interaction with Brønsted sites ($ZOH^+\cdots CO$ adducts),[229] whereas the band developed at 2138 cm^{-1} at high P_{CO} only is due to liquid-like CO formed inside the zeolite channels.[226,227,267,268] The high polarizing power of extraframework aluminum makes $Al^{3+}\cdots CO$ adducts stable at 77 K upon prolonged outgassing to pressures as low as 1.0×10^{-2} Torr.

Being IR-inactive in its unperturbed form, a N_2 probe is more suitable than CO to detect a small fraction of highly polarizing Lewis acid centers like extraframework Al^{3+}.[204] This fact is clearly visible in Fig. 12b, which shows the IR spectra of the same H-MOR sample probed by N_2. The relative intensity of

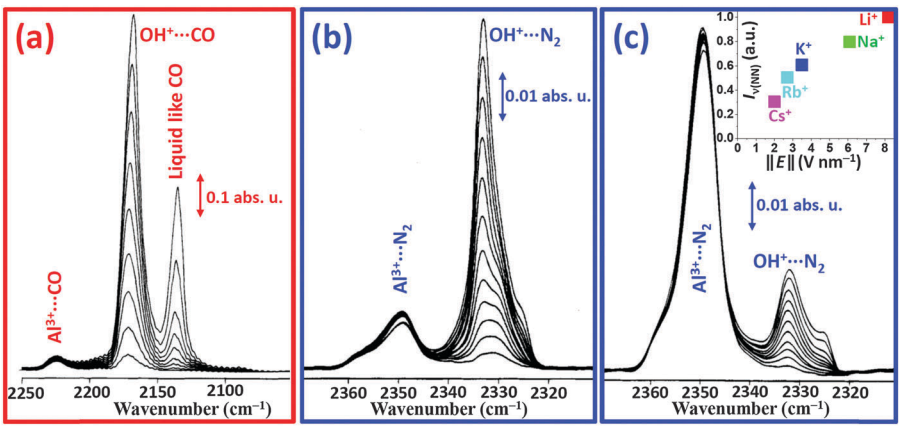

Fig. 12 Part (a): IR spectra of CO adsorbed at 77 K and increasing equilibrium pressures of CO (from 1.0×10^{-2} to 20 Torr) on H-MOR previously activated *in vacuo* at 673 K. Part (b): IR spectra of N_2 adsorbed at 77 K and increasing equilibrium pressures of N_2 (from 1.0×10^{-2} to 50 Torr) on H-MOR previously activated *in vacuo* at 673 K. Part (c): Similar to part (b) for H-MOR previously activated *in vacuo* at 973 K. All the spectra were background-subtracted using a spectrum collected before dosage of the probe as the background. The inset shows that for different alkali-metal-exchanged mordenites, the relative integrated area of the ν(NN) band *versus* the local electric field intensity $||\boldsymbol{E}||$ is generated at the cationic site and measured using a CO probe, as discussed in Section 3.1.1 and eqn (6). Part (a) has been adapted with permission from ref. 229, copyright American Chemical Society 1995; Parts (b) and (c) have been adapted with permission from ref. 204, copyright American Chemical Society 1995.

$Al^{3+}\cdots N_2$ adducts around 2350 cm^{-1}, with respect to that of the more abundant $ZOH^+\cdots CO$ adducts (band at 2334 cm^{-1}), is considerably higher than in the case of the CO probe, as shown in Fig. 12a. In fact, the molar absorption coefficient $\varepsilon(\tilde{\nu}_{NN})$ increases with increase in the local electric field strength, which is generated at the adsorption site, according to the empirical data reported in the inset of Fig. 12c. Moreover, a N_2 probe is able to distinguish between two families of extraframework Al^{3+} species (band at 2349 cm^{-1} and shoulder around 2357 cm^{-1}), whereas an almost uniform and featureless band was observed using CO as a probe (Fig. 12a).

With an increase in activation temperature from 673 to 973 K, the fraction of extraframework Al^{3+} species increases to the detriment of Brønsted sites, as observed by comparing parts (b) and (c) of Fig. 12. Again, because of its higher $\varepsilon(\tilde{\nu}_{NN})$, the band due to $Al^{3+}\cdots N_2$ adducts increases much more than the band due to $ZOH^+\cdots N_2$ adducts decreases.

The insets of Fig. 10a–c show the ν(NN) region of strong Lewis acid sites for vacuum-activated Cu-SSZ-13, Cu-ZSM-5 and Cu-β zeolites, respectively.[161] Again, in these examples, N_2 was more efficient than CO for the detection of a very small fraction of extraframework Al^{3+} species due to a dramatic increase in the absorption coefficient of the ν(NN) mode when the molecule was adsorbed on an highly polarizing Lewis acid center, which was able to produce a stronger induced dipole in the molecule.[161]

Finally, pyridine (Py) has also been widely used to probe the progressive migration of Al^{3+} species from framework into extraframework positions during progressive dealumination processes.[496,497,504–511] Indeed, its ability to detect both Brønsted and Lewis acidic centers enables the increase of $Al^{3+}\cdots$Py adducts around 2350 cm^{-1} to be followed, to the detriment of $ZOH^+\cdots$Py or $ZO\cdots PyH^+$ complexes (see Section 2.2).

3.3. Heteroatoms substituted in framework T positions

Microporous crystalline silica frameworks may incorporate heteroatoms, of which aluminum is the most common, leading to zeolites as extensively discussed in this review. Other examples of isomorphic substitution of framework silicon atoms are iron, titanium, gallium, germanium, boron, vanadium and tin.[31,159,163,247,447,512–531]

Framework trivalent heteroatoms (Al, Fe, Ga, In, and B) are responsible for Brønsted activity (see Section 2) of different strengths.[156,437,441,532,533] In the synthesized materials, heteroatoms occupy tetrahedral T sites, substituting silicon; however, depending on the heteroatom valence state and on the presence/absence of charge-balancing cations and their nature (template cation, alkali metal cation, NH_4^+, and H^+ Brønsted site), the local environment of a heteroatom at a framework position will exhibit different symmetries such as T_d and distorted T_d, as shown in Fig. 13. Moreover, depending on the nature of the heteroatom and the zeolite framework structure, heteroatoms have different stability and a simple template burning process or more severe post-synthetic treatments may cause the migration of a fraction of heteroatoms from framework into extraframework positions. IR spectroscopy of adsorbed probes has been a powerful technique for discriminating between framework and extraframework species.[140,249,250,298,303,438,442,443,445]

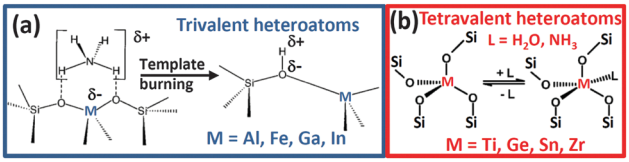

Fig. 13 Possible local environments of heteroatoms hosted in zeolitic frameworks. Part (a): M^{3+} heteroatoms induce a negative charge in the framework and experience a T_d-like environment when the framework charge is balanced by a NH_4^+ ion, a template molecule or an alkali metal cation (left part). When the charge is balanced by a proton (Brønsted site), the symmetry is distorted (right part). Part (b): M^{4+} heteroatoms do not induce any charge in the framework; they do not imply the presence of a charge-balancing cation or Brønsted site, and in vacuum-activated materials they experience a T_d-like environment. Upon interaction with ligands (L = H_2O or NH_3), M modifies its local environment by coordinating one ligand molecule in its first coordination sphere. Adapted with permission from ref. 257, copyright Elsevier 2014.

Depending on the activation and reaction conditions and local structure, the accessibility, reactivity and nuclearity of heteroatoms may significantly deviate from the initially synthesized ones. Because the location of heteroatoms in zeolitic frameworks defines their unique catalytic behavior, it is very important to shed light on this matter. Among the most useful characterization techniques applied for reaching this goal, we mention X-ray absorption spectroscopies (both XANES and EXAFS)[257] and vibrational spectroscopies (mainly IR and Raman).[22] In Section 3.3.1, we will discuss how insertion in an MFI framework of Ti, Fe, B, or Al, as well as Si vacancies, affects the vibrational modes of the zeolite skeleton, whereas Section 3.3.2 will show how resonant Raman spectroscopy is able to shed light on the Ti–peroxo complex formed in TS-1 upon contact with H_2O/H_2O_2 solution, which is the active site for several selective oxidation reactions that are relevant for fine chemistry.[247,528]

3.3.1. Modification of the framework modes. Zeolites and Al-free silicalites are characterized by strong framework modes that are associated with Si–O or more generally T–O (T = Si or Al) stretching modes.[46,224,534–537] The fundamental framework modes fall in the 1300–750 cm^{-1} region. These modes can be described both by using as a building unit the [SiO_4] tetrahedron that is interconnected with other units through the corner oxygen atoms or, in a simpler way, by considering that the smallest building block is represented by a [Si–O–Si] group (with a Si–O–Si angle of 140°–160°). The vibrational modes of the framework can be derived from the vibrational features of these species.[46] The stretching modes of the [SiO_4] unit are asymmetric $\nu[SiO_4]_{asym}$ modes (triply degenerate in perfect T_d symmetry), observed in the 1300–1000 cm^{-1} range, and totally symmetric $\nu[SiO_4]_{sym}$, observed in the 850–750 cm^{-1} range. The first is strongly IR-active and the second is weakly IR-active, whereas in Raman, the opposite is observed, as shown in Fig. 14a, bottom curves. The spectral region in the 1000–850 cm^{-1} window is known as the relative-transparency window of zeolites, where it is possible to measure the perturbation induced in [SiO_4] by (i) isomorphic insertion of heteroatoms;[22,45,46,156,245,246,532,536–545] (ii) strong interactions of extraframework cations with the framework;[381,404,436] and (iii) Si vacancies that generate internal silanol nests.[168,169,539]

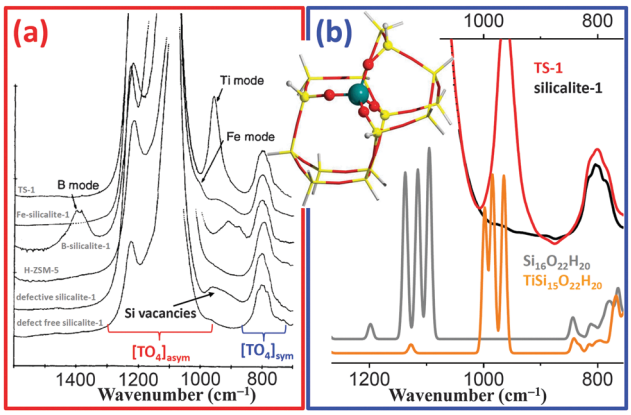

Fig. 14 Part (a): Diffuse reflectance IR spectra, in the framework skeleton stretching region, of pure and substituted silicalite-1 (diluted in KBr) activated at room temperature. From bottom to top: defect-free silicalite-1; defective silicalite-1 (with a high concentration of Si vacancies); H-ZSM-5 (Al-silicalite-1); B-silicalite-1; Fe-silicalite-1; and Ti silicalite-1 (TS-1). Part (b): Effect on the vibrational properties of diluted insertion of Ti in MFI framework; comparison between experimental (dehydrated TS-1, red curve and defect-free silicalite-1, black curve) and computational ($TiSi_{15}O_{22}H_{20}$ and $Si_{16}O_{22}H_{20}$ clusters) approaches. The inset shows a cluster extracted from the MFI framework and used in DFT calculations: Si (yellow), Ti (olive), O (red), and H (gray). Part (a) has been adapted with permission from ref. 539, copyright Royal Society of Chemistry 1992; Part (b) has been adapted with permission from ref. 536, copyright American Chemical Society 2002.

The insertion of heteroatoms affects the vibrational spectra of zeolites mostly in the region of the framework modes, even if some changes are also expected in the OH stretching region due to a change in the acid strength, which is expected when a Si species has been replaced by another element, such as Fe(III) or Ti(IV) sites. Among these vibrations, it is expected that the presence of heteroatoms in substitutional positions, such as B(III), Fe(III) or Ti(IV), causes the appearance of new IR and Raman bands, which are considered to be diagnostic of the presence of these guest atoms in the framework and are used to monitor the abundance of these species, because their intensity is proportional to the concentration of the heteroatoms. Isomorphic insertion of heteroatoms results in the appearance of a band around 960 cm^{-1} for Ti(IV), 1010 cm^{-1} for Fe(III) and two components around 1380 and 920–890 cm^{-1} for B(III), as shown in Fig. 14a, top curves.[539] A broad band, covering almost the whole transparency window (990–920 cm^{-1}), is observed for defective silicalite-1.

In this regard, the computational DFT study performed using the ONIOM scheme by Damin *et al.*[536,537] is very informative, as shown in Fig. 14b. By extracting a cluster with 16 T-centers ($Si_{16}O_{22}H_{20}$) from the MFI framework and optimizing its structure at the DFT level of theory, the authors were able to reproduce the spectrum of the fully siliceous silicalite-1 material and compare the theoretical spectrum (gray curve) with the experimental spectrum (black curve). By substituting the central Si atom in the cluster by Ti, Damin *et al.*[536,537] obtained the $TiSi_{15}O_{22}H_{20}$ cluster (see inset in Fig. 14b), of which the vibrational spectrum (orange curve) is able to reproduce the Ti-specific band at 960 cm^{-1} observed for Ti-silicalite-1 (TS-1, red spectrum in Fig. 14b).[22,46,245,246,536–539,544,545]

In the case of Raman spectroscopy, a further method of detecting the presence of even a very small amount of heteroatoms in the zeolitic lattice comes *via* the possibility of exploiting resonance effects.[45,46] Fig. 15b shows a series of Raman spectra collected for the same TS-1 material with different excitation lines. For the sake of comparison, part (a) of the figure shows the UV-Vis DRS spectrum of dehydrated TS-1. The band at 208 nm (48 000 cm^{-1}) is due to ligand-to-metal charge transfer (LMCT), which occurs from the four nearly equivalent oxygen atoms to the Ti(IV) centre in the quasi-tetrahedral [TiO_4] unit that leads to the symmetrical expansion of the tetrahedral unit.[46] In the same figure, the four laser lines are indicated by arrows. It is evident that by progressively increasing the energy of the exciting source we enter into the Ti-specific LMCT band and therefore we expect to observe a strong enhancement of the Ti-specific vibrational modes that fulfil the resonance Raman selection rules. In particular, we expect resonance when Raman spectroscopy is performed using a wavelength that is close to an electronic absorption of the sample most likely to be associated with an LMCT transition. This condition guarantees a high transfer of energy to the sample. If the electronic absorption is due to a localized centre, such as a transition from a ligand to a metal atom, the excitation is also partially localized, and the vibrational features in the immediate vicinity of the absorbing atom can be enhanced by several orders of magnitude, if they meet the appropriate enhancement selection rules. Two types of vibrations are enhanced: (a) totally symmetric vibrations with respect to the absorbing centre and (b) vibrations in modes that cause the same molecular deformation as induced by the electronic excitation.[46] Fig. 15b shows the Raman spectra collected for dehydrated TS-1 using four different lasers. Besides the typical modes of the siliceous MFI framework at 800 and 370 cm^{-1}, two Ti-specific bands at 960 and 1125 cm^{-1} are observed. It is evident that only the latter mode is enhanced by tuning the exciting laser source within the Ti-specific LMCT band.[46,48,546] The ratio between the intensities of the two Ti-specific modes increases progressively by moving from a near-IR to a far-UV source; specifically, $I(1125)/I(960)$ = 0.25, 0.48, 0.65 and 12.50 using 1064, 442, 325 and 244 nm lasers, respectively (Fig. 15b). Similar enhancements have been observed in the Raman studies of Ti-STT[545] and Ti-CHA[544] frameworks.

In the case of Ti-silicalite, where the Ti–O and Si–O bonds have different polarity and a different force constant, the ν_{asym}(Ti–O–Si) mode can be considered as a ν(Si–O) mode perturbed by an adjacent Ti centre. Moreover, the totally symmetric $\nu[SiO_4]_{sym}$ mode, where while the four Si–O bonds expand (or contract) in phase and the Ti–O bonds contract (or expand) in phase, should be IR-inactive and only weakly Raman-active. Indeed, a peak at 1125 cm^{-1} is present in the Raman spectrum (Fig. 15b). This peak is not observed with silicalite-1, as expected. DFT calculations[46] have shown that the Raman peak at 1125 cm^{-1} is associated with the expansion and contraction of the coordination sphere constituted by the four equivalent oxygen atoms surrounding the Ti center, which is

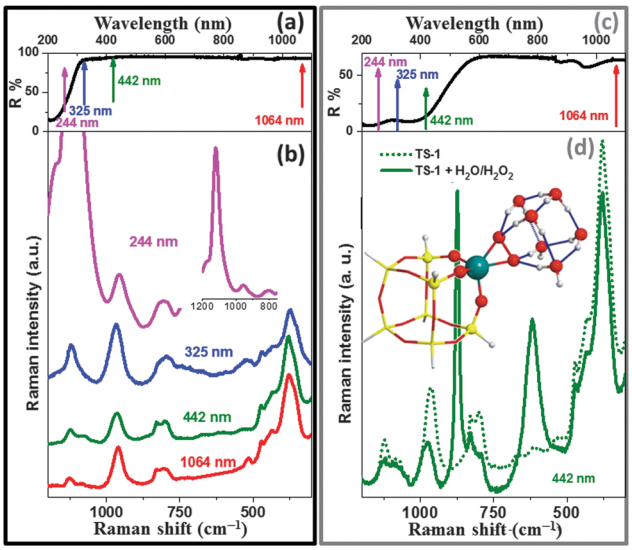

Fig. 15 Part (a): UV-Vis DRS spectrum of dehydrated TS-1 catalyst showing a typical LMCT band at 208 nm (48 000 cm^{-1}); the four excitation laser lines used in this Raman study are also shown: near-IR (red), visible (green), near-UV (blue) and far-UV (purple). The spectrum has been reported in reflectance units (R%), where absorption bands correspond to minima in the spectrum. Part (b): Raman spectra of dehydrated TS-1 obtained with four different lasers emitting at λ = 1064, 422, 325 and 244 nm (red, green, blue and purple lines, respectively). Raman spectra have been vertically shifted for clarity. Although the intensity of each spectrum depends upon different factors, the evolution of the *I*(1125)/*I*(960) ratio by changing the laser source is remarkable. The inset shows the Raman spectrum collected with a 244 nm laser on its full scale to appreciate the intensity of the 1125 cm^{-1} enhanced mode. Part (c): UV-Vis DRS spectrum of TS-1 catalyst in contact with H_2O_2/H_2O solution, showing a typical LMCT band of the Ti–peroxo complex at 385 nm (26 000 cm^{-1}); the four excitation laser lines used in this Raman study are also shown: near-IR (red), visible (green), near-UV (blue) and far-UV (purple). Part (d): Raman spectra collected with the 442 nm laser of TS-1 before and after interaction with H_2O_2/H_2O solution (dotted and full lines, respectively). The inset shows the optimized anhydrous [$^{-}O_2$–Ti(OSi)$_3$ + 5H_2O + H_3O^+] cluster adopted for the calculation (B3LYP/6-311+G(d,p) level). The ball-and-stick *vs.* stick notation distinguishes the zone of interest (treated at high level) from the complementary part of the cluster treated at low level only. Colour-coded: green, Ti; red, O; yellow, Si; white, H; blue lines represent H-bonds. The main parts have been adapted with permission from ref. 48, copyright Royal Society of Chemistry 2003; the inset in part (d) has been reproduced with permission from ref. 22, copyright Royal Society of Chemistry 2007.

further confirmed by the Raman resonance obtained using a 244 nm excitation line, *i.e.* a frequency close to the LMCT transition of tetrahedral TiO_4 in Ti–silicalite. In fact, the peak at 1125 cm^{-1} is enhanced by one to two orders of magnitude, as expected for a resonance-enhanced mode where UV excitation causes the simultaneous symmetric increase of all four Ti–O distances. The remaining three modes (asymmetric $\nu[SiO_4]_{asym}$ modes) are responsible for the band at 960 cm^{-1} (see orange spectrum in Fig. 14b), which is the fingerprint IR band of Ti-silicalite (red spectrum in Fig. 14b). From the point of view of the [Si–O–Ti] groups these modes have mixed ν_{sym} and ν_{asym} character. It is evident that these considerations are highly qualitative; a better description could be given on the basis of the stretching vibrations of the cluster shown in the inset of Fig. 15b or analysis of the elementary cell modes.

Following these considerations, the insertion of a lighter atom in the structure, for instance B, would be associated with a ν(B–O–Si) mode occurring at frequencies higher than those typical of silicalite and M-ZSM-5 (M = H, Na). Indeed, the spectrum of H-B-silicalite shows a strong peak at 1380 cm^{-1}, which confirms this simple model (Fig. 14a).[539] However, because it disappears upon dosing NH_3 (*i.e.* upon the formation of NH_4^+), it has been assigned to a local mode of the planar [BO_3] structure, which is transformed into a tetrahedral structure upon contact with NH_3. From this result, it is inferred that the ν_{asym} of genuine (B–O–Si) groups with regular framework B occurs at frequencies that are not substantially different from those of (Al–O–Si) and (Si–O–Si) units. Vibrational, B K-edge XANES and DFT studies of B-CHA have successively confirmed this interpretation.[156,532,533]

3.3.2. Reactivity of Ti centers in TS-1. TS-1 is an industrial catalyst that is used for several partial selective oxidation reactions using H_2O_2 as oxidizing agent.[247,547–550] Due to the presence of H_2O in the reaction medium (which precludes an extensive use of IR spectroscopy), the vibrational features of the active Ti–peroxo complex were clearly observed in 2002 (*i.e.* more than 20 years after the catalyst was patented) *via* a resonant Raman study.[47]

A previous Raman study by the same group,[551] which exploited an exciting source of 1064 nm, was only able to measure the O–O stretching of peroxo complexes formed at Ti sites upon contacting TS-1 with basic solutions of $H_2O_2/NH_3/H_2O$ (840 cm^{-1}) and H_2O_2/NaOH/H_2O (843 cm^{-1}). Note that the O–O stretching frequency of H_2O_2 molecules in an aqueous solution occurs at 875 cm^{-1}. The reason for the partial success is probably due to the fact that, in basic solutions, peroxo species are more stable, and therefore they are not readily destroyed by a laser beam. The same experiment on a H_2O_2/H_2O solution was not successful because of the labile nature of the complex. On this basis, it therefore becomes clear that the only route that can be followed to improve the quality of Raman spectra is to operate in resonance conditions.

Of course, because peroxo species absorb in the visible range, an exciting source in the same spectral region must be used, because in this way the vibration associated with the Ti–peroxo species can undergo a Raman enhancement phenomenon, if the selection rules are fulfilled. Among the four laser lines available, the most suitable for stimulating a resonance-enhanced response is the 442 nm (22 625 cm^{-1}) source, which is located in the low-energy tail of the LMCT band around 385 nm that is typical of the TS-1/H_2O_2/H_2O system (see Fig. 15c). Fig. 15d shows the Raman spectra collected with the 442 nm laser of TS-1 before and after interaction with a H_2O_2/H_2O solution (dashed and full lines, respectively). Interaction with H_2O_2 causes (i) a decrease in intensity and blue shift of the peak at 960 cm^{-1} to 976 cm^{-1}; (ii) the quenching of the 1125 cm^{-1} mode due to breaking of the T_d-like symmetry, as discussed in Section 3.3.1; (iii) the appearance of a strong, sharp (O–O) stretching mode at 875 cm^{-1} due to the H_2O_2/H_2O solution being physisorbed into the zeolite channels; and (iv) the appearance of a strong and complex new feature centered at 618 cm^{-1}.

Features (i–iii) are also observed when the same experiment is performed with a laser source of 1064 nm.[551] Conversely, the band at 618 cm^{-1} was not observed either with the TS-1/H_2O_2/H_2O system using a 1064 nm source or with a Ti-free silicalite-1 molecular sieve in a H_2O_2/H_2O solution using a 442 nm exciting source, and was therefore ascribed to a Raman-enhanced vibrational mode of the Ti–peroxo complex.[47,48]

The similarity between the spectroscopic features, both UV-Vis and Raman, of $(NH_4^+)_3(TiF_5O_2)^{3-}$ and TS-1/H_2O_2/H_2O systems allowed Bordiga *et al.*[47,48] to conclude definitively that the species responsible for the band at 26 000 cm^{-1} of the TS-1/H_2O_2/H_2O system is a "side-on" Ti–peroxo species characterized by a Raman mode at 618 cm^{-1}, which is resonance-enhanced using an exciting laser line that falls in the LMCT transition region. This vibrational assignment was successively supported by EXAFS[552,553] and DFT[22] data.

4. Basicity in zeolites

The basic properties of zeolites have generally been much less studied than their acidic properties; an extended bibliographic search on the basicity of zeolites typically yields ten times fewer entries than an equivalent query relating to acidity. This might partly reflect the fact that industrial heterogeneous catalytic processes using basic or amphoteric catalysts are considerably less developed than acid-catalyzed processes, and to the best of our knowledge, none of these uses basic zeolites.[554–556] Furthermore, even though basic zeolites are widely used in other relevant industrial processes such as drying, separation or ion exchange,[557,558] fundamental studies that specifically deal with the characterization of the basicity of these materials are scarce. As will be seen in more detail below, this reflects the fundamental difficulty in specifically probing zeolite basic sites (usually framework oxygen atoms) without the involvement of neighboring acidic centers (usually metal cations), while the symmetric situation (probing Lewis acidic centers while strongly limiting the interactions of the probe with framework oxygen atoms) is usually easier to realize (see Section 3 above). Although challenging, the characterization of the basic properties of zeolites is worthwhile to carry out, enabling the establishment of structure–activity or structure–selectivity relationships for current acid/base-catalyzed reactions or separation processes or for emerging applications such as the development of processes based on biomass for the production of fuels and chemicals, which often require basic functionalities. A number of comprehensive reviews on the structure and properties of basic zeolites[555,559–561] or on the characterization of the basic properties of surfaces by IR spectroscopy[4,562] have been published. In the following section, general remarks on the surface basicity of zeolites and its characterization by probe molecules monitored by IR spectroscopy are discussed. Then, this overview will focus on recent advances made in the characterization of zeolite basic centers by IR spectroscopy. Examples of recent infrared *operando* studies carried out on basic zeolites will be described in Section 9.

4.1 Basicity: general definition and applicability to zeolite basic centers

Although many definitions of basicity have been proposed,[563] only two of these are commonly used in surface chemistry, namely, the Brønsted–Lowry definition, which states that a base B^- hosted in a zeolite Z accepts a proton from an acid HA:

$$ZB^- + HA \rightarrow ZB{-}H + A^- \quad (8)$$

and the Lewis definition, which states that a base ZB: donates a lone pair to an acid A, resulting in the formation of an adduct ZB:A:

$$ZB: + A \rightarrow ZB{:}A \quad (9)$$

It is worth noting that in this section the situation is reversed with respect to that addressed in Section 2, where we reported on the characterization of Brønsted acidity in zeolites; here, the base is on the solid ZB and the acid HA is a molecule in the gas or liquid phase, whereas in Section 2, the base B was in the gas phase and the acid was on the internal surfaces of the solid ZH, as shown in eqn (1).

Any acid compound, acid function in a complex compound, or acidic center on a surface can generally be classified as Lewis or Brønsted without ambiguity or reference to a given base. For instance, as detailed in the preceding sections, extraframework cations of a zeolite are Lewis acid centers, whereas bridging OH groups are Brønsted acid sites. For basic centers, however, no such a priori classification can be made to date, as lone electron pair donors (Lewis bases) are also proton acceptors. In this respect, the class of a basic center, Lewis or Brønsted, is essentially context-dependent and defined by the class of the acid interacting with it, *i.e.* Lewis or Brønsted, be it a probe molecule used to characterize the basicity, a reactant involved in a base-catalyzed reaction, or an adsorbate for trapping or separating from a mixture. Therefore, distinguishing between surface Lewis and Brønsted bases is misleading and should be avoided.

The most important class of basic zeolites to date is the family of aprotic, ion-exchanged zeolites, in particular FAU zeolites (X or Y type, see Fig. 20 below for a view of the structure), which may be regarded as typical of basic zeolites. In these materials, as detailed in Section 3.1, the charge defect induced by framework Al^{3+} cations is compensated by extraframework mono- or multi-valent cations M^{n+} (for a detailed review of the position and distribution of these cations in FAU zeolites with respect to their type and composition, we refer the reader to the study of Frising and Leflaive[564]). In such materials, the negative charge carried by oxygen framework atoms primarily depends on the structure and chemical composition of the zeolite. A simple but powerful concept that enables the average negative charge of framework oxygen atoms *vs.* the composition to be assessed is the electronegativity equalization principle of Sanderson,[565,566] which was applied to zeolites by Mortier.[224] Within this paradigm, the average partial charge of the framework oxygen atoms δ_O is proportional to the

difference between the intermediate electronegativity of the zeolite atoms S_{int} and the electronegativity of oxygen (S_O = 5.21):

$$\delta_O \propto S_{int} - S_O \quad (10)$$

where S_{int} is the geometric mean of the electronegativities of the component atoms of the zeolite. In other words, the lower the electronegativities of the cations, the lower is the intermediate electronegativity, and more negative are the oxygen framework atoms. Therefore, the charge on oxygen increases with the amount of Al in the framework (S_{Al} = 2.22 *vs.* S_{Si} = 2.84) or when the electronegativity of the extraframework counter-cations is low (for instance, for alkali metal-exchanged zeolites, the charge on oxygen increases from Li- to Cs-exchanged zeolites: S_{Li} = 0.74, S_{Cs} = 0.28).

Besides, although framework oxygen atoms have been by far the most frequently investigated in the literature, other basic centers can be encountered in zeolites for instance hydroxy groups resulting from the dissociation of water in hydrated extraframework cations,[567] basic oxygen atoms or hydroxy groups in oxide clusters,[568] or basic NH groups obtained by nitridation.[569]

The characterization of the basicity of a zeolite involves determining the number and strength of these basic centers. As IR spectroscopy is sensitive to chemical bonds, it generally does not allow the detection of basic sites themselves, with the notable exception of basic extraframework OH groups[567,570] and NH groups of nitrided zeolites.[571,572] Thus, the general approach to the characterization of zeolite basicity involves the use of acidic probe molecules that ideally would react with the basic centers according to reactions (8) or (9) mentioned above. It must be noted, however, that while such equilibria may be investigated in dilute solutions, the surface density of basic sites and the proximity of acidic centers often prevent the selective observation of reactions (8) or (9) in zeolites. This is virtually always the case for the Brønsted equilibrium (8), where the conjugate base of the acid (A^-) forms a complex with Lewis acid centers (M^{n+}) in the vicinity of the basic center:

$$Z[B^-,M^{n+}] + HA \rightarrow Z[B\text{–}H,M^{n+}\text{–}A^-] \quad (11)$$

Therefore, within basic zeolites, for a given acid HA, the realization of the Brønsted equilibrium (11) is simultaneously driven by the strength of vicinal basic and acidic centers, which does not allow conclusions regarding basicity alone. The characterization of basic centers using protic probe molecules is thus generally carried out in conditions that prevent dissociation (8) and restrict acid–base interactions for the formation of hydrogen bonds between the acidic protons and the basic centers:

$$ZB^- + HA \rightarrow ZB^-\cdots HA \quad (12)$$

Although seemingly paradoxical (the reaction that defines basicity is avoided), such a situation allows one to selectively probe basic sites. With respect to the Brønsted definition, the hydrogen-bonding interactions can be viewed as incipient proton-transfer reactions, *i.e.* a suspended stage of reaction (8) in which a partial bond $ZB^-\cdots H$ is formed, whereas the H–A bond is weakened.[573] Within this approach, the Brønsted strength of the basic site can be heuristically approximated *via* the strength of the hydrogen bond, which has been shown to be generally strongly correlated in the case of gas-phase or liquid-phase complexes.[105] Alternatively, the formation of hydrogen-bonded complexes (12) can also be considered to some extent as a particular case of the Lewis definition (9) because it generally involves a small charge transfer from the proton acceptor (base) to the proton donor (acid), in the order of 0.01 to 0.03 electrons.[105] Deviations from the ideal case of the Lewis (9) or hydrogen-bond formation equilibria (12) are, however, generally encountered because the acid probe can usually interact with a vicinal acid center *via* a basic moiety b:

$$Z[B^-,M^{n+}] + HAb: \rightarrow Z[B^-\cdots HAb{:}M^{n+}] \quad (13)$$

$$Z[B{:}M^{n+}] + Ab: \rightarrow Z[B{:}Ab{:}M^{n+}] \quad (14)$$

Although the same complication can also occur when probing acidic centers (see Section 3 above), it is virtually always present for the characterization of basicity, where the probe, for obvious geometrical reasons, is often located between the basic center and the acid site. In other cases, a basic probe molecule may even undergo dissociation, leading to the *in situ* generation of an acid A^+, which interacts with the basic center:

$$Z[B:,M^{n+}] + Ab: \rightarrow Z[B{:}A^+,b^-{:}M^{n+}] \quad (15)$$

Once these limitations are taken into consideration, *i.e.* a suitable probe that interacts as selectively as possible with the basic centers has been found, the basic strength is often assessed *via* the spectrum of the acid–base complex. Ideally, the stretching vibration between the acid and the base ($ZB\cdots A$ or $ZB\cdots HA$) would be the most direct spectroscopic indicator of such interactions, but these bands are in the far infrared region, which generally prevents their observation, particularly in the condensed phase. Moreover, while in the gas or liquid phase the base often presents group vibrations that are selectively affected by the formation of a Lewis or hydrogen-bonded complex, zeolite Al–O and Si–O bond vibrations are strongly coupled and the perturbation of the resulting framework modes, which is induced by adsorption, cannot be directly related to the strength of the adsorption. Therefore, the only spectroscopic indicators that are available for the characterization of zeolite basicity are generally the vibration modes of the acidic probe molecule, which are perturbed by the nature and strength of the acid–base interaction. The following part briefly describes the most important probe molecules used for this purpose with illustrations from recent findings in this field.

4.2 Probe molecules for characterization of zeolite basicity

4.2.1. X–H acids as probes. The largest and most frequently used class of probe molecules for the characterization of zeolite basicity consist of acidic, non-reactive molecules containing an acid functional group X–H (X = C, N, and O), which forms a hydrogen bond with basic centers according to reaction (12) or more often (13) mentioned above. The formation of these complexes is generally indicated by a significant downward shift and broadening of the ν(X–H) stretching band, the extent of which is usually quantified by a shift in frequency $\Delta\tilde{\nu}$(X–H)

with respect to that observed in the gas phase or dilute solution, is indicative of the hydrogen bond strength, and hence the basic strength of the oxygen center. Although generally straightforward to detect, hydrogen bonding always complicates the spectra with broad and poorly resolved features, which often hinder conclusions regarding the heterogeneity of these sites. Moreover, the intensity of these bands increases with the strength of the hydrogen bond, thus preventing the quantification. See the parallel discussion in Section 2.2 regarding Brønsted acidity.

Pyrrole (C_4H_4NH) was one of the probe molecules that were first employed for this purpose.[574] On alkali-exchanged X zeolites, its ν(N–H) is shifted by an amount ranging from ~ -200 cm^{-1} for Li-X to ~ -300 cm^{-1} for Cs-X with respect to dilute solution: $\tilde{\nu}_0$(N–H) = (3497 cm^{-1}).[3,4,31,575–578] Such shifts are indicative of relatively weak hydrogen bonds (relative shift in frequency less than 10%),[573] and no dissociation or surface transformation of pyrrole over basic zeolites is generally reported when adsorption is carried out at room temperature. This fact contrasts with even weakly basic metal oxides such as γ-Al_2O_3, on which the formation of pyrrolate species has been confirmed.[4] Moreover, for a given zeolite structure, the observed shifts are strongly correlated with the negative charge of the oxygen framework, derived from the electronegativity equalization principle.[4,575,576,579] Pyrrole thus appears to be an excellent probe for the study of zeolite basicity. Although early studies mostly considered the global maximum of the ν(N–H) band to be a measure of average basicity, more recent studies have generally attempted to decompose the broad ν(N–H) band into several components to obtain more insight into the heterogeneity of basic sites. Individual components are assigned to basic framework oxygen sites that differ in the nature of the extraframework cation in the case of partially exchanged zeolites,[576] the position of the cation,[580] or the number of aluminum atoms in the rings of the site where the cation is located.[576,580,581] Kučera *et al.* investigated the heterogeneity of zeolite basic sites *via* a combined experimental and theoretical study of the adsorption of pyrrole on alkali-exchanged MFI zeolites.[581] Fig. 16a shows the spectra obtained after the adsorption of pyrrole followed by desorption at increasing temperatures on two K-MFI zeolites that differ in their Si/Al ratio. The ν(N–H) band clearly exhibits two main components I and II at high and low frequency, respectively, which both increase with the concentration of framework aluminum and hence with zeolite basicity. Interestingly, the low-frequency component, which corresponds to stronger sites (lower $\tilde{\nu}$(NH), higher $|\Delta\tilde{\nu}$(NH)| and higher thermal stability), is the most increased. In parallel, modeling of the adsorption of pyrrole in these systems using hybrid DFT/molecular mechanics calculations indicated that the extent of the shift in $\Delta\tilde{\nu}$(N–H) frequency is primarily governed by the nature of the T atoms that bind the framework oxygen atoms. Complexes that are H-bonded with [≡Si–O–Si≡] centers such as structure I (Fig. 16b) display moderate shifts in frequency ($\Delta\tilde{\nu}$(N–H) from −50 to −100 cm^{-1}), whereas those formed with [≡Al–O–Si≡] centers (Fig. 16c, structure II) lead to much larger shifts: $\Delta\tilde{\nu}$(N–H) < −150 cm^{-1}. The content and distribution of Al in the ring was also found to have a significant impact on the $\tilde{\nu}$(NH) frequency. For instance, when Al pairs are separated by two *vs.* three SiO_4 tetrahedra, N–H stretching frequencies can be lowered by ~50–100 cm^{-1}, thus confirming the substantial impact of the distribution of Al proposed by previous studies.[575–577,582,583]

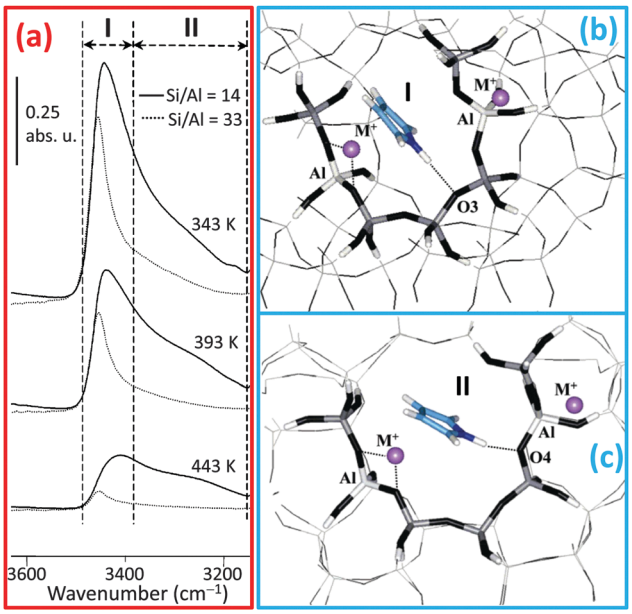

Fig. 16 Part (a): FTIR spectra of pyrrole adsorbed on K-MFI with Si/Al ratios of 14 and 33 (full and dotted curves, respectively.) after desorption of pyrrole at 342, 393, and 443 K (top, middle and bottom curves, respectively). Part (b): Pyrrole adsorption complexes with Si–O–Si centers (I), as computed *via* a hybrid quantum mechanics/interatomic potential function approach. Part (c): Similar to Part (b) for the adsorption of pyrrole on Al–O–Si centers (II). Adapted with permission from ref. 581, copyright American Chemical Society, 2004.

The shifts in ν(N–H) frequency are dominated by the framework oxygen basicity; moreover, these theoretical calculations also show that the cation–π-ring interaction, which is clearly seen in the complexes shown in Fig. 16b and c, plays an important role in the stabilization of these complexes, which is in line with previous theoretical studies on alkali-exchanged FAU zeolites.[584,585] Such interactions, which can be detected *via* a significant upward shift in the ν(C–H) out-of-plane deformation modes,[584] can be strong enough to displace extra-framework cations within the FAU structure. Therefore, the adsorption of pyrrole on basic zeolites essentially proceeds according to reaction (13) mentioned above and is governed by basic and acidic centers.[580] In this respect, the energetics of pyrrole adsorption, as evaluated by, for example, conventional TPD experiments, should not be considered as an indicator of framework basicity unless validated by parallel IR experiments.

Halocarbons, in particular chloroform (CCl_3H), are also classically used for the characterization of basicity. Chloroform, although has the same deprotonation energy as pyrrole (1500 kJ mol^{-1}),[586] generally exhibits considerably lower shifts in frequency when adsorbed on basic zeolites: from ~ -20 cm^{-1} for Li-X to −100 cm^{-1} for Cs-X zeolites, and these are still strongly correlated with the negative charge on oxygen.[587] Such low shifts

in frequency are due to significant interactions of the halogen atoms with extraframework cations.[588] Besides, because C–Cl bonds have ionic character, chloroform can also be reactive, in particular when traces of water are present;[587] in addition, according to the recommendations given for pyrrole, extra precautions should be taken when using this probe on zeolites. Fluoroform (CF_3H), which has stronger carbon–halogen bonds, is more stable than chloroform. However, when adsorbed on a basic zeolite, the ν(C–H) band can be shifted toward higher frequencies with respect to the free molecule. This behavior was initially interpreted to be resulting from strong interactions of fluorine with extraframework cations, which prevented the formation of hydrogen-bonded complexes.[562,588] Recently, however, the use of this probe has been re-investigated by Tsyganenko *et al.* on metal oxides and basic zeolites.[589,590] They showed that the modifications of the frequency and intensity of the ν(C–H) band upon adsorption actually follow the trends expected for so-called blue-shifting or improper H-bonds, which have attracted a lot of attention since the early 2000.[591–594]

Such a behavior occurs when an isolated H-bond donor has a negative derivative of the dipole moment (*i.e.* corresponding to a bond dipole directed in the sense $C^{\delta+}$–$H^{\delta-}$). In such a case, weak hydrogen-bonding interactions first lead to an upward shift in frequency (*i.e.* blue-shifting H-bond) and then to a decrease in intensity, whereas for sufficiently strong hydrogen bonds, a normal downward shift in frequency and increase in the intensity of the ν(C–H) band are observed. This is illustrated in Fig. 17, which shows the evolution of the frequency of the ν(C–H) mode (squares, left ordinate axis) and its intensity normalized to that of the δ(C–H) mode (circles, right ordinate axis) of adsorbed fluoroform. Framework oxygen centers with very weak or intermediate basicity, such as those of Al-free silicalite-1 or Na-Y zeolite, give rise to improper, blue-shifting hydrogen bonds (red and blue squares in Fig. 17), whereas the stronger basic centers of Na-X zeolite lead to normal, red-shifting hydrogen bonds (green square). Finally, the upward shift in the δ(C–H) mode appears to be roughly correlated with the basic strength of the oxides investigated in this study and the authors suggested that it could be used as an approximate measure of surface basicity, as for 'normal' H-bonds. The non-monotonic behavior of the ν(C–H) band with the basic strength, however, makes analysis of the spectra not straightforward, which prevents the use of this probe for routine analysis of surface basicity. Sánchez-Sánchez *et al.* investigated the use of a chlorofluorocarbon probe molecule, CCl_2FH, on alkali-exchanged zeolites and found that the correlation between the shift in ν(C–H) frequency and the negative charge on oxygen is generally less than that obtained for chloroform, which they ascribed to the influence of fluorine–cation interactions, as confirmed by NMR.[595] It should also be noted that this molecule was also later found to form blue-shifting hydrogen bonds,[596] which could thus contribute to a decline in such correlations.

The other class of C–H acids used for the characterization of basicity is the family of acetylenic compounds. Acetylene (C_2H_2), first proposed by Uvarova *et al.*,[597] exhibits shifts in ν(C–H) frequency, which are sensitive to the strength of basic

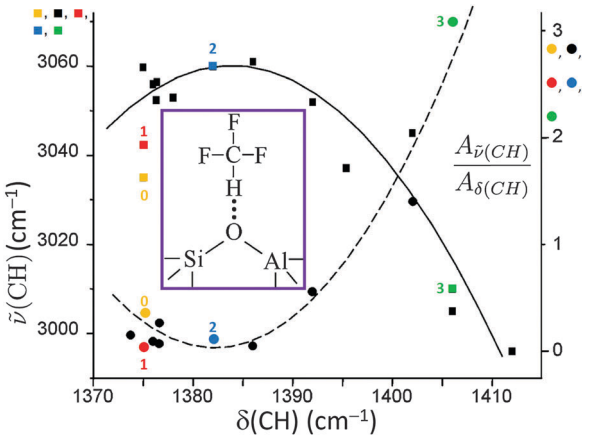

Fig. 17 Positions of ν(CH) band (squares, left scale) and ratios of integrated intensities of C–H stretching and bending vibrations $A_{\tilde{\nu}(CH)}/A_{\delta(CH)}$ (circles, right scale) of H-bonded fluoroform plotted against δ(CH) values on metal oxides and zeolites. For this review, the more relevant set of data are those marked with colored symbols: 0 – free molecule; 1 – Al-free silicalite; 2 – Na-Y; and 3 – Na-X. The central inset shows a representation of fluoroform H-bonded with a basic framework oxygen atom of a zeolitic framework. Adapted with permission from ref. 590, copyright Elsevier, 2014.

sites of alkali-exchanged zeolites that are ~ -80 and -115 cm^{-1} for Na-Y and Na-X zeolites, respectively. More recently, the use of this probe has been extended to the study of a large series of metal oxides, which confirms its interest for the study of basicity.[598] It should be noted, however, that the C-H stretching mode of acetylenic compounds is generally coupled with the C≡C stretching vibration, and in the case of acetylene, it is coupled with the second C–H vibration, leading to symmetric and antisymmetric ν(C–H) modes. To limit the latter coupling, heavier alk-1-ynes, such as propyne or but-1-yne, could be used. Although not reported with much detail, propyne was also used by Uvarova *et al.* and Knözinger and Huber on alkali-exchanged FAU zeolites, which exhibited shifts in ν(C–H) frequency that were consistent with oxygen framework basicity.[9,597] Finally, Lavalley *et al.* proposed the use of but-1-yne (CH_3CH_2CCH) and showed that this probe could be used for zeolites with moderate basicity such as Na-Y or Na-X zeolites and could be more sensitive to the heterogeneity of basic sites than pyrrole.[599] On more basic zeolites, such as Cs-exchanged FAU, but-1-yne, however, undergoes isomerization reactions, preventing its use over such solids.

4.2.2. Lewis acids as probes. Carbon dioxide (CO_2) is certainly the most employed probe for the characterization of surface basicity. On basic zeolites, however, the most striking adsorption mode for CO_2 is generally the formation of linear complexes with extraframework cations, which leads to intense bands around 2360 cm^{-1} due to the asymmetric stretching vibration ν_3, which shifts toward high wavenumbers as the polarizing power of the cation increases[600,601] (for more details, see Sections 3.1 and 7.2). In addition to the bands of linearly adsorbed CO_2, the formation of carbonate species, characterized by ν(COO) bands in the 1300–1700 cm^{-1} range, is generally evidenced on zeolites with medium to high basic strength such as Na- or heavier alkali ion-exchanged X zeolites,[4,568] K-, or Cs-exchanged

zeolites,[602,603] whereas no such species are detected on zeolites with weaker sites (*e.g.* Li-X, Li-Y or Na-Y).[602] The carbonate species formed are characterized by two ν(CO) bands, resulting from a lowering in symmetry, as compared to the free CO_3^{2-} ion. On alkali-exchanged zeolites, these bands, which are assigned to symmetric and asymmetric COO vibrations, generally appear at $\sim$1650–1700 cm^{-1} and $\sim$1300–1400 cm^{-1}, which, by analogy with metal oxides,[39] are indicative of bridged carbonate species formed with basic framework atoms (Fig. 18a). However, to the best of our knowledge, in contrast to the case of other probe molecules, no systematic trends between the position of these bands and the expected basic strength of the zeolite have been reported. Generally, these species are irreversibly adsorbed at room temperature and are thus much more strongly adsorbed than CO_2 complexes, but represent a minority species. By comparing successive CO_2 adsorption isotherms on K-Y and Cs-Y zeolites, Pirngruber *et al.* estimated that the amount of carbonate species is $\sim$5 per unit cell (UC), which can be compared with the total CO_2 capacity of $\sim$70–90 molecules per UC.[602] This result is in line with the much earlier estimate of $\sim$3 irreversibly adsorbed CO_2 species per UC in Na-X zeolites by Jacobs *et al.*[604] Although many recent theoretical studies have been devoted to the adsorption of CO_2 on alkali-exchanged zeolites, none of them have modeled the structure or formation of such species. On the basis of DFT calculations carried out on linear ion–CO_2 complexes, however, Pirngruber *et al.* discussed the formation of such species by noting that on basic zeolites, such as K-Y or Cs-Y zeolites, the carbon atom of CO_2 adsorbed in 12-ring windows (supercages) does interact with zeolite framework oxygen atoms, leading to a slight bending of the O=C=O angle (<3°), and can be considered as a precursor of bridged carbonate species (Fig. 18b).[602] The impossibility of forming carbonate species on light alkali-exchanged zeolites, such as Li- or Na-Y, is explained within this qualitative model by (i) the lower basicity of framework oxygen atoms and (ii) the position of the small cations, which are close to a hexagonal window, leading to short $M^+\cdots$OCO distances (Fig. 18c) and preventing the interaction of the carbon atom with framework oxygen atoms. Finally, it is worth noting that CO_2 can probe other basic sites than framework oxygen atoms. It is the case, for instance, of extraframework aluminum species of acidic BEA zeolites that are slightly basic and can lead to carbonate or hydrogen carbonate species (Fig. 18a);[603,605] of basic hydroxy groups resulting from the dissociation of water in hydrated extraframework cations and leading to hydrogen carbonate species;[567] and of metal oxide clusters, which lead to (hydrogen)carbonate species similar to those formed on amorphous oxides.[568,603]

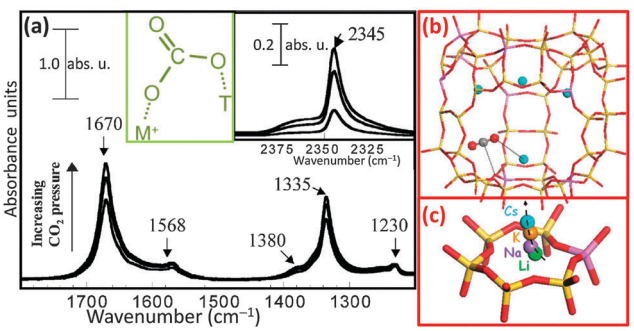

Fig. 18 Part (a): IR spectra of the adsorption of CO_2 on K-X zeolite at 373 K, showing the formation of carbonate and hydrogen carbonate species. Black inset: Linearly adsorbed CO_2 species. Green inset: Schematic structure of bridged carbonate species in an alkaline zeolite (T=Si or Al). Part (b): stick (zeolite framework) and ball (CO_2 and extraframework cations) representation of a CO_2 molecule (carbonate precursor) adsorbed in a 12-membered ring window of Cs-Y zeolite (supercage). The shortest C$\cdots$O and O$\cdots Cs^+$ distances are represented by the dashed lines. The O=C=O angle is 177.7°. Part (c): Structure of the hexagonal window, separating the supercage and the sodalite cage (see the inset in Fig. 20 below for a larger view of the Y structure) with the optimized position of (Li, Na, K, and Cs) cations in site II. Color code of part (b): Si atoms, yellow sticks; Al atoms, red sticks; framework oxygen atoms, red sticks, while red and gray balls refers to the O and C atoms of the CO_2 molecule, and the blue balls refer to Cs cations. For part (c), green ball, Li; violet ball, Na; orange ball, K; blue ball, Cs. Part (a): Adapted with permission from ref. 567, copyright American Chemical Society 2003; parts (b) and (c): adapted with permission from ref. 602, copyright Royal Society of Chemistry 2010.

For completeness, it should be noted that boric acid trimethyl ester ($B(OCH_3)_3$) was proposed as a Lewis acid probe molecule by Li *et al.* for the characterization of the basic properties of metal oxides[546] and zeolites.[606] The formation of Lewis complexes with framework oxygen anions changes the planar symmetry of this molecule into a pyramidal form, leading to the splitting of a degenerate vibration involving B–O bonds (1360 cm^{-1}). However, the position and splitting of these bands were not sensitive to the strength of basic centers and this probe has not been used much since these early studies.

4.2.3. *In situ* generated probe: NO^+. Recently, the disproportionation reaction of NO_2, leading to a nitrate anion and a NO^+ cation (nitrosonium), has been used to characterize the basicity of alkali-exchanged FAU zeolites:[607,608]

$$[ZO^-, M^+] + 2NO_2 \rightarrow [ZO^-{:}NO^+, M^+{:}NO_3^-] \quad (16)$$

In this reaction, which is formally equivalent to (15) mentioned above, nitrate ions are stabilized by extraframework cations, whereas NO^+ directly interacts with framework oxygen atoms. The $\nu(NO^+)$ stretching frequency was found to be strongly sensitive to the electron density of the oxygen atom, decreasing from 2110 cm^{-1} to 1970 cm^{-1} for Li-Y to Rb-Y zeolites and from 1976 to 1903 cm^{-1} for Li-X to Rb-X zeolites (Fig. 19a). These species were studied by periodic DFT calculations, which confirmed such a trend, *e.g.* a decrease in $\nu(NO^+)$ frequency with increasing size of the alkali cation on the one hand and from Y- to X-zeolites on the other hand (Fig. 19b).[609,610]

5. Identification and location of sites in the framework of zeolites by the size of probe molecules

Pores are the main feature of zeolites. Molecular sieving can influence reactants and probe molecules. The catalytic activity and selectivity of zeolites can only be understood by knowing

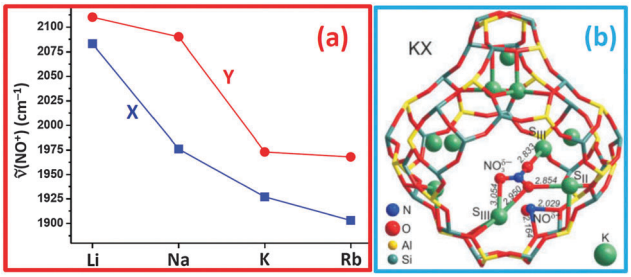

Fig. 19 Part (a): Positions of $\nu(NO^+)$ bands on alkali-exchanged X- and Y-zeolites. Previously unpublished figure, summarizing data reported in ref. 607 and 608. Part (b): Stabilization of the NO^+/NO_3^- ion pair formed by disproportionation of N_2O_4 at site III of K-X zeolite (D_{2h} symmetry), see also inset in Fig. 20. Selected interatomic distances (Å) are shown in italics. Adapted with permission from ref. 610, copyright Wiley 2010.

the location of sites and by knowing how easily these sites can be reached by reactants. This question is also valid for all sites, and not only for those that are catalytically active. Silanol groups and simple adsorption sites, namely, Brønsted and Lewis sites (see Sections 2 and 3, respectively) can be accessible or not, or subject to other factors such as diffusion limitation and confinement. Infrared spectroscopy is a major tool for determining and studying these effects.

The difference in behaviour and catalytic activity between internal and external sites (silanols, lattice OH groups) in zeolites has long been a matter of study.[168,169,611–616] In recent years, hierarchical materials have provided a method for overcoming diffusion limitations in zeolites.[89–91,97,617–654] The question of the accessibility of catalytic sites in these materials has raised new interest in the use of infrared spectroscopy of probe molecules.[90,91,97,629–634,636,637,641,653]

This section is divided into five subsections. The first is devoted to the IR investigation of the influence of pores and confinement on the acid strength of OH groups in the supercage and sodalite cage of H-USY zeolite. Section 5.2 discusses the accessibility of Brønsted sites in defect-free and defective zeolites. Section 5.3 shows how the use of different methyl-substituted Py allows discrimination between internal and external OH groups in zeolite H-ZSM-5. The methodology of using a set of different probes with increasing steric hindrance for investigating the accessibility of zeolitic pore systems is discussed in Section 5.4 with several examples. Section 5.5 presents IR characterizations of hierarchical zeolites. Finally, the use of two nitrile probes of different sizes, namely, CH_3CN and benzonitrile (PhCN), for characterizing the accessibility of Brønsted sites in progressively dealuminated mordenites, which is potentially relevant to this section, is reviewed in Section 8.3 because it is based on stimulated Raman scattering (SRS) microscopy.[655]

5.1. Influence of pores and confinement on the spectrum and acid strength of OH groups: H-USY zeolite as a key study

The protonic form of ultrastable Y zeolite (H-USY) is obtained by prolonged steaming at high temperature of H-Y zeolite. This process aims at removing the more unstable Al^{3+} species from the zeolitic framework, resulting in the loss of the corresponding Brønsted sites and the appearance of extraframework Al^{3+} Lewis sites (see Section 3.2). This benefits the catalytic application of the material in industrial plants because it guarantees more stable activity of the catalyst over time.[240,499–501] Among all the catalytic applications of USY, in the industrial field, the most important is the fluid catalytic cracking (FCC) of the high-boiling hydrocarbon fraction of petroleum crude oil, which is converted to more valuable gasoline, olefinic gases, and other products.[71,72,582,656–660] Furthermore, the mesopore network, which is formed during steaming, improves the transport properties of the catalyst, and therefore its overall efficiency.[72,661]

As already discussed in Section 2.1, in first approximation, the frequency of ν(OH) vibrations depends on the electron density in the OH bond. Silanol groups, which are non-acidic with a fairly strong O–H bond, appear in the IR spectrum as a sharp band in the 3750–3740 cm^{-1} range, whereas acidic bridged OH groups have considerably less electron density in their weaker O–H bond, and that bond vibrates around 3600 cm^{-1}, as shown in Fig. 1 above and Fig. 20 below.

As already briefly mentioned in Section 2.1, any interaction between the OH group and an electron donor (zeolite wall or extraframework phase) will shift the ν(OH) vibration band towards lower frequency. This is particularly clear for H-USY zeolites, as shown in Fig. 20. Bridged OH groups located in the large supercage of the FAU structure appear at 3630 cm^{-1}, whereas they appear at 3565 cm^{-1} when located in the sodalite units (these ν(OH) bands are therefore often denoted as high and low frequency bands, HF and LF, respectively). The IR spectrum of H-USY zeolite shown in Fig. 20 differs significantly from that of H-Y zeolite shown in Fig. 1 (bottom curve). The relative intensity of the silanol band with respect to those of Brønsted sites reflects the much smaller crystal size of the H-USY sample, whereas the steaming process results in structured bands for both HF and LF components.

As mentioned in Section 2.1, the red shift in the LF component is due to the interaction of the OH group with the neighbouring walls of the sodalite cage (H-bonding with adjacent framework oxygen atoms, scheme shown in Fig. 20). As discussed later, this has no influence on the acid strength of the bridged OH group. The main difference for any catalytic activity is that the access to OH groups in sodalite cages is highly hindered, and that no reactant can usually interact with LF OH groups. Interaction can also occur between OH group and a neighbouring extraframework phase. In acidic USY zeolite, the extraframework phase withdraws electrons from the O–H bond. This results in an increase in the acidity of the bridged OH groups and a further red shift in the ν(OH) vibration bands; in fact, the maximum of the HF band occurs at 3645 cm^{-1} for H-Y (bottom curve in Fig. 1) and at 3630 cm^{-1} for H-USY (Fig. 20). Depending on the type and location of the interacting extraframework phase, four different ν(OH) vibration bands were identified with two different types and two different locations of the extraframework phase for each HF and LF OH group.[662]

5.2. Non-hierarchical zeolites. Are OH groups accessible or not? The influence of structural defects

In zeolites without defects, a perfect crystalline structure will exhibit the expected pore channels, and fairly simple reasoning

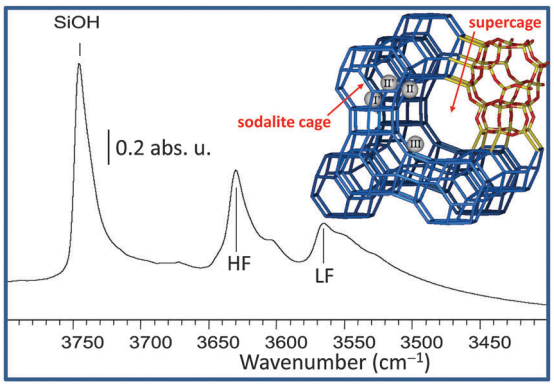

Fig. 20 Main part: IR spectrum of H-USY zeolite in the region of ν(OH) vibration bands. HF and LF bridged OH groups in supercages and sodalite units are visible together with their red-shifted part due to interaction with an extraframework phase. The top right-hand corner contains a stick representation of Y zeolite (FAU topology[165]) showing a supercage and several sodalite cages. The locations of the Brønsted sites in the supercage (site II) and the sodalite cages (sites I′ and II′) are also shown. Site III, also located in the supercage, is only occupied for X zeolites, which have a lower Si/Al ratio. Main part: Adapted with permission from ref. 662, copyright Elsevier, 2007.

will be able to predict and understand the accessibility of sites. Silanol groups will only be external with no silanol nests, and access to Brønsted sites (see Section 2) will be geometrically restricted by pore windows. There will be, in a general case, no Lewis sites (no defects and extraframework phase, see Section 3). The absence of Lewis sites can be confirmed after measurement by cleaning the surface of the solid under vacuum and adsorbing pyridine as the last probe molecule. If pyridine detects Lewis sites, this is an indication of framework damage, either before or during the experiment. Framework damage can facilitate the transport of a probe molecule to adsorption sites by creating defects in the pore system. It can also have the opposite effect: too rapid calcination of a sensitive zeolite (*e.g.* mordenite) can completely block the pore system and pyridine will detect only a fraction of the Brønsted sites (but might detect unexpected Lewis sites due to an extraframework aluminium phase).

The general case is that of a zeolite that contains defects. Steamed or stabilized zeolites, as well as zeolites thermally treated with a fast heating ramp, contain a significant amount of defects and Lewis sites. Some sites that would not have been accessible in a perfect crystal have now become within reach to many probe molecules. Many studies about the accessibility to some peculiar sites in zeolites (such as side pockets in mordenites) are seriously concerned about the thermal history of the zeolite and the presence of defects. Such fragile zeolites should be activated by heating very slowly, sometimes at 1 K min^{-1}, but always at less than 3 K min^{-1}. Access to hindered sites has been claimed in zeolites, where the structure was in fact damaged, and the structure of the pore around the adsorption site was not as expected (which would have been detected by confirming the absence of Lewis sites at the end of the experiment).

It has long been said that probe molecules must be small to probe all the sites in zeolites. However, adjusting the probe size is a useful tool for understanding the relationship between acidity and activity. In both perfect and defect-containing zeolites, exploring of the pores can be carried out using probe molecules of various sizes. The interaction of the probe molecule with the site for this purpose can vary; *e.g.*, protonation, H-bonding, and deuterium exchange.

5.3. Substituted pyridines: distinguishing internal and external silanol groups

Py is a common probe for characterising acid sites in zeolites. It penetrates into most catalytically important pores. Methyl-substituted pyridines, such as 2,4,6-collidine (2,4,6-trimethylpyridine), are larger molecules, and their access to some micropores is limited. In H-MFI, collidine was used to distinguish OH groups located inside or outside the pore system, schematically represented as blue and red spheres in Fig. 21c, respectively. The acidic Brønsted SiOHAl groups, which are located inside the micropores, are out of reach of collidine. T atom vacancies result in internal silanol nests,[168–170] which consist of internal Si–OH groups that are located inside the micropores (not represented in Fig. 21c), and they vibrate at a slightly lower frequency than the usual external silanol groups, see the spectral region labelled as "internal silanols" in Fig. 1 in Section 2. Adding 2,4,6-collidine to H-ZSM-5 results in a decline in the silanol bands at 3745 cm^{-1}, whereas the band around 3610 cm^{-1}, due to internal Brønsted sites, is left unperturbed, which can be inferred by comparing the full and dashed spectra in Fig. 21a. Actually, a minor fraction of the silanol band is still present in the dashed spectrum; this persistent component is centered and tails off toward lower frequencies with respect to the band of external silanols. The spectra shown in Fig. 21a are direct spectroscopic proofs of the presence of internal silanols in ZSM-5, which are not reachable by a 2,4,6-collidine probe. Interestingly, the internal silanols in H-MFI disappear *via* interaction with traces of coke generated during xylene isomerisation (Fig. 21b). Traces of coke can only be formed in the additional space in structural defects, and this is where these internal silanols are present.[414]

5.4. Different probes for studying pore systems

5.4.1. Py and CO co-adsorption in mordenite. The difference in size between probe molecules is a very sensitive tool for exploring pores. Combining probe molecules by adsorbing them together is a way of obtaining information from both probes on the accessibility and strength of sites.[664] In this regard, the mordenite framework provides a clear example. As is the case for H-Y (see Fig. 1 and 20 above and related discussions), H-mordenite also exhibits two different types of Brønsted sites, characterized by a ν(OH) mode absorbing around 3612 and 3585 cm^{-1},[133,204,229,665–667] also defined as HF and LF components, respectively (Fig. 22a). Compared to H-Y, a much smaller difference in the corresponding $\tilde{\nu}$(OH) characterizes the HF and LF components in H-mordenite and a careful deconvolution process was needed to separate them.[666,667] The HF component appears due to Brønsted sites hosted in the main channels (a straight 12-membered ring channel running along the [001] direction and characterized by

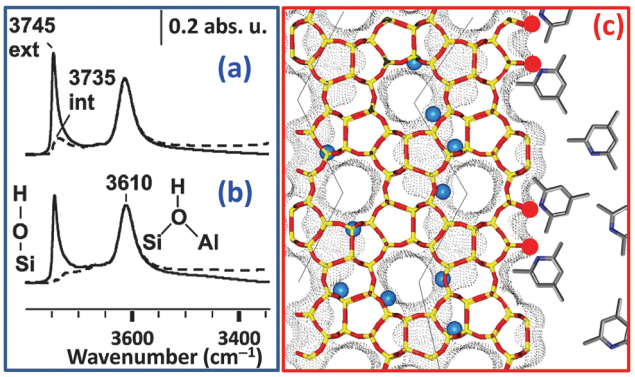

Fig. 21 Part (a): IR spectra in the ν(OH) stretching region of H-ZSM-5 before (full line) and after (dashed line) the adsorption of collidine. Because 2,4,6-collidine does not enter the micropores of ZSM-5, only the OH groups located on the external faces of the zeolite crystals are consumed, leaving internal Brønsted sites untouched and providing evidence of the band due to internal silanols. Part (b): Similar to part (a) for H-ZSM-5 that was subjected to a coke formation process after xylene isomerisation. On the coked sample, internal silanols have disappeared. Part (c): Stick representation of ZSM-5 zeolite fragment (MFI topology[165]) viewed along the [010] direction of the straight channels; sinusoidal channels, running along the perpendicular [100] direction, are indicated by black segments. Moreover, the crystal surface is represented, where 2,4,6-collidine (stick representation) has been dosed in excess. Red and blue spheres represent possible locations of external (silanols) and internal (Brønsted sites) OH groups, respectively, whereas the stick color code is as follows: Si or Al (yellow), O (red), N (blue), and C (grey). Dots outline the Connolly surface[663] obtained with a probe molecule that is 2.8 Å in diameter. This scheme represents an ideal defect-free crystal, where internal silanols are absent. Part (c): Previously unpublished; parts (a) and (b): adapted with permission from ref. 414, copyright Elsevier, 2001.

an elliptical cross-section of 0.65 nm × 0.70 nm in diameter).[165] These channels have side pockets in the perpendicular [010] direction, circumscribed by 8-membered rings that are accessible through windows with a free diameter of *ca.* 0.39 nm and hosting the Brønsted sites responsible for the LF component. See Fig. 22b for a view of the mordenite structure along the main channel direction. A Py probe has access to the Brønsted sites located in the main channels, but not to those hosted in the smaller side pockets. This can be seen on the spectra of the ν(OH) vibration band (main part in Fig. 22a). After the adsorption of Py, only the HF part of the band for acidic lattice OH groups is perturbed and disappears; this corresponds to the two-thirds of the lattice OH groups that are located in the main channels. The lower-frequency part of the band (spectrum n in Fig. 22a) can therefore be assigned to the OH groups in the side pockets of mordenite.

CO is a small probe molecule that interacts with all acidic sites wherever they are located in the pore system of mordenite.[379,664] As discussed in Section 2, the strength of the interaction of CO with acidic sites gives information on the acidic strength. When CO is adsorbed on a clean and empty zeolite, all the sites are measured together (inset in Fig. 22a). When CO is adsorbed on mordenite with pre-adsorbed pyridine, CO only measures the strength of H-bonding in small side pockets, where pyridine cannot enter. The acidic strength of the OH groups in the main channels can be obtained by difference. Thus, by co-adsorbing Py and CO, the steric hindrance of pyridine allows the location of sites to be differentiated and the acidic strength of OH in various locations to be measured by CO. In particular, CO molecules interacting with Brønsted sites in the main channel give rise to an IR band, which upon an increase in the equilibrium pressure of CO moves from 2180 to 2175 cm^{-1}, whereas those probing Brønsted sites in the side pockets are characterized by ν(CO) that shifts from 2171 to 2169 cm^{-1}.[664] A more recent and more detailed analysis of mordenite was even capable of identifying and measuring a third possible location for OH groups in the window between the main channels and side pockets.[664]

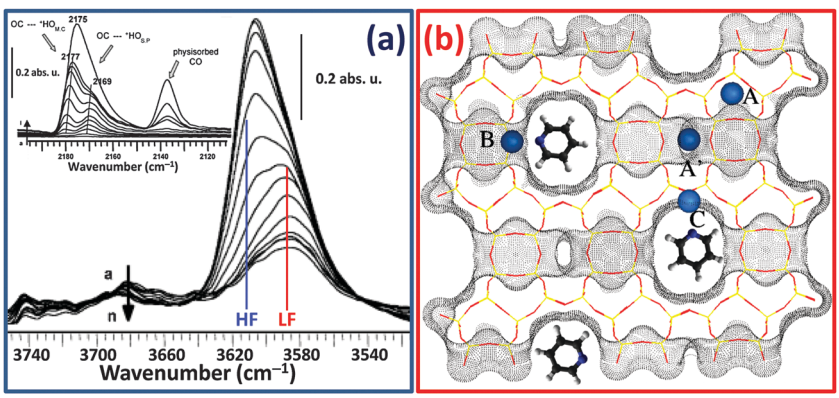

Fig. 22 Part (a) IR spectra in the ν(OH) stretching region of thermally activated H-mordenite before (curve a) and during adsorption of increasing amounts of Py (curves b to n). Inset: IR spectra in the ν(CO) stretching region of thermally activated H-mordenite before (curve a) and during adsorption of increasing amounts of CO (curves b to l). Vertical colored lines highlight the positions of the partially overlapping HF and LF components. $^{+}HO_{MC}$ and $^{+}HO_{SP}$ represent Brønsted sites in the main channel and side pockets, respectively. Adapted with permission from ref. 664, copyright American Chemical Society, 2004. Part (b): Stick representation of the mordenite structure (MOR topology[165]) projected along the [001] direction, showing possible locations of internal Brønsted sites. Sites B and C are located in the 12-membered ring main channel and are accessible to Py molecules (also drawn in ball-and-stick representation), whereas sites A and A′ are located inside the side pocket and cannot be perturbed by Py. The colour code is as follows: Si or Al (yellow), O (red), N (blue), C (dark grey), H (white). Dots outline the Connolly surface obtained with a probe molecule that is 2.8 Å in diameter. Adapted with permission from ref. 386, copyright American Chemical Society, 2003.

5.4.2. Acetonitrile and substituted acetonitrile. (Deuterated) acetonitrile is a small and versatile probe molecule. It can detect Lewis and Brønsted sites,[4,136,137,146,177,198,202,317,668–673] and is able to locate sites in small pores, even side pockets of mordenite,[212,674] as shown in Fig. 22b. The size of the probe molecule can be increased and tuned by introducing methyl or larger substituents onto the methyl group of acetonitrile. An accessibility scale was thus introduced by Busca by first using pivalonitrile (2,2-dimethylpropionitrile)[675,676] and then propionitrile, isobutyronitrile (2-methylpropionitrile), 2,2-diphenylpropionitrile, benzonitrile, and *ortho*-toluonitrile.[677] The Genoa group used that first accessibility scale to investigate external *vs.* internal sites in many different zeolite structures. They showed that bridged acidic OH groups only form inside the pore system and not on the external surface, whereas aluminium atoms on the external surface cannot form bridging OH Brønsted sites and are the origin of strong external Lewis acidity.

5.4.3. H-bonding: decrease of the interaction by steric hindrance. Onida *et al.*[211] have shown that large molecules are limited in their H-bonding inside zeolites. The larger the molecule, the larger is the deviation from the strength expected. Using a series of weak bases with increasing size and steric hindrance for the interaction of a probe molecule with an acidic site is a possible measure of the accessibility of a zeolite. The following molecules were employed in this study: N_2 (0.31 nm), CO (0.34 nm), ethylene (C_2H_4, 0.48 nm), propene (C_3H_6, 0.65 nm), benzene (C_6H_6, 0.72 nm), toluene (C_7H_8, 0.82 nm) and 1,3,5-trimethylbenzene (TMB, 0.88 nm). The parentheses present the corresponding molecular cross-sections and, when needed, the chemical formula or acronym used to plot the data in Fig. 23.

As discussed in depth in Section 2.2 (see Fig. 4), the strength of H-bonding between an acidic solid and probe molecules is usually measured by a procedure similar to BHW plots,[189–193,195] comparing the shift in ν(OH) caused by adsorption of the probe on the solid, $\Delta\tilde{\nu}_{\text{Brønsted}}(\text{OH})$, with the shift that would be observed on a reference material such as silica (open surface, $\Delta\tilde{\nu}_{\text{Silica}}(\text{OH})$). On zeolites, large molecules deviate from the expected linear plot for an open surface. In fact, the BHW relation holds only if the base B is free to optimize its orientation to maximize hydrogen-bonding interaction with the acidic site. For a given zeolite topology, this assumption starts to be no longer valid when molecular hindrance (defined as the largest transverse molecular diameter) exceeds a given value related to the zeolite pore dimensions. This is clearly shown in Fig. 23a–d. As an example, Fig. 23a shows that in SAPO-40, which exhibits large 12-membered rings along the [001] direction (6.7 Å × 6.9 Å),[165] only benzene and TMB deviate from BHW linear behavior. Analogously, for a given base B used to probe different zeolitic frameworks, the hydrogen-bonding interaction can be optimized in large-pore zeolites, whereas this may not be the case in small-pore zeolites. This is the case with propene, of which the spectroscopic data lie on the BHW line (dotted lines in Fig. 23a–d) for SAPO-40 and ZSM-5 frameworks (parts a and b), whereas they deviate slightly for MCM-22 (part c) and significantly for Theta-1 frameworks (part d). This observation agrees with the topologies of the investigated zeolites, of which the frameworks are illustrated in stick representation in Fig. 23e–h. ZSM-5 exhibits a couple of interconnected 10-membered ring pores running along the [100] (5.1 Å × 5.5 Å, sinusoidal) and [010] (5.3 Å × 5.6 Å, linear) directions; MCM-22 possesses a complex two-dimensional pore structure with sinusoidal 10-membered ring channels with elliptical ring cross-sections of 4.1 Å × 5.1 Å and 4.0 Å × 5.1 Å; and Theta-1 has 1-dimensional linear channels formed by 10-membered rings with an elliptical cross-section of 4.6 Å × 5.7 Å.[165]

Onida *et al.*[678] defined the percentage deviation (D) for each molecule B as well as for each zeolite as follows:

$$D = 100\,\frac{[\Delta\tilde{\nu}_{\text{Brønsted}}(\text{OH})]_{\text{BHW}} - [\Delta\tilde{\nu}_{\text{Brønsted(OH)}}]_{\text{Exp}}}{[\Delta\tilde{\nu}_{\text{Brønsted}}(\text{OH})]_{\text{BHW}}}, \qquad (17)$$

where $[\Delta\tilde{\nu}_{\text{Brønsted}}(\text{OH})]_{\text{Exp}}$ is the experimental shift (ordinate of the scattered data in Fig. 23a–d) and $[\Delta\tilde{\nu}_{\text{Brønsted}}(\text{OH})]_{\text{BHW}}$ is the expected shift in the case of absence of hindrance. The latter is obtained as the ordinate at the corresponding $\Delta\tilde{\nu}_{\text{Silica}}(\text{OH})$ abscissa value of the linear fit obtained for the fraction of data (see dotted lines in Fig. 23a–d and Table 7 for quantitative values). D values that were computed for all IR experiments and plotted against the molecular hindrance resulted in the plots of Fig. 23e–h.

This study provides evidence that at more constrained acid sites, the deviation from BHW linearity is more important.[678] The validity of the measurement of acidity using large probe molecules is therefore shown to be questionable, but an interesting scale of ''hindrance to the acid site'' among zeolites has been established (*i.e.*, opposite to accessibility): SAPO-40 ≈ ZSM-5 < MCM-22 < Theta-1. This is clearly seen in the plots shown in Fig. 23e–h. Moreover, if care is taken to calculate the slope of the BHW plot using only the fraction of data that are not subject to hindrance problems, then a spectroscopic determination of the acidic strength can still be obtained, as shown by the dotted lines in Fig. 23a–d and Table 7 for quantitative values. From such data, the following scale of acidity emerges: SAPO-40 < ZSM-5 ≈ MCM-22. Unfortunately, no conclusive estimation can be made for Theta-1, because the slope of the BHW line has been obtained using only two pairs of experimental data and resulted in a very large relative error to make a conclusive comparison with the remaining three zeolitic systems. Nevertheless, a quantitative result can in principle be obtained by selecting other small molecules with different proton affinities.

5.5. Hierarchical zeolites: the accessibility index ACI

Hierarchical zeolites are now one of the main interests for industrial applications of zeolites,[89–91,97,617–654] especially in the field of oil refining and processing. The main feature of interest in hierarchical zeolites is their increased accessibility to the active site and reduction in diffusion limitations. Therefore, the exploration of a reliable tool for comparing and quantifying accessibility in hierarchical zeolites has become a key issue.

Py can be substituted with methyl groups to produce a family of probe molecules that are often used to study the

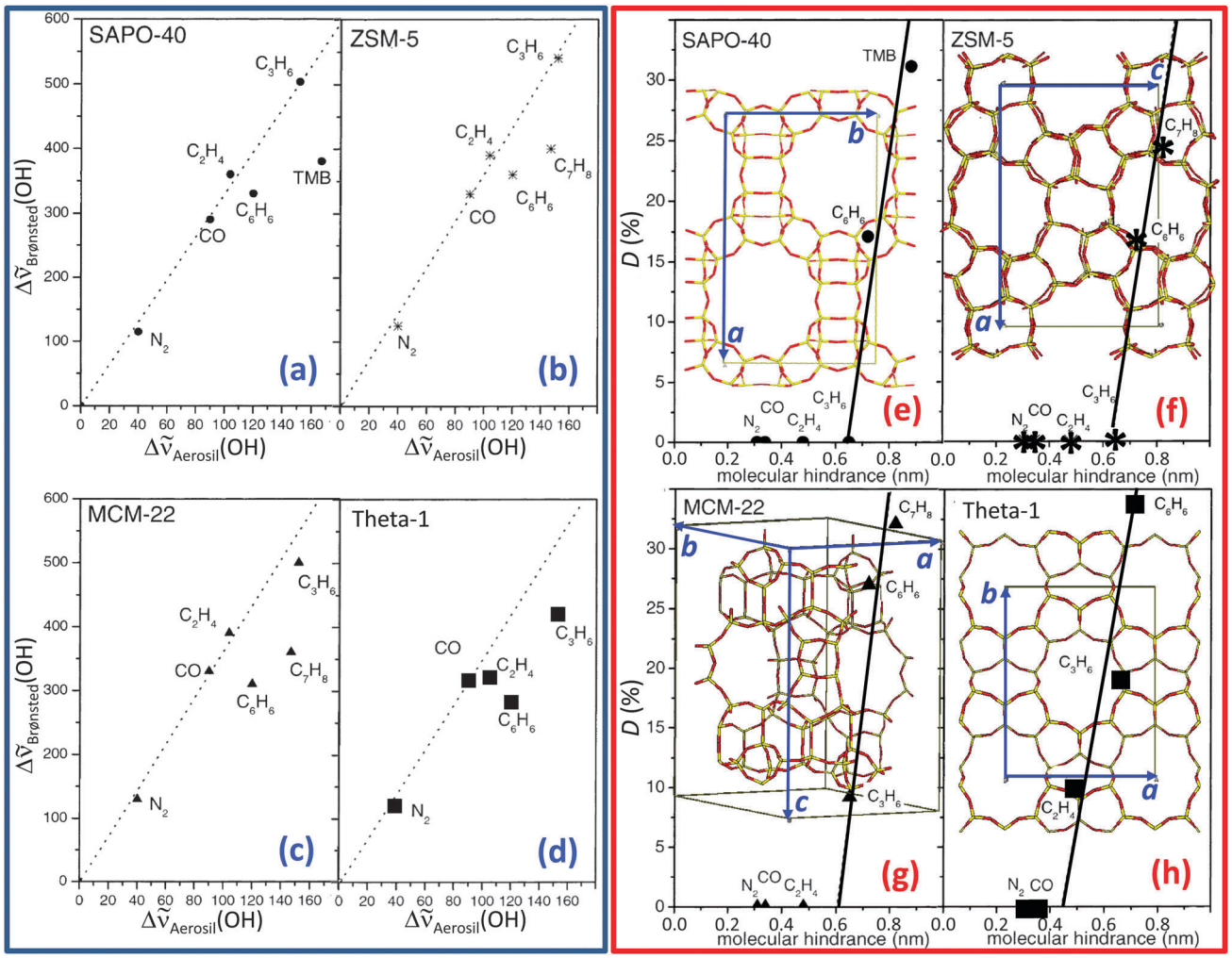

Fig. 23 Parts (a–d): BHW plots (see Fig. 4 above and related discussion) referring to SAPO-40, ZSM-5, MCM-22, and Theta-1 zeolites, respectively, obtained by taking the values for the isolated silanol on the surface of Aerosil (amorphous high-surface-area SiO_2) as reference. Dotted lines represent the best linear fits obtained for the fraction of data that obey the BHW linear correlation. Parts (e–h): Correlation between the deviation from the BHW model defined according to eqn (17) and the molecular hindrance defined as the largest transverse molecular diameter of the probe molecule for SAPO-40 (AFR topology), ZSM-5 (MFI topology), MCM-22 (MWW topology), and Theta-1 (TON topology).[165] Parts (e–h) also show graphical stick representations of the corresponding zeolite structure with the corresponding unit cell and crystallographic *a*, *b* and *c* axes (when not along the viewing direction). Si or Al atoms (yellow) and O atoms (red). The zeolite structures are new graphical materials, whereas all the remaining items have been adapted with permission from ref. 211, copyright American Chemical Society, 2002.

location of sites inside or outside zeolite pores: pyridine (Py, ~6 Å, entering 10-MR but not 8-MR), lutidine (Lu, 2,6-dimethylpyridine, ~7 Å), collidine (Coll, 2,4,6-trimethylpyridine, 7–8 Å, entering 12-MR) and di-*tert*-butylpyridine (DTBPy, 2,4-di-*tert*-butylpyridine, not entering 12-MR openings). By increasing the size of the probe molecule, it is possible to tune the size of the pores under investigation. The fairly small Py does not penetrate the small side pockets of mordenite but will enter any other larger pore system, whereas larger molecules, such as Coll[99] or DTBPy,[652] will only come in contact with the external surface of many hierarchical zeolites.

The co-adsorption of carbon monoxide and a series of substituted pyridines was used to measure accessibility in progressively dealuminated mordenites.[679,680] The largest probe molecule (DTBPy) was adsorbed first, followed by the others in decreasing order of size to finish with CO, which is one of the smallest possible probe molecules. On the parent sample, only Py and CO entered the pore system, with two-thirds of the sites accessible to Py and one-third only accessible to CO, as expected from the main channels-side pockets ratio for lattice OH groups (see Fig. 22b for a view of the mordenite structure). During the progressive dealumination process, mesopores were created and accessibility was progressively increased. Thus, larger probes like Coll, Lu or even DTBPy could make their way to the acid sites in the pores, leaving increasing fewer adsorption sites for CO only (Fig. 24). Quantities can be determined using the molar absorption coefficients for Brønsted or Lewis sites. The authors used $\varepsilon_{\text{Brønsted}}$ (1545) = 1.02 cm μmol^{-1} and $\varepsilon_{\text{Lewis}}$(1454) = 0.89 cm μmol^{-1} for Py; for Coll, $\varepsilon_{\text{Brønsted}}$(1632–1648) = 10.1 cm μmol^{-1}, as determined on dealuminated mordenites;[679,680] and for Lu, $\varepsilon_{\text{Lewis}}$(1609–1617) = 4.4 cm μmol^{-1}, $\varepsilon_{\text{Brønsted}}$(1643–1655 + 1627–1630) = 6.8 cm μmol^{-1},

Table 7 Summary of the best linear fits obtained for the fraction of $\Delta\tilde{\nu}_{Brønsted}(OH)$ *vs.* $\Delta\tilde{\nu}_{Aerosil}(OH)$ data shown in Fig. 23a–d that lie on the BHW line for the different zeolites. Due to the low number of available pairs of shifts in experimental frequency (4 for SAPO-40 and ZSM-5, 3 for MCM-2 and only 2 for Theta-1), the data for the unperturbed systems ($\Delta\tilde{\nu}_{Brønsted}(OH)$ = 0 cm^{-1}; $\Delta\tilde{\nu}_{Aerosil}(OH)$ = 0 cm^{-1}) have been added to all fits. Previously unpublished table analyzing data reported in ref. 211. These data cannot be directly compared with those reported in Table 2 because the reference shift has been taken from different materials: high-surface-area amorphous Aerosil in the present case and external silanols of the same zeolite in the study of Pazè *et al.*[145]

System	Slope	Intercept (cm^{-1})	R^2
H-SAPO-40	3.37 ± 0.11	−7 ± 10	0.9956
H-ZSM-5	3.65 ± 0.13	−5 ± 12	0.9953
H-MCM-22	3.77 ± 0.14	−8 ± 10	0.9959
H-Theta-1	3.53 ± 0.26	−8 ± 15	0.9891

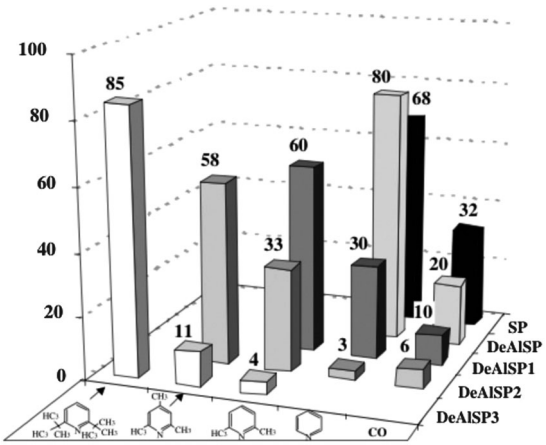

Fig. 24 Co-adsorption of a series of substituted pyridines and CO on increasingly dealuminated mordenites. On the parent zeolite (denoted as SP), 2/3 of acid sites are accessible to Py and 1/3 remain for CO. On the first dealuminated mordenite, DeAlSP, the accessibility to Py increases to 80%, leaving only 20% for CO. During progressive dealumination to the sample DeAlSP3, the accessibility increases for larger probes such as Lu, Coll and DTBPy to eventually reach 85% accessibility to DTBPy, leaving 11% for Coll, 4% for Lu, and nothing for smaller molecules. Reproduced with permission from ref. 679, copyright Elsevier, 2004.

as determined on various solids.[681] It should be noted that the values for various ε can differ from one experimental system to another, as will be explained in Section 6, and the values used here appear reasonable in view of the rest of the literature.

Substituted pyridines were adsorbed and co-adsorbed with CO to confirm the extreme accessibility of bridged acid sites in delaminated MFI zeolites.[89] All the acidic sites were shown to be in close proximity to the external surface or to be located in pore mouths. A careful and detailed analysis of the adsorption and transport of benzene and cyclohexane in various hierarchical ZSM-5-based materials confirmed that strong Brønsted sites are only located in micropores, and showed that the structure and acidity in micropores were preserved during the creation of mesopores.[636]

A reliable tool for comparing and quantifying accessibility in hierarchical zeolites was made available with the accessibility

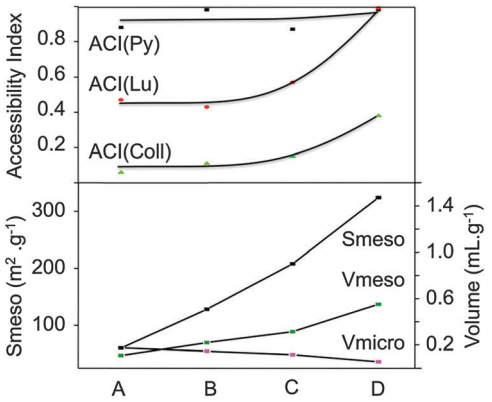

Fig. 25 Changes in ACI for Py, Lu and Coll on a series of progressively desilicated H-ZSM-5 (from A to D). Upon desilication, the mesopore surface area and volume of the samples increase and the micropore volume decreases. At the same time, changes in ACI for bulky molecules (Lu and Coll) show the increase in accessibility of the samples. Previously unpublished figure summarizing data reported in ref. 630.

index (ACI). The accessibility index for a given probe molecule is the number of sites detected by that particular probe, divided by the total number of sites.[630] The total number of sites can be the number that is expected theoretically (for example, based on chemical analysis of Al) or measured with a probe that reaches all possible sites, such as CO or pyridine, depending on the type of sample. The first series of probe molecules for measuring ACI were substituted alkylpyridines of different sizes (Py, Lu and Coll). It was applied to hierarchical ZSM-5 crystals that were prepared by selective extraction of silicon from a parent commercial sample in an alkaline medium (desilication). The samples exhibited different degrees of intracrystalline mesoporosity. The accessibility index for pyridine, ACI(Py), did not change in the series containing increasing amounts of mesopores and was already above 0.9 for the parent sample, as expected. An increase in ACI(Lu) was noticed upon the introduction of mesopores and this increased from *ca.* 0.5 for the parent sample to nearly 1 for a highly mesoporous sample. The value of ACI(Coll) also changed noticeably, progressively increasing from nearly 0 for the parent sample to ~0.4 for the final sample. ACI is a powerful tool for standardizing the accessibility of acid sites in zeolites and can be used to rank the effectiveness of synthetic strategies towards hierarchical zeolites (mesoporous crystals, nanocrystals, and composites) (Fig. 25).

Other probe molecules were used for measuring ACI depending on the type of sites measured, for example substituted nitriles for the quantification of accessible Lewis sites.[641]

6. Determination of the absorption coefficients of the IR modes: combined IR and microgravimetric experiments

6.1. Basic definitions

Infrared spectroscopy is a quantitative tool in homogeneous systems and the Beer–Lambert law[682,683] is used to measure the amount of

species under investigation in liquids and gases. The same is very often assumed to be true in transmission spectroscopy on a pellet (wafer), and IR is commonly used to determine the number of surface species on powders. This enables the determination of the amount of probe molecules on the surface and therefore the amount of adsorption sites: acidic or basic sites and accessible metallic sites.

The Beer–Lambert's law describes the attenuation of light through a sample:

$$T(\tilde{\nu}) = \frac{I(\tilde{\nu})}{I_0(\tilde{\nu})} = e^{-\kappa(\tilde{\nu})cd}, \quad (18)$$

where $T(\tilde{\nu})$ is the transmittance, $I(\tilde{\nu})$ is the intensity of transmitted light, $I_0(\tilde{\nu})$ is the intensity of incident light on the sample, d is the thickness of the sample (wafer) (in cm), c is the concentration of absorbing species (in mol dm^{-3}), and $\kappa(\tilde{\nu})$ is the molar absorption coefficient (in mol^{-1} dm^3 cm^{-1}) at a given frequency ($\tilde{\nu}$). This law can also be written for optical density ($A(\tilde{\nu})$ or absorbance):

$$A(\tilde{\nu}) = \varepsilon'(\tilde{\nu})cd, \quad (19)$$

where $\varepsilon'(\tilde{\nu})$ is the molar absorption coefficient (in mol^{-1} dm^3 cm^{-1}) and $\varepsilon'(\tilde{\nu}) = \kappa(\tilde{\nu})/2.3$. The amount of species that interact with the light beam is cd, and the following formula is used for the commonly used pellets:

$$cd = \frac{n}{S}, \quad (20)$$

where n is the number of absorbing species in the pellet (in μmol) and S is the area of the pellet (in cm^2). From eqn (19) and (20) the following equation is obtained:

$$A(\tilde{\nu}) = \varepsilon'(\tilde{\nu})\ [10^{-3}\ n/S] \rightarrow \varepsilon'(\tilde{\nu}) = A(\tilde{\nu})[10^{+3}\ S/n] \quad (21)$$

In the following section, we will refer to the molar absorption coefficient $\varepsilon'(\tilde{\nu}_0)$ of a given vibrational mode of a given adduct that occurs at a given wavenumber $\tilde{\nu}_0$; thus, when there is no risk of ambiguity, we will refer to it simply as ε'. Depending on authors, and to simplify formulas, the units of ε' can commonly be mol^{-1} dm^3 cm^{-1} or mol^{-1} cm^2, which differ by three orders of magnitude. For quantitative evaluations, both maximum absorbance and integrated area can be used for measuring a band. The latter is much more sensitive to baseline perturbations, but much less sensitive to differences in temperature, resolution, or most other perturbations of vibrator. The integrated area $I(\tilde{\nu}_0)$ of a given IR band that absorbs at $\tilde{\nu}_0$ is expressed in cm^{-1}, and the integrated molar absorption coefficient $\varepsilon(\tilde{\nu}_0)$ is given as follows:

$$\varepsilon(\tilde{\nu}_0) = I(\tilde{\nu}_0)\ [10^{+3}\ S/n], \quad (22)$$

which is consequently expressed in cm mol^{-1} or more commonly in cm μmol^{-1}.

6.2. Selected examples

The key to quantitative measurements is thus the determination of ε, the (integrated) molar absorption coefficient for a given absorption band of a given (adsorbed) species. The simplest and oldest method for the determination of the integrated molar absorption coefficient is by introducing known amounts of a probe molecule into the cell and following the progressive change of the band under investigation, with the assumption that all the probe molecules are chemisorbed on the sample, at least for the first doses introduced. In fact, for the first few doses, there is a linear relationship between the amount introduced into the cell and the change in intensity for bands of surface species on the solid. The integrated molar absorption coefficient is then the slope of the straight line obtained (see Fig. 26a). When most of the adsorption sites are saturated, some of the adsorbed probe molecule is only physisorbed and a plateau is progressively observed.[667,684–686] The data shown in Fig. 26 refer to the dosage of progressive and carefully calibrated amounts of Py onto H-mordenite.[667] The first dosages of Py only affect the HF ν(OH) component (Fig. 26b). Py molecules that interact with the Brønsted sites in the main channel are protonated according to the reaction $Z_{MC}H\cdots Py \rightarrow Z_{MC}^{-}\cdots PyH^{+}$ (MC = main channel, see Section 2.2 above), as shown by comparison with the typical PyH^{+} component at 1545 cm^{-1}. From the data shown in Fig. 26, Maache *et al.*[667] determined that the amount of Py necessary to completely remove the HF component is 5 μmol (point C and spectrum C in parts (a) and (b) of Fig. 26, respectively). Above this amount of dosed Py, the curve in Fig. 26a indicates that a fraction of the additional Py is not protonated. This is due to the fact that additional Py molecules have to interact with Brønsted sites hosted in the side pockets, where hindrance problems

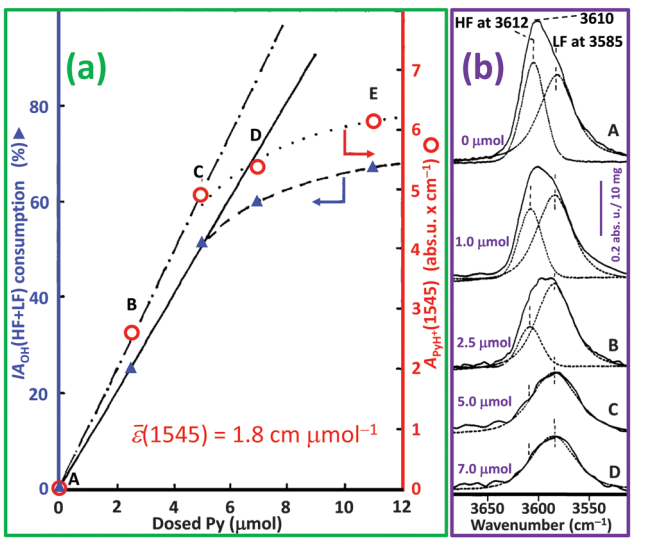

Fig. 26 Part (a): Variation of the intensity of the pyridinium complex formed on the Brønsted sites hosted in the main channel (IR band at 1545 cm^{-1}, red open circles and right ordinate axis) and of the proportion of correspondingly affected Brønsted ν(OH) (complex IR band initially at 3610 cm^{-1}, blue full triangles and left ordinate axis) with the amount of Py introduced into H-mordenite (activated at 723 K). The latter has been defined as 100 × [I(dose 0) − I(dose x)]/I(dose 0). Point C corresponds to the complete disappearance of the HF ν(OH) band due to Brønsted sites hosted in the main channel of mordenite (Fig. 22). The slope of the dot-dashed line implies that ε(1545) = 1.8 cm μmol^{-1}. Part (b): Selection of IR spectra showing the effect of increased amounts of adsorbed Py on the complex ν(OH) band of acidic Brønsted sites and the deconvolutions performed to quantitatively separate the HF and LF components. Adapted with permission from ref. 667, copyright Elsevier, 1995.

prevent the formation of a fully optimized H-bond (see Section 5.4.3). Indeed, as already discussed in Section 5.4.1 (see Fig. 22), the small 8-membered ring windows (free diameter of *ca.* 0.39 nm), which give access to the side pockets, limit the strength of the H-bonding interaction, resulting in a coordination reaction: $Z_{SP}H + Py \rightarrow Z_{SP}H\cdots Py$ (SP = side pocket). From the slope of the straight line obtained when plotting the intensity of the pyridinium band *versus* the amount of pyridine introduced, Maache *et al.*[667] deduced that the integrated molar absorption coefficient for the PyH^+ band $\varepsilon(1545) = 1.8$ cm μmol^{-1}. The same value was measured by Khabtou *et al.*[504] for the band resulting from the formation of $Z_{SC}^-\cdots PyH^+$ adducts in the supercage (SC) of Y zeolite.

It is well known that with solids, calibration curves are necessary, and that the Beer–Lambert's law is not always valid (especially with H-bonds). However, huge differences were observed between values reported by the different laboratories working in this domain. This was often attributed to a poor description of the experimental approach.[504] Morterra *et al.* questioned the whole approach and made a thorough examination of the adsorption of methanol on various samples of silica. They reproduced an adsorption isotherm in a spectrometer (optical adsorption isotherm) and in a gas volumetric apparatus connected to a heat flow microcalorimeter.[687,688] They showed that, although ε is in the same range for solids as for liquids, it can greatly vary from one solid to another for the same adsorbed species. The geometry and physical properties of the sample have a large influence: the thickness of a wafer (5 mg cm^{-2} is very different from 30 mg cm^{-2}), pressure during formation, particle size, and all parameters that influence the optical path and diffraction and scattering of light in the sample (*e.g.* specific surface area and morphology of the particles) will affect the apparent ε. It then became clear that integrated molar absorption coefficients had to be measured for each sample and each type and size of wafer.

The accuracy of volumetric measurement in an infrared cell was also questioned, and the intensity of infrared bands for adsorbed species at saturation was compared with the amount of sites that was expected based on chemical analysis.[670] However, by measuring the weight of probe species adsorbed on the solid and by plotting that value *versus* the intensity of the corresponding infrared bands, the greatest accuracy was obtained. This was first achieved by reproducing the same adsorption and temperature-programmed desorption experiments (under the same pressure and temperature conditions with the same waiting time for diffusion) in a microbalance and an infrared cell.[504,680,681] In a second step, and to be sure that conditions were rigorously the same, the experiment was performed in a combined experimental set-up by *in situ* gravimetry with a MacBain balance inside an infrared spectrometer.[689]

In an improved set-up developed in Caen, a sample inside an infrared cell was attached by a platinum wire to the beam of a microbalance; its weight (*ca.* 20 mg) was measured with 1 μg accuracy during adsorption and desorption experiments.[42] With this set-up, qualitative as well as quantitative information are obtained simultaneously by combining thermogravimetry and *operando* IR spectroscopy with online mass spectrometry (see Fig. 27a). The weight (and therefore the number of adsorbed probe molecules) and IR spectra of a solid sample can be measured simultaneously in real-time *operando* conditions in a gas flow at a temperature between room temperature and 773 K. Integrated molar absorbance coefficients ε can consequently be obtained directly. This approach was used to study the quantitative infrared response of adsorbed water and ammonium ions in NH_4^+-Y zeolite during calcination. Online analysis of gases exiting the cell was performed by mass spectrometry (MS), shown as the black curves (left ordinate axis) in Fig. 27b. The desorption of water alone was observed first, during which the infrared spectrum of ammonium ions was fundamentally modified, moving from 1643 to 1455 cm^{-1} (Fig. 27c), but the corresponding integrated molar absorption coefficient for the whole band not was not modified, which was found to be $\varepsilon(1643–1455) = 12 \pm 1$ cm μmol^{-1}. Conversely, due to strong H-bonding between water molecules, the integrated molar absorption coefficient of the bending mode of water was water coverage-dependent, varying in the 1–4 cm μmol^{-1} interval.[42]

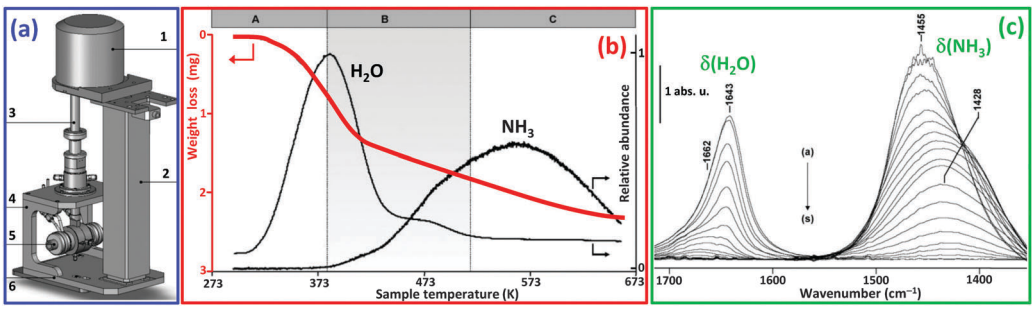

Fig. 27 Part (a): General view of the integrated IR-microbalance system (AGIR set-up), consisting of a Setaram microbalance B Setsys (1); telescopic column (2); IR cell-balance link (3); IR cell support (4); IR cell/*operando* reactor (5); and support and spectrometer base plate (6). Part (b): Data recorded *vs.* temperature during the calcination of NH_4-Y zeolite under a flow of Ar (heating ramp from 300 K to 660 K at 3 K min^{-1}). Black curves (right ordinate axis, MS data) show the relative intensity of $m/z = 18$ (water) and $m/z = 15$ (ammonia, intensity × 100); the red curve (left ordinate axis, microbalance data) shows the weight loss of the sample (activated weight = 20 mg). The experiment can be divided into 3 steps: A: desorption of water alone, B: desorption of both water and ammonia, and C: desorption of ammonia alone. Part (c): IR spectra in the bending region of water and ammonium recorded during the experiment shown in part (b), taken every 5 min. (from a to s): The bands of the $\delta(H_2O)$ and $\delta(NH)$ modes are visible at 1643 and 1455 cm^{-1}, respectively. The latter moves downward to 1428 cm^{-1} once water is totally desorbed (step C in part (b)). Adapted with permission from ref. 42, copyright the Royal Society of Chemistry, 2010.

By comparing the results obtained in this so-called AGIR set-up (shortform for analysis by combined gravimetry and IR) with those obtained in a glass cell by usual volumetric dosing, it was shown that, depending on the vapor pressure of the probe molecule and its affinity for glass and gaskets, the results could be markedly different from one cell to another. Phenol, for example, has a very low vapor pressure and is adsorbed on the cell walls at the same time as it is chemisorbed on oxide samples. The measurement of its molar absorption coefficient was very difficult and unreliable with a conventional approach. When measured by AGIR, it was two orders of magnitude greater than the value that was approximately measured volumetrically in a glass cell.[690] Thus, not only do the physical optical properties of the solid influence the absorption coefficient, but the results can also be greatly influenced by the geometry of the infrared cell employed, and simultaneous *in situ* gravimetric measurements must be made to calibrate quantitative infrared experiments with adsorbed species on oxides and zeolites.

This experimental set-up works *in vacuo* or (preferentially) under a gas flow, and can therefore be used to measure the weight of a catalytic sample together with its infrared spectrum under reaction conditions; it is thus perfectly adapted for *operando* studies.

7. Determination of the adsorption enthalpies and entropies: variable-temperature IR experiments

In the last decade, infrared spectroscopy has been widely used to determine the thermodynamics of molecular adsorption on internal sites of zeolites, mainly by the groups of Tsyganenko (Saint Petersburg, Russian Federation), Otero Arean (Palma de Mallorca, Spain), Garrone (Turin Polytechnic, Italy) and Zecchina (Turin University, Italy) on the experimental side and by the group of Nachtigall (Prague, Czech Republic) on the computational side.[17,154,274–281,283–285,288,691–721] In brief, the technique is based on displacement of the equilibrium between molecules in the gas phase and those adsorbed on a given type of surface site, which is carried out by changing the temperature T of the system, as shown in Fig. 28a for CO adsorbed on chromocene (Cp_2Cr) hosted inside a polystyrene (PS) porous polymeric matrix.

$$\text{Surface\_site} + (\text{Molecule})_{\text{gas}} \rightleftharpoons \text{Surface\_site\_}(\text{Molecule})_{\text{adsorbed}} \quad (23)$$

$\theta(T)$ is defined as the fractional occupation of a given surface site:

$$\theta(T) = N_{\text{occ}}(T)/N_{\text{tot}} \propto \exp(-\Delta H^{\circ}/k_{\text{B}}T) \quad (24)$$

where N_{tot} is the total number of surface sites, $N_{\text{occ}}(T)$ is the number of sites occupied by the molecule, and its dependence on T is driven by third-order proportionality; $-\Delta H^{\circ}$ is the adsorption enthalpy, *i.e.* the variation in enthalpy that occurs during the adsorption process from the gas phase to the formation of the surface molecular adduct (23), and k_{B} is the Boltzmann constant ($k_{\text{B}} = 1.3806 \times 10^{-23}$ J K^{-1} = 8.6173×10^{-5} eV K^{-1}). From eqn (24), it emerges that $\theta(T)$ will increase with a decrease in T and *vice versa*.

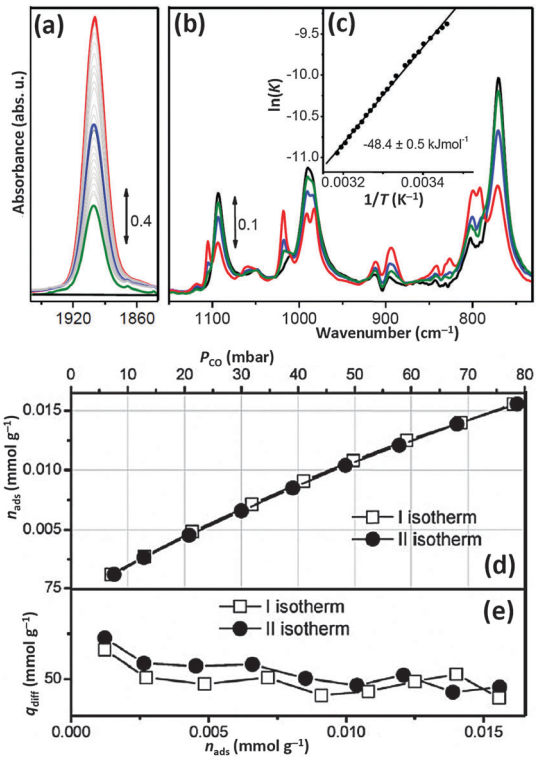

Fig. 28 Examples of adsorption enthalpy determined for the same system by VTIR, parts (a–c), and by standard microcalorimetry, parts (d and e). FTIR spectra in the ν(CO) region (part a) and in the region of Cp modes (part b) of the $Cp_2Cr\cdots CO$/PS system as a function of the CO coverage, tuned by varying the sample temperature. Green, blue and red curves indicate spectra collected at T = 315, 300 and 288 K, respectively. The black curve indicates the spectrum collected before dosage of CO. All spectra are background-subtracted. Part (c): Dependence of $\ln(K) = \ln\{I(T)/[(I_M - I(T))(p/p_0)]\}$ as a function of $(1/T)$ for adsorption of CO on the Cp_2Cr/PS system, see eqn (30) and (31). The enthalpy of formation of the $Cp_2Cr\cdots CO$ complex is also shown with the statistical error associated with the linear fit. Part (d): Primary (open squares) and secondary (solid circles) absolute volumetric isotherms obtained for the adsorption of CO on Cp_2Cr/PS at 303 K as a function of the equilibrium pressure P_e. Part (e): Dependence of the differential molar heat of adsorption q_{diff} on CO coverage. Adapted by permission of the Royal Society of Chemistry (copyright 2009) from ref. 734.

Once adsorbed on the surface, the molecule gives rise to a peculiar IR band that reflects the perturbation induced by the surface site. More peculiar bands are obtained in the event that the probe molecule is more complex than a simple diatomic molecule. The integrated area of such bands, $I(T)$, provides a direct measurement of the number of occupied surface sites at a given temperature T, which can be measured quantitatively as a fraction of total surface sites once data collection has been performed at a sufficiently low temperature to achieve total occupancy ($\theta = 1$) of the surface sites. Experimentally speaking, $\theta = 1$ is reached once a further decrease in T will not result in an increase in $I(T)$; such an area is defined as I_M. In such a way, the surface coverage at any temperature is simply obtained as $\theta(T) = I(T)/I_M$. A detailed description of the thermodynamic

relations related to VTIR spectroscopy enabling the determination of accurate ΔH° and ΔS° values of the adsorption process is reported in Section 7.1, whereas in this introductory section only qualitative aspects will be discussed.

Usually the adsorption enthalpy is measured by the isosteric method[717,722–725] or by microcalorimetry,[168,170,266,336,405,537,600,716,722,726–733] both are widely employed in the investigation of molecular adsorption in zeolites.

Isosteric method is applied to at least two isotherms at different temperatures, which must not be very far apart (typically $\Delta T = \sim 10$ K). Whenever possible, more than two isotherms should be measured and the plot of $\ln(P)$ *versus* $1/T$ should be checked for linearity. The isosteric method is very sensitive to any error in the measurement of the equilibrium pressure, and particular care must be taken when applying the isosteric method at surface coverage of $\theta < 0.5$. In spite of these limitations, the accuracy of the method improves as the pressure is increased; this is unlike calorimetry, which tends to become less accurate at higher pressures.[722]

Microcalorimetry requires that a carefully weighed amount of activated sample is loaded in a calorimeter, whose temperature is kept fixed during the experiment. A small amount of probe is dosed onto the sample and the number of adsorbed mmol (Δn_{ads}) is obtained *via* an accurate measurement of the equilibrium pressure (P_e) and from an accurate knowledge of the expansion volume (V) according to the following equation:

$$\Delta n_{ads} = \Delta n_{dosed} - (P_e V)/(k_B T), \quad (25)$$

where Δn_{dosed} is the number of mmol dosed onto the sample, which is known from the experiment.[168,170,266,336,405,537,600,729,730] The calorimeter measures the energy release ΔQ due to the adsorption of Δn_{ads} mmol of gas; thus, the adsorption enthalpy is obtained as follows:

$$-\Delta H^\circ \equiv q_{diff} = \Delta Q/\Delta n_{ads}. \quad (26)$$

When the heat signal from the calorimeter becomes zero and the pressure is constant, equilibrium is reached and a new dose Δn_{dosed} can be added to the sample. Note that depending on the system, the time needed to reach equilibrium may range from minutes to hours. Fig. 28d shows the primary and secondary volumetric isotherms for CO adsorbed on Cp_2Cr/PS, which show the integrated number of adsorbed mmol ($n_{ads} = \sum \Delta n_{ads}$) as a function of the equilibrium pressure P_e. The equivalence of the two isotherms reflects the absence of irreversible adsorption in this system. Fig. 28e presents the calorimetric isotherm, which shows the differential heat of adsorption as a function of the coverage. This example reported by Groppo *et al.*[734] is relevant because it is one of the few studies where both standard microcalorimetric and spectroscopic VTIR methods were applied simultaneously to the same system, allowing the equivalence of the two approaches to be appreciated. Besides the first point, which is always related to some more energetic defect sites, all the remaining points of the primary and secondary calorimetric isotherms lie between 54.1 and 46.5 kJ mol^{-1} (see Fig. 28e); these values are in excellent agreement with the value of 48.4 kJ mol^{-1} obtained by VTIR, as shown in Fig. 28c.

The VTIR approach has two main advantages with respect to standard calorimetry methods, for example the isosteric method and microcalorimetry described above. VTIR is in fact site-specific (the value obtained is not averaged over different adsorption sites, as with most calorimetry methods) and also allows determination of the enthalpy of adsorption for molecules with a very low interaction energy, for which cryogenic temperatures need to be used. For this reason, VTIR has been particularly relevant for investigating weakly bonded adducts in zeolites such as those formed by adsorption of H_2, Ar, O_2, and N_2 probes. Section 7.1 deals with a concise but rigorous approach to the thermodynamics underlying the VTIR methodology, whereas Section 7.2 is devoted to the description of a few selected examples.

Obviously, VTIR technique requires the development of specific IR cells that allow the activation of the zeolite, dosage of the desired probe molecule and accurate tuning of both the equilibrium pressure and the sample temperature. This is the case with the cell developed by Tsyganenko *et al.*[694] in Saint Petersburg, which allows a precise control of the sample temperature to as low as liquid-nitrogen temperature, and of that developed by Spoto *et al.* in Turin University, which works at temperatures as low as liquid-helium temperature.[39]

7.1. VTIR: theory

At any given temperature T, the integrated intensity, $I(T)$, of the IR absorption band of a molecule adsorbed on a surface site is proportional to surface coverage θ, thus giving information on the activity (in the thermodynamic sense) of both adsorbed species and empty adsorbing sites. Simultaneously, the equilibrium pressure (p) performs the same function for the gas phase. Therefore, the corresponding adsorption equilibrium constant, K, can be determined. The variation of K with temperature leads to the corresponding values of adsorption enthalpy and entropy. Assuming Langmuir-type adsorption, we obtain the following equation:[17,39,735,736]

$$\theta(T) = I(T)/I_M = K(T)(p/p_0)/[1 + K(T)(p/p_0)] \quad (27)$$

where I_M stands for the integrated intensity corresponding to full coverage ($\theta = 1$) and p_0 is the reference pressure (usually taken as 1 Torr or 1 mbar, whereas in a few cases some authors have chosen 1 bar, *vide infra*). By inverting eqn (27), the equilibrium constant $K(T)$ can be obtained as follows:

$$K(T) = \frac{I(T)}{[I_M - I(T)](p/p_0)} \quad (28)$$

The combination of eqn (28) with the well-known van't Hoff eqn (29)

$$K(T) = \exp(-\Delta H^\circ/RT)\exp(\Delta S^\circ/R) \quad (29)$$

leads to eqn (30):[17,39,736]

$$\ln\left[\frac{I(T)}{[I_M - I(T)](p/p_0)}\right] = (-\Delta H^\circ/RT) + (\Delta S^\circ/R), \quad (30)$$

where R is the gas constant (8.314 J K^{-1} mol^{-1}) and $-\Delta H^\circ$ and ΔS° are the variations in enthalpy and entropy that occur during the adsorption process from the gas phase to the formation of

the surface molecular adduct, as shown in eqn (23). By defining $Y = \ln\{I(T)/[(I_M - I(T))(p/p_0)]\}$, eqn (30) becomes

$$Y = (-\Delta H^\circ/R)T^{-1} + (\Delta S^\circ/R). \quad (31)$$

Eqn (31) is the equation of a straight line in the (Y, T^{-1}) plane; thus, different pairs of (Y_i, T_i^{-1}) values obtained by VTIR experiments at different temperatures will allow the derivation of both ΔH° and ΔS° values through a standard linear fit procedure, with ΔH° related to the slope of the line Y and ΔS° related to its intercept with the ordinate axis, as shown in Fig. 28c. Obviously, this approach assumes that both ΔH° and ΔS° are independent of temperature.

It is now worth discussing the effect that a different choice of p_0 has on the ΔH° and ΔS° values derived by this method. Note that ΔH° and ΔS° are differences in two thermodynamic functions (H and S) between two states: the adsorbed state where the molecule is adsorbed on the surface and the reference state where the molecule is in the gas phase. From eqn (30), it emerges that by changing from p_0 to p_0' the left-hand side of eqn (30) will change by a constant value of $\ln(p_0/p_0')$. This change will not affect the slope of the Y line; thus, an arbitrary choice of p_0 does not affect the ΔH° value extrapolated from the VTIR data. Conversely, it will change the intercept with the ordinate axis and thus the extrapolated ΔS° value by a factor of $R\ln(p_0/p_0')$.[736,737] This makes sense because, for an ideal gas, H does not depend on p, whereas S does. It is obvious that a change in the reference pressure p_0 will affect the entropy of the reference gas phase and so the extrapolated value of ΔS°. As a consequence, when discussing ΔS° values reported in the literature from different authors, attention must be paid to the adopted reference value of p_0. Changing the reference pressure p_0 from 1 mbar to 1 Torr (1.32 mbar) will result in a change in ΔS° of $R\ln(1.32) = 2.28$ J K^{-1} mol^{-1}; however, changing from 1 Torr to 1 atm (760 Torr) will result in a change of $R\ln(760) = 55.15$ J K^{-1} mol^{-1}.[736,737] Because the error associated with the determination of ΔS° by the VTIR method is about ± 10 J K^{-1} mol^{-1} (Table 8), literature values obtained using $p_0 = 1$ mbar can be, at a first approximation, directly compared with values obtained using $p_0 = 1$ Torr, whereas a correction of 55.15 J K^{-1} mol^{-1} must be applied when comparison is made with values obtained using $p_0 = 1$ bar.[736,737]

7.2. VTIR: examples

7.2.1. Adsorption of Ar, H_2, O_2, N_2 and CO on H-Na-Y zeolite. Gribov *et al.*[154] investigated the adsorption of Ar, H_2, O_2, N_2 and CO on H-Na-Y zeolite (Si/Al = 2.9; $H^+/Na^+ = 5$) by means of VTIR in the temperature range of 90–20 K and pressure range of 0–40 mbar. Two pressure regimes were selected, characterized by (a) specific interaction at low pressure of the probe molecules with internal Brønsted and Lewis sites and (b) multilayer adsorption at higher pressure. In this review we will focus on regime (a) only. When a probe molecule (B) is adsorbed on a Brønsted site hosted in a zeolitic framework, there are three independent ways of calculating the adsorption enthalpy from VTIR data. This is achieved by studying the dependence of (i) the intensity of the ν(OH) band of free HF Brønsted groups in the supercage (Z–OH, decreasing upon an increase in θ, as shown in Fig. 29a); (ii) the intensity of ν(OH) of perturbed HF Brønsted groups (Z–OH$\cdots$B increasing upon an increase in θ, as shown in Section 2 and Fig. 29a); and (iii) the intensity of the stretching vibration band of the adsorbed base (when possible, see Fig. 29b) upon T. Eqn (31) has been used to plot the three sets of experimental data (Fig. 29c) and the ΔH° and ΔS° values extracted from the corresponding linear fits are equivalent, within the error bars. A significant difference in the slope (and therefore in ΔH°) is evident from a simple inspection of the data referring to CO (open squares), N_2 (open circles), O_2 (crosses), Ar (open stars) and H_2 (open diamonds) molecules adsorbed on H-Na-Y, which are plotted in Fig. 29d together with the corresponding best linear fits. Quantitative values for $-\Delta H^\circ$ are 11.4 (H_2), 14.8 (O_2), 15.2 (Ar), 22.2 (N_2), and 30.6 (CO), in kJ mol^{-1},[154] as shown in Table 8.

7.2.2. Discrimination between two different adsorption sites for CO on Na-ferrierite zeolite. As anticipated above, the greatest advantage of the VTIR technique *versus* standard microcalorimetry and isosteric heat of adsorption measurements lies in its site selectivity. A typical example where this advantage has been exploited is reported in the joint experimental and theoretical study of Arean and Nachtigall.[719] Fig. 30a shows the VTIR spectra of the adsorption of CO on Na-ferrierite zeolite with a Si : Al ratio of 8 : 1. Two IR bands are clearly observed at 2175 and 2158 cm^{-1}, which are due to the presence of two families of adsorption sites. The weak IR absorption band observed at 2113 cm^{-1} is due to a minority of CO molecules interacting through the oxygen atom with a single Na^+ cation.[288] This species is no longer discussed in this section as Section 7.2.3 will be devoted to it.

Periodic DFT calculations allowed the authors to attribute the former band to CO molecules that interact with a single Na^+ cation through the carbon end (see Fig. 30c) and the latter band to CO molecules that interact with two adjacent Na^+ cations through both ends (see Fig. 30d). Accurate band deconvolution was used to separate the integrated areas of the two components in all the series of spectra shown in Fig. 30a, allowing the authors to use eqn (31) for the two separated datasets, and thus to obtain $-\Delta H^\circ = 30$ and 35 kJ mol^{-1} for the $Na^+\cdots$CO and $Na^+\cdots$CO$\cdots Na^+$ complexes, respectively. It is evident that standard microcalorimetry and isosteric heat of adsorption measurements would have provided only averaged values in this case. Periodic DFT calculations further supported the energetic values derived from VTIR: the computed values of $-\Delta H^\circ$ were found to be 29 and 32–35 kJ mol^{-1} for the $Na^+\cdots$CO and $Na^+\cdots$CO$\cdots Na^+$ complexes, respectively, as shown in Table 8.

Table 8 summarizes the adsorption enthalpies, entropies (when available) and wavenumbers of the measured IR bands for relevant examples of molecular adsorption on Brønsted and Lewis acidic sites in zeolitic frameworks as determined by VTIR, which could not be discussed in detail for the sake of brevity. When referring to the same system, a few $-\Delta H^\circ$ values obtained *via* other experimental approaches (or DFT calculations) are also reported for comparison. Fig. 31 summarizes some correlations between the $-\Delta H^\circ$, $-\Delta S^\circ$, $\tilde{\nu}$(HH) and $\tilde{\nu}$(CO) values obtained by VTIR experiments for the adsorption of

Table 8 Summary of relevant adsorption enthalpies ($-\Delta H^\circ$), entropies ($-\Delta S^\circ$) and wavenumbers of the measured IR bands ($\tilde{\nu}$) for molecular adsorption on Brønsted and Lewis acidic sites in zeolitic frameworks as determined by VTIR. When provided by the original studies, the corresponding uncertainties have also been reported. For comparison, some results obtained for adsorption by microcalorimetry (μCal), isosteric heat of adsorption (Qisost), chromatography pulse (CP) and periodic DFT (pDFT) techniques are also reported. NR = not reported; NM = not measurable. Some correlations between the values reported in this table are shown in Fig. 31. Previously unpublished table analyzing data are reported in the references quoted in the last column

Probe	Zeolite, site	Method	$\tilde{\nu}$ (cm^{-1})	$-\Delta H^\circ$ (kJ mol^{-1})	$-\Delta S^\circ$ (J K^{-1} mol^{-1})	Ref.
H_2	H-Na-Y, Brønsted site in supercage	VTIR	4115	11.4	NR	154
H_2	Li-FER, Li^+ site	VTIR	4090	4.1 ± 0.8	57 ± 10	704
H_2	Li-ZSM-5, isolated Na^+ site	VTIR	4092	6.5 ± 0.5	90 ± 10	275
H_2	Na-FER, Na^+ site	VTIR	4100	6.0 ± 0.8	78 ± 10	274
H_2	Na-ZSM-5, isolated Na^+ site	VTIR	4101	10.3 ± 0.5	121 ± 10	275
H_2	Na-ZSM-5, isolated Na^+ site	VTIR	4100	11	NR	702
H_2	K-FER, K^+ site	VTIR	4111	3.5 ± 0.8	57 ± 10	274
H_2	K-ZSM-5, isolated Na^+ site	VTIR	4112	9.1 ± 0.5	124 ± 10	275
H_2	Mg-Na-Y, Mg^{2+} site in supercage	VTIR	4056	18.2 ± 0.8	136 ± 10	706
H_2	Mg-X, Mg^{2+} site in supercage	VTIR	4065	13 ± 0.8	114 ± 10	738
H_2	Ca-A, Ca^{2+} site	VTIR	4083	12 ± 1	121 ± 10	739
H_2	Ca-Na-Y, Ca^{2+} site in supercage	VTIR	4078	15 ± 1	127 ± 10	710
H_2	Ca-X, Ca^{2+} site in supercage	VTIR	4082	11 ± 1	118 ± 10	712
N_2	H-Y, Brønsted site in supercage	VTIR	2334	15.7 ± 0.8	121 ± 10	708
N_2	H-Na-Y, Brønsted site in supercage	VTIR	2336	20.2	NR	154
N_2	H-ZSM-5, Brønsted site	VTIR	2331[a]	19.7 ± 0.5	125 ± 5	697
N_2	H-FER, Brønsted site	VTIR	2331[a]	19.1 ± 1.0	131 ± 10	707
N_2	H-β, Brønsted site	VTIR	2333	19 ± 1.0	140 ± 10	715
N_2	H-MCM-22, Brønsted site	VTIR	2332	14.5 ± 2.0	105 ± 10	721
O_2	H-Na-Y, Brønsted site in supercage	VTIR	1553	14.8	NR	154
Ar	H-Na-Y, Brønsted site in supercage	VTIR	3616[b]	15.2	NR	154
CO	H-ZSM-5, Brønsted site	VTIR	2173	29.4 ± 0.8	148 ± 10	708
CO	H-ZSM-5, average of all sites	μCal	NM	27	NM	728
CO	H-Y, Brønsted site in supercage	VTIR	2173	25.6	161	693
CO	H-Na-Y, Brønsted site in supercage	VTIR	2162	30.6	NR	154
CO	H-FER, Brønsted site	VTIR	2172	28.4 ± 0.8	147 ± 10	708
CO	H-FER, Brønsted site	VTIR	2173	28.4 ± 1.0	145 ± 10	719
CO	H-β, Brønsted site	VTIR	2174	27 ± 1.0	150 ± 10	715
CO	H-MCM-22, Brønsted site	VTIR	2174	23.5 ± 2.0	130 ± 10	721
CO	Na-β, isolated Na^+ site	VTIR	2180	29.3	NR	285
CO	Na-FER, isolated Na^+ site	VTIR	2175	30.5 ± 3.0	150 ± 10	278
CO	Na-FER, isolated Na^+ site	pDFT	2178	29	NR	719
CO	Na-FER, interaction with 2 Na^+ sites	VTIR	2158	34.5 ± 3.0	152 ± 10	278
CO	Na-FER, interaction with 2 Na^+ sites	pDFT	2153–2175	32–35	NR	719
CO	Na-Y, isolated Na^+ site	VTIR	2172	27 ± 2	NR	719
CO	Na-Y, isolated Na^+ site	pDFT	2172	24–26	NR	719
CO	Na-A, interaction with 2 Na^+ sites	VTIR	2163	27	NR	719
CO	Na-A, interaction with 2 Na^+ sites	pDFT	2160	30	NR	719
CO	K-β, isolated K^+ site	VTIR	2167	25.7	NR	285
CO	K-FER, isolated K^+ site	VTIR	2163	25 ± 2.0	NR	719
CO	K-FER, isolated K^+ site	pDFT	2164	18–20	NR	719
CO	Cs-X, basic framework O	VTIR	2124	25 ± 1.0	71 ± 5	705
CO	Ca-A, Ca^{2+} site S1	VTIR	2179	31.3 ± 2.0	176 ± 10	281
CO	Ca-A, Ca^{2+} site S2	VTIR	2188	45.6 ± 2.0	170 ± 10	281
CO	Ca-Y, site in supercage	VTIR	2197	47	NR	284
CO	Ca-Y, $Ca(CO) \rightarrow Ca(CO)_2$ equilibrium	VTIR	2191	36	NR	284
CO	Sr-Y, site in supercage	VTIR	2191	45.3	179	283
CO	Sr-Y, $Sr(CO) \rightarrow Sr(CO)_2$ equilibrium	VTIR	2187	30.2	138	283
CO_2	H-Y, Brønsted site in supercage	VTIR	2353	28.5 ± 1.0	129 ± 10	713
CO_2	H-Y, Brønsted site in supercage	Qisost	2360	27	NM	723
CO_2	H-ZSM-5, Brønsted site	VTIR	2345	31.2 ± 1.0	140 ± 10	711
CO_2	H-ZSM-5, Brønsted site	μCal	NM	30	NM	727
CO_2	H-ZSM-5, Brønsted site	Qisost	NM	28.8	NM	724
CO_2	H-ZSM-5, Brønsted site	Qisost	NM	28.7 ± 0.7	83	725
CO_2	H-ZSM-5, Brønsted site	CP	NM	33	83	740
CO_2	H-β, Brønsted site	VTIR	2348	33 ± 1.0	146 ± 10	715
CO_2	H-FER, Brønsted site	VTIR	2346	30.2 ± 1.0	125 ± 10	741
CO_2	Na-A, interaction with 2 Na^+ sites	VTIR	2360	42 ± 2.0	135 ± 10	717
CO_2	Na-A, interaction with 3 Na^+ sites	VTIR	2349	44 ± 2.0	140 ± 10	717
CO_2	Na-A, average of Na^+ sites	Qisost	NM	47	NM	717
CO_2	K-FER, isolated K^+ site	VTIR	2346	40 ± 1.0	148 ± 10	716

Table 8 (*continued*)

Probe	Zeolite, site	Method	$\tilde{\nu}$ (cm^{-1})	$-\Delta H^{\circ}$ (kJ mol^{-1})	$-\Delta S^{\circ}$ (J K^{-1} mol^{-1})	Ref.
CO_2	K-FER, interaction with 2 K^+ sites	VTIR	2355	43 ± 1.0	152 ± 10	716
CO_2	K-FER, average of all sites	μCal	2347	50–59[c]	NM	716
NH_3	H-ZSM-5, Brønsted site, NH_4^+ formation	VTIR	1410	128 ± 5.0	184 ± 10	714

[a] The reported values refer to the average of the $-\Delta H^{\circ}$ and $-\Delta S^{\circ}$ values obtained by applying the VTIR approach to both ν(OH) band of the occupied Brønsted sites and the ν(CO) or ν(NN) band of the adsorbed molecules. [b] In this case, the VTIR approach was applied to the perturbation of the HF band of Brønsted sites in the Y supercage, of which the wavenumber moves downward from 3650 cm^{-1} to 3616 cm^{-1} upon the formation of ZOH···Ar adducts, resulting in $\Delta\tilde{\nu}$(OH) = 34 cm^{-1}, as shown in Section 2.1. [c] Depending on the Si/Al ratio.

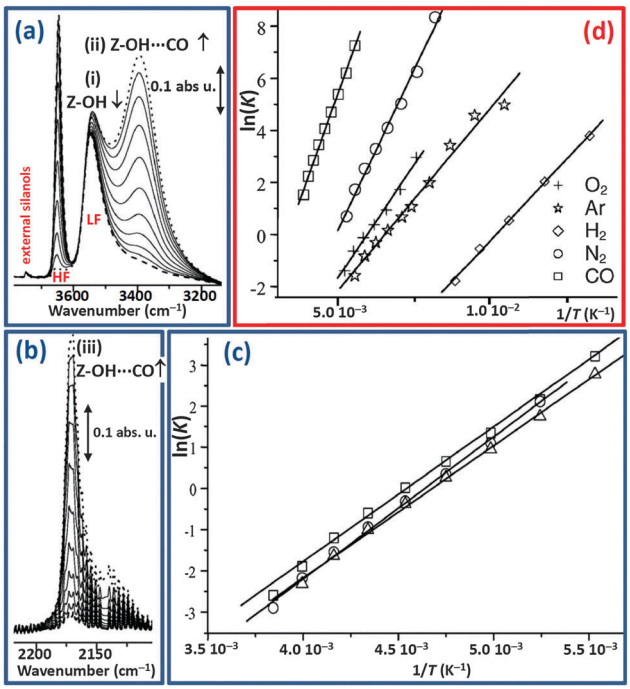

Fig. 29 Part (a): VTIR spectra in the ν(OH) stretching region, collected by dosing CO onto H-Na-Y zeolite at constant p and changing T in the 280 K (dashed spectrum) – 170 K (dotted spectrum) interval. Part (b): Similar to Part (a) in the ν(CO) stretching region. Part (c): The plots of $\ln(K) = \ln\{I(T)/[(I_M - I(T))(p/p_0)]\}$ *vs.* $1/T$, mentioned as eqn (30) and (31), obtained from the decrease in band (i) in part (a) and from the increase in bands (ii) or (iii) in parts (a) and (b), respectively. Part (d): The plots of $\ln(K)$ *vs.* $1/T$ for CO (averaged over the 3 datasets shown in part (c), open squares), N_2 (open circles), O_2 (crosses), Ar (open stars) and H_2 (open diamonds). The different slopes clearly reflect the different adsorption enthalpies of the different molecules. Adapted by permission of the Royal Society of Chemistry (copyright 2006) from ref. 154.

molecules in zeolitic frameworks. The overall data do not show a common simple trend (Fig. 31); nevertheless, there is a rough positive correlation between enthalpy and entropy of adsorption:

$$-\Delta H^{\circ} \propto -\Delta S^{\circ} \quad (32)$$

This correlation is better defined within the subsets of data that refer to a single molecule. Besides molecular adsorption in zeolites,[735,736,742] such a trend, already referred to as entropy–enthalpy compensation, has been observed in the literature for a range of chemical processes that involve weak interaction forces such as the formation of weakly associated molecular complexes,[743,744] weak hydrogen bonding[745,746] and Langmuir-type adsorption from solution.[746]

Correlation (32) is related to the fact that the stronger the interaction between the probe molecule and the adsorbing centre is, the greater will be the corresponding decrease in freedom of molecular motion, which results in increasing order of the system. Thus, referring to absolute values, a greater $-\Delta H^{\circ}$ value will result in a correspondingly greater value of $-\Delta S^{\circ}$.[735,736,742]

Otero Arean and Garrone have recently shown that within zeolites and Cr-MIL MOFs, the enthalpy–entropy correlation ($-\Delta H^{\circ} \propto -\Delta S^{\circ}$) does not follow a straight line but a concave curve.[735,742] This trend, which is also clearly observed in the entire set of data shown in Fig. 31a, is due to the fact that the adsorbed molecules cannot lose more than all their degrees of freedom of motion and that $-\Delta S^{\circ}$ has consequently an inherent limit, whereas (in principle) $-\Delta H^{\circ}$ has not. The limit for $-\Delta S^{\circ}$ is not reached in the adsorption process, because some rotational and vibrational freedom (with respect to the adsorption site) remains in the adsorbed state. The summary of the data obtained for zeolites (Fig. 31a), which represents a larger dataset with respect to that considered in the works of Otero Arean and Garrone,[735,742] confirms their model because a sharp increase in $-\Delta H^{\circ}$ is observed when $-\Delta S^{\circ}$ reaches values beyond 120 J mol^{-1} K^{-1}.

From Fig. 31(b) and (c) a rough negative (positive) correlation between enthalpy and the $\tilde{\nu}$(HH) ($\tilde{\nu}$(CO)) stretching frequency is clearly observed. This behaviour is due to the fact that higher adsorption enthalpy results in a larger perturbation of the stretching mode of the molecule $|\Delta\tilde{\nu}|$, which is negative for H_2 ($\Delta\tilde{\nu}$(HH) < 0) and positive for CO ($\Delta\tilde{\nu}$(CO) > 0).[23,29,231] See Section 3.1.4 for a discussion on the respective signs of $\Delta\nu$(CO) and $\Delta\nu$(HH).

7.2.3. Linkage isomerism of simple molecules adsorbed on zeolites: determination of the difference in ΔH° for the two isomers by VTIR. Linkage isomerism is present when two (or more) coordination compounds coexist while having the same composition but differing in the connectivity of the metal (M) to a ligand (L). If the ligand is a diatomic molecule (L = AB) then only two linkage isomers are possible: M···AB and M···BA. Linkage isomer complexes have different vibrational frequencies, and thus can be distinguished by IR[747,748] if both are energetically stable. The relative populations of the two isomers will be determined by the relative difference in ΔH° and the temperature of the experiment; thus, an appropriate VTIR experiment will allow the determination of the difference in the relative stability $\Delta[\Delta H^{\circ}]$ of the two complexes. The phenomenon of isomerism on adsorption has relevant importance in

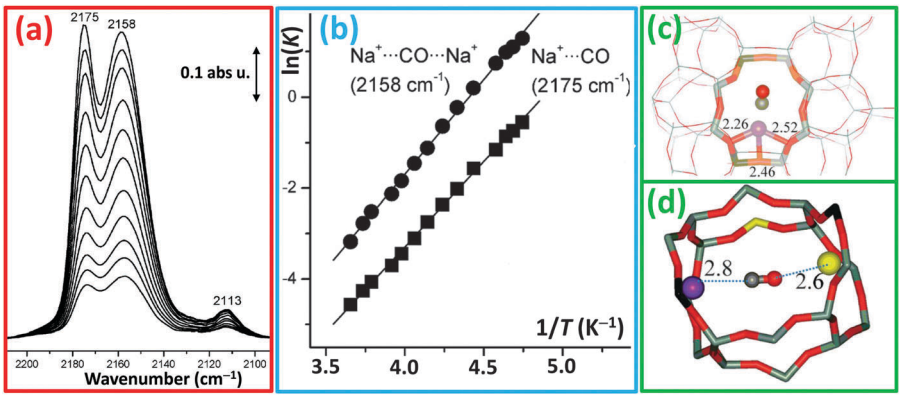

Fig. 30 Part (a): VTIR spectra (zeolite blank-subtracted) of CO adsorbed on Na-FER, Si : Al = 8 : 1. From top to bottom, the temperature ranges from 207 to 264 K and the equilibrium pressure from 0.19 to 1.17 mbar. Part (b): Plots of $\ln(K) = \ln\{I(T)/[(I_M - I(T))(p/p_0)]\}$ *vs.* $1/T$, eqn (30) and (31), for the deconvoluted components of the bands at 2175 and 2158 cm^{-1} shown in part (a). Part (c): Optimized coordination of Na^+ cation and the corresponding single-site CO adsorption complex responsible for the 2175 cm^{-1} band. Framework Al, Si, and O atoms are depicted as black, grey, and red sticks, respectively; Na^+ ions and C and O atoms of CO are shown as violet, grey and red balls, respectively. Distances are given in Å. Part (d): Optimized CO adsorption complex formed on dual cation sites responsible for the 2158 cm^{-1} band. The CO molecule interacts with the primary Na^+ cation (violet ball) through the C atom (grey ball) and with the secondary Na^+ cation (yellow ball) through the O atom (red ball). Framework Al, Si, and O atoms are depicted as black, grey and red sticks, respectively. Adapted by permission of the Royal Society of Chemistry (copyright 2012) from ref. 719.

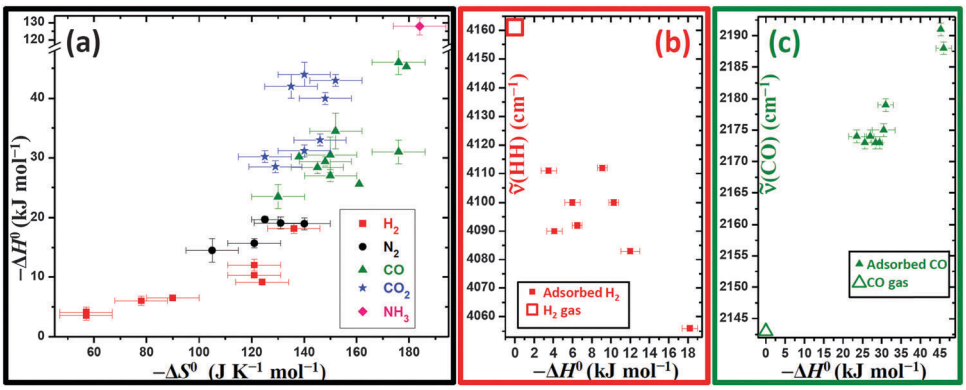

Fig. 31 Part (a): Correlation between $-\Delta H^\circ$ and $-\Delta S^\circ$ values obtained by VTIR experiments for the adsorption of H_2 (red squares), N_2 (black circles), CO (green triangles), CO_2 (blue stars) and NH_3 (pink rhombus) molecules in zeolitic frameworks. Part (b): Correlation between $\tilde{\nu}$(HH) and $-\Delta H^\circ$ for H_2 molecules adsorbed in zeolites (full red squares); the open red square represents an unperturbed H_2 molecule ($-\Delta H^\circ$ = 0 kJ mol^{-1}; $\tilde{\nu}$(HH) = 4161 cm^{-1}). Part (c): Correlation between $\tilde{\nu}$(CO) and $-\Delta H^\circ$ for CO molecules adsorbed in zeolites (full green triangles); the open green triangle represents an unperturbed CO molecule ($-\Delta H^\circ$ = 0 kJ mol^{-1}; $\tilde{\nu}$(CO) = 2143 cm^{-1}). When reported in the original articles the uncertainties in $-\Delta H^\circ$ and $-\Delta S^\circ$ values have also been plotted; for both $\tilde{\nu}$(HH) and $\tilde{\nu}$(CO), we assumed an error of ±1 cm^{-1}, because most experiments have been performed with a resolution of 2 cm^{-1}. Previously unpublished figure analyzing data are reported in the references quoted in the last column of Table 8.

catalysis, because the energetically less favorable state has different chemical properties and excess energy, which could be used to overcome activation barriers. It can therefore be considered to be an activated state and could play the role of an intermediate in catalytic reactions.[748]

As discussed in detail in Section 3.1.1, CO with alkali metal cations hosted in zeolite channels and cavities forms linear $M^+\cdots CO$ adducts through the carbon end, for which IR spectra are characterized by a main blue-shifted cation-specific IR band that appears in the 2150–2180 cm^{-1} range (M = Li, Na, K, Rb, and Cs). At lower frequencies, a weak band always mirrors the main band (compare the trends of the full and open symbols in Fig. 7), being red-shifted to about the same extent as the blue shift undergone by the main band (see Table 9):[226–228] lower $|\Delta\tilde{\nu}|$ for Cs, higher for Li. Several different attributions were assigned to the red-shifted band; a coordination to the cation site *via* the oxygen end, forming a linear $M^+\cdots OC$ linkage isomer was also among these. The definitive proof that this was the correct assignation came some years later and was due to a VTIR experiment performed on Na-ZSM-5 by Arean *et al.*[288]

The IR spectra of that experiment are shown in Fig. 32: part (a) refers to the temperature range of 83–203 K, whereas part (b) refers to the 223–303 K interval. In part (a), the main band at 2178 cm^{-1} due to the standard $Na^+\cdots CO$ adduct, widely discussed in Section 3.1.1, behaves in an expected way, as shown in eqn (24), showing a decrease in its intensity upon an increase in temperature (see blue arrow); however, the small band at 2113 cm^{-1} behaves in the opposite way, as it increases

Table 9 Summary of differences in adsorption enthalpy $\Delta[\Delta H^\circ]$ for the $ZM^+\cdots CO \rightleftharpoons ZM^+\cdots OC$ equilibrium between the two linkage isomers in different zeolites and the wavenumbers of the corresponding C- and O-bonded adducts, as determined by VTIR. Previously unpublished table analyzing data are reported in the references quoted in the last column

Zeolite	$\tilde{\nu}$(CO) of $ZM^+\cdots CO$ (cm^{-1})	$\tilde{\nu}$(CO) of $ZM^+\cdots OC$ (cm^{-1})	$\Delta[\Delta H^\circ]$ (kJ mol^{-1})	Ref.
H-ZSM-5	2174	2120	4.6	698
Li-ZSM-5	2195	2100	7.8[a]	696
Li-ZSM-5[b]	2188	2110	5.1[a]	696
Na-ZSM-5	2178	2113	3.8	288
K-ZSM-5	2166	2117	3.2	694
Rb-ZSM-5	2161	2120	1.8	698
Cs-ZSM-5	2157	2122	—	284
Silicalite-1	2160	2122	3.0	700
Na-β	2180	2112	5.8	285
K-β	2167	2120	5.6	285
Cs-β	2156	2124	—	286
Na-FER	2175	2113	4.0	278
H-Y	2173	2124	4.3	692
Na-Y	2171	2122	2.4	691
Ca-Y	2197	2094	11.0	284
Ca-Y[b]	2191	2094	8.0	284
Sr-Y	2191	2095	9.8	283
Sr-Y[b]	2187	2098	7.6	283
Na-ETS-10	2176	2115	—	382
K-ETS-10	2166	2125	—	382

[a] In this case a quantitative determination of $\Delta[\Delta H^\circ]$ was more complex because of the concomitant presence of the bands for dicarbonyl $Li^+(CO)_2$ and Li^+(CO,OC) species, which partially overlapped the bands of Li^+(CO) and Li^+(OC) monocarbonyl species; this complicated the equilibria present in the system and made the quantitative calculation of the $I(T)_{Na\cdots OC}$ and $I(T)_{Na\cdots CO}$ integrated areas more difficult.[695,696] [b] Values referring to the $ZM^{2+}\cdots(CO)_2 \rightleftharpoons ZM^{2+}\cdots$(CO,OC) equilibrium between dicarbonyl species (M = Ca or Sr). In this case, the presence of more than one equilibrium makes the determination of the $\Delta[\Delta H^\circ]$ value more complex than that explained here in eqn (34)–(37), which refer to the simple equilibrium (33), and the reader should refer to the original studies for the complete set of equations.

upon an increase in T (see red arrow). In the temperature range covered by panel (b), both bands decrease upon increasing T (see corresponding arrows). This observation allowed Arean *et al.* to definitively assign the 2113 cm^{-1} band to the $Na^+\cdots OC$ adduct and to derive the enthalpy needed to change from C-bonded adducts to O-bonded adducts from the IR data.

In fact, the two linkage isomers are in thermodynamic equilibrium:

$$ZM^+\cdots CO \rightleftharpoons ZM^+\cdots OC \quad (33)$$

which is driven by temperature T and the difference in adsorption enthalpies between the two linkage isomers:

$$\Delta[\Delta H^\circ] = \Delta H^\circ(M^+\cdots OC) - \Delta H^\circ(M^+\cdots CO) \quad (34)$$

A VTIR experiment, which involves variation in the temperature, is able to displace this equilibrium. The constant K of equilibrium (33) is given as follows:

$$K = \frac{\theta(T)_{M\cdots OC}}{\theta(T)_{M\cdots CO}} = \frac{I(T)_{M\cdots OC}}{I(T)_{M\cdots CO}}\frac{\varepsilon_{M\cdots CO}}{\varepsilon_{M\cdots OC}} \quad (35)$$

where $\theta(T)_{M\cdots OC}$ and $\theta(T)_{M\cdots CO}$ are the fractional coverages of the O- and C-bonded complexes (at temperature T), respectively, and the corresponding $I(T)$ and ε are the integrated IR band area and the molar absorption coefficient. The far right-hand side of eqn (35) is valid because for both complexes $I(T) \propto \theta(T)\varepsilon$ with the same proportionality constant that is related to the thickness of the sample and the cation concentration in the sample. Combining eqn (35) with the van't Hoff eqn (29), the following equation is obtained:

$$\frac{I(T)_{M\cdots OC}}{I(T)_{M\cdots CO}}\frac{\varepsilon_{M\cdots CO}}{\varepsilon_{M\cdots OC}} = \exp(-\Delta[\Delta H^\circ]/RT)\exp(\Delta[\Delta S^\circ]/R) \quad (36)$$

By taking the natural logarithm, the following equation is finally obtained:

$$\ln\left[\frac{I(T)_{M\cdots OC}}{I(T)_{M\cdots CO}}\right] = -\frac{\Delta[\Delta H^\circ]}{RT} + \frac{\Delta[\Delta S^\circ]}{R} + \ln\left[\frac{\varepsilon_{M\cdots CO}}{\varepsilon_{M\cdots CO}}\right]. \quad (37)$$

According to eqn (37), measurement of the integrated area of the IR bands of the two linkage isomers as a function of T allows the derivation of $\Delta[\Delta H^\circ]$ as the slope of the best linear fit of the experimental data (Fig. 32c, red dots), yielding $\Delta[\Delta H^\circ]$ = 3.8 kJ mol^{-1}. Unfortunately, in this case, $\Delta[\Delta S^\circ]$ can be obtained only if the two molar absorption coefficients of the two adducts have been carefully determined (see Section 6).

After this important experiment, several others performed this experiment on different zeolites, of which the results are summarized in Table 9, whereas for some of them the corresponding van't Hoff's plots are reported in Fig. 32c: Na-Y (blue circles),[691] K-ZSM-5 (orange triangles),[694] and Rb-ZSM-5 (green squares).[698] Note that in all the cases, $\Delta[\Delta H^\circ]$, as defined in eqn (34), is positive because the O-bonded complexes are always less stable than the corresponding C-bonded forms; thus, the slopes of the van't Hoff's plots are negative, whereas in all the other examples reported in Section 7.2, they were positive (see Fig. 28c, 29c and d and 30b) and the corresponding ΔH° values were negative, as shown in Table 8.

CO molecule is not the only one that is able to form linkage isomers once adsorbed in zeolites. Tsyganenko *et al.*[748] observed the linkage isomerism phenomenon for the CN^- anion adsorbed on different alkali metal-exchanged X zeolites. By performing VTIR experiments, they were able to obtain the differences in adsorption enthalpy, $\Delta[\Delta H^\circ]$, for the $ZM^+\cdots NC^- \rightleftharpoons ZM^+\cdots CN^-$ equilibrium, as summarized in the top part of Table 10. It is interesting to note that no linkage isomerism was found for CO adsorbed on M-X-zeolites (M = alkali metal cation). This is due to the strong interaction of CO with basic oxygen anions, which have a higher negative charge in these systems[705] (see Section 4). For this reason, the interaction of CO with the framework oxygen atoms of Cs-X zeolites is even stronger than that with Cs^+ cations, which results in a band at 2124 cm^{-1} for low coverages corresponding to a ν(CO) mode that is red-shifted instead of blue-shifted, as is always observed for $M^{n+}\cdots CO$ adducts with alkali and alkaline earth cations, as discussed in Section 3.1.1, Fig. 7, 8, and Table 8. On this basis, Tsyganenko *et al.* attributed this band to CO molecules, which form side-on $O^{\delta-}\cdots CO$ complexes with the most basic surface O anions.[705] This attribution

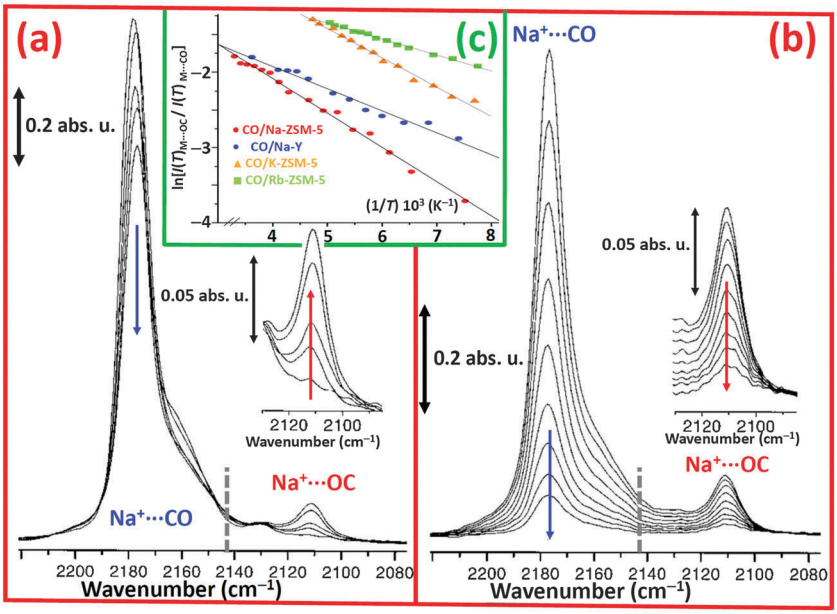

Fig. 32 VTIR spectra of CO (*ca.* 0.8 Torr) adsorbed on Na-ZSM-5. Part (a) from top to bottom: 83, 133, 153, 183, and 203 K. Part (b) from top to bottom: 223, 233, 243, 253, 263, 273, 283, 293, and 303 K. The two insets show an expanded view of the $ZNa^+\cdots OC$ band. The blue and red arrows indicate the evolution of the $ZNa^+\cdots CO$ and $ZNa^+\cdots OC$ bands, respectively, in the temperature intervals covered by the two parts of the figure. The gray dashed lines indicate the position of the ν(CO) stretching frequency of the unperturbed molecule: $\tilde{\nu}_0$(CO) = 2143 cm^{-1}. Part (c): Plots of $\ln[I(T)_{M\cdots OC}/I(T)_{M\cdots CO}]$ *vs.* $1/T$, eqn (37), obtained from the spectra shown in parts (a) and (b) (red circles). The remaining data refer to similar experiments performed on other zeolites and reported in successive articles: Na-Y (blue circles),[691] K-ZSM-5 (orange triangles),[694] and Rb-ZSM-5 (green squares).[698] The corresponding full lines represent the best linear fits of the experimental data. See Table 9 for the quantitative values of $\Delta[\Delta H^\circ]$ determined from the slopes of the best fit lines. Parts (a) and (b) are adapted by permission of Wiley-VCH (copyright 1998) from ref. 288. Part (c) adapted by permission of MDPI AG (copyright 2002) from ref. 287

Table 10 Top part: Summary of the differences in adsorption enthalpy $\Delta[\Delta H^\circ]$ for the $ZM^+\cdots NC^- \rightleftharpoons ZM^+\cdots CN^-$ equilibrium in different cation-exchanged forms of X zeolite and the wavenumbers of the corresponding N- and C-bonded adducts, as determined by VTIR. Table reproduced with permission from ref. 748, copyright Royal Society of Chemistry, 2010. Bottom part: Similar to top part for the $ZM^+\cdots NO \rightleftharpoons ZM^+\cdots ON$ equilibrium in different cation-exchanged forms of ETS-10 zeotype; unpublished table reporting data from ref. 382

Zeolite	$\tilde{\nu}$(CN) of $ZM^+\cdots NC^-$ (cm^{-1})	$\tilde{\nu}$(CN) of $ZM^+\cdots CN^-$ (cm^{-1})	$\Delta[\Delta H^\circ]$ (kJ mol^{-1})
Na-X	2195	2184	>20
K-X	2157	2144	21 ± 5
Rb-X	2150	2138	17 ± 3
Cs-X	2149	2138	7.7 ± 1.0
Zeolite	$\tilde{\nu}$(NO) of $ZM^+\cdots NO$ (cm^{-1})	$\tilde{\nu}$(NO) of $ZM^+\cdots ON$ (cm^{-1})	$\Delta[\Delta H^\circ]$ (kJ mol^{-1})
Na-ETS-10	1898	1857	—
K-ETS-10	1891	1868	—

is in agreement with the high basicity of Cs-X zeolites, as shown in Section 4. The anionic nature of the CN^- ion (which is isoelectronic with CO) minimizes integration with the negatively charged framework oxygen atoms and makes linkage isomerism possible.

Linkage isomers have also been reported by Zecchina *et al.*[382] for a NO molecule adsorbed on alkali metal-exchanged ETS-10 zeolites, as shown in the bottom part of Table 10. It is worth noting that the $\tilde{\nu}$(CO) and $\tilde{\nu}$(NO) frequencies of the linkage isomers observed on Na-ETS-10 and K-ETS-10 exhibit a perfect linear correlation, shown as full and open orange squares in Fig. 11b.

8. Space-resolved experiments: IR microscopes, IR beamlines at synchrotron facilities and stimulated Raman scattering (SRS) microscopy

This section is divided into three subsections. The first deals with a general overview of microspectroscopic techniques applied to heterogeneous catalysts. Section 8.2 deals with a scanning IR microspectrometric study of styrene oligomerization in H-ZSM-5 performed at the U10B beamline of the NSLS synchrotron. Finally, Section 8.3 discusses how stimulated Raman scattering microscopy reveals the evolution of the accessibility and 3D distribution of Brønsted sites in mordenites subjected to a progressive dealumination treatment.

8.1. Development of microspectroscopic techniques to study heterogeneous catalysts

Besides the development of environmental TEM[749–766] and *in situ* diffraction set-ups,[767] several *in situ* microspectroscopic techniques have recently been developed to investigate, on the micrometer and sub-micrometer scale, catalytic reactions in heterogeneous catalysts: XAFS,[24,768–775] fluorescence,[24,655,771,776–797] UV-Vis,[798] Raman,[24,26,799–801] and IR,[24,26,40,661,770,790,802–819] particularly

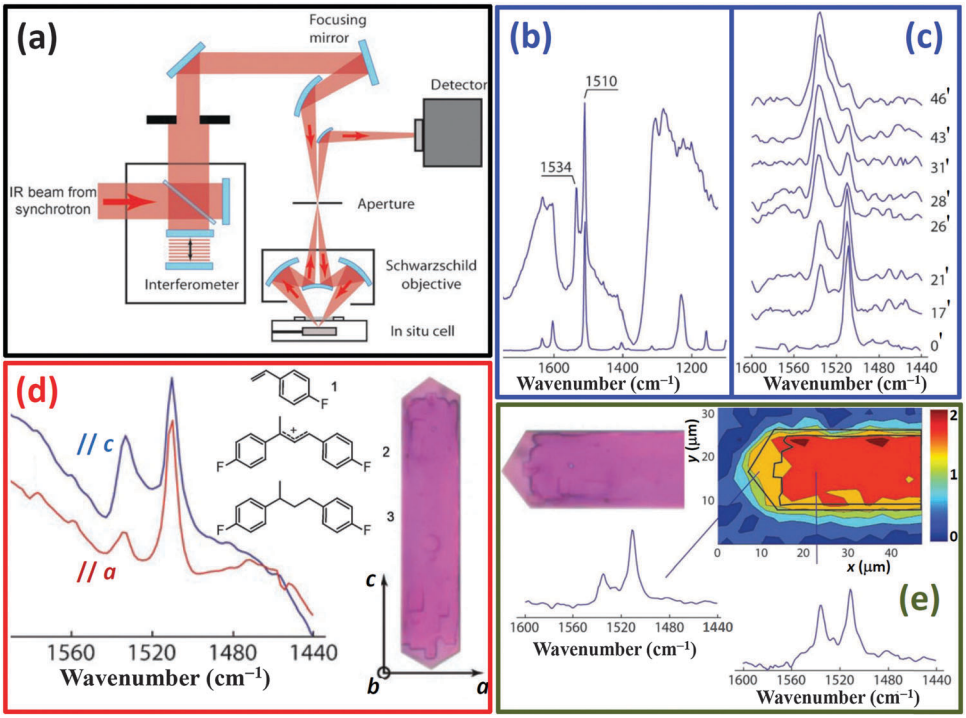

Fig. 33 Part (a): Scheme of the scanning IR microspectrometer system working in reflection mode. The microscope uses a Schwarzschild-type objective. An area of the sample defined by the aperture is spectroscopically sampled by the instrument and an image is obtained by raster-scanning the specimen using the focused beam. Part (b): IR spectrum of an individual H-ZSM-5 crystal in contact with 4-fluorostyrene (top spectrum); IR spectrum of liquid 4-fluorostyrene (bottom spectrum). Part (c): Time evolution (from bottom to top in minutes) of the background-subtracted IR spectra recorded *in situ* during the oligomerization reaction of 4-fluorostyrene. Part (d): Optical microphotograph of a H-ZSM-5 crystal after reaction with 4-fluorostyrene, showing the crystallographic directions *a*, *b* and *c* (right). *In situ* IR spectra recorded with two light polarizations parallel to the *a* (red curve) and *c* (blue curve) MFI axes (left). The central part shows the chemical structures of 4-fluorostyrene monomer **1** and the two dimeric reaction products **2** and **3**. Part (e): Fragment of optical microphotograph of a ZSM-5 crystal after reaction with 4-fluorostyrene (top left). Intensity of the IR band at 1534 cm^{-1} mapped over that of the crystal after the reaction (top right). IR spectra obtained from the edge (bottom left) and body (bottom right) of the crystal, illustrating the differences in the intensity ratio of the bands. Adapted by permission from ref. 40, copyright Wiley-VCH (2008).

using synchrotron radiation IR sources. These spectroscopic methods have proven to be very successful in elucidating valuable structure–function relationships for catalytic reactions.

The great advantage of combining vibrational spectroscopies with microspectroscopic methodology provides a direct insight into the chemical nature of reagent molecules, potential reaction intermediates, and reaction products on the μm scale. Coupling an IR spectrometer with an optical microscope allows us to ensure that only a localized area of a catalyst sample is probed.[40] This innovative technique has been particularly informative in the characterization of zeolitic and microporous materials. Published studies have covered several aspects, including the decomposition of organic templates,[802] mapping of the boron distribution in B-ZSM-5,[782] diffusion phenomena,[661,790,803,805,806,808,809,814–816,819] mass transport,[810–812] hydrogen and deuterium spillover in Y zeolite,[804] ethene oligomerization in H-ZSM-5,[799] and styrene oligomerization in H-ZSM-5.[40]

8.2. Styrene oligomerization in H-ZSM-5

Weckhuysen *et al.*[40] developed a scanning IR microspectrometer system that works in reflection mode, which is illustrated in Fig. 33a, and it operates at the U10B beamline of the National Synchrotron Light Source (NSLS), Brookhaven National Laboratory (Upton, NY, USA). Using this instrument, the authors carried out the *in situ* oligomerization of styrene in H-ZSM-5 zeolite. A coffin-shaped H-ZSM-5 crystal (100 μm × 20 μm × 20 μm; see microphotographs in parts (d) and (e) of Fig. 33) was exposed to 4-fluorostyrene, heated to 373 K for 10 min and the IR spectrum from a 5 μm × 5 μm region in the center of the crystal was recorded (top curve in Fig. 33b). Two sharp features, at 1534 cm^{-1} (with a shoulder at 1521 cm^{-1}) and 1510 cm^{-1}, are due to the oligomeric products (structures **2** and **3** in Fig. 33d) and the reactant (structure **1** in Fig. 33d and bottom IR spectrum in Fig. 33b), respectively. Fig. 33c shows spectra recorded *in situ* during the reaction at 373 K, showing the decrease of the reactant band and the increase of the product band.

It is interesting to note that the intensity of the band at 1534 cm^{-1} strongly depends on the relative orientation between the polarization vector of the synchrotron radiation IR light and the crystal axis (Fig. 33d). Based on the dependence of the optical absorption on the polarization of light, only straight channels of ZSM-5 were found to host the oligomerization products.[780] In the spectra shown in Fig. 33d, the intensity of the IR band associated with the oligomeric products is higher

when the light is polarized along the *c* direction, which implies that the transition moment associated with this vibrational mode is likely to be directed perpendicular to the long molecular axis of the dimeric carbocation.[40] It is also interesting to note that the electric dipole moment that is associated with optical transitions coincides with the long molecular dimension,[780] *i.e.*, it is orthogonal to the vibrational moment.

In a second series of experiments reported in the same study, Weckhuysen *et al.*[40] mapped the distribution of the reaction products **2** and **3** over a H-ZSM-5 crystal by scanning an individual crystal under an IR microscope. A spatial map of the 1534 cm^{-1} band is shown in Fig. 33e. In a previous study, UV/Vis microspectroscopy results have shown that dimeric carbocations are exclusively formed in the case of 4-fluorostyrene[779] with lower concentrations at the edges of the crystals compared to that in the center. The structure of ZSM-5 crystals[820–822] entails that the two-dimensional channel network is oriented nonuniformly, *i.e.*, at the edges of the crystal straight pores, open to the top surface of the crystal are accessible. On the contrary, in the center region of the crystals, sinusoidal pores are accessible. The non-uniform product distribution was rationalized in terms of the blockage of straight *versus* zigzag pores, as discussed in previous publications of the same group.[779,780] The spatially resolved IR spectra reviewed here (see spectra in Fig. 33e) are fully in line with the results of optical absorption, with lower intensity of the 1534 cm^{-1} band at the edges as compared to the body of the crystal, further supporting the attribution.

8.3. Stimulated Raman scattering microscopy revealing the 3D acid site distribution in acid zeolite catalysts

3D mapping on the nanoscale of catalytic reactions in zeolite catalysts has become possible using visible light. Infrared microspectroscopy (see previous sections) does not offer the required 3D spatial resolution, but Raman microspectroscopy does, and it could lead to very interesting information on the location of catalytic sites in the pore system. Raman microspectroscopy is, however, not interesting as such because of the strongly interfering background fluorescence and inherently weak signals. The sensitivity of Raman microspectroscopy was increased recently by several orders of magnitude by combining two picosecond lasers (Stokes and pump lasers) for obtaining a non-linear spectra.[57–59] By matching the difference in photon energy between the two lasers to a vibrational frequency in the sample, the Raman response can be detected; intensity increase in the Stokes and decrease in the pump. This has been used to design a spectroscopic technique with spatial resolution better than 1 μm,[60] which is widely applied in biological studies.[823–831] The technique, named as stimulated Raman scattering (SRS) microscopy, is a newly developed label-free chemical imaging technique that overcomes the speed limitation of confocal Raman microscopy, while avoiding the non-resonant background problem of coherent anti-Stokes Raman scattering (CARS) microscopy.[59,61,62]

SRS microscopy was recently applied by Roeffaers *et al.*[655] to nitrile probes (CH_3CN and benzonitrile, hereafter PhCN) in small-port mordenite crystals (5–10 μm size), as shown in Fig. 34. They applied this sophisticated technique to shed light on an old open question in the zeolite community, related to the small-port (SP)/large-port (LP) transition in mordenites.[832–835] It has been known for decades that mordenite exists in two forms that differ in their adsorption behavior: SP-MOR and LP-MOR, which have effective apertures of *ca.* 4 and *ca.* 7 Å, respectively. The effective aperture of LP-MOR is in accordance with the diameter of the large channels in the ideal crystal structure of mordenite,[165] as shown in Fig. 22b. The SP to LP transition is achieved by a simple thermal treatment, in which dealumination of the zeolite framework occurs and is complete when about 20% of the tetrahedral framework aluminum is converted into octahedrally coordinated extraframework species. According to Van Geem *et al.*,[834] pore blocking in SP-MOR is caused by structural defects originating from differently oriented mordenite chains. The transition involves the removal of framework Al from the 4-membered rings that form the walls of the 8-membered ring side channels. Thus, connections between segments of the main channel system are formed.

By tuning the polarization of the laser beams, Roeffaers *et al.*,[655] could demonstrate the specific orientation of deuterated acetonitrile in the side pockets and isolate the corresponding spectrum (Fig. 34a–d). Uniaxial symmetry was observed with a signal about 2.3 times stronger when the lasers were polarized in the crystallographic *b*-axis than in either the *a*- or *c*-axis, which indicates that a fraction of nitriles is symmetrically oriented with respect to the crystallographic *b*-axis.

They mapped the concentration of the CD_3CN probe in the crystal from 0 to 2.5 molecules per nm^3, which matched the density of framework aluminum atoms (Fig. 34e–i). The authors followed the dealumination of the samples and showed that this occurred preferentially in the main channels, leading to extraframework aluminum preferentially located in the side pockets that were close to the remaining acid sites. Following the methodological scheme of using probes of increasing size (see Section 5), the increased accessibility of larger nitriles (PhCN) to the pores was also studied with increasing dealumination (Fig. 34l–o). The influence on catalytic performance confirmed these observations, with increased accessibility but decreased density of acid sites.[655]

9. Time-resolved experiments

The full understanding of a catalytic reaction requires a thorough identification of precursor and intermediate species. Active species should be distinguished from spectators, which are often present on the surface of heterogeneous catalysts in general and inside zeolite pores in particular. In this regard, spectroscopies in general and infrared (IR) spectroscopy in particular can play an important role. However, the spectroscopic identification of precursor and intermediate species is often difficult owing to their transient nature. The control of experimental parameters, such as temperature, equilibrium pressure, composition of the reactant feed, and reactant-catalyst contact time, allows experimentalists to alter the rates of dynamic processes and consequently to appreciably modify

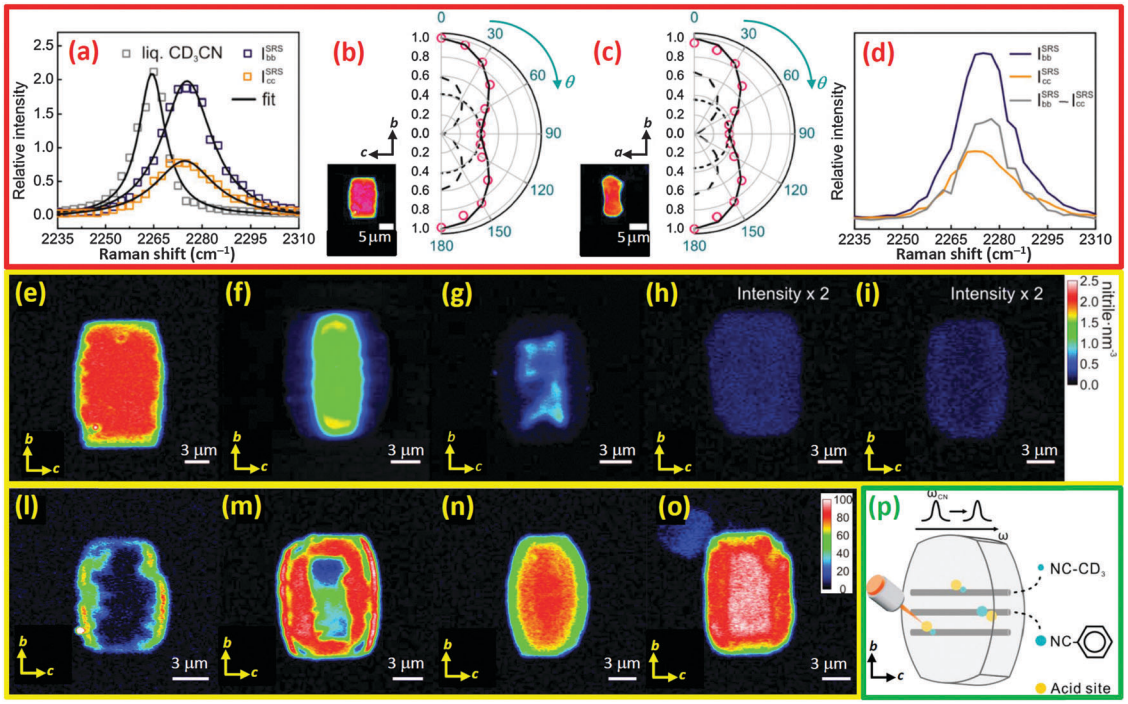

Fig. 34 Top parts (a–d): SRS microspectroscopy and polarization dependence of CD_3CN adsorbed in parent SP-MOR. Part (a): SRS response of the $\nu(C\equiv N)$ stretching region of liquid CD_3CN (×0.2, black data) and CD_3CN adsorbed in zeolite pores (averaged over a whole crystal) recorded with lasers polarized in the crystallographic *b*- (violet data) and *c*-axes (orange data); the experimental spectra (scattered data) are fitted by a single Lorentzian curve (solid line). Parts (b and c): Polar plot of $\nu(C\equiv N)$ stretching (2275 cm^{-1}) in zeolite crystals with different crystal orientations (shown in the insets) as a function of θ (angle between laser polarization and crystallographic *b*-axis); the polar plots can be simulated by the sum (solid line) of a $\cos(2\theta)$ function (anisotropic component, dashed line) and a circle (isotropic component, dotted line). Part (d): Spectra of the anisotropic (violet curve) and isotropic (orange curve) components of $\nu(C\equiv N)$ stretching and their difference (gray curve). Middle parts (e–i): Chemical mapping of CD_3CN adsorbed in H-MORs at progressive stages of dealumination from parent SP-MOR (e) to a strongly dealuminated form on the right (i). The false-colour scale indicates the density of acid sites: from 0 to 2.5 nitriles per nm^3 for parts (e–g) and from 0 to 1.25 nitriles per nm^3 for parts (h and i). Crystal axes are indicated by arrows. Bottom parts (l–o): Chemical mapping (2249 cm^{-1}) of PhCN adsorbed in H-MORs, revealing the accessibility of acid sites; gradual increase in the availability of acid sites in mildly dealuminated MOR from early (l) and intermediate (m) to late stages (n) of dealumination, as well as severely dealuminated MOR (o). Images were recorded with lasers polarized along the crystallographic *c*-axis. The false-color scale indicates the relative abundance of PhCN (from 0 to 100 a.u.). Crystal axes *b* and *c* are indicated by arrows. Part (p): Cartoon representation of the SRS microscopy method. Adapted by permission from ref. 655, copyright American Chemical Society (2014).

the relative concentrations of precursor, intermediate, and product species that are present under reaction conditions. In this context, time-resolved FTIR spectroscopy (with constant temperature and pressure during the experiment) and also temperature-time resolved methods (with both temperature and time changing simultaneously in a controlled way during the experiment) can be useful for kinetic investigations of several types of reactions.

The replacement of dispersive spectrometers by FTIR instruments in the 1980s drastically reduced the time scale for the acquisition of an IR spectrum, from minutes to seconds. Today, with conventional FTIR instruments, fast FTIR acquisition mode allows sub-second time resolution. Fast FTIR spectra can be obtained by reducing the spectral resolution (which is proportional to the translation of the movable mirror) and collecting interferograms without performing the Fourier transform. The latter is performed preferably at the end of the experiment.[23,135,143,836–840] In this case, the time resolution can reach 25–50 scans per second (still producing spectra with favorable signal-to-noise ratios), because the time scale is determined by the translation of a movable mirror. In such experimental conditions, FTIR spectroscopy can be a useful tool for the investigation of processes that proceed on time scales associated with kinetic effects.

The different approach of step-scan mode allows, in principle, a time resolution to be reached that is limited by the readout time of the IR detectors, typically in the order of 10^{-9} s, *i.e.* in the ns range.[34,839,841–850] To perform a step-scan investigation, a single kinetics experiment must be repeated n times (where n is the number of points on the interferogram) with the movable mirror fixed in each position x_j of the Michelson interferometer, at which the usual acquisition of the interferogram should have taken place. Under these conditions, the data are signals $S_{x_j}(t_i)$ as a function of time t_i for each position x_j. Time-resolved interferograms are then constructed by reading signals $S_{x_j}(t_i)$ that are collected at the same time (in different experiments) as a function of x_j. This method is extremely powerful; however, it can only be applied to systems that guarantee full reproducibility at the $\Delta t = (t_{i+1} - t_i)$ level. Because most of the important catalysts have extremely complex structures, such a severe constraint of

reproducibility is only rarely achieved. Moreover, the overall time resolution of catalytic kinetic experiments may still be limited by other factors such as the excitation source used to trigger the reaction; pressure pulses or temperature jumps may take milliseconds, limiting the overall kinetics resolution.[34] For these reasons, the actual time resolution of step-scan FTIR experiments performed on zeolites is, at best, of the order of 10^{-6} s (*i.e.* in the few μs range). There have been only a few reports on the use of step-scan FTIR to characterize homogeneous[851] and heterogeneous[852–854] catalytic systems in general and zeolites[855–862] in particular.

This section is divided into five subsections: 9.1, where IR spectroscopy is the sole technique used to investigate temporal evolution inside a working zeolite (*in situ* experiments); 9.2, where the catalyst performance is monitored by MS or GC in parallel with IR spectroscopy (*operando* experiments); and 9.3, where additional spectroscopies are added to the IR *operando* set-up. Finally, Section 9.4 is devoted to discussing an example of CO molecules generated by the photodissociation of diphenylcyclopropenone using a nanosecond laser pulse inside the channels of a mesoporous MCM-41 silica sieve,[862] whereas Section 9.5 deals with 2D IR pressure-jump spectroscopy of adsorbed species in zeolites followed by step-scan FTIR.

9.1. *In situ* IR studies on reactivity in zeolites

9.1.1. Reactivity of CO with Cp_2Cr encapsulated inside Na-Y zeolite. The interaction of CO with Cp_2Cr hosted inside a non-polar polystyrene (PS) matrix system resulted in a temporally stable $Cp_2Cr(CO)$ monocarbonyl complex characterized by an intense ν(CO) band at 1900 cm^{-1} (Fig. 28a),[734,863] which is very similar to that previously reported in the literature in the case of $Cp_2Cr(CO)$ in toluene solution.[864,865] Conversely, when Cp_2Cr is hosted in a polar Na-Y matrix, upon dosage of CO, a rapid evolution over time is observed.[866,867] An intense ν(CO) band immediately appears at 1850 cm^{-1} (blue circle and blue curve in Fig. 35a), which is due to the formation of the $Cp_2Cr(CO)$ monocarbonyl complex, as shown in the reaction (38). The red shift in ν(CO) with respect to the values found in PS and toluene is induced by the high ionicity of the Na-Y environment, which contains extraframework Na^+ and framework $O^{\delta-}$ Lewis acid–base pairs, as discussed in Sections 4.1 and 4.2.2. Over time, this band progressively declines and simultaneously three new bands at 1893, 1773 and 1724 cm^{-1} (red triangles in Fig. 35a) appear, accompanied by a weak component at ~1980 cm^{-1} (red square), which grows in a similar way.

$$2Cp_2Cr + Na^+Y^- + 2CO \rightarrow 2Cp_2Cr(CO) + Na^+\cdots Y^- \quad (38)$$

$$2Cp_2Cr(CO) + Na^+\cdots Y^- + 2CO \rightarrow [Cp_2Cr(CO)]^+\cdots Y^- + [CpCr(CO)_3]^-\cdots Na^+ + Cp \quad (39)$$

The evolution of the spectra indicates that the monocarbonyl precursor (band at 1850 cm^{-1}) is transformed into a charged tricarbonyl species $[CpCr(CO)_3]^-$ (triplet at 1893, 1773 and 1724 cm^{-1})[868] *via* the loss of a Cp ring, whereas the weak component at ~1980 cm^{-1} is due to a fraction of $[Cp_2Cr(CO)]^+$ cationic species (Fig. 35b).[868–870] On this basis, reaction (39) was inferred and supported by parallel Cr K-edge EXAFS analysis.[866,867] This reaction requires the presence of two Cp_2Cr molecules inside the same supercage, as shown in the top-left inset in Fig. 35a.

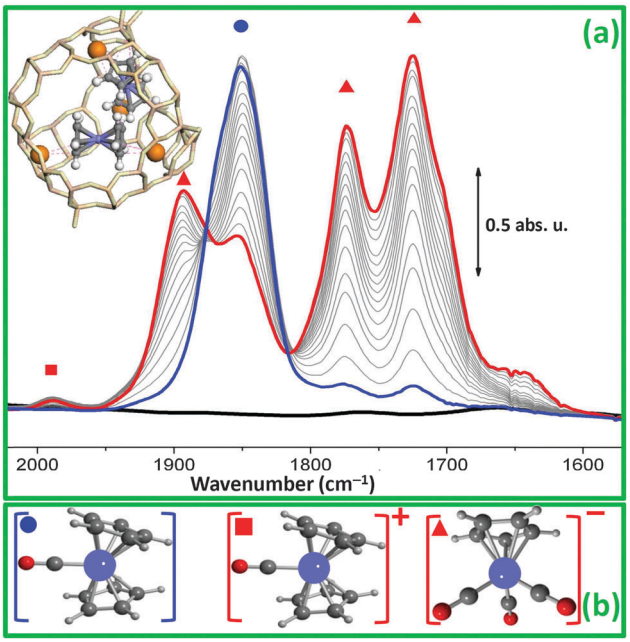

Fig. 35 Part (a): Temporal evolution of the FTIR spectra (at RT) of Cp_2Cr/NaY systems before dosage of CO (black), immediately after (blue), and 1 h after the exposure to CO (red). Gray spectra are intermediate between the blue and red spectra. The inset in the top left corner shows two Cp_2Cr molecules encapsulated inside the supercage cavity of Na-Y zeolite represented in stick mode (Si and Al, light orange; O, light yellow), whereas Na^+ cations and Cr, C and H atoms of the Cp_2Cr molecule are presented as orange, violet, grey and white spheres, respectively. Part (b): Ball-and-stick representations of the complexes responsible for the IR bands shown in part (a): neutral $Cp_2Cr(CO)$ (band labelled with a blue circle), cationic $[Cp_2Cr(CO)]^+$ complex (weak band labelled with a red square) and anionic $[CpCr(CO)_3]^-$ complex (three bands labelled with red triangles). Previously unpublished figure reporting data from ref. 866 and 867.

9.1.2. O_2 activation of H-Cu-SSZ-13 catalyst: *in situ* independent IR and XANES studies. Activation of a zeolite is a fundamental step for both catalysis and characterization purposes. In fact, the evacuation of water and other molecules adsorbed in the channels and cavities is necessary in catalysis to make the active sites accessible to reactants. Incomplete activation would result in residual water molecules, which may block the activity of a fraction of the sites. The same is true when activation is aimed to study the zeolite with a specific probe molecule; the simultaneous presence of water may prevent adsorption of the probe and/or may result in misleading results because of competition for the adsorption on the same site.

IR spectroscopy is one of the best characterization techniques for following the progressive activation of a zeolite and to confirm the completeness of the process, because both the stretching ν(OH) and bending δ(HOH) modes of the water molecule are IR-active with a very high molar absorption coefficient (see Section 6.1); this makes possible the detection of very small amounts of adsorbed water molecules by IR spectroscopy. This important IR check allows to avoid starting

a catalytic test or characterization study using samples that are not properly activated.

Fig. 36a shows the dehydration of H-Cu-SSZ-13 zeolite in an O_2 flow in the 30–400 °C range as monitored by *in situ* FTIR spectroscopy. The desorption of adsorbed water molecules is confirmed by the disappearance of both the huge and broad absorption in the 3600–2600 cm^{-1} range, which is due to the ν(OH) mode of H-bonded water molecules (see Section 2.2), and the narrower and better-defined band at 1623 cm^{-1}.[871,872] As the spectra are not subtracted, framework contributions, *i.e.*, overtones from ν(T–O–T) modes, are always visible in the series at 1998, 1858, 1680 and 1535 cm^{-1}. The total disappearance of the 1623 cm^{-1} band at 250 °C (bold grey curve) is an indication that molecular water is almost completely desorbed at this temperature (as observed from the magnification in the inset of Fig. 36a). The gradual appearance of 3611 and 3584 cm^{-1} bands related to the ν(OH) of non-H-bonded Brønsted groups is also observed, together with that of free silanols located on the external surface of the zeolite (3737 cm^{-1} band) and a component that is peculiar to this zeolite at 3656 cm^{-1}, which is assigned to $[Cu^{II}–OH]^+$ groups.[161,363] Finally, it is interesting to note that for temperatures ranging from 30 to 200 °C, the band at 2420 cm^{-1} increases in intensity. Prior studies on the adsorption of water on protonic zeolites, reviewed in depth here in Section 2.2 (see Fig. 2), demonstrated that this band is due to Fermi resonances between perturbed zeolitic O–H stretching and O–H bending overtones of hydrogen-bonded water molecules and that its intensity is most clearly evident at moderate water coverages in the zeolite.[136,145,177,200,873,874]

Borfecchia *et al.*[363] have supported the laboratory time-resolved IR experiment reported in Fig. 36a by a parallel XAS experiment performed at the ESRF synchrotron (Fig. 36b) to follow the evolution of the coordination and oxidation state of copper cations. The loss of water molecules coordinated to Cu^{2+} cations is confirmed by the decrease in the white line (main resonance around 8995 eV). In agreement with the IR experiment, this desorption occurs in the 30–250 °C interval, whereas the XANES spectra collected in the 250–400 °C interval are almost unchanged. The presence of O_2 in the outgassing flow guarantees the retention of the +2 oxidation state of copper species, as confirmed by the 1s → 3d weak (because dipole-forbidden) transition at 8977.5 eV, which is peculiar of Cu^{2+} species (d^9 cations). Activations performed in the absence of O_2 (under vacuum or flux of inert gas) follow a similar path till 250 °C, when all H_2O molecules adsorbed on Cu^{2+} are lost, whereas the 250–400 °C interval results in a progressive and almost complete Cu^{2+} → Cu^+ reduction (Fig. 36c).[363] The EXAFS parts of the XAS spectrum (not shown here) reveal that in fully dehydrated conditions, Cu^+ exhibits less coordination to framework oxygen atoms than Cu^{2+}.

In Section 9.3.1, we will review the same experiment performed by Kwak *et al.*,[436] where both IR (in diffuse-reflectance mode) and XANES spectra were collected simultaneously at the synchrotron (see Fig. 45). This approach has the evident advantage that IR and XANES spectra are collected on exactly the same sample in the same environmental conditions, allowing an almost direct one-to-one comparison between IR and XANES spectra collected along the temperature series; "almost" because the acquisition time for collecting one spectrum is not the same for the two techniques. The price to pay for this important benefit is related to compromises in the experimental set-up that must be made to allow both techniques to

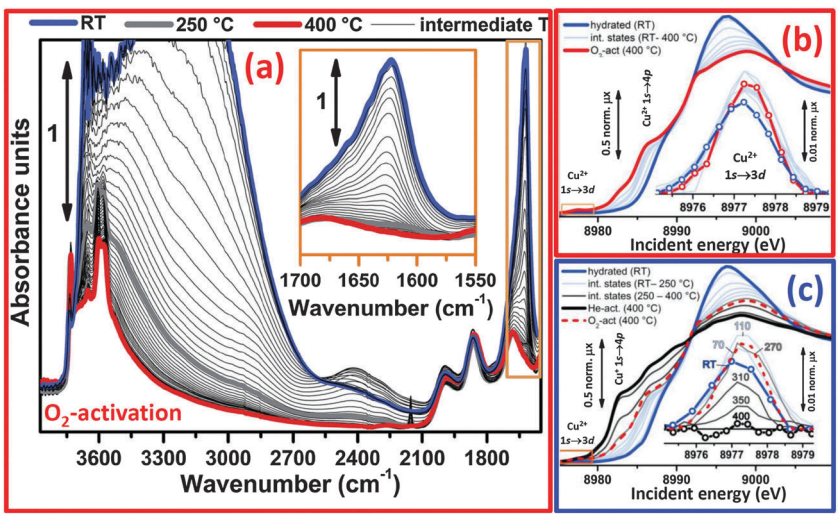

Fig. 36 Part (a): Dehydration of H-Cu-SSZ-13 zeolite in an O_2 flow (30 ml min^{-1}; O_2 : He = 1 : 1) as monitored by *in situ* FTIR spectroscopy. Spectral colors refer to different temperatures: the bold blue curve to 30 °C, the bold grey curve to 250 °C, the bold red curve to 400 °C, and thin black curves to intermediate temperatures. The inset shows a magnification of the signal related to the δ(HOH) bending mode of molecularly adsorbed water (spectral region highlighted by the orange box in the main panel). Part (b): *In situ* temperature-dependent XAS data collected during O_2 activation of H-Cu-SSZ-13 in the 30–400 °C range. The main part shows the XANES spectra collected at ESRF BM23. The inset shows the magnified, background-subtracted, 1s → 3d pre-edge peak typical of the d^9 Cu(II) cation, highlighted by the orange box in the main panel, for selected intermediate temperatures. Part (c): Similar to part (b) for He activation of the H-Cu-SSZ-13 catalyst. The final spectrum collected on an O_2-activated H-Cu-SSZ-13 sample at 400 °C is also shown for comparison as a red bold dashed curve. Adapted with permission from ref. 363, copyright Royal Society of Chemistry, 2015.

be simultaneously operative, which differ from the ideal set-up for each separate technique. This results in lower quality of the collected spectra, which can be clearly observed by comparing both the IR and XANES parts presented in Fig. 45 and 36.

9.1.3. NH_3-SCR reaction followed *in situ* on Cu-SSZ-13 catalyst. The current technology of choice for reducing NO_x emissions from power plants and exhausts from diesel-driven vehicles is based on the selective catalytic reduction (SCR) of nitrogen oxides by ammonia (NH_3-SCR).[366–374] The best known catalysts for this reaction are V_2O_5 supported on TiO_2[875–880] and Co-,[370,881,882] Fe-[372,883–887] or Cu-[162,363,364,374,430,888–899] exchanged zeolites. See Section 3.1.2 for a review of the IR characterization of Cu-exchanged zeolites using N_2, CO and NO probes.

In NH_3-SCR, NO is reduced by ammonia to N_2 and H_2O, according to the following equation:

$$4NO + 4NH_3 + O_2 \rightarrow 4N_2 + 6H_2O. \quad (40)$$

Among the Cu-exchanged zeolites, in the last few years, great effort has been devoted to studying a large variety of copper-containing systems with CHA topology.[165] Most of the studies have been performed on low-Al-content CHA, namely, SSZ-13 and SAPO-34, which is the aluminum phosphate homologue, by varying both the source of copper and the exchange procedure.[161,162,363,364,430,436,890–892,894,895,899–901] The reason for this interest in the CHA framework is related to its advantages with respect to other frameworks (MFI, BEA, and MOR), which include a wide thermal stability range and high activity during lean combustion, *e.g.* in fuel-efficient diesel engines.

Despite the fact that reaction (40) has been known since many years, its precise mechanism and rate-determining step are still under discussion. Very recently, Cu-SSZ-13 has been considered as a model system for proposing a fully consistent catalytic cycle based on a single redox-active copper center cycling through the oxidation states +1 and +2,[364] as shown in Fig. 37a. All the species reported in the cycle have been identified by parallel FTIR, EPR, XANES and EXAFS studies supported by DFT calculations. The proposed cycle is based on the presence of copper species and stable charge-neutral gas-phase molecules only, avoiding the use of $1/2O_2$ or the

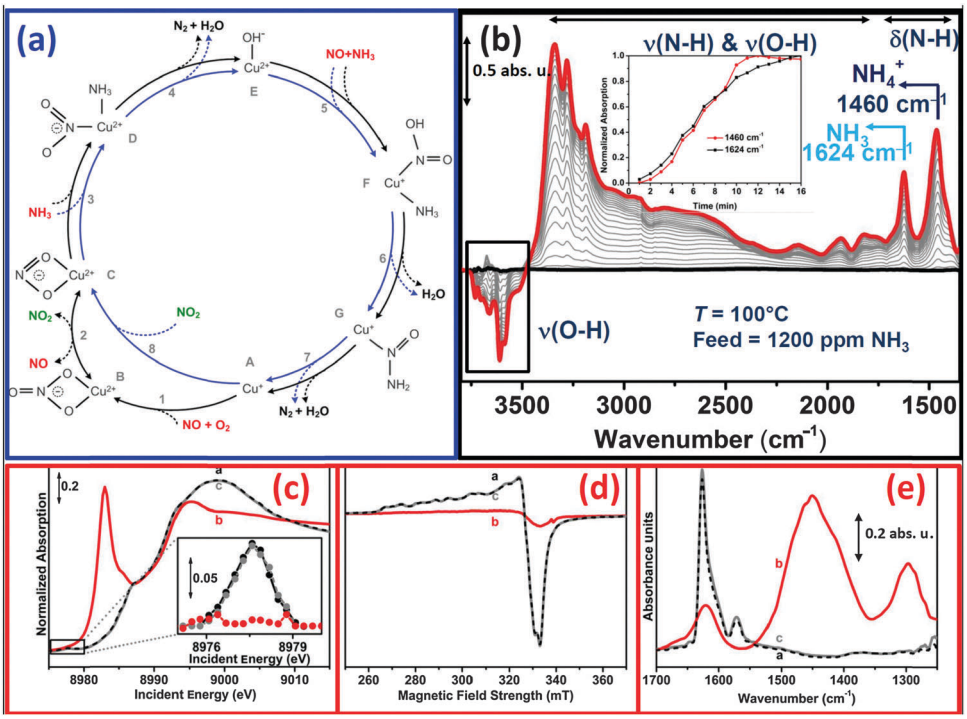

Fig. 37 Part (a): Reaction mechanism of the NH_3-SCR reaction in a Cu-zeolite according to Janssens *et al.*[364] The fast SCR cycle is represented in blue and the NO activation cycle is represented in black. Reactants are indicated in red, reaction products are indicated in black, and the NO_2 intermediate is indicated in green. In the standard SCR reaction, eqn (40), the NO activation cycle and fast SCR cycle proceed at equal rates; the stoichiometry of the standard SCR reaction is then found by adding these two cycles. The oxidation states of the Cu ions have been assigned according to the magnetic moment found *via* DFT: $M(Cu^{2+}) > 0.45$ and $M(Cu^{+}) < 0.1$. Part (b): Dynamic FTIR difference spectra of the adsorption of NH_3 onto Cu-SSZ-13 at $T = 100$ °C with a flow rate of 50 ml min^{-1} (feed: 1300 ppm NH_3, He = rest). The spectrum of O_2-activated material at 400 °C (bold red spectrum in Fig. 36a) has been used for subtraction. Black curve: O_2-activated material before adsorption of NH_3. Red curve: system saturated with NH_3. Grey curves: intermediate adsorption steps. The inset shows the normalized absorption of the 1460 and 1624 cm^{-1} bands as a function of the exposure time to the NH_3/He mixture. Part (c): *Operando* XANES spectra collected during reduction and oxidation in SCR over Cu–CHA (2.6 wt% Cu) at 200 °C in the following consecutive steps: (a) initial oxidation in 1000 ppm $NO/O_2 = 1:10$ (dashed black curves); (b) reduction in 1200 ppm NH_3/1000 ppm NO (solid red curve); (c) re-oxidation in 1000 ppm $NO/O_2 = 1:10$ (solid gray curve). The inset shows the background-subtracted XANES Cu^{2+} 1s → 3d dipole-forbidden transition pre-edge peak, which is proportional to the amount of Cu^{2+} species. Part (d): Similar to part (c) for EPR spectra. Part (e): Similar to part (c) for IR spectra. Parts (a) and (c)–(e): Adapted with permission from ref. 364, copyright American Chemistry Society, 2015; part (b) adapted with permission from ref. 902.

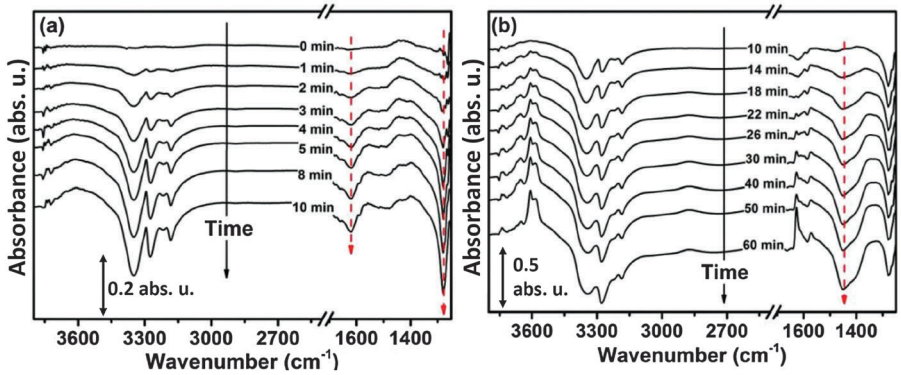

Fig. 38 Background-subtracted dynamic FTIR spectra of the interaction of NO + O_2 with pre-adsorbed NH_3 on Cu-SSZ-13. Parts (a) and (b) show series of spectra collected in the 0–10 min and 10–60 min ranges of contact time with NO + O_2, respectively. T = 200 °C, flow rate = 50 ml min^{-1}. Feed: NO = 1000 ppm, O_2 = 10%, He = rest. The spectrum of Cu-SSZ-13 pre-saturated with NH_3 at 200 °C (bold red spectrum in Fig. 37b) has been used for subtraction in both (a) and (b). Adapted with permission from ref. 902.

migration of charged species to match the stoichiometry of the reaction. Moreover, the suggested mechanism is relevant for the low end of the temperature interval relevant for the SCR reaction on these materials (250–300 °C), whereas other reactions may become important under harsher conditions. The steps of the suggested cycle have been followed spectroscopically by the combined use of XAS (*operando*), EPR (*in situ*) and IR (*operando*), as shown in Fig. 37c–e, respectively. Cu-SSZ-13 has been characterized by activation in diluted oxygen at 400 °C (see Section 9.1.2, Fig. 36a) and then contacted by ammonia in the gas phase at 100 °C. The effect of this treatment is indicated in Fig. 37b as a difference plot. The negative bands, corresponding to bands that have disappeared, are due to the ν(OH) modes of silanols (3737 cm^{-1}), Brønsted sites (3611 and 3584 cm^{-1}) and $[Cu^{II}–OH]^+$ groups (3656 cm^{-1}); the latter species being also characterized by the perturbation mode of the framework $[TO_4]$ units at 905 cm^{-1}, which is not visible in the spectral range shown;[161,162,363] this has also been discussed in Section 3.3.1.

Starting from a low contact time of exposure to NH_3, the low-frequency region is dominated by two maxima at 1624 and 1460 cm^{-1}, which are assigned to asymmetric N–H bending vibrations of molecular NH_3 adsorbed on Cu^{2+} Lewis sites and N–H bending vibrations of protonated NH_3 stabilized on Brønsted sites, respectively.[162] The multiple broad vibrational bands in the 3500–3000 cm^{-1} range are attributed to N–H stretching vibrations of both NH_4^+ and molecular NH_3, whereas the bands in the 2500–1700 cm^{-1} region are often assigned solely to NH_4^+.[162] The fact that 1624 and 1460 cm^{-1} bands develop with a similar dynamic trend as a function of the exposure time (see the inset in Fig. 37b) suggests comparable acid strength of Lewis and Brønsted adsorption sites. The growth in intensity of the 1460 cm^{-1} band is accompanied by a decline in the bands associated with ν(O–H) modes of Brønsted sites (negative bands observed at 3611 and 3584 cm^{-1}), which is due to the protonation of NH_3 at these specific sites with the consequent formation of NH_4^+ ions. Negative bands are also observed at 3737 and 3656 cm^{-1}, which indicates that NH_3 could also interact with the less acidic silanols and CuOH sites, respectively.

To better investigate the difference in reactivity between NH_3 adsorbed on Cu sites and on Brønsted sites, pre-adsorbed NH_3 was contacted with NO + O_2 at 200 °C as a fixed temperature (Fig. 38). Part (a) shows spectra collected in the first 10 minutes of contact time with NO + O_2: gradual consumption of molecular NH_3 on Cu sites is observed, as indicated by the negative bands at 1625 cm^{-1} and 1279 cm^{-1}; the latter contribution being assigned to symmetric N–H bending vibrations of molecular NH_3 adsorbed on Lewis sites.[903] These two bands completely disappear after 10 minutes. Concomitantly, negative bands of the corresponding stretching vibration modes (3348, 3272 and 3182 cm^{-1}) are clearly observed. Interestingly, at these low contact times, the band at 1460 cm^{-1} does not decrease in intensity, but is only slightly enhanced as a consequence of water formed *via* SCR. Only at longer contact times (see Fig. 38b) does the maximum at 1460 cm^{-1} start to decrease in intensity, almost totally disappearing after 50 minutes of exposure time. These results provide evidence that NH_3 adsorbed on Cu sites is more reactive towards NO + O_2 than NH_3 adsorbed on Brønsted sites. The fact that the latter species starts to react only when Cu sites are ammonia-free could be interpreted in two different ways. Assuming that the SCR reaction takes place at the metal center of the catalyst, the migration of ammonia molecules from Brønsted sites to Cu sites is likely. According to this view, if Brønsted sites are located close to Cu ions in the zeolite, it is conceivable that a NO_2 molecule on a Cu ion can interact directly with a NH_3 molecule on a neighboring Brønsted site, making the reaction possible without the desorption of NO_2. Alternatively, NO_2 could be produced *in situ* and desorbed from the metal centers, allowing gas-phase NO_2 to interact with NH_3 adsorbed on a Brønsted site. This second hypothesis is reinforced by the fact that NH_3 pre-adsorbed on H-SSZ-13, *i.e.* only NH_3 adsorbed on Brønsted sites is present, does not show any reactivity towards NO + O_2, but only towards NO_2. A possible pathway for the *in situ* formation of NO_2(g) over Cu sites is represented by the reaction of NO with Cu nitrate species according to the following equilibrium:[902]

$$Cu^{2+}\cdots NO_3^- + NO(g) \leftrightarrow Cu^{2+}\cdots NO_2^- + NO_2(g). \quad (41)$$

The formation of nitrate species stabilized on Cu^{2+} sites, *i.e.* $Cu^{2+}\cdots NO_3^-$, upon interaction with NO + O_2 is well known.[10]

In the experiment reported in Fig. 38b, the formation of these species was confirmed by the appearance of maxima at 1627 and 1570 cm^{-1} at long NO + O_2 contact times.

9.2. *Operando* experiments on zeolite catalysts

Operando spectroscopy consists of the simultaneous spectroscopic characterization (by IR, Raman, UV-Vis, EPR, XANES, and EXAFS, as discussed in Section 9.3) of surface species and determination of catalytic activity and selectivity.[35] Herein, we will limit our discussion to vibrational spectroscopies. By establishing relationships between the nature and concentration of surface species on the one hand and the catalytic activity on the other hand, important insight into surface reaction mechanisms can be obtained. In the steady state, however, the concentrations of surface intermediate species are often very low, except in favorable cases (*e.g.* low temperatures or high absorption coefficients), the concentration of the not very reactive most abundant reactive intermediates (*mari*).[904,905] Their identification by IR or Raman spectroscopy, however, can be crucial in understanding the reaction as it may, for instance, help to decide between plausible reaction mechanisms proposed in the literature. Other surface species that can be sufficiently abundant to be observable are those that accumulate on an inactive part of the catalyst and do not participate in the reaction (spectator species).[23] Although such species are not generally worth studying, their observation during the reaction can sometimes be misleading and a lot of care should be taken to distinguish them from species that actually take part in the reaction. Much more important are the species that accumulate on the active sites, leading to a decrease in the reaction rate (poison species). Such species can naturally form during the reaction as a (side) product or be added in the feed. In both cases, the study of these species (structure and location) implicitly gives important information on the nature of the active sites they are blocking. In the following section, typical examples are given that illustrate how *operando* IR spectroscopy studies can provide insight on the mechanisms of reactions that occur within zeolite pores.

9.2.1. *Operando* for characterizing the active Brønsted acidic sites in hydrocarbon conversion reactions. To the best of our knowledge, the earliest *operando* study carried out on a zeolite-catalyzed reaction was published by Ward nearly 50 years ago,[906] who recorded the IR spectra of H-Y hydroxyl groups during cumene cracking. He reported a simultaneous increase in catalytic activity and decrease in free hydroxyl groups with the reaction temperature, which he assigned to an increase in the interaction of cumene with the zeolite active sites; however, without excluding the formation of coke species. Although this interpretation is now highly disputable (the catalytic activity actually increased with temperature *despite* both a lower coverage of OH groups by cumene and coke formation), this early study clearly showed that ''by studying a catalytic reaction by *in situ* [*operando*] infrared spectroscopy, new evidence concerning the centers of adsorption and catalytically active sites can be obtained''[906] and opened the way to further studies. Therefore, in the early 1990s, Saussey *et al.*[907] studied the transformation of cyclohexene over H-Y zeolites and were able to establish relationships between the simultaneous decrease in the amount of zeolitic OH groups (assessed by the intensity of the ν(OH) bands (see Section 2.1 above)), the formation of 'coke' species (evidenced by the ν(CC) bands at *ca.* 1600 cm^{-1}), and catalytic activity (changes in conversion and selectivity). They could show, in particular, that the most acidic OH groups were primarily responsible and affected by coke formation.

Another strategy allowing the establishment of relationships between Brønsted acid sites and catalytic activity involves the selective *in situ* poisoning of zeolite Brønsted acid sites. Such an approach was used by Jolly *et al.*[908] in the case of *n*-hexane cracking on dealuminated zeolites by dosing known amounts of lutidine, which is a probe molecule that is very selective for Brönsted acid sites; they could determine the particular role of strongly acidic OH groups at 3600 cm^{-1} (see Section 2.1 above) in this reaction and exclude the participation of Lewis acid sites in the catalytic activity.

More recently, Marie *et al.*[909] used *ex situ* Na^+-selective poisoning of the Brønsted acid sites of mordenite zeolites to provide experimental evidence for the catalytic role of each type of OH group in these zeolites. A similar strategy, although not using *operando* spectroscopy, has also been recently used by Gounder and Iglesia to determine the individual activities of mordenite OH groups for the protolytic cracking of light alkanes.[910] As already discussed in Section 5, mordenites have two very different pore systems: 12-MR main channels and 8-MR side pockets (Fig. 22). The three different types of acidic OH groups (already mentioned in Section 5.4.1) are located in the main channels (crystallographic position O_7), the side pockets (O_9), and the interconnecting window (O_2). During the progressive introduction of sodium by cation exchange of the zeolite, hydroxyls O_9H are removed preferentially (in the side pockets), followed by the exchange of O_2H and O_7H at last. Using a series of progressively exchanged mordenites with increasing sodium content, the selectivity of xylene isomerization (Fig. 39a) was progressively tuned to decrease the extent of disproportionation (Fig. 39b), and then to increase the production of toluene while that of trimethylbenzene was suppressed. By comparing the intensity of ν(OH) for each of the three possible locations of OH groups (Fig. 39c) with the simultaneously collected gas-phase chromatography data (Fig. 39d), it was possible to assign the various reactions, which produced each of the products, to a specific acidic OH group at a specific location in the pores. The role of sodium atoms could also be understood: Na^+ in the side pockets would favor the adsorption of trimethylbenzene at the window opening, thus changing the available space in the main channels. Constrained hydroxyls in the side pockets were not accessible to the reactants under the reaction conditions, but their presence led to a global increase in activity without any modification in selectivity. Acid strength considerations, together with the observation of ''working hydroxyls,'' indicated an indirect effect of O_9H on the overall activity, which was probably related to a modification in the void space inside the micropores.

9.2.2. *Operando* studies on ion-exchanged zeolites. In contrast to acid zeolites (see Section 2), the active sites of ion-exchanged zeolites are not detected by IR spectroscopy

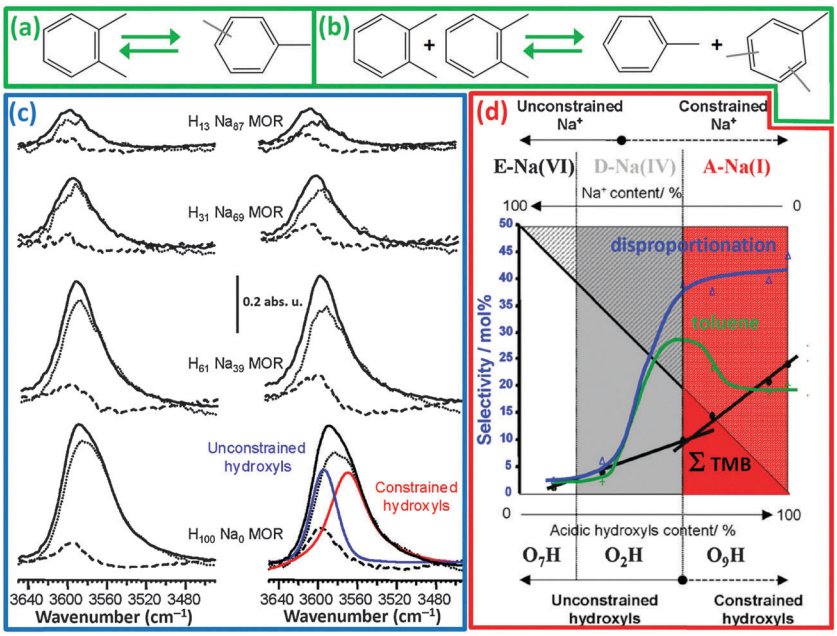

Fig. 39 The two main routes for *o*-xylene conversion over acidic catalysts: Part (a): Isomerization, which gives a mixture of *m*-xylene and *p*-xylene. Part (b): Disproportionation, which gives toluene and a mixture of trimethylbenzene isomers (1,2,3-, 1,2,4- and 1,3,5-TMB). Part (c): Left: IR spectra in the ν(OH) stretching region for selected H_xNa_{1-x} MOR samples (at different proton exchange rates: $13 \leq x \leq 100$) collected at 573 K before reaction with *o*-xylene (—) and after 1 min reaction (•••). Right: As the left part with the (•••) spectra collected after 3 h reaction. Spectra in dashed lines (- - -) correspond to subtraction between (—) and (•••) and represent the hydroxyls consumed during the reaction. Spectra in the bottom right-hand corner represent the spectra expected for constrained and unconstrained OH (at high and low frequency, respectively) at 573 K before reaction. Part (d): Evolution of the selectivity for disproportionation products with the acidic hydroxyls content for isoconversion (42%) conditions obtained during the first moments of reaction at 573 K. $\sum$TMB represents the sum of trimethylbenzene isomers. O_7H, O_2H and O_9H are the three possible crystallographic locations of OH groups. Reproduced from ref. 909 with permission, copyright Elsevier, 2005.

(see Sections 3 and 4), and spectroscopic observations are therefore limited to the spectra of adsorbed species, from which one has to infer the nature or structure of the corresponding active site. Recent IR *operando* studies carried out over alkali-exchanged zeolites will be illustrated here by the study of Groult *et al.*,[911] who studied the conversion of methylbutynol (MBOH, 2-methylbut-3-yn-2-ol, $(CH_3)_2C(OH)C{\equiv}CH$) over Na-X zeolite. The understanding of the transformation of methylbutynol is of interest because it has been proposed as a test reaction for acid/base properties, allowing the discrimination of basic, amphoteric and acidic catalysts on the basis of their product selectivity. Basic surfaces, in particular, lead to the decomposition of MBOH into acetone and acetylene.[912] Moreover, when carried out over a series of basic zeolites, the yield of this process generally follows the trend that is expected from the basicity of framework oxygen (see Section 4.1 above). However, rapid deactivation generally occurs; thus, the relevance of this test reaction with respect to the basic properties of the fresh catalyst may be questioned when the activity is reported in the steady state.[911] To deal with rapid deactivation, Groult and co-workers monitored the catalytic activity of a Na-X zeolite using micro-GC, which enables a time resolution of the order of 150 s, in parallel with the spectroscopic characterization of surface species. Examination of the ν(≡C-H) stretching band (see Fig. 40a) allowed three types of adsorbed MBOH species to be distinguished: species A, which interacts with the acid–base pairs of the zeolite through their OH groups and leads to a nearly free $\nu({\equiv}C\text{–}H)$ frequency at $\sim$3325 cm^{-1}; species B, which forms a π-coordination complex with the Na^+ cation characterized by $\tilde{\nu}({\equiv}C\text{–}H)$ = 3277 cm^{-1}; and species C, which is a ${\equiv}C\text{–}H\cdots O$ hydrogen-bonded complex with the basic oxygen centers resulting in $\tilde{\nu}({\equiv}C\text{–}H)$ = 3215 cm^{-1}, as shown in the corresponding schemes in the insets of Fig. 40a. On the basis of mechanistic considerations, only the former species A, which has a much lower concentration than B or C, was proposed as the adsorbed intermediate that leads to the observed products (acetone and acetylene), whereas species B and C would be spectator or reservoir species.[911] Moreover, a striking feature of these spectra (Fig. 40b) is the continuous growth of intense bands at 1690–1703 cm^{-1}, which are characteristic of ν(C═O) stretching vibrations, during the deactivation period; the authors have assigned these to the surface accumulation of acetone and its dimerization product coordinated to extraframework Na^+ cations, which block the dissociation of MBOH.[911]

9.2.3. Plasma on zeolites and *operando* IR. Plasma-assisted heterogeneous catalysis is a new and quickly expanding field.[913–927] Gas-phase processes are very fast under plasma conditions and the role of the surface is hardly understood. Tracking adsorbed species by *operando* infrared spectroscopy is one of the few methods for obtaining information on the reaction mechanism. Infrared spectroscopy inside a plasma reactor showed that template removal in a zeolite was possible at very low temperatures. With respect to the calcination process, the use of plasma also allowed retaining a small crystal

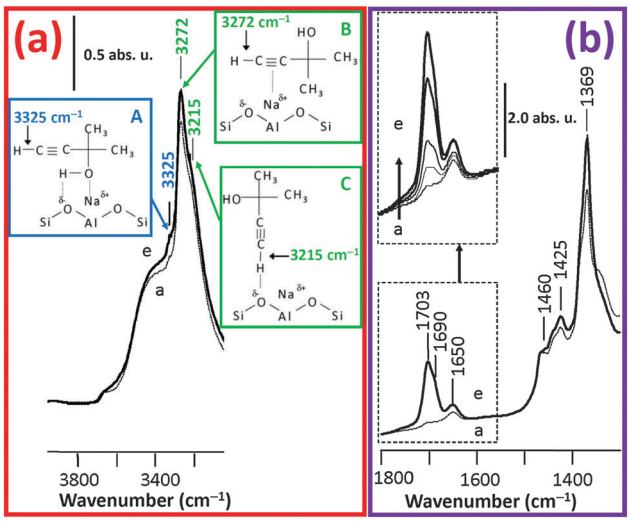

Fig. 40 Evolution of *operando* DRIFT spectra registered at 413 K during the deactivation period of the transformation of MBOH over Na-X. Part (a): Spectra in the 3900–3100 cm^{-1} range at 0 min (introduction of MBOH in a carrier gas; spectrum **a**) and at 20 min, when reaching the steady state (bold spectrum **e**). The complex $\nu(\equiv C-H)$ band exhibits three features assigned to reactive species (MBOH species A) and non-reactive spectators (MBOH species B and C). Part (b): Spectra in the 1800–1200 cm^{-1} range, showing the accumulation of ketonic species during the deactivation period; spectra similar to that in part (a). Adapted with permission from ref. 911, copyright Royal Society of Chemistry, 2010.

size of nanoparticles of beta zeolite and even reduced Pt inside the pores without any sintering of the metal or zeolite nanoparticles. The nature of the active species for the removal of hydrocarbons is still an open question.

Operando observation of surface species during template removal in an argon or oxygen plasma showed that the most active species originated in water (Fig. 41).[922] The intensity of the infrared band for hydrocarbons (ν(CH) at 2900–3000 cm^{-1}, Fig. 41a–c) was plotted *vs.* time during the reaction and compared with the intensity for adsorbed molecular water (δ(OH) at 1630 cm^{-1}). In an Ar plasma, hydrocarbon decomposition starts quickly and nearly stops after 5 s, when all water is removed from the surface. With an O_2 plasma, hydrocarbon decomposition starts at the same rate, but when all residual water is removed, the reaction still proceeds at a reduced pace (Fig. 41d), which is probably due to the presence of ionized oxygen that leads to ozone in the micropores. This ozone is the main agent for the decomposition of hydrocarbons in the second stage of the reaction. These experiments were performed without external heating, and the temperature in the solid remained below 150 °C. This showed that the most active species for the decomposition of hydrocarbons inside the pores of a zeolite under plasma originates from the ionization of water. The radicals that are generated are very active species and can remove hydrocarbons and templates (or even reduce Pt in that specific example) in the pores of a zeolite at very moderate temperatures below 150 °C, as confirmed by a TEM investigation (inset in Fig. 41e) and an IR study of adsorbed CO performed on Pt-β samples after treatment with cold O_2 plasma (Fig. 41f).

9.2.4. *Operando* IR studies in photocatalysis. The use of *operando* spectroscopy in photocatalysis on zeolites can be performed by adapting an *operando* reactor cell; thus, UV light is brought to the surface of the catalyst together with an infrared beam,[43] as shown in Fig. 42a. Mechanisms and surface species in photocatalysis are not well known and following the surface intermediates during the reaction provides very valuable information.

Using lasers as a light source, very short-lived transient species could be studied on metal oxides.[928] In an experiment at 10 ms time resolution, following 300 ms laser pulses in an ATR cell, surface superoxide species were shown to be kinetically competent intermediates in the photooxidation of water on 5 nm nanoparticles of Co_3O_4: the measured lifetime of superoxides was in the same range as the duration of the illumination pulse needed to produce O_2.

The decomposition of methanol by photocatalysis on titania-functionalized β zeolite (TiO_2/β) was followed at a more moderate time resolution.[43] Many key surface intermediates were detected, and the complexity of surface reactions was indicated by the different temporal behavior of adsorbed formyl species (monodentate formates: formic acid or methyl formate) and bidentate surface formates (Fig. 42b and c).

Reaction mechanisms in photocatalysis were further studied by combining *operando* spectroscopy with SSITKA (steady-state isotope transient kinetic analysis).[929] In this approach, while the reaction proceeded in a steady state on the catalyst, a reactant is suddenly replaced by its isotopically labeled version. Surface spectroscopy shows the rate of the replacement of the chemisorbed species by their labeled version, whereas online gas analysis shows the introduction of the labeled moiety into the final product. By comparing the two kinetic, linking a reaction product to surface intermediate species becomes straightforward, leading to the direct determination of reaction pathways. In the example shown in Fig. 43, natural methanol is suddenly replaced in the reactant flow by ^{13}C-labeled methanol and 3.5 min after the change, natural CO_2 is replaced by labeled $^{13}CO_2$ in the product flow exiting the reactor. However, on the surface of the catalyst, formate species are exchanged at a much slower rate, which shows that most surface formate species are not active intermediates but rather spectator species. It is only a minor fraction of surface formates that lies on the direct reaction pathway.

Operando IR is also about to approach important questions about quantitative results in heterogeneous photocatalysis: the determination of the number of active sites is a very difficult challenge and actual turnover numbers are at present out of reach. *Operando* IR spectroscopy will probably be a key tool for their determination, and this is now an important research field.

9.2.5. MTH reaction followed by *operando* Raman. Raman spectroscopy is based on the so-called Raman effect,[930,931] where monochromatic light interacts with matter; thus, photon energy is either transferred to or from matter (inelastic scattering). The difference or shift in energy between the laser excitation and the scattered light is related to rotational, vibrational, phonon or spin-flip processes in the sample. Due to the usually

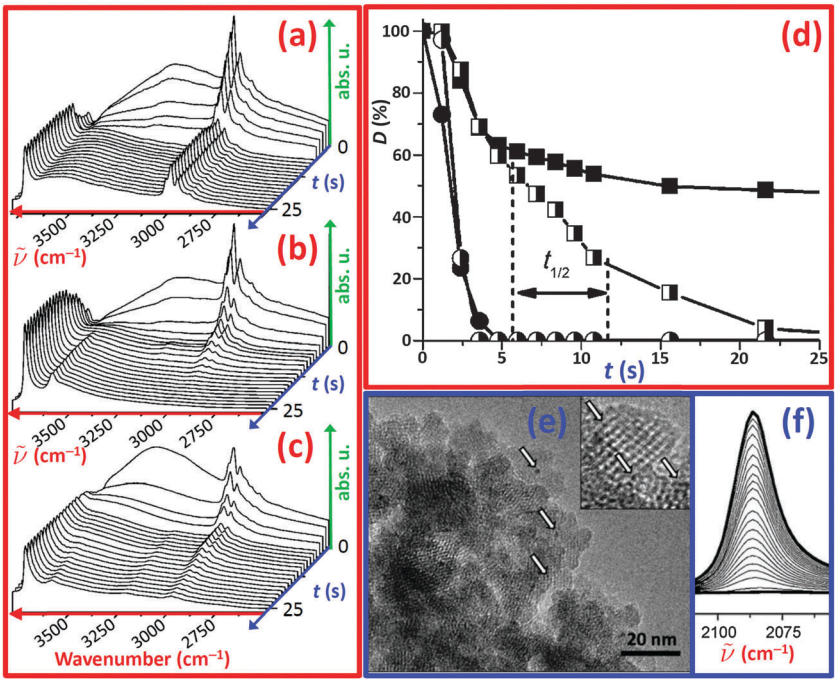

Fig. 41 Part (a): Time-resolved (0–25 s) *operando* IR spectra of template removal of Pt-β in cold Ar plasma. t = 0 s corresponds to the introduction of the plasma into the cell. Platinum was introduced into H-β as Pt^{2+} *via* ion exchange with $[Pt(NH_3)_4(NO_3)_2]$ salt (0.75 wt% Pt). Part (b): Similar to part (a) for Pt-β in cold O_2 plasma. Part (c): Similar to part (a) for parent H-β in cold O_2 plasma. Part (d): Quantification of the percentage degradation (D) of the template (squares) and desorption of residual water (circles) for Pt-β in O_2 or Ar plasma (P = 350 Pa, half and full symbols, respectively) as a function of time, measured *via* the variations in intensity of the characteristic IR bands shown in parts (a) and (b) for the template modes. Part (e): TEM image of Pt-β nanocrystals after treatment with cold O_2 plasma, as reported in part (b). The inset reports an higher magnification image. Part (f): IR spectra of C adsorbed on Pt-β nanocrystals after treatment with cold O_2 plasma. Reproduced from ref. 922 with permission, copyright Wiley-VCH, 2010.

low Raman cross-sections of molecules and solids, high-powered lasers need to be applied to produce a detectable signal. One inherent problem is therefore the risk of laser-induced damage in the sample. A critical issue, in particular in the field of heterogeneous catalysis, is that laser-induced heating may also lead to a significant temperature gradient between the integral catalyst bed and the sampling point.[41,44,932] However, in the case of *operando* Raman spectroscopy, it is very important to know the exact temperature at which the chemical transformations occur. In the cases of both laser heating and laser damage, the final goal of *operando* spectroscopy, namely, to establish some kind of structure–reactivity relationship, will be biased.[44]

For these reasons, researchers in the field of heterogeneous catalysis have attempted to design special experimental set-ups to circumvent laser-induced heating and damage while still using high-powered lasers, by reducing the contact time between the laser spot and the sample by either moving the solid catalyst or the laser beam in a continuous manner.[36–38,44] In this regard, of particular interest is the new technology for homogeneously fluidizing catalyst particles inside a microreactor and allowing Raman spectra of heterogeneous catalytic reactions to be monitored with high-powered lasers without the drawbacks of laser heating or damage, which has recently been developed at Haldor Topsøe A/S by Beato *et al.*[44]

The authors modified a commercial CCR1000 catalyst cell from Linkam Scientific Instruments (Fig. 44a). The reaction gas flows downwards from the top to the bottom of the reactor, passing through the sample, which is supported in a ceramic sample holder on a ceramic fiber filter. Fluidization is achieved *via* a microdevice placed downstream from the reactor, which provokes pressure oscillations in such a way that the flow direction is reversed in discrete pulses of about 40–100 Hz. The particles are lifted upwards by the reverse-flow pulses but the net flow direction is still downwards and thereby ensures that the particles stay in the sample holder (Fig. 44b).[44] Due to the particular design of the sample holder and the length and frequency of the pulses, the particles move homogeneously in a quasi-circular manner.

With the cell represented in Fig. 44a and b, the authors investigated the methanol-to-hydrocarbons (MTH) reaction over H-ZSM-5 (Fig. 44c and d) and H-ZSM-22 (Fig. 44e and f) catalysts using *operando* conditions. This reaction is of major relevance for the modern oil industry, because liquid hydrocarbon fuels play an essential part in the global energy chain, owing to their high energy density and ease of transportation.[81,83,88,933] Olefins play a similar role in the production of consumer goods. In a post-oil society, fuel and olefin production will rely on alternative carbon sources such as biomass, coal, natural gas, and CO_2. The MTH process is a key step in such routes and can be applied for the production of gasoline-rich (methanol-to-gasoline; MTG) or olefin-rich (methanol-to-olefins; MTO)[88] products. The major problem that is related to the MTH, MTG and MTO reactions is the slow formation of

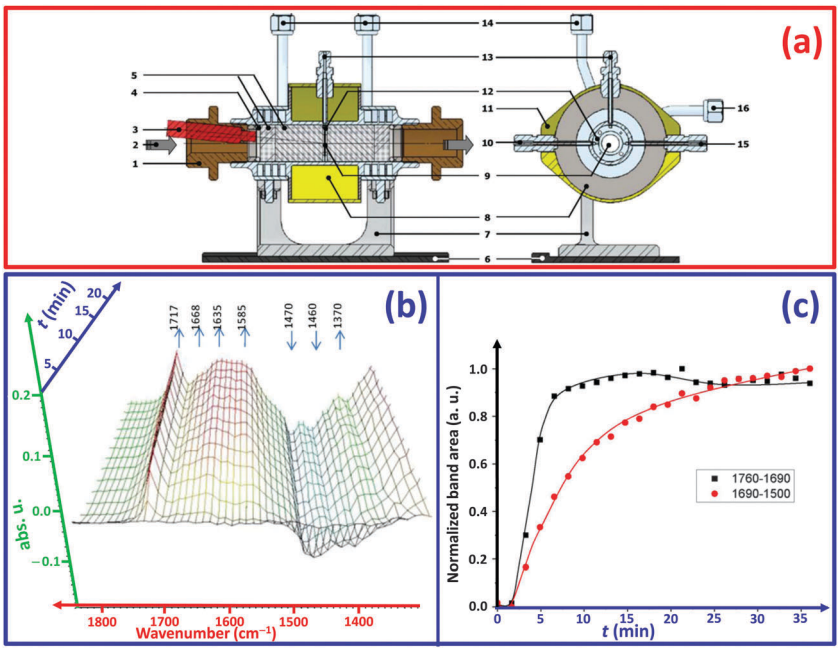

Fig. 42 Part (a): Longitudinal (left) view and radial (right) view of the reactor-IR cell modified for UV study of catalysis. (1) adjusting nut for airtightness (modified for UV guide position), (2) IR beam, (3) UV light guide, (4) Kalrez O-ring, (5) KBr windows, (6) spectrometer base plate, (7) IR cell support, (8) oven location, (9) sample (wafer), (10) gas inlet, (11) external shell, (12) wafer holder, (13) thermocouple location, (14) air cooling outlet, (15) gas outlet, (16) air cooling inlet. Part (b): Evolution of IR spectra at RT during photooxidation of methanol (1% methanol in N_2/O_2 20%/79%, vol%, 25 cm^3 min^{-1}) *vs.* time for species adsorbed on TiO_2/β during UV irradiation (result of subtraction from spectra before irradiation). Part (c): Evolution of integrated band area of CO and formate species (OCO) during UV irradiation. t = 0 min corresponds to the time when irradiation was commenced. Reproduced from ref. 43 with permission, copyright Elsevier, 2013.

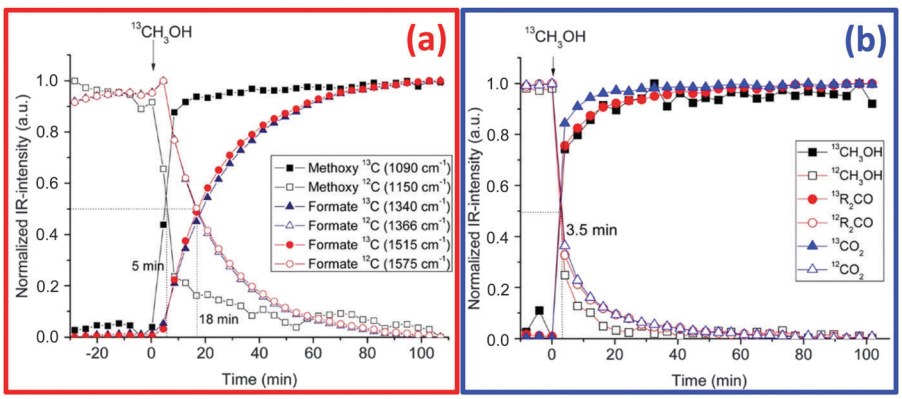

Fig. 43 Part (a): Evolution of the IR band intensities for adsorbed species on TiO_2-P25 *versus* irradiation time. t = 0 represents the isotopic exchange from $^{12}CH_3OH$ to $^{13}CH_3OH$ in the feed. Part (b): Similar to part (a) for the final products detected in the gas phase. Reproduced from ref. 929 with permission, copyright American Chemical Society, 2013.

coke that takes place inside the zeolite pores, and catalytic activity must be restored by controlled burn-off of coke. Therefore, their industrial application consists of parallel reactors, allowing for intermittent regeneration.

In the *operando* study by Beato *et al.*,[44] CH_3OH was first introduced gradually by means of three small pulses (red curves in Fig. 44c and e) and then by a prolonged dosage (blue curves in parts (d) and (f)). The reaction products were followed semi-quantitatively by online mass spectrometry (results not reported here). Finally, the methanol feed was stopped and the whole reactor was flushed by a He stream (20 ml min^{-1}) to remove weakly adsorbed species formed upon the reaction of methanol (green curves in parts (d) and (f)).

In the case of H-ZSM-5, right from the first pulse, a band at 1602 cm^{-1} starts to grow, whereas upon the second and third pulses, two more bands at 1376 and 1225 cm^{-1} start to grow (red curves in Fig. 44c). At the same time, the intensity of the bands related to the framework vibrations of H-ZSM-5 is strongly reduced. It is clear that during this phase, hydrocarbon molecules start to build up in the pores of the zeolite. The fact that the band at 1602 cm^{-1} starts to grow first could indicate that some non-cyclic olefins (*e.g.* butadienes or pentadienes, *etc.*)

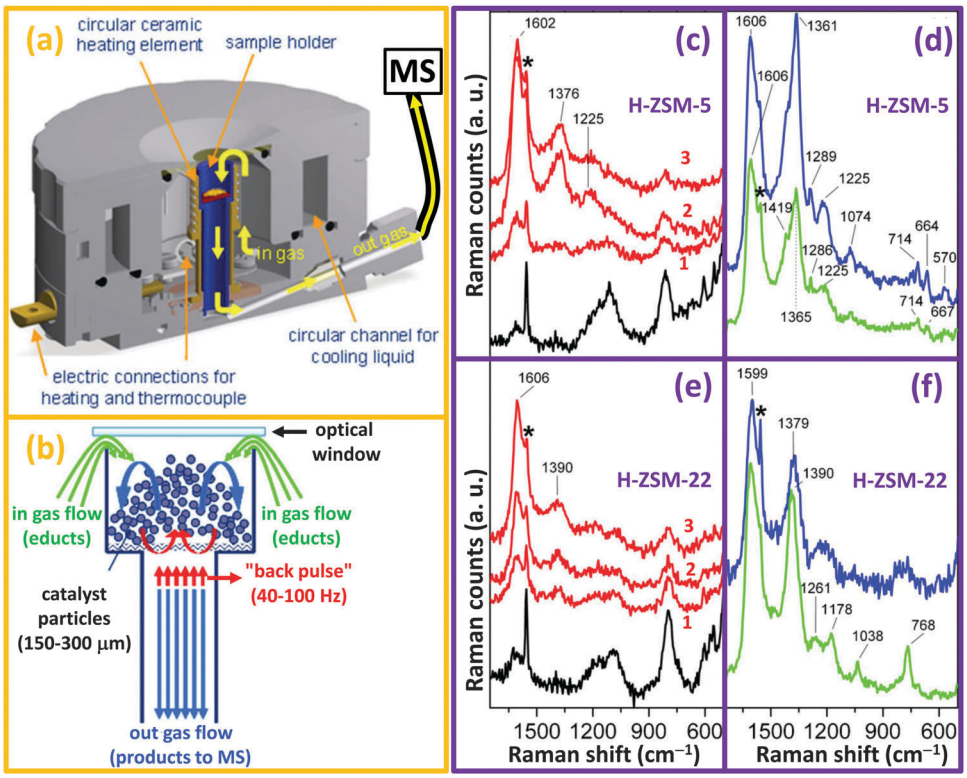

Fig. 44 Part (a): Detailed sketch of the Linkam CCR1000 reactor connected with MS for product analysis. Part (b): Schematic drawing of the sample holder with indications of the flow, using arrows to illustrate the fluidization principle. Parts (c) and (d): *Operando* Raman spectra of H-ZSM-5 zeolite during the conversion of methanol to hydrocarbons (MTH), collected using an excitation line at λ = 244 nm. Parts (e) and (f): Similar to parts (c) and (d) for H-ZSM-22 zeolite. The black spectra in parts (c) and (e) are the Raman spectra after activation in air at 550 °C. The red spectra correspond to the first, second and third successive pulses of methanol (c and e). The blue spectra in parts (d) and (f) correspond to the spectra after a long methanol pulse, whereas the green spectra correspond to subsequent flushing with He. Reproduced with permission from ref. 44, Copyright Elsevier, 2013.

are adsorbed initially and transformed subsequently into aromatic molecules *via* cyclization reactions. During the long methanol pulse (blue spectrum in Fig. 44d), a band at 1361 cm^{-1}, together with a shoulder at higher frequencies, grows significantly and becomes even stronger than the 1606 cm^{-1} band. In addition, a number of well-defined bands of lower intensity develop (1289, 1225, 1077, 714, 664 and 570 cm^{-1}). This strong increase in the band at 1361 cm^{-1}, which is characteristic of the aromatic breathing mode of benzenes, together with the characteristic bands at lower frequencies indicates that at this stage the zeolite is filled with polymethylated benzenes and naphthalenes. However, most of these species are not strongly bound to the zeolite surface and are sufficiently small to be desorbed again, which is demonstrated by flushing with He at the reaction temperature (green spectrum in Fig. 44d). The intensity of the band at 1365 cm^{-1} and the bands between 1300 and 550 cm^{-1} is halved after flushing with the inert gas. At the same time, the higher-frequency shoulder develops into a band at 1419 cm^{-1}, which indicates that this band is related to some polycondensed aromatics that are trapped in the zeolite pores.[44]

For H-ZSM-22, the picture looks generally similar but some striking differences can be observed. Again, the band at 1606 cm^{-1} starts to grow first (red curves in Fig. 44e), but during the subsequent pulses, the band at 1390 cm^{-1} does not grow to the same extent as for H-ZSM-5, which indicates a lower content of aromatic ring molecules. This assumption is confirmed during the long methanol pulse (blue curve in Fig. 44f), where the band at 1390 cm^{-1} grows, but to a much lower extent than for H-ZSM-5. The higher-frequency shoulder is absent in the case of H-ZSM-22, supporting the assumption that this band is related to larger molecules, which do not fit into the more restricted 1D structure of ZSM-22. Conversely, for H-ZSM-22, flushing with He at 420 °C (green curve in Fig. 44f) does not decrease the area of the band at 1390 cm^{-1}. Instead, the spectrum becomes better resolved and bands below 1300 cm^{-1} are clearly observed. For H-ZSM-22, the aromatics appear to be trapped in the zeolite and are not able to be desorbed but are transformed into thermodynamically more stable aromatic structures.[44]

In summary, the *operando* Raman study by Beato *et al.* was able to identify the first steps of the formation of aromatic molecules inside the zeolite channels, which will progressively evolve into coke during the catalyst life. They succeeded in highlighting the role of zeolite topology in this industrially relevant process. In fact, the ZSM-5 framework (MFI topology; see structure in Fig. 23f) exhibits a couple of interconnected 10-membered ring pores running along the [100] (5.1 Å × 5.5 Å, sinusoidal) and [010] (5.3 Å × 5.6 Å, linear) directions, whereas

the ZSM-22 framework (TON topology; see structure in Fig. 23g) has a 1-dimensional set of linear channels formed by 10-membered rings with an elliptical cross-section of 4.6 Å × 5.7 Å.[165] On these topological bases, the greater difficulty in desorbing aromatic products in H-ZSM-22 with respect to H-ZSM-5 is logical and fully in agreement with the spectroscopic study reported in Fig. 44c–f.

A further step in this direction has recently been carried out by Signorile *et al.*[65] They characterized a pool of representative polycyclic aromatic hydrocarbons by UV Raman spectroscopy. An excitation wavelength of λ = 244 nm was used to exploit the resonance effect and avoid interference due to the visible fluorescence typical of these molecules. The polycyclic aromatic hydrocarbons were analyzed in their pure form, in diluted solution, and dispersed on high-surface-area microporous supports. The collected data constitute a reference database to be compared with the deactivation products observed during petrochemical reactions, such as MTH, MTG and MTO, offering the possibility of unequivocally identifying them under Raman *operando* conditions.

9.3. Multi-technical *operando* experiments on working zeolite catalysts: combining IR and X-rays

The full investigation of complex systems, such as zeolites under working conditions, requires the combined use of different vibrational (IR and Raman), structural (XRD, PDF, SAXS, and EXAFS), electronic (UV-Vis, UPS, XPS, XANES, and XES) and magnetic (NMR and EPR) characterization techniques,[162,364,378,383,494,544,545,737,934–950] possibly supported by DFT calculations.[22,46,202,364,536,537,553,673,736,863,949,951–955]

Combining information from different experimental techniques is the only way to avoid the intrinsic limitations that each technique possesses such as (ia) the inability of XRD to analyze amorphous phases; (ib) the inability of EPR to detect diamagnetic species; (ic) the inability of NMR to detect nuclei with zero spin; (id) the inability of XRD, PDF, and SAXS to discriminate between different possible oxidation states; (ie) the inability of standard XRD, PDF, SAXS, IR, and Raman to be element-specific; (iia) the difficulty of XRD, PDF, SAXS, and EXAFS to detect elements with low Z and to discriminate between scattering centers with similar Z values; (iib) the difficulty of EXAFS to disentangle signals from different phases; and (iic) the difficulty of all the mentioned techniques, except for UPS, XPS and IR, to be surface-sensitive.

Possibly, different experiments should be performed separately because this is the way to obtain the best spectrum (or pattern) for each technique. In fact, the different techniques use photons (electrons for UPS and XPS) of which the energy differs by several orders of magnitude, and consequently exhibit completely different penetration depths, which implies that the ideal sample thickness for different experiments performed in transmission mode (*e.g.* IR, XRD, and EXAFS) can be very different. This is clearly the case for spent catalysts that are no longer air-sensitive and can be investigated under ambient pressure, temperature and gas composition conditions, where the experiment consists of a single collection of data. In such cases, the simultaneous collection of two or more sets of spectroscopic (or scattering) data will result in worse spectra (patterns) than those collected in independent single experiments.

Conversely, the situation is more complex in studies of a living catalyst, where particular temperatures and pressures or specific oxidative/reductive gas atmospheres or reactant flows are required. Indeed, ad hoc catalytic reactors that allow the simultaneous collection of spectroscopic or diffraction data may differ from technique to technique; thus, systematic errors may arise in two independent experimental set-ups operating formally under the same conditions. An analogous problem in the comparison of results that derive from separate experiments may arise when the goal of the experiment is to follow a characteristic of the sample as a function of an external parameter such as temperature, pressure, and reactant feed. Indeed, in such cases, it may be very important to guarantee that the spectra (patterns) collected by the different instruments can really be compared, *i.e.*, the external parameter that is varied during the experiment is really the same in the collection of data from different techniques. If this key point cannot be verified, misleading results may be obtained in comparison of the datasets collected by different techniques. In these cases, an approach where different datasets are collected simultaneously for the same sample in the same cell under exactly the same environmental conditions may be a winning approach, even if it will be unavoidably affected by degradation of the S/N quality of the spectra (patterns).

In such cases, important compromises must be reached. Hard X-rays, which are used for XRD, EXAFS and XANES, represent penetrating radiation, whereas IR and UV-Vis radiations do not. Optimizing the sample thickness for an X-ray experiment in transmission mode will imply that the volume probed by X-rays will be considerably larger than that probed by IR, UV-Vis or Raman spectroscopies. This limitation is, however, alleviated in the case of dispersive XAS (or when using microfocus in other XAS detection modalities), because the size of the X-ray beam in two dimensions can be tuned, as desired, in the range from 1 to 100 microns, thus sampling a volume of the same order of magnitude as IR or UV-Vis. For IR measurement, this implies that diffuse-reflectance mode (DRIFT) should be used instead of the optimal transmission mode. Such a choice is the best if the investigated process is supposed to uniformly modify the sample in all its volume (such as zeolite crystallization experiments or pressure/temperature-induced solid-state transformation). If this is not the case, such as an oxidation/reduction process that evolves from the surface through the bulk, then much thinner samples must be used with the unavoidable drawback of having XAS spectra characterized by a low edge-jump ($\Delta\mu x$) and consequently a poorer S/N ratio and limited counts of elastically scattered photons in the XRD detector.

9.3.1. O_2 activation of H-Cu-SSZ-13 catalyst: an *operando* IR/XANES and XRPD study. The relevance of Cu-exchanged zeolites in general and of SSZ-13 zeolite in particular to the selective catalytic reduction (SCR) of NO by NH_3 has already been emphasized in Section 9.1.3 and will not be repeated here.

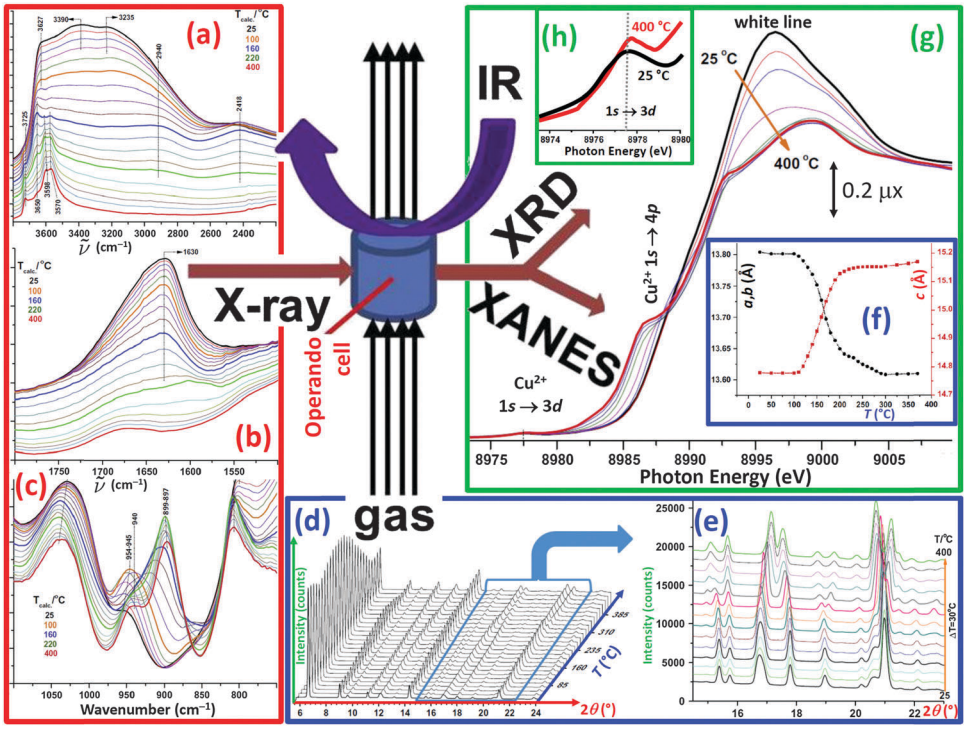

Fig. 45 O_2 activation of H-Cu-SSZ-13 catalyst in the 25–400 °C range followed by *operando* DRIFT, parts (a)–(c); XRD, parts (d)–(f) and XANES, parts (g) and (h). Heating rate: 10 °C min^{-1}; total flow rate: 10 cm^3 min^{-1}. Part (a): ν(OH) stretching region. Part (b): $\delta(H_2O)$ bending region. Part (c): Framework ν(Si–O) stretching region. Part (d): 3D view of the XRPD patterns. Part (e) Selection of XRPD patterns shown in a 2D view in the 2θ region of 15.5°–23.0°. Part (f): Evolution of the $a \equiv b$ and c lattice parameters of the CHA framework (space group $R\bar{3}m$) during thermal activation, as refined from the XRPD data shown in parts (d) and (e). Part (g): Normalized XANES spectra collected during thermal activation. Part (h): Magnification of the weak dipole-forbidden 1s → 3d transition for the first (25 °C) and last (400 °C) spectrum of the series shown in part (g). The drawing in the centre represents the experimental set-up available at the X18A beamline of the National Synchrotron Light Source at Brookhaven National Laboratory. Reproduced from ref. 436 with permission, Copyright Elsevier, 2014.

It has been shown that the state of a catalyst depends on the procedure adopted during its activation procedure,[363,436] as discussed in Section 9.1.2 and Fig. 36. Kwak *et al.* were able to follow the activation of H-Cu-SSZ-13 catalyst in the 25–400 °C interval under a 20 : 80 O_2 : He gas stream with a heating rate of 10 °C min^{-1} by simultaneously collecting DRIFT (Fig. 45a–c) and XANES (Fig. 45g and h) spectra and XRPD patterns (Fig. 45d–f). IR spectroscopy allowed them to follow the whole dehydration process, showing the decline in the broad band in the 3600–2600 cm^{-1} region, which is due to the ν(OH) stretching of confined H_2O molecules in mutual H-bonding inside the CHA framework (Fig. 45a) (see Section 2) and the parallel disappearance of the water bending mode at 1630 cm^{-1} (Fig. 45b). Also in the framework ν(T–O–T) region (Fig. 45c) where, between the broad $\nu_{sym}(TO_4)$ and $\nu_{asym}(TO_4)$ modes of the framework $[TO_4]$ units it is possible to follow the dehydration process. In this region, Cu^{2+} cations are able to perturb the $\nu_{sym}(TO_4)$ and $\nu_{asym}(TO_4)$ modes, and this perturbation depends on the hydrated form of the cation, resulting in a band around 950 cm^{-1} for the hydrated form of H-Cu-SSZ-13, which progressively moves towards 900 cm^{-1} during dehydration (Fig. 45c). The XANES data shown in Fig. 45g confirm the dehydration observed by IR (decrease in intensity and blue shift of the white-line resonance around 8995 eV) and indicate that the oxidation state of copper cations after an activation process in an O_2 flux up to 400 °C is +2. The results of Kwak *et al.*[436] (Fig. 45a, b, and g) are in full agreement with those of Borfecchia *et al.*[363] (Fig. 36), with the additional advantage that they have been collected simultaneously on the same sample in the same temperature/flux/history conditions.

Finally, the time/temperature-dependent XRPD study reported in the same study (Fig. 45d–f) allowed the authors to follow the evolution of the lattice parameters $a \equiv b$ and c during the dehydration process. Interestingly, while the unit cell parameters $a \equiv b$ decreased by about 0.2 Å as the sample was dehydrated, the unit cell parameter c increased by about 0.6 Å. The authors interpreted these variations in terms of a movement of Cu^{2+} ions from the large zeolite cages into cation positions, which allows a stronger interaction with the oxygen ions of the framework.

9.4. Photoinduced reactions monitored by the FTIR step-scan mode

Microsecond time-resolved step-scan FTIR absorption spectroscopy has been used by the group of Frei in Berkeley to obtain the IR spectrum of triplet-excited duroquinone occluded in Na-Y zeolite.[855] To the best of our knowledge, this result represented the first time-resolved IR spectrum of a transient molecule in a zeolite. Authors used ^{18}O isotopic labeling to

assign the strong absorption observed at 1542 cm^{-1} to the ν(CO) stretching mode of the excited state. The observed $\Delta\tilde{\nu}$(CO) = −100 cm^{-1} of this band, relative to the ν(CO) of the ground state, confirms the $\pi\pi^*$ character of the lowest triplet state of duroquinone, as expected due to the highly polar environment of the Na-Y zeolite cage. The lifetime of the excited triplet state was found to be 20 μs at −50 °C.[855] Subsequently, the same group used the step-scan FTIR method to monitor short-lived radicals (formyl and acetyl radicals) in zeolites[857,858,860] and Fe-AlPOs[859] molecular sieves.

Subsequently, Andersen and Frei used time-resolved FTIR spectroscopy to follow the formation of CO molecules in the channels of a mesoporous MCM-41 silica sieve generated by the photodissociation of diphenylcyclopropenone (DPCP), which was achieved with a nanosecond laser pulse,[862] according to the scheme shown in Fig. 46a. The precursor was selected based on its ultrafast dissociation time and a quantum yield close to unity.[956] They monitored the process using both step-scan (Fig. 46b and d) and rapid-scan (Fig. 46c and e) methods.

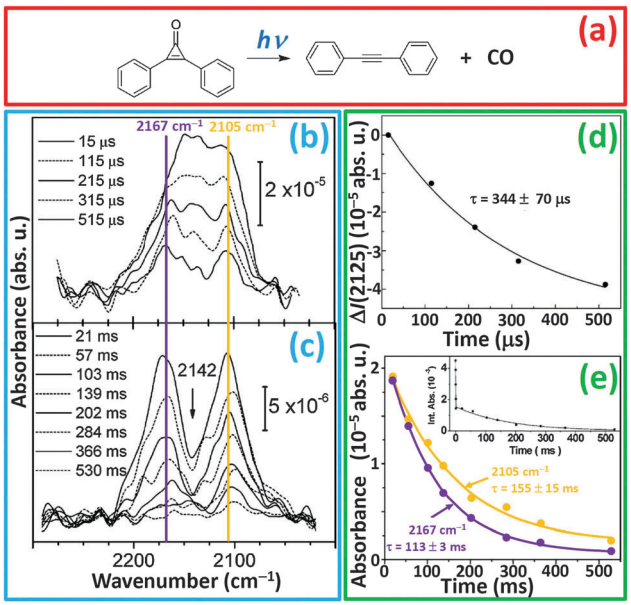

Fig. 46 Part (a): Reaction scheme representing the generation of transient CO molecules by the photodissociation of DPCP present inside the solvent-free mesopores of MCM-41 using a nanosecond UV laser pulse. Parts (b and c): Time-resolved FTIR absorption spectra of CO formed inside MCM-41 recorded upon laser-induced photolysis of DPCP, collected in step-scan mode (average of 21 experiments) and rapid-scan mode (average of 12 experiments), (parts (b) and (c), respectively). The rapid-scan spectra were normalized so that the spectra in parts (b) and (c) correspond to the same amount of DPCP used (and CO produced) per laser pulse. Note that the absorbance scale of the millisecond spectra is enlarged. Part (d): Single-exponential fit of the difference in absorbance at 2125 cm^{-1} (obtained by plotting the spectra in part (b) in difference mode), yielding a decay time of 344 ± 70 μs (once corrected by the detector response). Part (e): Single-exponential fits of the decay in absorbance at 2105 and 2167 cm^{-1} (part c), yielding decay times τ of 155 ± 15 ms and 113 ± 3 ms, respectively. The inset shows the decay of the full CO profile (integrated from 2220 to 2060 cm^{-1}) in both step-scan data and rapid-scan data. Reproduced from ref. 862 with permission, copyright American Chemical Society, 2006.

The experimental set-up relied on the generation of the species of interest (CO molecule in this case) from a photolabile precursor using a nanosecond laser pulse. The temporal resolution of the step-scan method covers a continuous range from a few ns to several ms. The slower part of the processes can be monitored by the rapid-scan FTIR method, which covers the range from 15 ms to several seconds. The wide timespan of the combined techniques is likely to encompass the time it takes for CO molecules to escape from the mesopores of MCM-41 particles. Andersen and Frei monitored the diffusion of CO generated inside the mesopores of MCM-41 at room temperature using these techniques. Transient CO was generated by the photodissociation of diphenylcyclopropenone (DPCP) present inside the solvent-free mesopores of MCM-41 using a nanosecond UV laser pulse.

The time-resolved spectra showed a very broad absorption of CO in the 2200–2080 cm^{-1} region, which decayed in a biphasic mode (Fig. 46b and c). Two-thirds of the band intensity decayed on the hundreds of μs scale with a lifetime of τ = 344 ± 70 μs. The decrease is due to the escape of CO molecules through the mesopores into the surrounding gas phase and a diffusion constant of 1.5 × 10^{-9} m^2 s^{-1} was derived (assuming control by diffusion inside MCM-41 particles). The broad profile of the absorption is attributed to contact of randomly moving CO with siloxane and silanol groups of the pore surface. Measurements using MCM-41 with the silanols partially capped by trimethylsilyl groups (data not reported in this review, see the original study[862]) gave further insight into the nature of the IR band profile. The residual carbon monoxide remained much longer in the pores and exhibited distinct peaks at 2167 and 2105 cm^{-1} that were characteristic of CO adsorbed on SiOH groups C-end-on and O-end-on, respectively (see the discussion of linkage isomerism of simple molecules in Sections 3.1.1 and 7.2.3). The bands decreased with time constants of 113 ± 3 ms (2167 cm^{-1}) and 155 ± 15 ms (2105 cm^{-1}), which suggests that CO in these sites is additionally trapped by surrounding diphenylacetylene co-product and/or precursor molecules.[862]

Andersen and Frei[862] concluded their study by underlining the relevance of their findings for a mechanistic understanding of the photoreduction of CO_2 in nanoporous transition metal-silica hosts like Ti-MCM-41.[957] The finding that CO escapes from the mesopores at room temperature in less than a millisecond shows that the nanoporous silica environment of MCM-41 will not limit photocatalytic turnover rates and is favorable in terms of preventing back reactions.[958]

9.5. 2D IR pressure-jump spectroscopy of adsorbed species in zeolites followed by the step-scan mode

As discussed above, step-scan Fourier-transform interferometers can easily reach the μs timescale if the observation can be repeated with sufficient reproducibility. On this timescale, each type of adsorbed molecule in a zeolite has its own eigen-response frequency to a pressure perturbation or modulation. Using pressure and temperature measurements, Grenier *et al.*[959] and Rees *et al.*[960–962] investigated pressure modulation frequencies, indicated these frequencies for given adsorbates

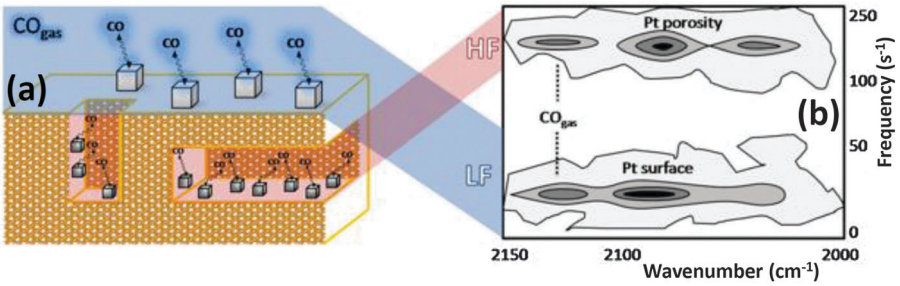

Fig. 47 Part (a): Cartoon showing CO molecules adsorbed on Pt nanoparticles located both inside the wet-impregnated ZSM-5 channels and on the zeolite external surface. Part (b): 2D-PJAS-IR maps (at 573 K) of CO adsorbed on WI Pt/ZSM-5. Ion-exchanged ZSM-5 at LF and colloidally impregnated ZSM-5 at HF do not give rise to any signal (HF = high frequency; LF = low frequency). Adapted from ref. 964 with permission, copyright Wiley VCH, 2010.

on given zeolites, and obtained diffusion kinetics parameters from their results. Chenevarin and Thibault-Starzyk[963] showed that it is possible to use these frequencies to obtain IR spectral information for complex mixtures on surfaces. Thus, several adsorption sites or several adsorbed molecules in a mixture would lead to a specific eigen-response frequency to a pressure modulation, which will result in the spectral signature for each individual species on each individual adsorption site. This technique is named two-dimensional pressure-jump IR spectroscopy of adsorbed species (2D-PJAS-IR).[861,963]

2D-PJAS-IR is based on millisecond time-resolved spectroscopy and sudden pressure changes in the IR cell that contains the solid sample and the gas probe molecule. The pressure jump leads to a relaxation process by diffusion and adsorption, which is monitored by IR spectroscopy. The 2D spectrum is obtained by two Fourier transforms in the IR wavelength and time domains. The potential of the technique was shown by studying the adsorption of a probe molecule (acetonitrile) on mordenite. 2D-PJAS-IR allowed the first direct detection of three distinct OH vibration bands in the IR spectrum of mordenite and revealed three different interactions with acetonitrile, which depend on the adsorption site.[963] Protonation of acetonitrile at high temperatures was shown to take place only in the side pockets. In summary, they used the high time resolution of the technique to obtain dynamic adsorption parameters on the μs timescale. These dynamic properties were used to distinguish the various adsorption sites of the acetonitrile probe in mordenite. In ref. 861, they analyzed the collected spectra in the context of two-dimensional correlation spectroscopy (2D-COS).[408–417]

Subsequently, the 2D-PJAS-IR technique was applied by Rivallan *et al.*[964] to the adsorption of CO on Pt-ZSM-5 catalyst. Three different methods were used for dispersing Pt in ZSM-5: (i) wet impregnation, which resulted in two classes of Pt nanoparticles that differed in size hosted in the zeolite channels (smaller class) and mesopores and external surfaces (larger class >2.5 nm); colloidal impregnation, which did not lead to Pt nanoparticles inside the channels owing to the very large size of the colloid and (ii) ion exchange, which produced long, thin and cylindrical Pt particles shaped by the zeolite channels.

Moreover, in this case, the technique was capable of discriminating the adsorption sites (Pt nanoparticles located inside the ZSM-5 channels and on its external surface, see the cartoon shown in Fig. 47a) by Fourier analysis of the evolution of the IR spectrum after a sudden change in the pressure of CO. In the corresponding 2D maps (Fig. 47b), two different frequency regions appeared for the IR bands of both CO gas (2140–2120 cm^{-1}) and adsorbed CO on Pt nanoparticles (2100–2000 cm^{-1}). One resonance is at a high frequency (HF) of 130 Hz or 250 Hz, depending on the Si/Al ratio and textural properties, and the second one is at a low frequency (LF; below 50 Hz). The ion-exchanged sample, which contains only platinum in the channels, exhibited essentially one single response at 130 Hz, which was higher than that on a colloidally impregnated sample (<50 Hz). This latter frequency was attributed to a CO adsorption–desorption oscillation process occurring on the external surface. The difference in frequency observed between the two resonances can be explained in terms of the mean free path, which is shorter in the channels than on the outer surface. The wet-impregnated sample gives rise to oscillations at HF and LF (Fig. 47b), which confirms the presence of Pt particles both in the mesopores and on the external surface. In the same study, two different sintering mechanisms of Pt nanoparticles were observed in the mesopores and on the external surface of the ZSM-5 support.[964]

10. Conclusions and perspectives

IR spectroscopy has been a major tool for characterising zeolites since the 1950s and several major authors have summarized the achievements of this technique in their time.[1–34] Some very important aspects of zeolite science have made considerable progress during the last ten years: knowledge of the structure of the Brønsted acid site, its interaction with Lewis sites, new preparation methods with increased accessibility—all these investigations needed a careful look back and a rational presentation (Sections 2 and 3). At the same time, new experimental approaches have appeared and new information can now be provided by spectrometers evolving at a very rapid pace.

We first presented here a review of more than 30 years of the study of acidity in zeolites. It appears that a coherent and comprehensive understanding of acidity in zeolites is now

possible. Even the frontiers of superacidity (Section 2.3) are better understood and scales of acid strength have been established, which cover the whole range of our materials. This is not, however, a simple topic and the accessibility of the acid site to reactants, adsorbates and probe molecules leads to significant perturbations in measurements. These perturbations are now well understood and described. IR has shown itself as a reliable tool for a quantitative description of such parameters.

Our understanding of zeolite basicity has also progressed significantly (Section 4). New probe molecules have appeared, and modelling has confirmed the proposed relationships between probe molecules and the solid.

In the last decade, hierarchical pore systems progressively became one of the most important methods for increasing the applicability of zeolites in oil refining and dealing with heavier products. Mesopores are very efficient for optimising transport in a catalyst. Infrared has established itself quickly as a major characterization tool for describing improved accessibility (Section 5). Adjusting the size of the probe molecule is now standard for the infrared spectroscopist who is given a new sample to describe. The accessibility index, applied with many different probe molecules, has provided a scale for comparing different solids and different methods for improving diffusion limitations. The location of the various sites in zeolites can now be determined: silanols, Brønsted sites, Lewis sites or metals. New experimental tools, such as time-resolved perturbations (Section 9) or microscopy (Section 8), have been employed successfully and they have given new insights on these questions.

It is probably in quantitative measurements that the most important advances were made. High-precision gravimetry can be combined with *in situ* spectroscopy and the question of the quantitative aspect of infrared spectroscopy (Section 6) can be finally solved. The amount of adsorbed species or OH groups on the surface can be determined with great accuracy. This approach has started to provide reliable molar absorption coefficient values for some common probes, and in the near future, will give every experimentalist the tools to always obtain reliable quantitative measurements for all adsorbed species (tables of ε values and clear experimental guidelines). The determination of thermodynamic values is also a quantitative measurement that has became standard in recent years. Adsorption enthalpies can now be measured and adsorption modes can be described in great depth. New data treatment methods can extract a great deal of information and identify individual adsorption states and their corresponding spectrum and energy (Section 7).

Vibrational spectroscopy has long been limited in space and time resolution. New methods in Raman spectroscopy increased its sensitivity enough to use it in microscopy (Section 8.3), and spectroscopic mapping of catalyst crystals can be performed at 0.5 μm (Section 8.2). Infrared has now established itself as one of the fastest characterisation methods (Section 9), potentially reaching nanosecond timescales. Very short-lived intermediates can be identified and the dynamics of adsorption can be investigated. This is of course only part of the now highly important *operando* spectroscopy (Section 9.2). *Operando* spectroscopy is the study of working catalysts, the system being under real reaction conditions. *Operando* obviously means time-resolved, but most often on the scale of the second. This is far enough to describe most reaction mechanisms and for the identification of the intermediates, sometimes using kinetic tools such as isotopic transient methods for determining the kinetic parameters of the reaction. Vibrational spectroscopy is the ideal tool for *operando* studies; it is easy, fast and versatile. It has been applied to most catalytic applications, even in the field of photochemistry or plasma-assisted catalysis.

All these new tools are only just leaving the characterisation laboratory. They still need to be spread and widely used by application scientists. This will lead to new advances in zeolite science and we can hope for further progress with these spectroscopic methods.

After this global tour, it is clear that the field is still progressing quickly. The new tools obtained in recent years will be applied for many other problems and some unexpected applications will be possible. Tunable lasers will change the way we perform spectroscopy. Stimulated Raman scattering has been used for microscopy but it will also be applied to the ''simple'' Raman characterisation of zeolite samples, which was until now limited by fluorescence and low sensitivity. Tunable lasers will also be used to perform Raman-enhanced experiments (Section 3.3.2) and replace Fourier-transform spectroscopy, and their availability in the mid-infrared will lead to completely new infrared spectrometers with unexpected time resolution and ease of use. This will surely change the whole domain of vibrational spectroscopy of zeolites in the next ten years.

Abbreviations

2D-COS	Two-dimensional correlation spectroscopy
2D-PJASIR	Two-dimensional pressure-jump IR spectroscopy of adsorbed species
abs.u.	Absorbance units
a.u.	Arbitrary units
ACI	Accessibility index
AFM	Atomic force microscopy
AGIR	Analysis by combined gravimetry and IR
ATR	Attenuated total reflectance (spectroscopy)
BHW	Bellamy–Hallam–Williams (plot or relation)
CARS	Coherent anti-Stokes Raman scattering
Coll	2,4,6-Trimethylpyridine (collidine)
Cp_2Cr	Chromocene
CT	Charge transfer
DFT	Density functional theory
DPCP	Diphenylcyclopropenone
DRIFT	Diffuse-reflectance infrared Fourier transform
DRS	Diffuse reflectance spectroscopy
DTBPy	Di-*tert*-butylpyridine
EELS	Electron energy loss spectroscopy

EPR	Electron paramagnetic resonance
ESRF	European synchrotron radiation facility (Grenoble, France)
EXAFS	Extended X-ray absorption fine structure
FT	Fourier transform
FTIR	Fourier transform infrared
FWHM	Full width at half maximum
GC	Gas chromatography
HF	High frequency (band in FAU and MOR frameworks)
H-USY	Protonic form of USY zeolite
I	Intensity (of an IR band)
INS	Inelastic neutron scattering
IR	Infrared
LF	Low frequency (band in FAU and MOR frameworks)
LMCT	Ligand-to-metal charge transfer
LP-MOR	Large-port mordenite
Lu	2,6-Dimethylpyridine (lutidine)
mari	Most abundant reactive intermediate
MBOH	Methylbutynol
MC	Main channel (in MOR framework)
MS	Mass spectrometer (spectrometry)
MTG	Methanol-to-gasoline
MTH	Methanol-to-hydrocarbons
MTO	Methanol-to-olefins
NIR	Near-IR
NMR	Nuclear magnetic resonance
NSLS	National synchrotron light source (Brookhaven National Laboratory, NY, USA)
ONIUM	Our own N-layered integrated molecular orbital and molecular mechanics
PA	Proton affinity
P_{CO}	CO equilibrium pressures
PDF	Pair distribution function analysis
PhCN	Benzonitrile
P_{NO}	NO equilibrium pressures
PS	Polystyrene
Py	Pyridine
RT	Room temperature
SCR	Selective catalytic reduction
SERS	Surface-enhanced Raman spectroscopy
S/N	Signal-to-noise ratio
SP	Side pocket (in MOR framework)
SP-MOR	Small-port mordenite
SRS	Stimulated Raman scattering
SSITKA	Steady-state isotope transient kinetic analysis
TERS	Tip-enhanced Raman spectroscopy
THF	Tetrahydrofuran
TMB	1,3,5-Trimethylbenzene
TPD	Temperature-programmed desorption
TS-1	Titanosilicate with MFI topology
UC	Unit cell
UPS	Ultraviolet photoelectron spectroscopy
USY	Ultrastable Y zeolites (dealuminated form)
UV-Vis	Ultraviolet-Visible
VTIR	Variable-temperature IR
XANES	X-ray absorption near-edge structure
XAS	X-ray absorption spectroscopy
XES	X-ray emission spectroscopy
XPS	X-ray photoelectron spectroscopy
XRD	X-ray diffraction
XRPD	X-ray powder diffraction

Acknowledgements

We thank Dr. Jean-Claude Lavalley, Dr. Jacques Saussey and Prof. Adriano Zecchina for their inspirational guidance in the field of *in situ* and *operando* IR spectroscopy of zeolites. The figure of the TOC has been kindly created by Dr Elisa Borfecchia (University of Turin). C.L. acknowledges the Mega-grant of the Russian Federation Government to support scientific research at Southern Federal University, No. 14.Y26.31.0001.

References

1 A. Janin, J. C. Lavalley, A. Macedo and F. Raatz, *Zeolites*, 1988, **368**, 117.
2 G. A. Ozin and S. Ozkar, *Chem. Mater.*, 1992, **4**, 511.
3 A. Zecchina and C. O. Arean, *Catal. Rev.: Sci. Eng.*, 1993, **35**, 261.
4 J. C. Lavalley, *Catal. Today*, 1996, **27**, 377.
5 J. A. Lercher, C. Grundling and G. EderMirth, *Catal. Today*, 1996, **27**, 353.
6 A. Zecchina and C. O. Arean, *Chem. Soc. Rev.*, 1996, **25**, 187.
7 P. P. KnopsGerrits, D. E. DeVos, E. J. P. Feijen and P. A. Jacobs, *Microporous Mater.*, 1997, **8**, 3.
8 L. M. Kustov, *Top. Catal.*, 1997, **4**, 131.
9 H. Knözinger and S. Huber, *J. Chem. Soc., Faraday Trans.*, 1998, **94**, 2047.
10 K. I. Hadjiivanov, *Catal. Rev.: Sci. Eng.*, 2000, **42**, 71.
11 C. O. Arean, *Comments Inorg. Chem.*, 2000, **22**, 241.
12 P. C. Stair, *Curr. Opin. Solid State Mater. Sci.*, 2001, **5**, 365.
13 M. Hunger and J. Weitkamp, *Angew. Chem., Int. Ed.*, 2001, **40**, 2954.
14 J. Ryczkowski, *Catal. Today*, 2001, **68**, 263.
15 K. I. Hadjiivanov and G. N. Vayssilov, *Adv. Catal.*, 2002, **47**, 307.
16 J. Guzman and B. C. Gates, *Dalton Trans.*, 2003, 3303.
17 E. Garrone and C. Otero Arean, *Chem. Soc. Rev.*, 2005, **34**, 846.
18 A. Zecchina, G. Spoto and S. Bordiga, *Phys. Chem. Chem. Phys.*, 2005, **7**, 1627.
19 J. C. Fierro-Gonzalez, S. Kuba, Y. L. Hao and B. C. Gates, *J. Phys. Chem. B*, 2006, **110**, 13326.
20 P. C. Stair, *Adv. Catal.*, 2007, **51**, 75.
21 A. Zecchina, M. Rivallan, G. Berlier, C. Lamberti and G. Ricchiardi, *Phys. Chem. Chem. Phys.*, 2007, **9**, 3483.
22 S. Bordiga, F. Bonino, A. Damin and C. Lamberti, *Phys. Chem. Chem. Phys.*, 2007, **9**, 4854.
23 C. Lamberti, E. Groppo, G. Spoto, S. Bordiga and A. Zecchina, *Adv. Catal.*, 2007, **51**, 1.

24 B. M. Weckhuysen, *Angew. Chem., Int. Ed.*, 2009, **48**, 4910.
25 A. Aerts, C. E. A. Kirschhock and J. A. Martens, *Chem. Soc. Rev.*, 2010, **39**, 4626.
26 E. Stavitski and B. M. Weckhuysen, *Chem. Soc. Rev.*, 2010, **39**, 4615.
27 I. E. Wachs and C. A. Roberts, *Chem. Soc. Rev.*, 2010, **39**, 5002.
28 A. Vimont, F. Thibault-Starzyk and M. Daturi, *Chem. Soc. Rev.*, 2010, **39**, 4928.
29 C. Lamberti, E. Groppo, A. Zecchina and S. Bordiga, *Chem. Soc. Rev.*, 2010, **39**, 4951.
30 F. T. Fan, Z. C. Feng and C. Li, *Chem. Soc. Rev.*, 2010, **39**, 4794.
31 F. T. Fan, Z. C. Feng and C. Li, *Acc. Chem. Res.*, 2010, **43**, 378.
32 E. G. Derouane, J. C. Vedrine, R. R. Pinto, P. M. Borges, L. Costa, M. Lemos, F. Lemos and F. R. Ribeiro, *Catal. Rev.: Sci. Eng.*, 2013, **55**, 454.
33 P. Serna and B. C. Gates, *Acc. Chem. Res.*, 2014, **47**, 2612.
34 F. Zaera, *Chem. Soc. Rev.*, 2014, **43**, 7624.
35 M. A. Banares, *Catal. Today*, 2005, **100**, 71.
36 W. Kiefer and H. J. Bernstein, *Appl. Spectrosc.*, 1971, **25**, 609.
37 A. Muller and T. Weber, *Appl. Catal.*, 1991, **77**, 243.
38 Y. T. Chua and P. C. Stair, *J. Catal.*, 2000, **196**, 66.
39 G. Spoto, E. N. Gribov, G. Ricchiardi, A. Damin, D. Scarano, S. Bordiga, C. Lamberti and A. Zecchina, *Prog. Surf. Sci.*, 2004, **76**, 71.
40 E. Stavitski, M. H. F. Kox, I. Swart, F. M. F. de Groot and B. M. Weckhuysen, *Angew. Chem., Int. Ed.*, 2008, **47**, 3543.
41 F. C. Meunier, *Chem. Soc. Rev.*, 2010, **39**, 4602.
42 P. Bazin, A. Alenda and F. Thibault-Starzyk, *Dalton Trans.*, 2010, **39**, 8432.
43 M. El-Roz, P. Bazin and F. Thibault-Starzyk, *Catal. Today*, 2013, **205**, 111.
44 P. Beato, E. Schachtl, K. Barbera, F. Bonino and S. Bordiga, *Catal. Today*, 2013, **205**, 128.
45 C. Li, G. Xiong, Q. Xin, J. Liu, P. Ying, Z. Feng, J. Li, W. Yang, Y. Wang, G. Wang, X. Liu, M. Lin, X. Wang and E. Min, *Angew. Chem., Int. Ed.*, 1999, **38**, 2220.
46 G. Ricchiardi, A. Damin, S. Bordiga, C. Lamberti, G. Spanò, F. Rivetti and A. Zecchina, *J. Am. Chem. Soc.*, 2001, **123**, 11409.
47 S. Bordiga, A. Damin, F. Bonino, G. Ricchiardi, C. Lamberti and A. Zecchina, *Angew. Chem., Int. Ed.*, 2002, **41**, 4734.
48 S. Bordiga, A. Damin, F. Bonino, G. Ricchiardi, A. Zecchina, R. Tagliapietra and C. Lamberti, *Phys. Chem. Chem. Phys.*, 2003, **5**, 4390.
49 H. Kim, K. M. Kosuda, R. P. Van Duyne and P. C. Stair, *Chem. Soc. Rev.*, 2010, **39**, 4820.
50 P. K. Dutta and D. Robins, *Langmuir*, 1991, **7**, 2004.
51 W. F. Yan, L. L. Bao, S. M. Mahurin and S. Dai, *Appl. Spectrosc.*, 2004, **58**, 18.
52 N. Liu, M. Z. Gong, P. Zhang, L. X. Li, W. B. Li and R. Lee, *J. Mater. Sci.*, 2011, **46**, 3162.
53 M. Severance and P. K. Dutta, *J. Phys. Chem. C*, 2014, **118**, 28580.
54 M. Fleischmann, P. J. Hendra and A. J. McQuillan, *Chem. Phys. Lett.*, 1974, **26**, 163.
55 J. A. Dieringer, A. D. McFarland, N. C. Shah, D. A. Stuart, A. V. Whitney, C. R. Yonzon, M. A. Young, X. Y. Zhang and R. P. Van Duyne, *Faraday Discuss.*, 2006, **132**, 9.
56 S. M. Nie and S. R. Emery, *Science*, 1997, **275**, 1102.
57 C. W. Freudiger, W. Min, B. G. Saar, S. Lu, G. R. Holtom, C. W. He, J. C. Tsai, J. X. Kang and X. S. Xie, *Science*, 2008, **322**, 1857.
58 P. Nandakumar, A. Kovalev and A. Volkmer, *New J. Phys.*, 2009, **11**, 9.
59 W. Min, C. W. Freudiger, S. J. Lu and X. S. Xie, *Annu. Rev. Phys. Chem.*, 2011, **62**, 507.
60 Y. Ozeki, F. Dake, S. Kajiyama, K. Fukui and K. Itoh, *Opt. Express*, 2009, **17**, 3651.
61 D. Fu, F. K. Lu, X. Zhang, C. Freudiger, D. R. Pernik, G. Holtom and X. S. Xie, *J. Am. Chem. Soc.*, 2012, **134**, 3623.
62 C. W. Freudiger, W. L. Yang, G. R. Holtom, N. Peyghambarian, X. S. Xie and K. Q. Kieu, *Nat. Photonics*, 2014, **8**, 153.
63 B. Pettinger, B. Ren, G. Picardi, R. Schuster and G. Ertl, *Phys. Rev. Lett.*, 2004, **92**, 4.
64 J. F. Li, Y. F. Huang, Y. Ding, Z. L. Yang, S. B. Li, X. S. Zhou, F. R. Fan, W. Zhang, Z. Y. Zhou, D. Y. Wu, B. Ren, Z. L. Wang and Z. Q. Tian, *Nature*, 2010, **464**, 392.
65 M. Signorile, F. Bonino, A. Damin and S. Bordiga, *J. Phys. Chem. C*, 2015, **119**, 11694.
66 V. Van Speybroeck, K. Hemelsoet, L. Joos, M. Waroquier, R. G. Bell and C. R. A. Catlow, *Chem. Soc. Rev.*, 2015, DOI: 10.1039/C5CS00029G.
67 W. Holderich, M. Hesse and F. Naumann, *Angew. Chem., Int. Ed. Engl.*, 1988, **27**, 226.
68 A. Corma, *Chem. Rev.*, 1995, **95**, 559.
69 A. Corma and A. Martinez, *Adv. Mater.*, 1995, **7**, 137.
70 A. Corma, V. Fornes, J. B. Monton and A. V. Orchilles, *J. Catal.*, 1987, **107**, 288.
71 S. M. Babitz, B. A. Williams, J. T. Miller, R. Q. Snurr, W. O. Haag and H. H. Kung, *Appl. Catal., A*, 1999, **179**, 71.
72 B. A. Williams, S. M. Babitz, J. T. Miller, R. Q. Snurr and H. H. Kung, *Appl. Catal., A*, 1999, **177**, 161.
73 N. Rahimi and R. Karimzadeh, *Appl. Catal., A*, 2011, **398**, 1.
74 G. Bellussi, G. Pazzuconi, C. Perego, G. Girotti and G. Terzoni, *J. Catal.*, 1995, **157**, 227.
75 T. Matsuda, T. Urata and E. Kikuchi, *Appl. Catal., A*, 1995, **123**, 205.
76 P. G. Smirniotis and E. Ruckenstein, *Ind. Eng. Chem. Res.*, 1995, **34**, 1517.
77 S. Gopal and P. G. Smirniotis, *J. Catal.*, 2004, **225**, 278.
78 J. F. Denayer, G. V. Baron, G. Vanbutsele, P. A. Jacobs and J. A. Martens, *J. Catal.*, 2000, **190**, 469.
79 C. Woltz, A. Jentys and J. A. Lercher, *J. Catal.*, 2006, **237**, 337.
80 A. Martins, J. M. Silva and M. F. Ribeiro, *Appl. Catal., A*, 2013, **466**, 293.
81 M. Stocker, *Microporous Mesoporous Mater.*, 1999, **29**, 3.
82 M. Bjorgen, U. Olsbye and S. Kolboe, *J. Catal.*, 2003, **215**, 30.

83 J. F. Haw, W. G. Song, D. M. Marcus and J. B. Nicholas, *Acc. Chem. Res.*, 2003, **36**, 317.
84 M. Bjorgen, U. Olsbye, D. Petersen and S. Kolboe, *J. Catal.*, 2004, **221**, 1.
85 U. Olsbye, M. Bjorgen, S. Svelle, K. P. Lillerud and S. Kolboe, *Catal. Today*, 2005, **106**, 108.
86 M. Bjorgen, S. Svelle, F. Joensen, J. Nerlov, S. Kolboe, F. Bonino, L. Palumbo, S. Bordiga and U. Olsbye, *J. Catal.*, 2007, **249**, 195.
87 F. Bleken, W. Skistad, K. Barbera, M. Kustova, S. Bordiga, P. Beato, K. P. Lillerud, S. Svelle and U. Olsbye, *Phys. Chem. Chem. Phys.*, 2011, **13**, 2539.
88 U. Olsbye, S. Svelle, M. Bjorgen, P. Beato, T. V. W. Janssens, F. Joensen, S. Bordiga and K. P. Lillerud, *Angew. Chem., Int. Ed.*, 2012, **51**, 5810.
89 F. L. Bleken, K. Barbera, F. Bonino, U. Olsbye, K. P. Lillerud, S. Bordiga, P. Beato, T. V. W. Janssens and S. Svelle, *J. Catal.*, 2013, **307**, 62.
90 F. Schmidt, C. Hoffmann, F. Giordanino, S. Bordiga, P. Simon, W. Carrillo-Cabrera and S. Kaskel, *J. Catal.*, 2013, **307**, 238.
91 M. Milina, S. Mitchell, P. Crivelli, D. Cooke and J. Perez-Ramirez, *Nat. Commun.*, 2014, **5**, 10.
92 J. F. Haw, J. B. Nicholas, W. G. Song, F. Deng, Z. K. Wang, T. Xu and C. S. Heneghan, *J. Am. Chem. Soc.*, 2000, **122**, 4763.
93 W. G. Song, H. Fu and J. F. Haw, *J. Am. Chem. Soc.*, 2001, **123**, 4749.
94 W. Wang and M. Hunger, *Acc. Chem. Res.*, 2008, **41**, 895.
95 F. Bleken, M. Bjorgen, L. Palumbo, S. Bordiga, S. Svelle, K. P. Lillerud and U. Olsbye, *Top. Catal.*, 2009, **52**, 218.
96 B. P. C. Hereijgers, F. Bleken, M. H. Nilsen, S. Svelle, K. P. Lillerud, M. Bjorgen, B. M. Weckhuysen and U. Olsbye, *J. Catal.*, 2009, **264**, 77.
97 S. Lopez-Orozco, A. Inayat, A. Schwab, T. Selvam and W. Schwieger, *Adv. Mater.*, 2011, **23**, 2602.
98 M. Bjorgen, F. Joensen, M. S. Holm, U. Olsbye, K. P. Lillerud and S. Svelle, *Appl. Catal., A*, 2008, **345**, 43.
99 M. S. Holm, S. Svelle, F. Joensen, P. Beato, C. H. Christensen, S. Bordiga and M. Bjorgen, *Appl. Catal., A*, 2009, **356**, 23.
100 G. J. Hutchings, P. Johnston, D. F. Lee, A. Warwick, C. D. Williams and M. Wilkinson, *J. Catal.*, 1994, **147**, 177.
101 G. J. Kramer, R. A. van Santen, C. A. Emeis and A. K. Nowak, *Nature*, 1993, **363**, 529.
102 A. G. Pelmenschikov and R. A. Vansanten, *J. Phys. Chem.*, 1993, **97**, 10678.
103 U. Fleischer, W. Kutzelnigg, A. Bleiber and J. Sauer, *J. Am. Chem. Soc.*, 1993, **115**, 7833.
104 J. Sauer, *Stud. Surf. Sci. Catal.*, 1994, **84**, 2039.
105 S. Scheiner, *Hydrogen Bonding, A Theoretical Perspective*, Oxford University Press, New York, Oxford, 1997.
106 R. A. van Santen, *Catal. Today*, 1997, **38**, 377.
107 T. Xu, N. Kob, R. S. Drago, J. B. Nicholas and J. F. Haw, *J. Am. Chem. Soc.*, 1997, **119**, 12231.
108 U. Eichler, M. Brandle and J. Sauer, *J. Phys. Chem. B*, 1997, **101**, 10035.
109 R. Duchateau, R. J. Harmsen, H. C. L. Abbenhuis, R. A. van Santen, A. Meetsma, S. K. H. Thiele and M. Kranenburg, *Chem. – Eur. J.*, 1999, **5**, 3130.
110 J. F. Haw, J. H. Zhang, K. Shimizu, T. N. Venkatraman, D. P. Luigi, W. G. Song, D. H. Barich and J. B. Nicholas, *J. Am. Chem. Soc.*, 2000, **122**, 12561.
111 A. Simperler, R. G. Bell and M. W. Anderson, *J. Phys. Chem. B*, 2004, **108**, 7142.
112 A. Simperler, R. G. Bell, M. D. Foster, A. E. Gray, D. W. Lewis and M. W. Anderson, *J. Phys. Chem. B*, 2004, **108**, 7152.
113 S. H. Li, A. M. Zheng, Y. C. Su, H. L. Zhang, L. Chen, J. Yang, C. H. Ye and F. Deng, *J. Am. Chem. Soc.*, 2007, **129**, 11161.
114 W. F. Kladnig, *J. Phys. Chem.*, 1979, **83**, 765.
115 A. K. Ghosh and G. Curthoys, *J. Chem. Soc., Faraday Trans.*, 1983, **1**, 79–147.
116 M. W. Anderson and J. Klinowski, *Zeolites*, 1986, **6**, 150.
117 D. Freude, M. Hunger, H. Pfeifer and W. Schwieger, *Chem. Phys. Lett.*, 1986, **128**, 62.
118 D. J. Parrillo and R. J. Gorte, *J. Phys. Chem.*, 1993, **97**, 8786.
119 D. J. Parrillo, R. J. Gorte and W. E. Farneth, *J. Am. Chem. Soc.*, 1993, **115**, 12441.
120 H. Sato, *Catal. Rev.: Sci. Eng.*, 1997, **39**, 395.
121 C. Jia, P. Massiani and D. Barthomeuf, *J. Chem. Soc., Faraday Trans.*, 1993, **89**, 3659.
122 J. F. Haw, M. B. Hall, A. E. Alvarado-Swaisgood, E. J. Munson, Z. Lin, L. W. Beck and T. Howard, *J. Am. Chem. Soc.*, 1994, **116**, 7308.
123 W. E. Farneth and R. J. Gorte, *Chem. Rev.*, 1995, **95**, 615.
124 M. Hunger, *Solid State Nucl. Magn. Reson.*, 1996, **6**, 1.
125 M. Hunger, U. Schenk, M. Breuninger, R. Glaser and J. Weitkamp, *Microporous Mesoporous Mater.*, 1999, **27**, 261.
126 C. Pazé, A. Zecchina, S. Spera, G. Spano and F. Rivetti, *Phys. Chem. Chem. Phys.*, 2000, **2**, 5756.
127 G. Busca, *Chem. Rev.*, 2007, **107**, 5366.
128 B. Gil, S. I. Zones, S. J. Hwang, M. Bejblova and J. Cejka, *J. Phys. Chem. C*, 2008, **112**, 2997.
129 W. P. Zhang, S. T. Xu, X. W. Han and X. H. Bao, *Chem. Soc. Rev.*, 2012, **41**, 192.
130 L. M. Peng, Y. Liu, N. J. Kim, J. E. Readman and C. P. Grey, *Nat. Mater.*, 2005, **4**, 216.
131 L. Peng, H. Huo, Y. Liu and C. P. Grey, *J. Am. Chem. Soc.*, 2007, **129**, 335.
132 V. L. Zholobenko, L. M. Kustov, V. Y. Borovkov and V. B. Kazansky, *Zeolites*, 1988, **8**, 175.
133 A. Zecchina, S. Bordiga, G. Spoto, D. Scarano, G. Petrini, G. Leofanti, M. Padovan and C. O. Arean, *J. Chem. Soc., Faraday Trans.*, 1992, **88**, 2959.
134 A. G. Pelmenschikov, G. Morosi, A. Gamba, A. Zecchina, S. Bordiga and E. A. Paukshtis, *J. Phys. Chem.*, 1993, **97**, 11979.
135 G. Spoto, S. Bordiga, G. Ricchiardi, D. Scarano, A. Zecchina and E. Borello, *J. Chem. Soc., Faraday Trans.*, 1994, **90**, 2827.
136 R. Buzzoni, S. Bordiga, G. Ricchiardi, G. Spoto and A. Zecchina, *J. Phys. Chem.*, 1995, **99**, 11937.

137 A. Zecchina, R. Buzzoni, S. Bordiga, F. Geobaldo, D. Scarano, G. Ricchiardi and G. Spoto, *Stud. Surf. Sci. Catal.*, 1995, **97**, 213.
138 R. Buzzoni, S. Bordiga, G. Ricchiardi, C. Lamberti, A. Zecchina and G. Bellussi, *Langmuir*, 1996, **12**, 930.
139 A. Zecchina, S. Bordiga, G. Spoto, D. Scarano, G. Spano and F. Geobaldo, *J. Chem. Soc., Faraday Trans.*, 1996, **92**, 4863.
140 A. Zecchina, F. Geobaldo, C. Lamberti, S. Bordiga, G. T. Palomino and C. O. Arean, *Catal. Lett.*, 1996, **42**, 25.
141 F. Wakabayashi, J. N. Kondo, K. Domen and C. Hirose, *J. Phys. Chem.*, 1996, **100**, 1442.
142 S. Bordiga, B. Civalleri, G. Spoto, C. Paze, C. Lamberti, P. Ugliengo and A. Zecchina, *J. Chem. Soc., Faraday Trans.*, 1997, **93**, 3893.
143 F. Geobaldo, G. Spoto, S. Bordiga, C. Lamberti and A. Zecchina, *J. Chem. Soc., Faraday Trans.*, 1997, **93**, 1243.
144 A. Zecchina, L. Marchese, S. Bordiga, C. Paze and E. Gianotti, *J. Phys. Chem. B*, 1997, **101**, 10128.
145 C. Pazé, S. Bordiga, C. Lamberti, M. Salvalaggio, A. Zecchina and G. Bellussi, *J. Phys. Chem. B*, 1997, **101**, 4740.
146 C. Pazé, S. Bordiga, G. Spoto, C. Lamberti and A. Zecchina, *J. Chem. Soc., Faraday Trans.*, 1998, **94**, 309.
147 C. Pazé, B. Civalleri, S. Bordiga and A. Zecchina, *J. Phys. Chem. B*, 1998, **102**, 10753.
148 A. Zecchina, C. Lamberti and S. Bordiga, *Catal. Today*, 1998, **41**, 169.
149 G. Spoto, F. Geobaldo, S. Bordiga, C. Lamberti, D. Scarano and A. Zecchina, *Top. Catal.*, 1999, **8**, 279.
150 A. Zecchina, F. Xamena, C. Paze, G. T. Palomino, S. Bordiga and C. O. Arean, *Phys. Chem. Chem. Phys.*, 2001, **3**, 1228.
151 A. Zecchina, G. Spoto, G. Ricchiardi, S. Bordiga, F. Bonino, C. Prestipino and C. Lamberti, *Stud. Surf. Sci. Catal.*, 2002, **142**, 3.
152 S. Bordiga, L. Regli, D. Cocina, C. Lamberti, M. Bjorgen and K. P. Lillerud, *J. Phys. Chem. B*, 2005, **109**, 2779.
153 L. Regli, A. Zecchina, J. G. Vitillo, D. Cocina, G. Spoto, C. Lamberti, K. P. Lillerud, U. Olsbye and S. Bordiga, *Phys. Chem. Chem. Phys.*, 2005, **7**, 3197.
154 E. N. Gribov, D. Cocina, G. Spoto, S. Bordiga, G. Ricchiardi and A. Zecchina, *Phys. Chem. Chem. Phys.*, 2006, **8**, 1186.
155 M. Bregolato, V. Bolis, C. Busco, P. Ugliengo, S. Bordiga, F. Cavani, N. Ballarini, L. Maselli, S. Passeri, I. Rossetti and L. Forni, *J. Catal.*, 2007, **245**, 285.
156 L. Regli, S. Bordiga, C. Lamberti, K. P. Lillerud, S. I. Zones and A. Zecchina, *J. Phys. Chem. C*, 2007, **111**, 2992.
157 P. Sazama, J. Dedecek, V. Gabova, B. Wichterlova, G. Spoto and S. Bordiga, *J. Catal.*, 2008, **254**, 180.
158 K. Barbera, F. Bonino, S. Bordiga, T. V. W. Janssens and P. Beato, *J. Catal.*, 2011, **280**, 196.
159 R. Skorpa, S. Bordiga, F. Bleken, U. Olsbye, B. Arstad, J. Tolchard, K. Mathisen, S. Svelle and M. Bjorgen, *Microporous Mesoporous Mater.*, 2011, **141**, 146.
160 B. T. L. Bleken, L. Mino, F. Giordanino, P. Beato, S. Svelle, K. P. Lillerud and S. Bordiga, *Phys. Chem. Chem. Phys.*, 2013, **15**, 13363.
161 F. Giordanino, P. N. R. Vennestrom, L. F. Lundegaard, F. N. Stappen, S. Mossin, P. Beato, S. Bordiga and C. Lamberti, *Dalton Trans.*, 2013, **42**, 12741.
162 F. Giordanino, E. Borfecchia, K. A. Lomachenko, A. Lazzarini, G. Agostini, E. Gallo, A. V. Soldatov, P. Beato, S. Bordiga and C. Lamberti, *J. Phys. Chem. Lett.*, 2014, **5**, 1552.
163 W. Skistad, S. Teketel, F. L. Bleken, P. Beato, S. Bordiga, M. H. Nilsen, U. Olsbye, S. Svelle and K. P. Lillerud, *Top. Catal.*, 2014, **57**, 143.
164 R. M. Szostak, *Molecular Sieves*, Van Nostrand Reinhold, New York, 1989.
165 C. Baerlocher, W. M. Meier and D. H. Olson, *Atlas of Zeolite Frameworks Types*, Elsevier, Amsterdam, 2001.
166 G. P. Heitmann, G. Dahlhoff and W. F. Holderich, *J. Catal.*, 1999, **186**, 12.
167 G. P. Heitmann, G. Dahlhoff, J. P. M. Niederer and W. F. Holderich, *J. Catal.*, 2000, **194**, 122.
168 S. Bordiga, I. Roggero, P. Ugliengo, A. Zecchina, V. Bolis, G. Artioli, R. Buzzoni, G. Marra, F. Rivetti, G. Spano and C. Lamberti, *J. Chem. Soc., Dalton Trans.*, 2000, 3921.
169 S. Bordiga, P. Ugliengo, A. Damin, C. Lamberti, G. Spoto, A. Zecchina, G. Spano, R. Buzzoni, L. Dalloro and F. Rivetti, *Top. Catal.*, 2001, **15**, 43.
170 V. Bolis, C. Busco, S. Bordiga, P. Ugliengo, C. Lamberti and A. Zecchina, *Appl. Surf. Sci.*, 2002, **196**, 56.
171 A. B. Fernandez, A. Marinas, T. Blasco, V. Fornes and A. Corma, *J. Catal.*, 2006, **243**, 270.
172 K. Nakamoto, M. Margoshes and R. E. Rundle, *J. Am. Chem. Soc.*, 1955, **77**, 6480.
173 G. C. Pimentel and A. L. McClellan, *The Hydrogen bond*, Freeman, San Francisco, 1960.
174 L. Kubelkova, S. Beran and J. A. Lercher, *Zeolites*, 1989, **9**, 539.
175 A. V. Kiselev, *Surf. Sci.*, 1965, **3**, 292.
176 G. A. Galkin, A. V. Kiselev and V. I. Lygin, *Trans. Faraday Soc.*, 1964, **60**, 431.
177 A. Zecchina, F. Geobaldo, G. Spoto, S. Bordiga, G. Ricchiardi, R. Buzzoni and G. Petrini, *J. Phys. Chem.*, 1996, **100**, 16584.
178 U. Bohner and G. Zundel, *J. Phys. Chem.*, 1986, **90**, 964.
179 S. Bratos, *J. Chem. Phys.*, 1975, **63**, 3499.
180 G. Herzberg, *Molecular Spectra Molecular Structure. Vol. II Infrared Raman Spectra Polyatomic Molecules*, Van Nostrand, New York, 1996.
181 K. Nakamoto, *Infrared and Raman Spectra of Inorganic and Coordination Compounds. Part A: Theory and Applications in Inorganic Chemistry*, John Wiley & Sons, Hoboken, New Jersey, 6th edn, 2009.
182 P. Kondratyuk, *Spectrochim. Acta, Part A*, 2005, **61**, 589.
183 G. Herzberg, *Molecular Spectra and Molecular Structure. Vol. II: Infrared and Raman Spectra of Polyatomic Molecules*, Van Nostrand Company, Inc., New York, 1945.
184 S. E. Odinokov and A. V. Iogansen, *Spectrochim. Acta, Part A*, 1972, **28**, 2343.
185 U. Böhner and G. Zundel, *J. Phys. Chem.*, 1986, **90**, 964.
186 A. G. Pelmenschikov, J. Vanwolput, J. Janchen and R. A. van Santen, *J. Phys. Chem.*, 1995, **99**, 3612.

187 F. Wakabayashi, J. N. Kondo, K. Domen and C. Hirose, *J. Phys. Chem.*, 1995, **99**, 10573.
188 D. Hadzi and S. Bratos, in *The Hydrogen Bond*, ed. P. Shuster, G. Zundel and C. Sandorfy, North Holland, Amsterdam, 1976, vol. 2, p. 565.
189 L. J. Bellamy, H. E. Hallam and R. L. Williams, *Trans. Faraday Soc.*, 1958, **54**, 1120.
190 L. J. Bellamy and R. L. Williams, *Trans. Faraday Soc.*, 1959, **55**, 14.
191 L. J. Bellamy and H. E. Hallam, *Trans. Faraday Soc.*, 1959, **55**, 220.
192 L. J. Bellamy, C. P. Conduit, R. J. Pace and R. L. Williams, *Trans. Faraday Soc.*, 1959, **55**, 1677.
193 L. J. Bellamy, R. L. Williams and G. L. Caldow, *Proc. R. Soc. A*, 1960, **255**, 22.
194 J. G. David and H. E. Hallam, *Trans. Faraday Soc.*, 1964, **60**, 2013.
195 L. J. Bellamy and R. J. Pace, *Spectrochim. Acta, Part A*, 1969, **25**, 319.
196 P. G. Rouxhet and R. E. Sempels, *J. Chem. Soc., Faraday Trans. 1*, 1974, **70**, 2021.
197 G. Busca, in *Metal Oxides: Chemistry and Applications*, ed. J. L. C. Fierro, CRC Press, Boca Raton FL, 2006, p. 248.
198 A. G. Pelmenschikov, R. A. van Santen, J. Janchen and E. Meijer, *J. Phys. Chem.*, 1993, **97**, 11071.
199 L. Kubelkova, J. Kotrla and J. Florian, *J. Phys. Chem.*, 1995, **99**, 10285.
200 R. Buzzoni, S. Bordiga, G. Spoto, D. Scarano, G. Ricchiardi, C. Lamberti and A. Zecchina, *Stud. Surf. Sci. Catal.*, 1995, **98**, 104.
201 C. Pazé, A. Zecchina, S. Spera, A. Cosma, E. Merlo, G. Spano and G. Girotti, *Phys. Chem. Chem. Phys.*, 1999, **1**, 2627.
202 F. Bonino, A. Damin, S. Bordiga, C. Lamberti and A. Zecchina, *Langmuir*, 2003, **19**, 2155.
203 S. Bordiga, G. Ricchiardi, G. Spoto, D. Scarano, L. Carnelli, A. Zecchina and C. O. Arean, *J. Chem. Soc., Faraday Trans.*, 1993, **89**, 1843.
204 F. Geobaldo, C. Lamberti, G. Ricchiardi, S. Bordiga, A. Zecchina, G. T. Palomino and C. O. Arean, *J. Phys. Chem.*, 1995, **99**, 11167.
205 L. Andrews and G. L. Johnson, *J. Chem. Phys.*, 1983, **79**, 3670.
206 G. L. Johnson and L. Andrews, *J. Phys. Chem.*, 1983, **87**, 1852.
207 L. Andrews, *J. Mol. Struct.*, 1983, **100**, 281.
208 L. Andrews, *J. Phys. Chem.*, 1984, **88**, 2940.
209 L. Andrews and S. R. Davis, *J. Chem. Phys.*, 1985, **83**, 4983.
210 L. Andrews, R. B. Bohn, R. T. Arlinghaus and R. D. Hunt, *Chem. Phys. Lett.*, 1989, **158**, 564.
211 B. Onida, B. Bonelli, L. Borello, S. Fiorilli, F. Geobaldo and E. Garrone, *J. Phys. Chem. B*, 2002, **106**, 10518.
212 R. Anquetil, J. Saussey and J. C. Lavalley, *Phys. Chem. Chem. Phys.*, 1999, **1**, 555.
213 C. Morterra, G. Cerrato, F. Pinna, M. Signoretto and G. Strukul, *J. Catal.*, 1994, **149**, 181.
214 C. Morterra, G. Cerrato and M. Signoretto, *Catal. Lett.*, 1996, **41**, 101.
215 C. Morterra, G. Cerrato, V. Bolis, S. DiCiero and M. Signoretto, *J. Chem. Soc., Faraday Trans.*, 1997, **93**, 1179.
216 X. M. Song and A. Sayari, *Catal. Rev.: Sci. Eng.*, 1996, **38**, 329.
217 I. Palinko, B. Torok, G. K. S. Prakash and G. A. Olah, *Appl. Catal., A*, 1998, **174**, 147.
218 B. Torok, I. Kiricsi, A. Molnar and G. A. Olah, *J. Catal.*, 2000, **193**, 132.
219 H. Jobic, A. Tuel, M. Krossner and J. Sauer, *J. Phys. Chem.*, 1996, **100**, 19545.
220 V. F. Sears, *Neutron News*, 1992, **3**/**3**, 26.
221 H. Jobic, in *Catalyst Characterization*, ed. B. Imelik and J. C. Védrine, Plenum, New York, 1994, p. 347.
222 B. Cadioli, E. Gallinella, C. Coulombeau, H. Jobic and G. Berthier, *J. Phys. Chem.*, 1993, **97**, 7844.
223 M. Krossner and J. Sauer, *J. Phys. Chem.*, 1996, **100**, 6199.
224 W. J. Mortier, *J. Catal.*, 1978, **55**, 138.
225 W. J. Mortier, *Compilation of extraframework sites in zeolites*, Butterworth & Co., Guildfoed, UK, 1982.
226 S. Bordiga, E. E. Platero, C. O. Arean, C. Lamberti and A. Zecchina, *J. Catal.*, 1992, **137**, 179.
227 S. Bordiga, D. Scarano, G. Spoto, A. Zecchina, C. Lamberti and C. O. Arean, *Vib. Spectrosc.*, 1993, **5**, 69.
228 A. Zecchina, S. Bordiga, C. Lamberti, G. Spoto, L. Carnelli and C. O. Arean, *J. Phys. Chem.*, 1994, **98**, 9577.
229 S. Bordiga, C. Lamberti, F. Geobaldo, A. Zecchina, G. T. Palomino and C. O. Arean, *Langmuir*, 1995, **11**, 527.
230 C. Lamberti, S. Bordiga, F. Geobaldo, A. Zecchina and C. O. Arean, *J. Chem. Phys.*, 1995, **103**, 3158.
231 S. Bordiga, E. Garrone, C. Lamberti, A. Zecchina, C. O. Arean, V. B. Kazansky and L. M. Kustov, *J. Chem. Soc., Faraday Trans.*, 1994, **90**, 3367.
232 J. Sanz, V. Fornes and A. Corma, *J. Chem. Soc., Faraday Trans. 1*, 1988, **84**, 3113.
233 A. Corma, V. Fornes and F. Rey, *Appl. Catal.*, 1990, **59**, 267.
234 Q. L. Wang, G. Giannetto and M. Guisnet, *J. Catal.*, 1991, **130**, 471.
235 P. J. Kunkeler, B. J. Zuurdeeg, J. C. van der Waal, J. A. van Bokhoven, D. C. Koningsberger and H. van Bekkum, *J. Catal.*, 1998, **180**, 234.
236 K. S. Triantafyllidis, A. G. Vlessidis and N. P. Evmiridis, *Ind. Eng. Chem. Res.*, 2000, **39**, 307.
237 C. J. A. Mota, D. L. Bhering and N. Rosenbach, *Angew. Chem., Int. Ed.*, 2004, **43**, 3050.
238 M. J. Nash, A. M. Shough, D. W. Fickel, D. J. Doren and R. F. Lobo, *J. Am. Chem. Soc.*, 2008, **130**, 2460.
239 Y. Garcia-Basabe, I. Rodriguez-Iznaga, L. C. de Menorval, P. Llewellyn, G. Maurin, D. W. Lewis, R. Binions, M. Autie and A. R. Ruiz-Salvador, *Microporous Mesoporous Mater.*, 2010, **135**, 187.
240 G. Agostini, C. Lamberti, L. Palin, M. Milanesio, N. Danilina, B. Xu, M. Janousch and J. A. van Bokhoven, *J. Am. Chem. Soc.*, 2010, **132**, 667.
241 S. M. T. Almutairi, B. Mezari, G. A. Filonenko, P. Magusin, M. S. Rigutto, E. A. Pidko and E. J. M. Hensen, *ChemCatChem*, 2013, **5**, 452.
242 L. F. Isernia, *Mater. Res.-Ibero-am. J. Mater.*, 2013, **16**, 792.

243 Z. C. Wang, L. Z. Wang, Y. J. Jiang, M. Hunger and J. Huang, *ACS Catal.*, 2014, **4**, 1144.
244 T. Ennaert, J. Geboers, E. Gobechiya, C. M. Courtin, M. Kurttepeli, K. Houthoofd, C. E. A. Kirschhock, P. Magusin, S. Bals, P. A. Jacobs and B. F. Sels, *ACS Catal.*, 2015, **5**, 754.
245 S. Bordiga, F. Boscherini, S. Coluccia, F. Genoni, C. Lamberti, G. Leofanti, L. Marchese, G. Petrini, G. Vlaic and A. Zecchina, *Catal. Lett.*, 1994, **26**, 195.
246 S. Bordiga, S. Coluccia, C. Lamberti, L. Marchese, A. Zecchina, F. Boscherini, F. Buffa, F. Genoni, G. Leofanti, G. Petrini and G. Vlaic, *J. Phys. Chem.*, 1994, **98**, 4125.
247 B. Notari, in *Advances in Catalysis*, ed. D. D. Eley, W. O. Haag and B. Gates, Elsevier Academic Press Inc, San Diego, 1996, vol. 41, p. 253.
248 T. Armaroli, F. Milella, B. Notari, R. J. Willey and G. Busca, *Top. Catal.*, 2001, **15**, 63.
249 G. Berlier, G. Spoto, S. Bordiga, G. Ricchiardi, P. Fisicaro, A. Zecchina, I. Rossetti, E. Selli, L. Forni, E. Giamello and C. Lamberti, *J. Catal.*, 2002, **208**, 64.
250 A. M. Ferretti, C. Oliva, L. Forni, G. Berlier, A. Zecchina and C. Lamberti, *J. Catal.*, 2002, **208**, 83.
251 G. Berlier, A. Zecchina, G. Spoto, G. Ricchiardi, S. Bordiga and C. Lamberti, *J. Catal.*, 2003, **215**, 264.
252 M. Moliner, Y. Roman-Leshkov and M. E. Davis, *Proc. Natl. Acad. Sci. U. S. A.*, 2010, **107**, 6164.
253 M. Moliner, J. Gonzalez, M. T. Portilla, T. Willhammar, F. Rey, F. J. Llopis, X. D. Zou and A. Corma, *J. Am. Chem. Soc.*, 2011, **133**, 9497.
254 E. Nikolla, Y. Roman-Leshkov, M. Moliner and M. E. Davis, *ACS Catal.*, 2011, **1**, 408.
255 R. Bermejo-Deval, R. S. Assary, E. Nikolla, M. Moliner, Y. Roman-Leshkov, S. J. Hwang, A. Palsdottir, D. Silverman, R. F. Lobo, L. A. Curtiss and M. E. Davis, *Proc. Natl. Acad. Sci. U. S. A.*, 2012, **109**, 9727.
256 M. Moliner, *Dalton Trans.*, 2014, **43**, 4197.
257 J. A. van Bokhoven and C. Lamberti, *Coord. Chem. Rev.*, 2014, **277**, 275.
258 G. L. Marra, A. N. Fitch, A. Zecchina, G. Ricchiardi, M. Salvalaggio, S. Bordiga and C. Lamberti, *J. Phys. Chem. B*, 1997, **101**, 10653.
259 A. V. Larin, L. Leherte and D. P. Vercauteren, *Phys. Chem. Chem. Phys.*, 2002, **4**, 2416.
260 A. V. Larin, D. P. Vercauteren, C. Lamberti, S. Bordiga and A. Zecchina, *Phys. Chem. Chem. Phys.*, 2002, **4**, 2424.
261 G. E. Ewing, *J. Chem. Phys.*, 1962, **37**, 2250.
262 H. Willner and F. Aubke, *Angew. Chem., Int. Ed. Engl.*, 1997, **36**, 2403.
263 M. F. Zhou, L. Andrews and C. W. Bauschlicher, *Chem. Rev.*, 2001, **101**, 1931.
264 A. J. Lupinetti, S. H. Strauss and G. Frenking, *Prog. Inorg. Chem.*, 2001, **49**, 1.
265 S. H. Strauss, *J. Chem. Soc., Dalton Trans.*, 2000, 1.
266 V. Bolis, A. Barbaglia, S. Bordiga, C. Lamberti and A. Zecchina, *J. Phys. Chem. B*, 2004, **108**, 9970.
267 C. Lamberti, C. Morterra, S. Bordiga, G. Cerrato and D. Scarano, *Vib. Spectrosc.*, 1993, **4**, 273.
268 C. Lamberti, S. Bordiga, G. Cerrato, C. Morterra, D. Scarano, G. Spoto and A. Zecchina, *Comput. Phys. Commun.*, 1993, **74**, 119.
269 R. Shannon, *Acta Crystallogr., Sect. A: Cryst. Phys., Diffr., Theor. Gen. Crystallogr.*, 1976, **32**, 751.
270 G. E. Leoni, G. E. Ewing and G. C. Pimentel, *J. Chem. Phys.*, 1964, **40**, 2298.
271 R. H. Hauge, S. E. Gransden and J. L. Margrave, *J. Chem. Soc., Dalton Trans.*, 1979, 745.
272 A. M. Ferrari, P. Ugliengo and E. Garrone, *J. Chem. Phys.*, 1996, **105**, 4129.
273 A. M. Ferrari, K. M. Neymann and N. Rösch, *J. Phys. Chem.*, 1997, **101**, 9292.
274 C. O. Arean, G. T. Palomino, E. Garrone, D. Nachtigallova and P. Nachtigall, *J. Phys. Chem. B*, 2006, **110**, 395.
275 C. O. Arean, D. Nachtigallova, P. Nachtigall, E. Garrone and M. R. Delgado, *Phys. Chem. Chem. Phys.*, 2007, **9**, 1421.
276 C. O. Arean, M. R. Delgado, K. Frolich, R. Bulanek, A. Pulido, G. F. Bibiloni and P. Nachtigall, *J. Phys. Chem. C*, 2008, **112**, 4658.
277 E. Garrone, R. Bulanek, K. Frolich, C. O. Arean, M. R. Delgado, G. T. Palomino, D. Nachtigallova and P. Nachtigall, *J. Phys. Chem. B*, 2006, **110**, 22542.
278 P. Nachtigall, M. R. Delgado, K. Frolich, R. Bulanek, G. T. Palomino, C. L. Bauca and C. O. Arean, *Microporous Mesoporous Mater.*, 2007, **106**, 162.
279 P. Nachtigall, O. Bludsky, L. Grajciar, D. Nachtigallova, M. R. Delgado and C. O. Arean, *Phys. Chem. Chem. Phys.*, 2009, **11**, 791.
280 D. Nachtigallova, O. Bludsky, C. O. Arean, R. Bulanek and P. Nachtigall, *Phys. Chem. Chem. Phys.*, 2006, **8**, 4849.
281 A. Pulido, P. Nachtigall, M. R. Delgado and C. O. Arean, *ChemPhysChem*, 2009, **10**, 1058.
282 G. Pacchioni, G. Cogliandro and P. S. Bagus, *Int. J. Quantum Chem.*, 1992, **42**, 1115.
283 E. Garrone, B. Bonelli, A. A. Tsyganenko, M. R. Dalgado, G. T. Palomino, O. V. Manoilova and C. O. Arean, *J. Phys. Chem. B*, 2003, **107**, 2537.
284 A. A. Tsyganenko, P. Y. Storozhev and C. O. Arean, *Kinet. Catal.*, 2004, **45**, 530.
285 R. Bulanek and E. Koudelkova, *Microporous Mesoporous Mater.*, 2012, **151**, 149.
286 C. Bisio, P. Massiani, K. Fajerwerg, L. Sordelli, L. Stievano, E. R. Silva, S. Coluccia and G. Martra, *Microporous Mesoporous Mater.*, 2006, **90**, 175.
287 C. O. Arean, G. T. Palomino, A. A. Tsyganenko and E. Garrone, *Int. J. Mol. Sci.*, 2002, **3**, 764.
288 C. O. Arean, A. A. Tsyganenko, E. E. Platero, E. Garrone and A. Zecchina, *Angew. Chem., Int. Ed.*, 1998, **37**, 3161.
289 W. Mozgawa, *J. Mol. Struct.*, 2000, **555**, 299.
290 P. P. KnopsGerrits, D. E. DeVos and P. A. Jacobs, *J. Mol. Catal. A: Chem.*, 1997, **117**, 57.
291 M. C. Campa, D. Pietrogiacomi, S. Tuti, G. Ferraris and V. Indovina, *Appl. Catal., B*, 1998, **18**, 151.
292 S. P. Varkey, C. Ratnasamy and P. Ratnasamy, *J. Mol. Catal. A: Chem.*, 1998, **135**, 295.

293 M. Salavati-Niasari, M. Shaterian, M. R. Ganjali and P. Norouzi, *J. Mol. Catal. A: Chem.*, 2007, **261**, 147.
294 H. Y. Chen and W. M. H. Sachtler, *Catal. Today*, 1998, **42**, 73.
295 L. J. Lobree, I. C. Hwang, J. A. Reimer and A. T. Bell, *J. Catal.*, 1999, **186**, 242.
296 E. M. El-Malki, R. A. van Santen and W. M. H. Sachtler, *J. Catal.*, 2000, **196**, 212.
297 P. Marturano, L. Drozdova, A. Kogelbauer and R. Prins, *J. Catal.*, 2000, **192**, 236.
298 G. Berlier, G. Spoto, P. Fisicaro, S. Bordiga, A. Zecchina, E. Giamello and C. Lamberti, *Microchem. J.*, 2002, **71**, 101.
299 G. Berlier, G. Spoto, G. Ricchiardi, S. Bordiga, C. Lamberti and A. Zecchina, *J. Mol. Catal. A: Chem.*, 2002, **182**, 359.
300 G. Berlier, F. Bonino, A. Zecchina, S. Bordiga and C. Lamberti, *ChemPhysChem*, 2003, **4**, 1073.
301 D. Meloni, R. Monaci, V. Solinas, G. Berlier, S. Bordiga, I. Rossetti, C. Oliva and L. Forni, *J. Catal.*, 2003, **214**, 169.
302 G. Berlier, M. Pourny, S. Bordiga, G. Spoto, A. Zecchina and C. Lamberti, *J. Catal.*, 2005, **229**, 45.
303 G. Berlier, C. Prestipino, M. Rivallan, S. Bordiga, C. Lamberti and A. Zecchina, *J. Phys. Chem. B*, 2005, **109**, 22377.
304 G. Berlier, E. Gribov, D. Cocina, G. Spoto and A. Zecchina, *J. Catal.*, 2006, **238**, 243.
305 G. Berlier, C. Lamberti, M. Rivallan and G. Mul, *Phys. Chem. Chem. Phys.*, 2010, **12**, 358.
306 Y. J. Li and J. N. Armor, *J. Catal.*, 1994, **150**, 376.
307 Y. J. Li, T. L. Slager and J. N. Armor, *J. Catal.*, 1994, **150**, 388.
308 M. C. Campa, S. DeRossi, G. Ferraris and V. Indovina, *Appl. Catal., B*, 1996, **8**, 315.
309 R. S. da Cruz, A. J. S. Mascarenhas and H. M. C. Andrade, *Appl. Catal., B*, 1998, **18**, 223.
310 E. Ivanova, K. Hadjiivanov, D. Klissurski, M. Bevilacqua, T. Armaroli and G. Busca, *Microporous Mesoporous Mater.*, 2001, **46**, 299.
311 C. Resini, T. Montanari, L. Nappi, G. Bagnasco, M. Turco, G. Busca, F. Bregani, M. Notaro and G. Rocchini, *J. Catal.*, 2003, **214**, 179.
312 S. Dzwigaj and M. Che, *J. Phys. Chem. B*, 2006, **110**, 12490.
313 A. Mihaylova, K. Hadjiivanov, S. Dzwigaj and M. Che, *J. Phys. Chem. B*, 2006, **110**, 19530.
314 L. Daza, B. Pawelec, J. A. Anderson and J. L. G. Fierro, *Appl. Catal., A*, 1992, **87**, 145.
315 D. K. Murray, T. Howard, P. W. Goguen, T. R. Krawietz and J. F. Haw, *J. Am. Chem. Soc.*, 1994, **116**, 6354.
316 H. Berndt, G. Lietz, B. Lucke and J. Volter, *Appl. Catal., A*, 1996, **146**, 351.
317 E. M. El-Malki, R. A. van Santen and W. M. H. Sachtler, *J. Phys. Chem. B*, 1999, **103**, 4611.
318 V. B. Kazansky, V. Y. Borovkov, A. I. Serikh, R. A. van Santen and B. G. Anderson, *Catal. Lett.*, 2000, **66**, 39.
319 V. B. Kazansky, A. I. Serykh and E. A. Pidko, *J. Catal.*, 2004, **225**, 369.
320 V. B. Kazansky and E. A. Pidko, *J. Phys. Chem. B*, 2005, **109**, 2103.
321 A. N. Subbotin, G. M. Zhidomirov, I. R. Subbotina and V. B. Kazansky, *Kinet. Catal.*, 2013, **54**, 744.
322 J. Penzien, A. Abraham, J. A. van Bokhoven, A. Jentys, T. E. Muller, C. Sievers and J. A. Lercher, *J. Phys. Chem. B*, 2004, **108**, 4116.
323 Y. G. Kolyagin, V. V. Ordomsky, Y. Z. Khimyak, A. I. Rebrov, F. Fajula and I. I. Ivanova, *J. Catal.*, 2006, **238**, 122.
324 D. J. Wang, J. H. Lunsford and M. P. Rosynek, *J. Catal.*, 1997, **169**, 347.
325 W. Liu and Y. D. Xu, *J. Catal.*, 1999, **185**, 386.
326 L. L. Sheu, H. Knozinger and W. M. H. Sachtler, *J. Mol. Catal.*, 1989, **57**, 61.
327 D. Tessier, A. Rakai and F. Bozonverduraz, *J. Chem. Soc., Faraday Trans.*, 1992, **88**, 741.
328 C. Descorme, P. Gelin, M. Primet and C. Lecuyer, *Catal. Lett.*, 1996, **41**, 133.
329 K. Shimizu, F. Okada, Y. Nakamura, A. Satsuma and T. Hattori, *J. Catal.*, 2000, **195**, 151.
330 X. Wang, H. Y. Chen and W. M. H. Sachtler, *J. Catal.*, 2001, **197**, 281.
331 D. Scarano, S. Bordiga, C. Lamberti, G. Ricchiardi, S. Bertarione and G. Spoto, *Appl. Catal., A*, 2006, **307**, 3.
332 K. Hadjiivanov and H. Knozinger, *J. Phys. Chem. B*, 1998, **102**, 10936.
333 K. I. Hadjiivanov, *Microporous Mesoporous Mater.*, 1998, **24**, 41.
334 S. Bordiga, G. T. Palomino, D. Arduino, C. Lamberti, A. Zecchina and C. O. Arean, *J. Mol. Catal. A: Chem.*, 1999, **146**, 97.
335 S. Bordiga, C. Lamberti, G. T. Palomino, F. Geobaldo, D. Arduino and A. Zecchina, *Microporous Mesoporous Mater.*, 1999, **30**, 129.
336 V. Bolis, S. Bordiga, G. T. Palomino, A. Zecchina and C. Lamberti, *Thermochim. Acta*, 2001, **379**, 131.
337 Y. Kuroda, H. Onishi, T. Mori, Y. Yoshikawa, R. Kumashiro, M. Nagao and H. Kobayashi, *J. Phys. Chem. B*, 2002, **106**, 8976.
338 W. S. Ju, M. Matsuoka, K. Iino, H. Yamashita and M. Anpo, *J. Phys. Chem. B*, 2004, **108**, 2128.
339 G. Agostini, S. Usseglio, E. Groppo, M. J. Uddin, C. Prestipino, S. Bordiga, A. Zecchina, P. L. Solari and C. Lamberti, *Chem. Mater.*, 2009, **21**, 1343.
340 A. Uzun, V. A. Bhirud, P. W. Kletnieks, J. F. Haw and B. C. Gates, *J. Phys. Chem. C*, 2007, **111**, 15064.
341 L. M. Kustov, D. Ostgard and W. M. H. Sachtler, *Catal. Lett.*, 1991, **9**, 121.
342 G. J. Li, T. Fujimoto, A. Fukuoka and M. Ichikawa, *Catal. Lett.*, 1992, **12**, 171.
343 V. L. Zholobenko, G. D. Lei, B. T. Carvill, B. A. Lerner and W. M. H. Sachtler, *J. Chem. Soc., Faraday Trans.*, 1994, **90**, 233.
344 S. L. Qiu, R. Ohnishi and M. Ichikawa, *J. Phys. Chem.*, 1994, **98**, 2719.
345 T. M. Salama, T. Shido, H. Minagawa and M. Ichikawa, *J. Catal.*, 1995, **152**, 322.
346 T. M. Salama, R. Ohnishi, T. Shido and M. Ichikawa, *J. Catal.*, 1996, **162**, 169.

347 D. Guillemot, V. Y. Borovkov, V. B. Kazansky, M. PolissetThfoin and J. Fraissard, *J. Chem. Soc., Faraday Trans.*, 1997, **93**, 3587.
348 Z. X. Gao, Q. Sun, H. Y. Chen, X. Wang and W. M. H. Sachtler, *Catal. Lett.*, 2001, **72**, 1.
349 M. M. Mohamed, T. M. Salama, R. Ohnishi and M. Ichikawa, *Langmuir*, 2001, **17**, 5678.
350 J. C. Fierro-Gonzalez, B. G. Anderson, K. Ramesh, C. P. Vinod, J. W. Niemantsverdriet and B. C. Gates, *Catal. Lett.*, 2005, **101**, 265.
351 M. Y. Mihaylov, J. C. Fierro-Gonzalez, H. Knozinger, B. C. Gates and K. I. Hadjiivanov, *J. Phys. Chem. B*, 2006, **110**, 7695.
352 R. A. Schoonheydt, *Catal. Rev.: Sci. Eng.*, 1993, **35**, 129.
353 G. Centi and S. Perathoner, *Appl. Catal., A*, 1995, **132**, 179.
354 J. Sauer and M. Sierka, *J. Comput. Chem.*, 2000, **21**, 1470.
355 H. Yahiro and M. Iwamoto, *Appl. Catal., A*, 2001, **222**, 163.
356 A. Delabie, K. Pierloot, M. H. Groothaert, R. A. Schoonheydt and L. G. Vanquickenborne, *Eur. J. Inorg. Chem.*, 2002, 515.
357 G. Calzaferri, C. Leiggener, S. Glaus, D. Schurch and K. Kuge, *Chem. Soc. Rev.*, 2003, **32**, 29.
358 M. Matsuoka and M. Anpo, *Curr. Opin. Solid State Mater. Sci.*, 2003, **7**, 451.
359 P. Sherwood, A. H. de Vries, M. F. Guest, G. Schreckenbach, C. R. A. Catlow, S. A. French, A. A. Sokol, S. T. Bromley, W. Thiel, A. J. Turner, S. Billeter, F. Terstegen, S. Thiel, J. Kendrick, S. C. Rogers, J. Casci, M. Watson, F. King, E. Karlsen, M. Sjovoll, A. Fahmi, A. Schafer and C. Lennartz, *THEOCHEM*, 2003, **632**, 1.
360 Y. Kuroda and M. Iwamoto, *Top. Catal.*, 2004, **28**, 111.
361 D. Berthomieu and G. Delahay, *Catal. Rev.: Sci. Eng.*, 2006, **48**, 269.
362 P. Vanelderen, J. Vancauwenbergh, B. F. Sels and R. A. Schoonheydt, *Coord. Chem. Rev.*, 2013, **257**, 483.
363 E. Borfecchia, K. A. Lomachenko, F. Giordanino, H. Falsig, P. Beato, A. V. Soldatov, S. Bordiga and C. Lamberti, *Chem. Sci.*, 2015, **6**, 548.
364 T. V. W. Janssens, H. Falsig, L. F. Lundegaard, P. N. R. Vennestrøm, S. B. Rasmussen, P. G. Moses, F. Giordanino, E. Borfecchia, K. A. Lomachenko, C. Lamberti, S. Bordiga, A. Godiksen, S. Mossin and P. Beato, *ACS Catal.*, 2015, **5**, 2832.
365 T. Gunter, H. W. P. Carvalho, D. E. Doronkin, T. Sheppard, P. Glatzel, A. J. Atkins, J. Rudolph, C. R. Jacob, M. Casapu and J.-D. Grunwaldt, *Chem. Commun.*, 2015, **51**, 9227.
366 J. N. Armor, *Appl. Catal., B*, 1992, **1**, 221.
367 F. Kapteijn, J. RodriguezMirasol and J. A. Moulijn, *Appl. Catal., B*, 1996, **9**, 25.
368 A. Fritz and V. Pitchon, *Appl. Catal., B*, 1997, **13**, 1.
369 M. Shelef, *Chem. Rev.*, 1995, **95**, 209.
370 G. Busca, M. A. Larrubia, L. Arrighi and G. Ramis, *Catal. Today*, 2005, **107–108**, 139.
371 K. Rahkamaa-Tolonen, T. Maunula, M. Lomma, M. Huuhtanen and R. L. Keiski, *Catal. Today*, 2005, **100**, 217.
372 S. Brandenberger, O. Krocher, A. Tissler and R. Althoff, *Catal. Rev.: Sci. Eng.*, 2008, **50**, 492.
373 J. H. Li, H. Z. Chang, L. Ma, J. M. Hao and R. T. Yang, *Catal. Today*, 2011, **175**, 147.
374 A. M. Beale, F. Gao, I. Lezcano-Gonzalez, C. H. F. Peden and J. Szanyi, *Chem. Soc. Rev.*, 2015, **44**, DOI: 10.1039/C5CS00108K.
375 G. Spoto, S. Bordiga, D. Scarano and A. Zecchina, *Catal. Lett.*, 1992, **13**, 39.
376 G. Spoto, A. Zecchina, S. Bordiga, G. Ricchiardi, G. Martra, G. Leofanti and G. Petrini, *Appl. Catal., B*, 1994, **3**, 151.
377 G. Spoto, S. Bordiga, G. Ricchiardi, D. Scarano, A. Zecchina and F. Geobaldo, *J. Chem. Soc., Faraday Trans.*, 1995, **91**, 3285.
378 C. Lamberti, S. Bordiga, M. Salvalaggio, G. Spoto, A. Zecchina, F. Geobaldo, G. Vlaic and M. Bellatreccia, *J. Phys. Chem. B*, 1997, **101**, 344.
379 C. Lamberti, S. Bordiga, A. Zecchina, M. Salvalaggio, F. Geobaldo and C. O. Arean, *J. Chem. Soc., Faraday Trans.*, 1998, **94**, 1519.
380 A. Zecchina, S. Bordiga, M. Salvalaggio, G. Spoto, D. Scarano and C. Lamberti, *J. Catal.*, 1998, **173**, 540.
381 A. Zecchina, S. Bordiga, G. T. Palomino, D. Scarano, C. Lamberti and M. Salvalaggio, *J. Phys. Chem. B*, 1999, **103**, 3833.
382 A. Zecchina, C. O. Arean, G. T. Palomino, F. Geobaldo, C. Lamberti, G. Spoto and S. Bordiga, *Phys. Chem. Chem. Phys.*, 1999, **1**, 1649.
383 G. Turnes Palomino, P. Fisicaro, S. Bordiga, A. Zecchina, E. Giamello and C. Lamberti, *J. Phys. Chem. B*, 2000, **104**, 4064.
384 G. Turnes Palomino, S. Bordiga, A. Zecchina, G. L. Marra and C. Lamberti, *J. Phys. Chem. B*, 2000, **104**, 8641.
385 C. Prestipino, G. Berlier, F. Xamena, G. Spoto, S. Bordiga, A. Zecchina, G. T. Palomino, T. Yamamoto and C. Lamberti, *Chem. Phys. Lett.*, 2002, **363**, 389.
386 F. X. L. I. Xamena, P. Fisicaro, G. Berlier, A. Zecchina, G. T. Palomino, C. Prestipino, S. Bordiga, E. Giamello and C. Lamberti, *J. Phys. Chem. B*, 2003, **107**, 7036.
387 Q. Xu, *Coord. Chem. Rev.*, 2002, **231**, 83.
388 K. I. Hadjiivanov, M. M. Kantcheva and D. G. Klissurski, *J. Chem. Soc., Faraday Trans.*, 1996, **92**, 4595.
389 D. Nachtigallova, P. Nachtigall, M. Sierka and J. Sauer, *Phys. Chem. Chem. Phys.*, 1999, **1**, 2019.
390 D. Nachtigallova, P. Nachtigall and J. Sauer, *Phys. Chem. Chem. Phys.*, 2001, **3**, 1552.
391 Y. Kuroda, A. Kotani, H. Maeda, H. Moriwaki, T. Morimato and M. Nagao, *J. Chem. Soc., Faraday Trans.*, 1992, **88**, 1583.
392 Y. Kuroda, R. Kumashiro, A. Itadani, M. Nagao and H. Kobayashi, *Phys. Chem. Chem. Phys.*, 2001, **3**, 1383.
393 M. Iwamoto, H. Furukawa, Y. Mine, F. Uemura, S. I. Mikuriya and S. Kagawa, *J. Chem. Soc., Chem. Commun.*, 1986, 1272.
394 M. Iwamoto, H. Yahiro, Y. Mine and S. Kagawa, *Chem. Lett.*, 1989, 213.
395 M. Iwamoto and H. Hamada, *Catal. Today*, 1991, **10**, 57.
396 M. Iwamoto, H. Yahiro, K. Tanda, N. Mizuno, Y. Mine and S. Kagawa, *J. Phys. Chem.*, 1991, **95**, 3727.
397 M. Iwamoto, H. Yahiro, S. Shundo, Y. Yoshihiro and N. Mizuno, *Appl. Catal.*, 1991, **69**, L15.

398 M. Iwamoto, H. Yahiro, N. Mizuno, W. X. Zhang, Y. Mine, H. Furukawa and S. Kagawa, *J. Phys. Chem.*, 1992, **96**, 9360.
399 M. Iwamoto and H. Yahiro, *Catal. Today*, 1994, **22**, 5.
400 S. Sato, Y. Yoshihiro, H. Yahiro, N. Mizuno and M. Iwamoto, *Appl. Catal.*, 1991, **70**, L1.
401 M. H. Groothaert, K. Lievens, H. Leeman, B. M. Weckhuysen and R. A. Schoonheydt, *J. Catal.*, 2003, **220**, 500.
402 F. Amano, T. Tanaka and T. Funabiki, *J. Mol. Catal. A: Chem.*, 2004, **221**, 89.
403 M. Richter, M. J. G. Fait, R. Eckelt, E. Schreier, M. Schneider, M. M. Pohl and R. Fricke, *Appl. Catal., B*, 2007, **73**, 269.
404 C. Lamberti, G. T. Palomino, S. Bordiga, G. Berlier, F. D'Acapito and A. Zecchina, *Angew. Chem., Int. Ed.*, 2000, **39**, 2138.
405 V. Bolis, S. Maggiorini, L. Meda, F. D'Acapito, G. T. Palomino, S. Bordiga and C. Lamberti, *J. Chem. Phys.*, 2000, **113**, 9248.
406 M. Iwamoto and Y. Hoshino, *Inorg. Chem.*, 1996, **35**, 6918.
407 C. Prestipino, L. Capello, F. D'Acapito and C. Lamberti, *Phys. Chem. Chem. Phys.*, 2005, **7**, 1743.
408 I. Noda, *Appl. Spectrosc.*, 1990, **44**, 550.
409 I. Noda, *Appl. Spectrosc.*, 1993, **47**, 1329.
410 I. Noda, A. E. Dowrey and C. Marcott, *Appl. Spectrosc.*, 1993, **47**, 1317.
411 S. Ekgasit and H. Ishida, *Appl. Spectrosc.*, 1995, **49**, 1243.
412 I. Noda, A. E. Dowrey, C. Marcott, G. M. Story and Y. Ozaki, *Appl. Spectrosc.*, 2000, **54**, 236A.
413 F. Thibault-Starzyk, A. Vimont, C. Fernandez and J. P. Gilson, *Chem. Commun.*, 2000, 1003.
414 F. Thibault-Starzyk, A. Vimont and J. P. Gilson, *Catal. Today*, 2001, **70**, 227.
415 N. T. Hunt, *Chem. Soc. Rev.*, 2009, **38**, 1837.
416 S. Garrett-Roe and P. Hamm, *Acc. Chem. Res.*, 2009, **42**, 1412.
417 C. R. Baiz, P. L. McRobbie, J. M. Anna, E. Geva and K. J. Kubarych, *Acc. Chem. Res.*, 2009, **42**, 1395.
418 J. J. Rack, J. D. Webb and S. H. Strauss, *Inorg. Chem.*, 1996, **35**, 277.
419 D. Costa, G. Martra, M. Che, L. Manceron and M. Kermarec, *J. Am. Chem. Soc.*, 2002, **124**, 7210.
420 G. Martra, S. Coluccia, M. Che, L. Manceron, M. Kermarec and D. Costa, *J. Phys. Chem. B*, 2003, **107**, 6096.
421 D. Gianolio, E. Groppo, J. G. Vitillo, A. Damin, S. Bordiga, A. Zecchina and C. Lamberti, *Chem. Commun.*, 2010, **46**, 976.
422 D. Scarano, S. Bordiga, C. Lamberti, G. Spoto, G. Ricchiardi, A. Zecchina and C. O. Arean, *Surf. Sci.*, 1998, **411**, 272.
423 S. Bordiga, C. Pazé, G. Berlier, D. Scarano, G. Spoto, A. Zecchina and C. Lamberti, *Catal. Today*, 2001, **70**, 91.
424 G. T. Palomino, E. Giamello, P. Fisicaro, S. Bordiga, C. Lamberti and A. Zecchina, *Stud. Surf. Sci. Catal.*, 2000, **130**, 2915.
425 J. Szanyi, J. H. Kwak, H. Zhu and C. H. F. Peden, *Phys. Chem. Chem. Phys.*, 2013, **15**, 2368.
426 G. T. Palomino, S. Bordiga, C. Lamberti, A. Zecchina and C. O. Arean, *Stud. Surf. Sci. Catal.*, 2002, **142**, 199.
427 A. Zecchina, D. Scarano, G. Spoto, S. Bordiga, C. Lamberti and G. Bellussi, *Stud. Surf. Sci. Catal.*, 1998, **117**, 343.
428 Y. Kuroda, Y. Yoshikawa, S. Konno, H. Hamano, H. Maeda, R. Kumashiro and M. Nagao, *J. Phys. Chem.*, 1995, **99**, 10621.
429 J. Dedecek, B. Wichterlova and P. Kubat, *Microporous Mesoporous Mater.*, 1999, **32**, 63.
430 F. Gao, E. D. Walter, E. M. Karp, J. Y. Luo, R. G. Tonkyn, J. H. Kwak, J. Szanyi and C. H. F. Peden, *J. Catal.*, 2013, **300**, 20.
431 G. Leofanti, A. Marsella, B. Cremaschi, M. Garilli, A. Zecchina, G. Spoto, S. Bordiga, P. Fisicaro, G. Berlier, C. Prestipino, G. Casali and C. Lamberti, *J. Catal.*, 2001, **202**, 279.
432 A. Corma, V. Fornés and E. Palomares, *Appl. Catal., B*, 1997, **11**, 233.
433 J. Dedecek, Z. Sobalik, Z. Tvaruzkova, D. Kaucky and B. Wichterlova, *J. Phys. Chem.*, 1995, **99**, 16327.
434 A. A. Davydov and A. A. Budneva, *React. Kinet. Catal. Lett.*, 1983, **25**, 121.
435 K. Hadjiivanov, D. Klissurski, G. Ramis and G. Busca, *Appl. Catal., B*, 1996, **7**, 251.
436 J. H. Kwak, T. Varga, C. H. F. Peden, F. Gao, J. C. Hanson and J. Szanyi, *J. Catal.*, 2014, **314**, 83.
437 I. Mirsojew, S. Ernst, J. Weitkamp and H. Knozinger, *Catal. Lett.*, 1994, **24**, 235.
438 C. O. Arean, G. T. Palomino, F. Geobaldo and A. Zecchina, *J. Phys. Chem.*, 1996, **100**, 6678.
439 J. Halasz, Z. Konya, A. Fudala and I. Kiricsi, *Catal. Today*, 1996, **31**, 293.
440 E. Kikuchi, M. Ogura, I. Terasaki and Y. Goto, *J. Catal.*, 1996, **161**, 465.
441 M. Sigl, S. Ernst, J. Weitkamp and H. Knozinger, *Catal. Lett.*, 1997, **45**, 27.
442 H. Kosslick, G. Lischke, H. Landmesser, B. Parlitz, W. Storek and R. Fricke, *J. Catal.*, 1998, **176**, 102.
443 G. Mul, J. Perez-Ramirez, F. Kapteijn and J. A. Moulijn, *Catal. Lett.*, 2002, **80**, 129.
444 M. Garcia-Sanchez, P. Magusin, E. J. M. Hensen, P. C. Thune, X. Rozanska and R. A. van Santen, *J. Catal.*, 2003, **219**, 352.
445 G. T. Palomino, J. J. C. Pascual, M. R. Delgado, J. B. Parra and C. O. Arean, *Mater. Chem. Phys.*, 2004, **85**, 145.
446 S. Endud and K. L. Wong, *Microporous Mesoporous Mater.*, 2007, **101**, 256.
447 B. Tang, W. L. Dai, G. J. Wu, N. J. Guan, L. D. Li and M. Hunger, *ACS Catal.*, 2014, **4**, 2801.
448 M. Weihe, M. Hunger, M. Breuninger, H. G. Karge and J. Whitkamp, *J. Catal.*, 2001, **198**, 256.
449 X. N. Wang, Z. Zhao, C. M. Xu, A. J. Duan, L. Zhang and G. Y. Jiang, *J. Rare Earths*, 2007, **25**, 321.
450 Q. Shu, B. L. Yang, H. Yuan, S. Qing and G. L. Zhu, *Catal. Commun.*, 2007, **8**, 2159.
451 W. C. Zhan, Y. L. Guo, Y. Q. Wang, X. H. Liu, Y. Guo, Y. S. Wang, Z. G. Zhang and G. Z. Lu, *J. Phys. Chem. B*, 2007, **111**, 12103.
452 T. Noda, K. Suzuki, N. Katada and M. Niwa, *J. Catal.*, 2008, **259**, 203.
453 L. Gutierrez and E. A. Lombardo, *Appl. Catal., A*, 2009, **360**, 107.
454 M. Xue, R. Chitrakar, K. Sakane, T. Hirotsu, K. Ooi, Y. Yoshimura, M. Toba and Q. Feng, *J. Colloid Interface Sci.*, 2006, **298**, 535.

455 M. Alvaro, V. Fornes, S. Garcia, H. Garcia and J. C. Scaiano, *J. Phys. Chem. B*, 1998, **102**, 8744.
456 J. Rocha and L. D. Carlos, *Curr. Opin. Solid State Mater. Sci.*, 2003, **7**, 199.
457 Y. Hasegawa, Y. Wada and S. Yanagida, *J. Photochem. Photobiol., C*, 2004, **5**, 183.
458 Y. G. Wang, H. R. Li, L. J. Gu, Q. Y. Gan, Y. N. Li and G. Calzaferri, *Microporous Mesoporous Mater.*, 2009, **121**, 1.
459 Y. Wang, H. R. Li, Y. Feng, H. J. Zhang, G. Calzaferri and T. Z. Ren, *Angew. Chem., Int. Ed.*, 2010, **49**, 1434.
460 P. P. Cao, Y. G. Wang, H. R. Li and X. Y. Yu, *J. Mater. Chem.*, 2011, **21**, 2709.
461 L. Chen and B. Yan, *Dalton Trans.*, 2014, **43**, 14123.
462 J. N. Hao and B. Yan, *Dalton Trans.*, 2014, **43**, 2810.
463 P. Li, D. Y. Wang, D. Liang, L. Zhang, S. M. Zhang and Y. G. Wang, *Mater. Res. Bull.*, 2014, **55**, 216.
464 Y. Wang and H. R. Li, *CrystEngComm*, 2014, **16**, 9764.
465 S. E. Spiridonov, K. S. U. Nasukhanov, O. V. Kryukov, E. B. Podyacheva and S. N. Khadzhiev, *Kinet. Catal.*, 1992, **33**, 317.
466 P. Tynjala and T. T. Pakkanen, *J. Mol. Catal. A: Chem.*, 1996, **110**, 153.
467 E. F. Sousa-Aguiar, V. L. D. Camorim, F. M. Z. Zotin and R. L. C. dos Santos, *Microporous Mesoporous Mater.*, 1998, **25**, 25.
468 D. Li, F. Li, J. Ren and Y. H. Sun, *Appl. Catal., A*, 2003, **241**, 15.
469 S. E. Siporin, B. C. McClaine and R. J. Davis, *Langmuir*, 2003, **19**, 4707.
470 A. Martins, J. M. Silva, C. Henriques, F. R. Ribeiro and M. F. Ribeiro, *Catal. Today*, 2005, **107–108**, 663.
471 F. P. Tian, W. C. Wu, Z. X. Jiang, C. H. Liang, Y. X. Yang, P. L. Ying, X. P. Sun, T. X. Cai and C. Li, *J. Colloid Interface Sci.*, 2006, **301**, 395.
472 D. F. Jin, B. Zhu, Z. Y. Hou, J. H. Fel, H. Lou and X. M. Zheng, *Fuel*, 2007, **86**, 2707.
473 E. Ito, Y. J. Mergler, B. E. Nieuwenhuys, H. Vanbekkum and C. M. Vandenbleek, *Microporous Mater.*, 1995, **4**, 455.
474 E. Ito, Y. J. Mergler, B. E. Nieuwenhuys, H. P. A. Calis, H. vanBekkum and C. M. vandenBleek, *J. Chem. Soc., Faraday Trans.*, 1996, **92**, 1799.
475 V. I. Parvulescu, P. Grange and B. Delmon, *J. Phys. Chem. B*, 1997, **101**, 6933.
476 A. M. G. Pedrosa, M. J. B. Souza, A. O. S. Silva, D. M. A. Melo and A. S. Araujo, *J. Therm. Anal. Calorim.*, 2006, **84**, 503.
477 H. G. Wang, L. J. Song, H. Jiang, J. Xu, L. L. Jin, X. T. Zhang and Z. L. Sun, *Fuel Process. Technol.*, 2009, **90**, 835.
478 A. Goldbach, L. Iton, M. Grimsditch and M. L. Saboungi, *J. Am. Chem. Soc.*, 1996, **118**, 2004.
479 V. I. Parvulescu, P. Oelker, P. Grange and B. Delmon, *Appl. Catal., B*, 1998, **16**, 1.
480 T. Baba, S. Hikita, Y. Ono, T. Yoshida, T. Tanaka and S. Yoshida, *J. Mol. Catal. A: Chem.*, 1995, **98**, 49.
481 C. Kladis, S. K. Bhargava, K. Foger and D. B. Akolekar, *Catal. Today*, 2000, **63**, 297.
482 H. R. Li, H. H. Zhang, L. Y. Wang, D. Mu, S. T. Qi, X. J. Hu, L. Zhang and J. S. Yuan, *J. Mater. Chem.*, 2012, **22**, 9338.
483 Z. Q. Qin, H. S. Li and Y. G. Wang, *Opt. Mater.*, 2014, **37**, 483.
484 L. Chen and B. Yan, *Spectrochim. Acta, Part A*, 2014, **131**, 1.
485 C. Tiseanu, B. Gagea, V. I. Parvulescu, V. Lorenz-Fonfria, A. Gessner and M. U. Kumke, *Langmuir*, 2007, **23**, 6781.
486 J. P. Rainho, M. Pillinger, L. D. Carlos, S. J. L. Ribeiro, R. M. Almeida and J. Rocha, *J. Mater. Chem.*, 2002, **12**, 1162.
487 T. Baba, S. Hikita, R. Koide, Y. Ono, T. Hanada, T. Tanaka and S. Yoshida, *J. Chem. Soc., Faraday Trans.*, 1993, **89**, 3177.
488 E. Groppo, C. Lamberti, S. Bordiga, G. Spoto and A. Zecchina, *Chem. Rev.*, 2005, **105**, 115.
489 E. Groppo, C. Lamberti, S. Bordiga, G. Spoto and A. Zecchina, *J. Phys. Chem. B*, 2005, **109**, 15024.
490 S. Bordiga, G. T. Palomino, C. Paze and A. Zecchina, *Microporous Mesoporous Mater.*, 2000, **34**, 67.
491 M. Mihaylov, K. Chakarova and K. Hadjiivanov, *J. Catal.*, 2004, **228**, 273.
492 A. Zecchina, D. Scarano, S. Bordiga, G. Spoto and C. Lamberti, *Adv. Catal.*, 2001, **46**, 265.
493 E. Escalona Platero, D. Scarano, G. Spoto and A. Zecchina, *Faraday Discuss. Chem. Soc.*, 1985, **80**, 183.
494 F. Bonino, S. Chavan, J. G. Vitillo, E. Groppo, G. Agostini, C. Lamberti, P. D. C. Dietzel, C. Prestipino and S. Bordiga, *Chem. Mater.*, 2008, **20**, 4957.
495 S. Chavan, J. G. Vitillo, E. Groppo, F. Bonino, C. Lamberti, P. D. C. Dietzel and S. Bordiga, *J. Phys. Chem. C*, 2009, **113**, 3292.
496 M. Guisnet, P. Ayrault, C. Coutanceau, M. F. Alvarez and J. Datka, *J. Chem. Soc., Faraday Trans.*, 1997, **93**, 1661.
497 J. P. Marques, I. Gener, P. Ayrault, J. C. Bordado, J. M. Lopes, F. R. Ribeiro and M. Guisnet, *Microporous Mesoporous Mater.*, 2003, **60**, 251.
498 J. C. Groen, L. A. A. Peffer, J. A. Moulijn and J. Perez-Ramirez, *Chem. – Eur. J.*, 2005, **11**, 4983.
499 J. A. Martens, R. Parton, L. Uytterhoeven, P. A. Jacobs and G. F. Froment, *Appl. Catal.*, 1991, **76**, 95.
500 J. Wang, J. N. Park, Y. K. Park and C. W. Lee, *J. Catal.*, 2003, **220**, 265.
501 B. Xu, S. Bordiga, R. Prins and J. A. van Bokhoven, *Appl. Catal., A*, 2007, **333**, 245.
502 L. M. Kustov, V. B. Kazansky, S. Beran, L. Kubelkova and P. Jiru, *J. Phys. Chem.*, 1987, **91**, 5247.
503 E. Loeffler, U. Lohse, C. Peuker, G. Oehlmann, L. M. Kustov, V. L. Zholobenko and V. B. Kazansky, *Zeolites*, 1990, **10**, 266.
504 S. Khabtou, T. Chevreau and J. C. Lavalley, *Microporous Mater.*, 1994, **3**, 133.
505 P. Wu, T. Komatsu and T. Yashima, *J. Chem. Soc., Faraday Trans.*, 1996, **92**, 861.
506 J. Datka, B. Sulikowski and B. Gil, *J. Phys. Chem.*, 1996, **100**, 11242.

507 I. Ahmad, J. A. Anderson, T. J. Dines and C. H. Rochester, *J. Colloid Interface Sci.*, 1998, **207**, 371.
508 M. L. Occelli, S. Biz, A. Auroux and G. J. Ray, *Microporous Mesoporous Mater.*, 1998, **26**, 193.
509 J. Datka, B. Gil, J. Zlamaniec, P. Batamack, J. Fraissard and P. Massiani, *Pol. J. Chem.*, 1999, **73**, 1535.
510 Y. Fan, X. J. Bao, X. Y. Lin, G. Shi and H. Y. Liu, *J. Phys. Chem. B*, 2006, **110**, 15411.
511 V. Machado, J. Rocha, A. P. Carvalho and A. Martins, *Appl. Catal., A*, 2012, **445**, 329.
512 P. Ratnasamy and R. Kumar, *Catal. Today*, 1991, **9**, 329.
513 H. Kosslick, V. A. Tuan, R. Fricke, C. Peuker, W. Pilz and W. Storek, *J. Phys. Chem.*, 1993, **97**, 5678.
514 C. Peuker, *J. Mol. Struct.*, 1995, **349**, 317.
515 N. K. Mal, A. Bhaumik, R. Kumar and A. V. Ramaswamy, *Catal. Lett.*, 1995, **33**, 387.
516 B. Sulikowski, *Heterog. Chem. Rev.*, 1996, **3**, 203.
517 I. Arends, R. A. Sheldon, M. Wallau and U. Schuchardt, *Angew. Chem., Int. Ed.*, 1997, **36**, 1144.
518 R. J. Francis and D. O'Hare, *J. Chem. Soc., Dalton Trans.*, 1998, 3133.
519 Z. Gabelica and S. Valange, *Microporous Mesoporous Mater.*, 1999, **30**, 57.
520 R. Millini, G. Perego and G. Bellussi, *Top. Catal.*, 1999, **9**, 13.
521 G. M. Johnson, P. J. Mead and M. T. Weller, *Microporous Mesoporous Mater.*, 2000, **38**, 445.
522 Y. Ma, W. Tong, H. Zhou and S. L. Suib, *Microporous Mesoporous Mater.*, 2000, **37**, 243.
523 M. Renz, T. Blasco, A. Corma, V. Fornes, R. Jensen and L. Nemeth, *Chem. – Eur. J.*, 2002, **8**, 4708.
524 A. Corma, M. E. Domine and S. Valencia, *J. Catal.*, 2003, **215**, 294.
525 L. G. A. van de Water, M. A. Zwijnenburg, W. G. Sloof, J. C. van der Waal, J. C. Jansen and T. Maschmeyer, *ChemPhysChem*, 2004, **5**, 1328.
526 M. Boronat, P. Concepcion, A. Corma, M. Renz and S. Valencia, *J. Catal.*, 2005, **234**, 111.
527 L. Shi, K. E. Christensen, K. Jansson, J. Sun and X. Zou, *Chem. Mater.*, 2007, **19**, 5973.
528 M. G. Clerici, in *Metal Oxide Catalysis*, ed. S. D. Jackson and J. S. J. Hargreaves, Wiley-VCH Verlag GmbH & Co. KGaA, Weinheim, 2009, p. 705.
529 M. El-Roz, L. Lakiss, A. Vicente, K. N. Bozhilov, F. Thibault-Starzyk and V. Valtchev, *Chem. Sci.*, 2014, **5**, 68.
530 W. N. P. van der Graaff, G. N. Li, B. Mezari, E. A. Pidko and E. J. M. Hensen, *ChemCatChem*, 2015, **7**, 1152.
531 L. P. Li, X. J. Cui, S. T. Xu, J. F. Li, Z. F. Qin and J. G. Wang, *Mater. Express*, 2015, **5**, 73.
532 L. Regli, S. Bordiga, C. Busco, C. Prestipino, P. Ugliengo, A. Zecchina and C. Lamberti, *J. Am. Chem. Soc.*, 2007, **129**, 12131.
533 L. Regli, C. Lamberti, C. Busco, A. Zecchina, C. Prestipino, K. P. Lillerud, S. I. Zones and S. Bordiga, *Stud. Surf. Sci. Catal.*, 2007, **170**, 585.
534 E. M. Flanigen, H. Khatami and H. A. Szymanski, in *Molecular Sieve Zeolites-I*, ed. F. E. M. and L. B. Sand, American Chemical Society, Washinton, DC, 1974, ch. 16, vol. I, p. 201.
535 A. J. M. De Man, B. W. H. Van Beest, M. Leslie and R. A. Van Santen, *J. Phys. Chem.*, 1990, **94**, 2524.
536 A. Damin, F. Bonino, G. Ricchiardi, S. Bordiga, A. Zecchina and C. Lamberti, *J. Phys. Chem. B*, 2002, **106**, 7524.
537 S. Bordiga, A. Damin, F. Bonino, A. Zecchina, G. Spanò, F. Rivetti, V. Bolis and C. Lamberti, *J. Phys. Chem. B*, 2002, **106**, 9892.
538 M. R. Boccuti, K. M. Rao, A. Zecchina, G. Leofanti and G. Petrini, *Stud. Surf. Sci. Catal.*, 1989, **48**, 133.
539 D. Scarano, A. Zecchina, S. Bordiga, F. Geobaldo, G. Spoto, G. Petrini, G. Leofanti, M. Padovan and G. Tozzola, *J. Chem. Soc., Faraday Trans.*, 1993, **89**, 4123.
540 M. A. Camblor, A. Corma and J. Perezpariente, *J. Chem. Soc., Chem. Commun.*, 1993, 557.
541 E. Astorino, J. B. Peri, R. J. Willey and G. Busca, *J. Catal.*, 1995, **157**, 482.
542 T. Blasco, A. Corma, M. T. Navarro and J. P. Pariente, *J. Catal.*, 1995, **156**, 65.
543 T. Blasco, M. A. Camblor, A. Corma, P. Esteve, J. M. Guil, A. Martinez, J. A. Perdigon-Melon and S. Valencia, *J. Phys. Chem. B*, 1998, **102**, 75.
544 E. A. Eilertsen, S. Bordiga, C. Lamberti, A. Damin, F. Bonino, B. Arstad, S. Svelle, U. Olsbye and K. P. Lillerud, *ChemCatChem*, 2011, **3**, 1869.
545 E. A. Eilertsen, F. Giordanino, C. Lamberti, S. Bordiga, A. Damin, F. Bonino, U. Olsbye and K. P. Lillerud, *Chem. Commun.*, 2011, **47**, 11867.
546 C. Li, S.-F. Fu, H. Zhang and Q. Xin, *J. Chem. Soc., Chem. Commun.*, 1994, 17.
547 J. F. Bengoa, N. G. Gallegos, S. G. Marchetti, A. M. Alvarez, M. V. Cagnoli and A. A. Yeramian, *Microporous Mesoporous Mater.*, 1998, **24**, 163.
548 C. Perego, A. Carati, P. Ingallina, M. A. Mantegazza and G. Bellussi, *Appl. Catal., A*, 2001, **221**, 63.
549 A. Corma and H. Garcia, *Chem. Rev.*, 2002, **102**, 3837.
550 L. Dal Pozzo, G. Fornasari and T. Monti, *Catal. Commun.*, 2002, **3**, 369.
551 G. Tozzola, M. A. Mantegazza, G. Ranghino, G. Petrini, S. Bordiga, G. Ricchiardi, C. Lamberti, R. Zulian and A. Zecchina, *J. Catal.*, 1998, **179**, 64.
552 C. Prestipino, F. Bonino, S. Usseglio, A. Damin, A. Tasso, M. G. Clerici, S. Bordiga, F. D'Acapito, A. Zecchina and C. Lamberti, *ChemPhysChem*, 2004, **5**, 1799.
553 F. Bonino, A. Damin, G. Ricchiardi, M. Ricci, G. Spanò, R. D'Aloisio, A. Zecchina, C. Lamberti, C. Prestipino and S. Bordiga, *J. Phys. Chem. B*, 2004, **108**, 3573.
554 K. Tanabe and W. F. Holderich, *Appl. Catal., A*, 1999, **181**, 399.
555 R. J. Davis, *J. Catal.*, 2003, **216**, 396.
556 C. P. Nicholas, *Zeolites in Industrial Separation and Catalysis*, Wiley-VCH Verlag GmbH & Co. KGaA, Weinheim, 2010, p. 355.

557 S. Kulprathipanja and R. B. James, in *Zeolites in Industrial Separation and Catalysis*, Wiley-VCH Verlag GmbH & Co. KGaA, Weinheim, 2010, p. 173.
558 S. Kulprathipanja, in *Zeolites in Industrial Separation and Catalysis*, Wiley-VCH Verlag GmbH & Co. KGaA, Weinheim, 2010, p. 203.
559 D. Barthomeuf, *Catal. Rev.: Sci. Eng.*, 1996, **38**, 521.
560 J. Weitkamp, M. Hunger and U. Rymsa, *Microporous Mesoporous Mater.*, 2001, **48**, 255.
561 J. Weitkamp and M. Hunger, *Stud. Surf. Sci. Catal.*, 2007, **168**, 787.
562 M. Sánchez-Sánchez and T. Blasco, *Catal. Today*, 2009, **143**, 293.
563 H. Hattori, *Chem. Rev.*, 1995, **95**, 537.
564 T. Frising and P. Leflaive, *Microporous Mesoporous Mater.*, 2008, **114**, 27.
565 R. T. Sanderson, *Science*, 1951, **114**, 670.
566 R. T. Sanderson, *Chemical Bonds and Bond Energy*, Academic Press, New York, 1976.
567 S. E. Siporin, B. C. McClaine and R. J. Davis, *Langmuir*, 2003, **19**, 4707.
568 T. Belin, C. Mve Mfoumou, S. Mignard and Y. Pouilloux, *Microporous Mesoporous Mater.*, 2013, **182**, 109.
569 S. Ernst, M. Hartmann, S. Sauerbeck and T. Bongers, *Appl. Catal., A*, 2000, **200**, 117.
570 C. Mirodatos, P. Pichat and D. Barthomeuf, *J. Phys. Chem.*, 1976, **80**, 1335.
571 M. Srasra, P. Rouxhet, E. M. Gaigneaux and S. Delsarte, *J. Phys. Chem. C*, 2006, 114.
572 X. Chen, J. Guo, Z. Fu, H. He and Y. Lon, *J. Porous Mater.*, 2013, **20**, 1271.
573 T. Steiner, *Angew. Chem., Int. Ed.*, 2002, **41**, 48.
574 P. O. Scokart and P. G. Rouxhet, *Bull. Soc. Chim. Belg.*, 1981, **90**, 983.
575 D. Barthomeuf, *J. Phys. Chem.*, 1984, **88**, 42.
576 M. M. Huang and S. Kaliaguine, *J. Chem. Soc., Faraday Trans.*, 1992, **88**, 751.
577 J. A. van Bokhoven, T.-L. Lee, M. Drakopoulos, C. Lamberti, S. Thieß and J. Zegenhagen, *Nature Mater.*, 2008, **7**, 551.
578 D. Barthomeuf, *J. Phys. Chem.*, 1984, **88**, 42.
579 D. Murphy, P. Massiani, R. Franck and D. Barthomeuf, *J. Phys. Chem.*, 1996, **100**, 6731.
580 M. Sánchez-Sánchez and T. Blasco, *J. Am. Chem. Soc.*, 2002, **124**, 3443.
581 J. Kučera, P. Nachtigall, J. Kotrla, G. Košová and J. Čejka, *J. Phys. Chem. B*, 2004, **108**, 16012.
582 M. A. Sanchez-Castillo, N. Agarwal, C. Miller, R. D. Cortright, R. J. Madon and J. A. Dumesic, *J. Catal.*, 2002, **205**, 67.
583 M. Sánchez-Sánchez and T. Blasco, *J. Am. Chem. Soc.*, 2002, **124**, 3443.
584 H. Forster, H. Fuess, E. Geidel, B. Hunger, H. Jobic, C. Kirschhock, O. Klepel and K. Krause, *Phys. Chem. Chem. Phys.*, 1999, **1**, 593.
585 R. J. Corrêa, *Tetrahedron Lett.*, 2003, **44**, 7299.
586 http://webbook.nist.gov.
587 J. Xie, M. Huang and S. Kaliaguine, *React. Kinet. Catal. Lett.*, 1996, **58**, 217.
588 E. Bosch, S. Huber, J. Weitkamp and H. Knözinger, *Phys. Chem. Chem. Phys.*, 1999, **1**, 579.
589 A. A. Tsyganenko, *Top. Catal.*, 2013, **56**, 905.
590 A. A. Tsyganenko, N. V. Zakharov and P. D. Murzin, *Catal. Today*, 2014, **226**, 73.
591 P. Hobza and Z. Havlas, *Chem. Rev.*, 2000, **100**, 4253.
592 K. Hermansson, *J. Phys. Chem. A*, 2002, **106**, 4695.
593 S. Scheiner and T. Kar, *J. Phys. Chem. A*, 2002, **106**, 1784.
594 A. J. Barnes, *J. Mol. Struct.*, 2004, **704**, 3.
595 M. Sanchez-Sanchez, T. Blasco and A. Corma, *J. Phys. Chem. C*, 2008, **112**, 16961.
596 S. N. Delanoye, W. A. Herrebout and B. J. van der Veken, *J. Am. Chem. Soc.*, 2002, **124**, 7490.
597 E. B. Uvarova, L. M. Kustov and V. B. Kazansky, *Stud. Surf. Sci. Catal.*, 1995, **94**, 254.
598 A. V. Ivanov, A. E. Koklin, E. B. Uvarova and L. M. Kustov, *Phys. Chem. Chem. Phys.*, 2003, **5**, 4718.
599 J. C. Lavalley, J. Lamotte, A. Travert, J. Czyzniewska and M. Ziolek, *J. Chem. Soc., Faraday Trans.*, 1998, **94**, 331.
600 B. Bonelli, B. Civalleri, B. Fubini, P. Ugliengo, C. O. Arean and E. Garrone, *J. Phys. Chem. B*, 2000, **104**, 10978.
601 E. Garrone, B. Bonelli, C. Lamberti, B. Civalleri, M. Rocchia, P. Roy and C. O. Arean, *J. Chem. Phys.*, 2002, **117**, 10274.
602 G. D. Pirngruber, P. Raybaud, Y. Belmabkhout, J. Cejka and A. Zukal, *Phys. Chem. Chem. Phys.*, 2010, **12**, 13534.
603 C. Bisio, G. Martra, S. Coluccia and P. Massiani, *J. Phys. Chem. C*, 2008, **112**, 10520.
604 P. A. Jacobs, F. M. Van Cauwelaert and E. F. Vansant, *J. Chem. Soc., Faraday Trans.*, 1973, **1**, 69–2130.
605 A. Vimont, F. Thibault-Starzyk and J. C. Lavalley, *J. Phys. Chem. B*, 2000, **104**, 286.
606 J. Liu, P. L. Ying, Q. Xin and C. Li, *Zeolites*, 1997, **19**, 197.
607 F. Thibault-Starzyk, O. Marie, N. Malicki, A. Vos, R. Schoonheydt, P. Geerlings, C. Henriques, C. Pommier and P. Massiani, *Stud. Surf. Sci. Catal.*, 2005, **158**, 663.
608 O. Marie, N. Malicki, C. Pommier, P. Massiani, A. Vos, R. Schoonheydt, P. Geerlings, C. Henriques and F. Thibault-Starzyk, *Chem. Commun.*, 2005, 1049.
609 E. A. Pidko, P. Mignon, P. Geerlings, R. A. Schoonheydt and R. A. van Santen, *J. Phys. Chem. C*, 2008, **112**, 5510.
610 E. A. Pidko and R. A. Van Santen, *Int. J. Quantum Chem.*, 2010, **110**, 210.
611 G. L. Woolery, L. B. Alemany, R. M. Dessau and A. W. Chester, *Zeolites*, 1986, **6**, 14.
612 R. M. Dessau, K. D. Schmitt, G. T. Kerr, G. L. Woolery and L. B. Alemany, *J. Catal.*, 1987, **104**, 484.
613 B. Kraushaar, J. W. De Haan and J. H. C. Van Hooff, *J. Catal.*, 1988, **109**, 470.
614 R. W. Weber, J. C. Q. Fletcher, K. P. Moller and C. T. Oconnor, *Microporous Mater.*, 1996, **7**, 15.
615 A. Corma, V. Fornés, L. Forni, F. Márquez, J. Martínez-Triguero and D. Moscotti, *J. Catal.*, 1998, **179**, 451.

616 T. Armaroli, M. Trombetta, A. G. Alejandre, J. R. Solis and G. Busca, *Phys. Chem. Chem. Phys.*, 2000, **2**, 3341.
617 K. H. Rhodes, S. A. Davis, F. Caruso, B. J. Zhang and S. Mann, *Chem. Mater.*, 2000, **12**, 2832.
618 M. W. Anderson, S. M. Holmes, N. Hanif and C. S. Cundy, *Angew. Chem., Int. Ed.*, 2000, **39**, 2707.
619 S. van Donk, A. H. Janssen, J. H. Bitter and K. P. de Jong, *Catal. Rev.*, 2003, **45**, 297.
620 M. Hartmann, *Angew. Chem., Int. Ed.*, 2004, **43**, 5880.
621 L. Tosheva and V. P. Valtchev, *Chem. Mater.*, 2005, **17**, 2494.
622 J. C. Groen, J. A. Moulijn and J. Perez-Ramirez, *J. Mater. Chem.*, 2006, **16**, 2121.
623 F. S. Xiao, L. F. Wang, C. Y. Yin, K. F. Lin, Y. Di, J. X. Li, R. R. Xu, D. S. Su, R. Schlogl, T. Yokoi and T. Tatsumi, *Angew. Chem., Int. Ed.*, 2006, **45**, 3090.
624 M. A. Snyder and M. Tsapatsis, *Angew. Chem., Int. Ed.*, 2007, **46**, 7560.
625 K. Egeblad, C. H. Christensen, M. Kustova and C. H. Christensen, *Chem. Mater.*, 2008, **20**, 946.
626 W. Fan, M. A. Snyder, S. Kumar, P. S. Lee, W. C. Yoo, A. V. McCormick, R. L. Penn, A. Stein and M. Tsapatsis, *Nat. Mater.*, 2008, **7**, 984.
627 J. Perez-Ramirez, C. H. Christensen, K. Egeblad, C. H. Christensen and J. C. Groen, *Chem. Soc. Rev.*, 2008, **37**, 2530.
628 J. Perez-Ramirez, D. Verboekend, A. Bonilla and S. Abello, *Adv. Funct. Mater.*, 2009, **19**, 3972.
629 A. Bonilla, D. Baudouin and J. Perez-Ramirez, *J. Catal.*, 2009, **265**, 170.
630 F. Thibault-Starzyk, I. Stan, S. Abelló, A. Bonilla, K. Thomas, C. Fernandez, J.-P. Gilson and J. Pérez-Ramírez, *J. Catal.*, 2009, **264**, 11.
631 C. Fernandez, I. Stan, J. P. Gilson, K. Thomas, A. Vicente, A. Bonilla and J. Perez-Ramirez, *Chem. – Eur. J.*, 2010, **16**, 6224.
632 D. Verboekend, L. A. Villaescusa, K. Thomas, I. Stan and J. Perez-Ramirez, *Catal. Today*, 2010, **152**, 11.
633 Y. P. Khitev, Y. G. Kolyagin, I. I. Ivanova, O. A. Ponomareva, F. Thibault-Starzyk, J. P. Gilson, C. Fernandez and F. Fajula, *Microporous Mesoporous Mater.*, 2011, **146**, 201.
634 D. Verboekend, A. M. Chabaneix, K. Thomas, J. P. Gilson and J. Perez-Ramirez, *CrystEngComm*, 2011, **13**, 3408.
635 A. Inayat, B. Reinhardt, H. Uhlig, W. D. Einicke and D. Enke, *Chem. Soc. Rev.*, 2013, **42**, 3753.
636 D. Tzoulaki, A. Jentys, J. Perez-Ramirez, K. Egeblad and J. A. Lercher, *Catal. Today*, 2012, **198**, 3.
637 Z. Xue, T. Zhang, J. Ma, H. Miao, W. Fan, Y. Zhang and R. Li, *Microporous Mesoporous Mater.*, 2012, **151**, 271.
638 D. Verboekend, G. Vile and J. Perez-Ramirez, *Adv. Funct. Mater.*, 2012, **22**, 916.
639 P. Sazama, Z. Sobalik, J. Dedecek, I. Jakubec, V. Parvulescu, Z. Bastl, J. Rathousky and H. Jirglova, *Angew. Chem., Int. Ed.*, 2013, **52**, 2038.
640 D. P. Serrano, J. M. Escola and P. Pizarro, *Chem. Soc. Rev.*, 2013, **42**, 4004.
641 K. Sadowska, K. Góra-Marek and J. Datka, *J. Phys. Chem. C*, 2013, **117**, 9237.
642 W. Chaikittisilp, Y. Suzuki, R. R. Mukti, T. Suzuki, K. Sugita, K. Itabashi, A. Shimojima and T. Okubo, *Angew. Chem., Int. Ed.*, 2013, **52**, 3355.
643 I. I. Ivanova and E. E. Knyazeva, *Chem. Soc. Rev.*, 2013, **42**, 3671.
644 K. Moller and T. Bein, *Chem. Soc. Rev.*, 2013, **42**, 3689.
645 C. M. A. Parlett, K. Wilson and A. F. Lee, *Chem. Soc. Rev.*, 2013, **42**, 3876.
646 L. Gueudre, M. Milina, S. Mitchell and J. Perez-Ramirez, *Adv. Funct. Mater.*, 2014, **24**, 209.
647 P. A. Jacobs, M. Dusselier and B. F. Sels, *Angew. Chem., Int. Ed.*, 2014, **53**, 8621.
648 D. D. Xu, Y. H. Ma, Z. F. Jing, L. Han, B. Singh, J. Feng, X. F. Shen, F. L. Cao, P. Oleynikov, H. Sun, O. Terasaki and S. N. Che, *Nat. Commun.*, 2014, **5**, 9.
649 T. C. Keller, S. Isabettini, D. Verboekend, E. G. Rodrigues and J. Perez-Ramirez, *Chem. Sci.*, 2014, **5**, 677.
650 M. Khaleel, A. J. Wagner, K. A. Mkhoyan and M. Tsapatsis, *Angew. Chem., Int. Ed.*, 2014, **53**, 9456.
651 B. Li, Z. J. Hu, B. Kong, J. X. Wang, W. Li, Z. K. Sun, X. F. Qian, Y. S. Yang, W. Shen, H. L. Xu and D. Y. Zhao, *Chem. Sci.*, 2014, **5**, 1565.
652 K. Góra-Marek, K. Tarach and M. Choi, *J. Phys. Chem. C*, 2014, **118**, 12266.
653 K. Mlekodaj, K. Tarach, J. Datka, K. Gora-Marek and W. Makowski, *Microporous Mesoporous Mater.*, 2014, **183**, 54.
654 M. Milina, S. Mitchell, D. Cooke, P. Crivelli and J. Perez-Ramirez, *Angew. Chem., Int. Ed.*, 2015, **54**, 1591.
655 K. L. Liu, A. V. Kubarev, J. Van Loon, H. Uji-i, D. E. De Vos, J. Hofkens and M. B. J. Roeffaers, *ACS Nano*, 2014, **8**, 12650.
656 R. A. Beyerlein, C. ChoiFeng, J. B. Hall, B. J. Huggins and G. J. Ray, *Top. Catal.*, 1997, **4**, 27.
657 M. A. Kuehne, H. H. Kung and J. T. Miller, *J. Catal.*, 1997, **171**, 293.
658 M. A. Kuehne, S. M. Babitz, H. H. Kung and J. T. Miller, *Appl. Catal., A*, 1998, **166**, 293.
659 A. Corma, G. W. Huber, L. Sauvanaud and P. O'Connor, *J. Catal.*, 2007, **247**, 307.
660 H. S. Cerqueira, G. Caeiro, L. Costa and F. R. Ribeiro, *J. Mol. Catal. A: Chem.*, 2008, **292**, 1.
661 P. Kortunov, S. Vasenkov, J. Karger, R. Valiullin, P. Gottschalk, M. F. Elia, M. Perez, M. Stocker, B. Drescher, G. McElhiney, C. Berger, R. Glaser and J. Weitkamp, *J. Am. Chem. Soc.*, 2005, **127**, 13055.
662 N. Malicki, P. Beccat, P. Bourges, C. Fernandez, A.-A. Quoineaud, L. J. Simon and F. Thibault-Starzyk, *Stud. Surf. Sci. Catal.*, 2007, **170**, 762.
663 M. Connolly, *J. Appl. Crystallogr.*, 1983, **16**, 548.
664 O. Marie, P. Massiani and F. Thibault-Starzyk, *J. Phys. Chem. B*, 2004, **108**, 5073.
665 F. Wakabayashi, J. Kondo, A. Wada, K. Domen and C. Hirose, *J. Phys. Chem.*, 1993, **97**, 10761.

666 V. L. Zholobenko, M. A. Makarova and J. Dwyer, *J. Phys. Chem.*, 1993, **97**, 5962.
667 M. Maache, A. Janin, J. C. Lavalley and E. Benazzi, *Zeolites*, 1995, **15**, 507.
668 Z. Tvaruzkova, K. Habersberger and P. Jiru, *React. Kinet. Catal. Lett.*, 1991, **44**, 361.
669 S. Jolly, J. Saussey and J. C. Lavalley, *Catal. Lett.*, 1994, **24**, 141.
670 B. Wichterlova, Z. Tvaruzkova, Z. Sobalik and P. Sarv, *Microporous Mesoporous Mater.*, 1998, **24**, 223.
671 M. Trombetta, G. Busca, S. Rossini, V. Piccoli, U. Cornaro, A. Guercio, R. Catani and R. J. Willey, *J. Catal.*, 1998, **179**, 581.
672 P. Kubanek, B. Wichterlova and Z. Sobalik, *J. Catal.*, 2002, **211**, 109.
673 A. Damin, S. Bordiga, A. Zecchina, K. Doll and C. Lamberti, *J. Chem. Phys.*, 2003, **118**, 10183.
674 O. Marie, F. Thibault-Starzyk and J. C. Lavalley, *Phys. Chem. Chem. Phys.*, 2000, **2**, 5341.
675 M. Bevilacqua and G. Busca, *Catal. Commun.*, 2002, **3**, 497.
676 M. Bevilacqua, A. G. Alejandre, C. Resini, M. Casagrande, J. Ramirez and G. Busca, *Phys. Chem. Chem. Phys.*, 2002, **4**, 4575.
677 T. Montanari, M. Bevilacqua and G. Busca, *Appl. Catal., A*, 2006, **307**, 21.
678 B. Onida, F. Geobaldo, F. Testa, F. Crea and E. Garrone, *Microporous Mesoporous Mater.*, 1999, **30**, 119.
679 N. S. Nesterenko, F. Thibault-Starzyk, V. Montouillout, V. V. Yuschenko, C. Fernandez, J. P. Gilson, F. Fajula and I. I. Ivanova, *Microporous Mesoporous Mater.*, 2004, **71**, 157.
680 N. S. Nesterenko, F. Thibault-Starzyk, V. Montouillout, V. V. Yushchenko, C. Fernandez, J. P. Gilson, F. Fajula and I. I. Ivanova, *Kinet. Catal.*, 2006, **47**, 40.
681 T. Onfroy, G. Clet and M. Houalla, *Microporous Mesoporous Mater.*, 2005, **82**, 99.
682 D. F. Swinehart, *J. Chem. Educ.*, 1962, **39**, 333.
683 A. Rodger, in *Encyclopedia of Biophysics*, ed. G. K. Roberts, Springer, Berlin, Heidelberg, 2013, ch. 783, p. 184.
684 J. Datka, A. M. Turek, J. M. Jehng and I. E. Wachs, *J. Catal.*, 1992, **135**, 186.
685 M. Crocker, R. H. M. Herold, M. H. W. Sonnemans, C. A. Emeis, A. E. Wilson and J. N. Vandermoolen, *J. Phys. Chem.*, 1993, **97**, 432.
686 C. A. Emeis, *J. Catal.*, 1993, **141**, 347.
687 V. Bolis, G. Magnacca, G. Cerrato and C. Morterra, *Thermochim. Acta*, 2001, **379**, 147.
688 C. Morterra, G. Magnacca and V. Bolis, *Catal. Today*, 2001, **70**, 43.
689 F. Thibault-Starzyk, B. Gil, S. Aiello, T. Chevreau and J. P. Gilson, *Microporous Mesoporous Mater.*, 2004, **67**, 107.
690 A. Popov, E. Kondratieva, J. M. Goupil, L. Mariey, P. Bazin, J. P. Gilson, A. Travert and F. Mauge, *J. Phys. Chem. C*, 2010, **114**, 15661.
691 A. A. Tsyganenko, E. E. Platero, C. O. Arean, E. Garrone and A. Zecchina, *Catal. Lett.*, 1999, **61**, 187.
692 C. O. Arean, A. A. Tsyganenko, O. V. Manoilova, G. T. Palomino, M. P. Mentruit and E. Garrone, *Chem. Commun.*, 2001, 455.
693 C. O. Arean, O. V. Manoilova, A. A. Tsyganenko, G. T. Palomino, M. P. Mentruit, F. Geobaldo and E. Garrone, *Eur. J. Inorg. Chem.*, 2001, 1739.
694 O. V. Manoilova, M. P. Mentruit, G. T. Palomino, A. A. Tsyganenko and C. O. Arean, *Vib. Spectrosc.*, 2001, **26**, 107.
695 C. O. Arean, O. V. Manoilova, M. R. Delgado, A. A. Tsyganenko and E. Garrone, *Phys. Chem. Chem. Phys.*, 2001, **3**, 4187.
696 C. O. Arean, M. R. Delgado, O. V. Manoilova, G. T. Palomino, A. A. Tsyganenko and E. Garrone, *Chem. Phys. Lett.*, 2002, **362**, 109.
697 C. O. Arean, O. V. Manoilova, G. T. Palomino, M. R. Delgado, A. A. Tsyganenko, B. Bonelli and E. Garrone, *Phys. Chem. Chem. Phys.*, 2002, **4**, 5713.
698 C. P. Arean, M. P. Mentruit, M. R. Delgado, G. T. Palomino, O. V. Manoilova, A. A. Tsyganenko and E. Garrone, *Stud. Surf. Sci. Catal.*, 2002, **142**, 207.
699 C. O. Arean, O. V. Manoilova, B. Bonelli, M. R. Delgado, G. T. Palomino and E. Garrone, *Chem. Phys. Lett.*, 2003, **370**, 631.
700 P. Y. Storozhev, C. O. Arean, E. Garrone, P. Ugliengo, V. A. Ermoshin and A. A. Tsyganenko, *Chem. Phys. Lett.*, 2003, **374**, 439.
701 A. V. Rudakova, R. F. Lobo and K. M. Bulanin, *J. Phys. Chem. B*, 2003, **107**, 5212.
702 G. Spoto, E. Gribov, S. Bordiga, C. Lamberti, G. Ricchiardi, D. Scarano and A. Zecchina, *Chem. Commun.*, 2004, 2768.
703 C. O. Arean, M. R. Delgado, G. T. Palomino, M. T. Rubio, N. M. Tsyganenko, A. A. Tsyganenko and E. Garrone, *Microporous Mesoporous Mater.*, 2005, **80**, 247.
704 P. Nachtigall, E. Garrone, G. T. Palomino, M. R. Delgado, D. Nachtigallova and C. O. Arean, *Phys. Chem. Chem. Phys.*, 2006, **8**, 2286.
705 A. A. Tsyganenko, E. V. Kondratieva, V. S. Yanko and P. Y. Storozhev, *J. Mater. Chem.*, 2006, **16**, 2358.
706 C. O. Arean, G. T. Palomino and M. R. L. Carayol, *Appl. Surf. Sci.*, 2007, **253**, 5701.
707 M. R. Delgado and C. O. Area, *Appl. Surf. Sci.*, 2007, **253**, 5705.
708 C. O. Arean, *J. Mol. Struct.*, 2008, **880**, 31.
709 B. Bonelli, C. O. Arean, M. Armandi, M. R. Delgado and E. Garrone, *ChemPhysChem*, 2008, **9**, 1747.
710 G. T. Palomino, M. R. L. Carayol and C. O. Arean, *Catal. Today*, 2008, **138**, 249.
711 M. Armandi, E. Garrone, C. O. Arean and B. Bonelli, *ChemPhysChem*, 2009, **10**, 3316.
712 G. T. Palomino, B. Bonelli, C. O. Arean, J. B. Parra, M. R. L. Carayol, M. Armandi, C. O. Ania and E. Garrone, *Int. J. Hydrogen Energy*, 2009, **34**, 4371.
713 C. O. Arean and M. R. Delgado, *Appl. Surf. Sci.*, 2010, **256**, 5259.
714 M. Armandi, B. Bonelli, I. Bottero, C. O. Arean and E. Garrone, *J. Phys. Chem. C*, 2010, **114**, 6658.
715 M. R. Delgado and C. O. Arean, *Energy*, 2011, **36**, 5286.
716 C. O. Arean, M. R. Delgado, G. F. Bibiloni, O. Bludsky and P. Nachtigall, *ChemPhysChem*, 2011, **12**, 1435.
717 A. Zukal, C. O. Arean, M. R. Delgado, P. Nachtigall, A. Pulido, J. Mayerova and J. Cejka, *Microporous Mesoporous Mater.*, 2011, **146**, 97.

718 O. Zavorotynska, J. G. Vitillo, G. Spoto and A. Zecchina, *Int. J. Hydrogen Energy*, 2011, **36**, 7944.
719 P. Nachtigall, M. R. Delgado, D. Nachtigallova and C. O. Arean, *Phys. Chem. Chem. Phys.*, 2012, **14**, 1552.
720 R. Bulanek and E. Koudelkova, *J. Therm. Anal. Calorim.*, 2013, **113**, 97.
721 M. R. Delgado, R. Bulanek, P. Chlubna and C. O. Arean, *Catal. Today*, 2014, **227**, 45.
722 F. Rouquerol, J. Rouquerol and K. Sing, *Adsorption by Powders and Porous Solids Principles, Methodology and Applications*, Academic Press, London, 1999.
723 J. Pires, M. B. Decarvalho, F. R. Ribeiro and E. G. Derouane, *J. Mol. Catal.*, 1993, **85**, 295.
724 T. Yamazaki, M. Katoh, S. Ozawa and Y. Ogino, *Mol. Phys.*, 1993, **80**, 313.
725 S. K. Wirawan and D. Creaser, *Microporous Mesoporous Mater.*, 2006, **91**, 196.
726 J. A. Dunne, R. Mariwals, M. Rao, S. Sircar, R. J. Gorte and A. L. Myers, *Langmuir*, 1996, **12**, 5888.
727 J. A. Dunne, M. Rao, S. Sircar, R. J. Gorte and A. L. Myers, *Langmuir*, 1996, **12**, 5896.
728 S. Savitz, A. L. Myers and R. J. Gorte, *J. Phys. Chem. B*, 1999, **103**, 3687.
729 V. Bolis, S. Bordiga, C. Lamberti, A. Zecchina, A. Carati, F. Rivetti, G. Spano and G. Petrini, *Langmuir*, 1999, **15**, 5753.
730 V. Bolis, S. Bordiga, C. Lamberti, A. Zecchina, A. Carati, F. Rivetti, G. Spano and G. Petrini, *Microporous Mesoporous Mater.*, 1999, **30**, 67.
731 B. Bonelli, E. Garrone, B. Fubini, B. Onida, M. R. Delgado and C. O. Arean, *Phys. Chem. Chem. Phys.*, 2003, **5**, 2900.
732 A. Pulido, P. Nachtigall, A. Zukal, I. Dominguez and J. Cejka, *J. Phys. Chem. C*, 2009, **113**, 2928.
733 A. Zukal, A. Pulido, B. Gil, P. Nachtigall, O. Bludsky, M. Rubes and J. Cejka, *Phys. Chem. Chem. Phys.*, 2010, **12**, 6413.
734 J. Estephane, E. Groppo, J. G. Vitillo, A. Damin, C. Lamberti, S. Bordiga and A. Zecchina, *Phys. Chem. Chem. Phys.*, 2009, **11**, 2218.
735 G. Turnes Palomino, C. Palomino Cabello and C. Otero Arean, *Eur. J. Inorg. Chem.*, 2011, 1703.
736 S. M. Chavan, O. Zavorotynska, C. Lamberti and S. Bordiga, *Dalton Trans.*, 2013, **42**, 12586.
737 F. Bonino, C. Lamberti, S. Chavan, J. G. Vitillo and S. Bordiga, in *Metal-organic frameworks in heterogeneous catalysis*, ed. F. X. Llabrés i Xamena and J. Gascón, RSC, Cambridge, 2013, p. 76.
738 G. T. Palomino, C. O. Arean and M. R. L. Carayol, *Appl. Surf. Sci.*, 2010, **256**, 5281.
739 C. O. Arean, G. T. Palomino, M. R. L. Carayol, A. Pulido, M. Rubes, O. Bludsky and P. Nachtigall, *Chem. Phys. Lett.*, 2009, **477**, 139.
740 P. J. E. Harlick and F. H. Tezel, *Microporous Mesoporous Mater.*, 2004, **76**, 71.
741 A. Pulido, M. R. Delgado, O. Bludsky, M. Rubes, P. Nachtigall and C. O. Arean, *Energy Environ. Sci.*, 2009, **2**, 1187.
742 E. Garrone, B. Bonelli and C. Otero Arean, *Chem. Phys. Lett.*, 2008, **456**, 68.
743 M. S. Westwell, M. S. Searle, J. Klein and D. H. Williams, *J. Phys. Chem.*, 1996, **100**, 16000.
744 A. A. Stolov, W. A. Herrebout and B. J. van der Veken, *J. Am. Chem. Soc.*, 1998, **120**, 7310.
745 G. Sugihara, D. S. Shigematsu, S. Nagadome, S. Lee, Y. Sasaki and H. Igimi, *Langmuir*, 2000, **16**, 1825.
746 D. H. Williams, E. Stephens, D. P. O'Brien and M. Zhou, *Angew. Chem., Int. Ed.*, 2004, **43**, 6596.
747 A. A. Tsyganenko, *High Energy Chem.*, 2008, **42**, 610.
748 A. A. Tsyganenko, A. M. Chizhik and A. I. Chizhik, *Phys. Chem. Chem. Phys.*, 2010, **12**, 6387.
749 T. W. Hansen, J. B. Wagner, P. L. Hansen, S. Dahl, H. Topsoe and C. J. H. Jacobsen, *Science*, 2001, **294**, 1508.
750 P. L. Gai, *Microsc. Microanal.*, 2002, **8**, 21.
751 P. L. Hansen, J. B. Wagner, S. Helveg, J. R. Rostrup-Nielsen, B. S. Clausen and H. Topsoe, *Science*, 2002, **295**, 2053.
752 S. Helveg, C. Lopez-Cartes, J. Sehested, P. L. Hansen, B. S. Clausen, J. R. Rostrup-Nielsen, F. Abild-Pedersen and J. K. Norskov, *Nature*, 2004, **427**, 426.
753 R. Sharma, *J. Mater. Res.*, 2005, **20**, 1695.
754 J. F. Creemer, S. Helveg, G. H. Hoveling, S. Ullmann, A. M. Molenbroek, P. M. Sarro and H. W. Zandbergen, *Ultramicroscopy*, 2008, **108**, 993.
755 P. A. Crozier, R. G. Wang and R. Sharma, *Ultramicroscopy*, 2008, **108**, 1432.
756 S. B. Simonsen, S. Dahl, E. Johnson and S. Helveg, *J. Catal.*, 2008, **255**, 1.
757 A. D. Gamalski, J. Tersoff, R. Sharma, C. Ducati and S. Hofmann, *Nano Lett.*, 2010, **10**, 2972.
758 G. A. Somorjai, S. K. Beaumont and S. Alayoglu, *Angew. Chem., Int. Ed.*, 2011, **50**, 10116.
759 T. Fujita, P. F. Guan, K. McKenna, X. Y. Lang, A. Hirata, L. Zhang, T. Tokunaga, S. Arai, Y. Yamamoto, N. Tanaka, Y. Ishikawa, N. Asao, Y. Yamamoto, J. Erlebacher and M. W. Chen, *Nat. Mater.*, 2012, **11**, 775.
760 J. R. Jinschek and S. Helveg, *Micron*, 2012, **43**, 1156.
761 H. L. Xin, E. A. Pach, R. E. Diaz, E. A. Stach, M. Salmeron and H. M. Zheng, *ACS Nano*, 2012, **6**, 4241.
762 Y. Kuwauchi, S. Takeda, H. Yoshida, K. Sun, M. Haruta and H. Kohno, *Nano Lett.*, 2013, **13**, 3073.
763 E. Sayah, D. Brouri and P. Massiani, *Catal. Today*, 2013, **218**, 10.
764 S. R. Zhang, L. Nguyen, Y. Zhu, S. H. Zhan, C. K. Tsung and F. Tao, *Acc. Chem. Res.*, 2013, **46**, 1731.
765 S. R. Zhang, J. J. Shan, Y. Zhu, A. I. Frenkel, A. Patlolla, W. X. Huang, S. J. Yoon, L. Wang, H. Yoshida, S. Takeda and F. Tao, *J. Am. Chem. Soc.*, 2013, **135**, 8283.
766 H. L. L. Xin, S. Alayoglu, R. Z. Tao, A. Genc, C. M. Wang, L. Kovarik, E. A. Stach, L. W. Wang, M. Salmeron, G. A. Somorjai and H. M. Zheng, *Nano Lett.*, 2014, **14**, 3203.
767 Z. Ristanovic, J. P. Hofmann, U. Deka, T. U. Schulli, M. Rohnke, A. M. Beale and B. M. Weckhuysen, *Angew. Chem., Int. Ed.*, 2013, **52**, 13382.
768 J. D. Grunwaldt, *J. Phys.: Conf. Ser.*, 2009, **190**, 012151.
769 J. D. Grunwaldt and C. G. Schroer, *Chem. Soc. Rev.*, 2010, **39**, 4741.

770 A. M. Beale, S. D. M. Jacques and B. M. Weckhuysen, *Chem. Soc. Rev.*, 2010, **39**, 4656.
771 I. L. C. Buurmans and B. M. Weckhuysen, *Nat. Chem.*, 2012, **4**, 873.
772 S. Bordiga, E. Groppo, G. Agostini, J. A. van Bokhoven and C. Lamberti, *Chem. Rev.*, 2013, **113**, 1736.
773 J. D. Grunwaldt, J. B. Wagner and R. E. Dunin-Borkowski, *ChemCatChem*, 2013, **5**, 62.
774 L. Mino, G. Agostini, E. Borfecchia, D. Gianolio, A. Piovano, E. Gallo and C. Lamberti, *J. Phys. D: Appl. Phys.*, 2013, **46**, 423001.
775 C. Garino, E. Borfecchia, R. Gobetto, J. A. van Bokhoven and C. Lamberti, *Coord. Chem. Rev.*, 2014, **277**, 130.
776 S. Megelski, A. Lieb, M. Pauchard, A. Drechsler, S. Glaus, C. Debus, A. J. Meixner and G. Calzaferri, *J. Phys. Chem. B*, 2001, **105**, 25.
777 L. Karwacki, E. Stavitski, M. H. F. Kox, J. Kornatowski and B. M. Weckhuysen, *Angew. Chem., Int. Ed.*, 2007, **46**, 7228.
778 M. B. J. Roeffaers, B. F. Sels, H. Uji-i, B. Blanpain, P. L'Hoest, P. A. Jacobs, F. C. De Schryver, J. Hofkens and D. E. De Vos, *Angew. Chem., Int. Ed.*, 2007, **46**, 1706.
779 E. Stavitski, M. H. F. Kox and B. M. Weckhuysen, *Chem. – Eur. J.*, 2007, **13**, 7057.
780 M. H. F. Kox, E. Stavitski and B. M. Weckhuysen, *Angew. Chem., Int. Ed.*, 2007, **46**, 3652.
781 G. De Cremer, Y. Antoku, M. B. J. Roeffaers, M. Sliwa, J. Van Noyen, S. Smout, J. Hofkens, D. E. De Vos, B. F. Sels and T. Vosch, *Angew. Chem., Int. Ed.*, 2008, **47**, 2813.
782 M. H. F. Kox, E. Stavitski, J. C. Groen, J. Perez-Ramirez, F. Kapteijn and B. M. Weckhuysen, *Chem. – Eur. J.*, 2008, **14**, 1718.
783 D. Mores, E. Stavitski, M. H. F. Kox, J. Kornatowski, U. Olsbye and B. M. Weckhuysen, *Chem. – Eur. J.*, 2008, **14**, 11320.
784 M. B. J. Roeffaers, R. Ameloot, M. Baruah, H. Uji-i, M. Bulut, G. De Cremer, U. Muller, P. A. Jacobs, J. Hofkens, B. F. Sels and D. E. De Vos, *J. Am. Chem. Soc.*, 2008, **130**, 5763.
785 M. B. J. Roeffaers, R. Ameloot, A. J. Bons, W. Mortier, G. De Cremer, R. de Kloe, J. Hofkens, D. E. De Vos and B. F. Sels, *J. Am. Chem. Soc.*, 2008, **130**, 13516.
786 L. Karwacki, M. H. F. Kox, D. A. M. de Winter, M. R. Drury, J. D. Meeldijk, E. Stavitski, W. Schmidt, M. Mertens, P. Cubillas, N. John, A. Chan, N. Kahn, S. R. Bare, M. Anderson, J. Kornatowski and B. M. Weckhuysen, *Nat. Mater.*, 2009, **8**, 959.
787 M. B. J. Roeffaers, G. De Cremer, J. Libeert, R. Ameloot, P. Dedecker, A. J. Bons, M. Buckins, J. A. Martens, B. F. Sels, D. E. De Vos and J. Hofkens, *Angew. Chem., Int. Ed.*, 2009, **48**, 9285.
788 G. De Cremer, B. F. Sels, D. E. De Vos, J. Hofkens and M. B. J. Roeffaers, *Chem. Soc. Rev.*, 2010, **39**, 4703.
789 A. N. Parvulescu, D. Mores, E. Stavitski, C. M. Teodorescu, P. C. A. Bruijnincx, R. Gebbink and B. M. Weckhuysen, *J. Am. Chem. Soc.*, 2010, **132**, 10429.
790 C. Chmelik and J. Karger, *Chem. Soc. Rev.*, 2010, **39**, 4864.
791 M. A. van der Veen, B. F. Sels, D. E. De Vos and T. Verbiest, *J. Am. Chem. Soc.*, 2010, **132**, 6630.
792 I. L. C. Buurmans, J. Ruiz-Martinez, W. V. Knowles, D. van der Beek, J. A. Bergwerff, E. T. C. Vogt and B. M. Weckhuysen, *Nat. Chem.*, 2011, **3**, 862.
793 M. A. Karreman, I. L. C. Buurmans, J. W. Geus, A. V. Agronskaia, J. Ruiz-Martinez, H. C. Gerritsen and B. M. Weckhuysen, *Angew. Chem., Int. Ed.*, 2012, **51**, 1428.
794 R. Ameloot, F. Vermoortele, J. Hofkens, F. C. De Schryver, D. E. De Vos and M. B. J. Roeffaers, *Angew. Chem., Int. Ed.*, 2013, **52**, 401.
795 B. Ruhle, M. Davies, T. Bein and C. Brauchle, *Z. Naturforsch., B: J. Chem. Sci.*, 2013, **68**, 423.
796 D. P. Yan, Y. Q. Tang, H. Y. Lin and D. Wang, *Sci. Rep.*, 2014, **4**, 7.
797 C. Sprung and B. M. Weckhuysen, *J. Am. Chem. Soc.*, 2015, **137**, 1916.
798 R. A. Schoonheydt, *Chem. Soc. Rev.*, 2010, **39**, 5051.
799 K. T. Jackson and R. F. Howe, *Stud. Surf. Sci. Catal.*, 1994, **83**, 187.
800 R. L. Frost, M. Weier and W. N. Martens, *Spectrochim. Acta, Part A*, 2006, **63**, 685.
801 S. N. Azizi and S. E. Tilami, *J. Solid State Chem.*, 2013, **198**, 138.
802 M. Nowotny, J. A. Lercher and H. Kessler, *Zeolites*, 1991, **11**, 454.
803 F. Schuth, *J. Phys. Chem.*, 1992, **96**, 7493.
804 U. Roland, R. Salzer and S. Stolle, *Stud. Surf. Sci. Catal.*, 1994, **84**, 1231.
805 G. Muller, J. Bodis and J. Kornatowski, *Microporous Mesoporous Mater.*, 2004, **69**, 1.
806 J. Karger, R. Valiullin and S. Vasenkov, *New J. Phys.*, 2005, **7**, 15.
807 P. Kortunov, C. Chmelik, J. Karger, R. A. Rakoczy, D. M. Ruthven, Y. Traa, S. Vasenkov and J. Weitkamp, *Adsorpt.-J. Int. Adsorpt. Soc.*, 2005, **11**, 235.
808 C. Chmelik, P. Kortunov, S. Vasenkov and J. Karger, *Adsorpt.-J. Int. Adsorpt. Soc.*, 2005, **11**, 455.
809 C. Chmelik, E. Lehmann, S. Vasenkov, B. Staudte and J. Karger, *Application of interference and IR microscopy for studies of intracrystalline molecular transport in AFI type zeolites*, Springer, Dordrecht, 2006.
810 L. Heinke, C. Chmelik, P. Kortunov, D. M. Ruthven, D. B. Shah, S. Vasenkov and J. Karger, *Chem. Eng. Technol.*, 2007, **30**, 995.
811 L. Heinke, C. Chmelik, P. Kortunov, D. B. Shah, S. Brandani, D. M. Ruthven and J. Karger, *Microporous Mesoporous Mater.*, 2007, **104**, 18.
812 L. Heinke, C. Chmelik, P. Kortunov, S. Vasenkov, D. M. Ruthven, D. B. Shah and J. Karger, *Chem. Ing. Tech.*, 2007, **79**, 1195.
813 R. A. Schoonheydt, *Angew. Chem., Int. Ed.*, 2008, **47**, 9188.
814 C. Chmelik, L. Heinke, J. M. van Baten and R. Krishna, *Microporous Mesoporous Mater.*, 2009, **125**, 11.
815 J. Karger, J. Caro, P. Cool, M. O. Coppens, D. Jones, F. Kapteijn, F. Rodriguez-Reinoso, M. Stocker, D. Theodorou, E. F. Vansant and J. Weitkamp, *Chem. Eng. Technol.*, 2009, **32**, 1494.

816 C. Chmelik, L. Heinke, R. Valiullin and J. Karger, *Chem. Ing. Tech.*, 2010, **82**, 779.
817 C. Chmelik and J. Karger, *Adsorpt.-J. Int. Adsorpt. Soc.*, 2010, **16**, 515.
818 V. R. R. Marthala, M. Hunger, F. Kettner, H. Krautscheid, C. Chmelik, J. Karger and J. Weitkamp, *Chem. Mater.*, 2011, **23**, 2521.
819 J. Karger, *ChemPhysChem*, 2015, **16**, 24.
820 G. D. Price, J. J. Pluth, J. V. Smith, J. M. Bennett and R. L. Patton, *J. Am. Chem. Soc.*, 1982, **104**, 5971.
821 D. G. Hay, H. Jaeger and K. G. Wilshier, *Zeolites*, 1990, **10**, 571.
822 C. Weidenthaler, R. X. Fischer, R. D. Shannon and O. Medenbach, *J. Phys. Chem.*, 1994, **98**, 12687.
823 B. G. Saar, Y. N. Zeng, C. W. Freudiger, Y. S. Liu, M. E. Himmel, X. S. Xie and S. Y. Ding, *Angew. Chem., Int. Ed.*, 2010, **49**, 5476.
824 Y. Ozeki, W. Umemura, Y. Otsuka, S. Satoh, H. Hashimoto, K. Sumimura, N. Nishizawa, K. Fukui and K. Itoh, *Nat. Photonics*, 2012, **6**, 844.
825 P. Wang, J. J. Li, P. Wang, C. R. Hu, D. L. Zhang, M. Sturek and J. X. Cheng, *Angew. Chem., Int. Ed.*, 2013, **52**, 13042.
826 L. Wei, Y. Yu, Y. H. Shen, M. C. Wang and W. Min, *Proc. Natl. Acad. Sci. U. S. A.*, 2013, **110**, 11226.
827 Z. X. Chen, D. W. Paley, L. Wei, A. L. Weisman, R. A. Friesner, C. Nuckolls and W. Min, *J. Am. Chem. Soc.*, 2014, **136**, 8027.
828 D. Fu, Y. Yu, A. Folick, E. Currie, R. V. Farese, T. H. Tsai, X. S. Xie and M. C. Wang, *J. Am. Chem. Soc.*, 2014, **136**, 8820.
829 Y. H. Shen, F. Xu, L. Wei, F. H. Hu and W. Min, *Angew. Chem., Int. Ed.*, 2014, **53**, 5596.
830 D. L. Zhang, P. Wang, M. N. Slipchenko and J. X. Cheng, *Acc. Chem. Res.*, 2014, **47**, 2282.
831 W. S. Chiu, N. A. Belsey, N. L. Garrett, J. Moger, M. B. Delgado-Charro and R. H. Guy, *Proc. Natl. Acad. Sci. U. S. A.*, 2015, **112**, 7725.
832 F. Raatz, E. Freund and C. Marcilly, *J. Chem. Soc., Faraday Trans.*, 1983, **1**, 79–2299.
833 F. Raatz, C. Marcilly and E. Freund, *Zeolites*, 1985, **5**, 329.
834 P. C. Van Geem, K. F. M. G. J. Scholle, G. P. M. Van der Velden and W. S. Veeman, *J. Phys. Chem.*, 1988, **92**, 1585.
835 R. Fricke, H. Kosslick, G. Lischke and M. Richter, *Chem. Rev.*, 2000, **100**, 2303.
836 C. O. Arean, E. Escalona Platero, G. Spoto and A. Zecchina, *J. Mol. Catal.*, 1989, **56**, 211.
837 E. Escalona Platero, C. Otero Arean, D. Scarano, G. Spoto and A. Zecchina, *Mater. Chem. Phys.*, 1991, **29**, 347.
838 A. Zecchina, G. Spoto, G. Ghiotti and E. Garrone, *J. Mol. Catal.*, 1994, **86**, 423.
839 G. D. Smith and R. A. Palmer, in *Handbook of vibrational spectroscopy*, ed. J. M. Chalmers and P. R. Griffiths, John Wiley & Sons, Chichester, 2002, vol. 1, p. 625.
840 J. Saussey and F. Thibault-Starzyk, in *In-situ spectroscopy of catalysts*, ed. B. M. Weckhuysen, American Scientific Publisher, Stevenson Ranch, California, 2004.
841 P. R. Griffiths and J. A. de Haseth, *Fourier Transform Infrared Spectrometry*, John Wiley & Sons, New York, 1986.
842 V. G. Gregoriou, J. L. Chao, H. Toriumi and R. A. Palmer, *Chem. Phys. Lett.*, 1991, **179**, 491.
843 W. Uhmann, A. Becker, C. Taran and F. Siebert, *Appl. Spectrosc.*, 1991, **45**, 390.
844 T. J. Johnson, A. Simon, J. M. Weil and G. W. Harris, *Appl. Spectrosc.*, 1993, **47**, 1376.
845 T. Nakano, T. Yokoyama and H. Toriumi, *Appl. Spectrosc.*, 1993, **47**, 1354.
846 R. A. Palmer, J. L. Chao, R. M. Dittmar, V. G. Gregoriou and S. E. Plunkett, *Appl. Spectrosc.*, 1993, **47**, 1297.
847 S. V. Shilov, S. Okretic, H. W. Siesler and M. A. Czarnecki, *Appl. Spectrosc. Rev.*, 1996, **31**, 125.
848 C. Zscherp, R. Schlesinger, J. Tittor, D. Oesterhelt and J. Heberle, *Proc. Natl. Acad. Sci. U. S. A.*, 1999, **96**, 5498.
849 R. Brudler, R. Rammelsberg, T. T. Woo, E. D. Getzoff and K. Gerwert, *Nat. Struct. Biol.*, 2001, **8**, 265.
850 Y. H. Yeom and H. Frei, in *In-situ spectroscopy of catalysts*, ed. B. M. Weckhuysen, American Scientific Publisher, Stevenson Ranch, California, 2004.
851 S. M. Massick, J. G. Rabor, S. Elbers, J. Marhenke, S. Bernhard, J. R. Schoonover and P. C. Ford, *Inorg. Chem.*, 2000, **39**, 3098.
852 B. O. Budevska and P. R. Griffiths, *Anal. Chem.*, 1993, **65**, 2963.
853 A. Wille and E. Fridell, *Appl. Catal., B*, 2007, **70**, 294.
854 F. Thibault-Starzyk, E. Seguin, S. Thomas, M. Daturi, H. Arnolds and D. A. King, *Science*, 2009, **324**, 1048.
855 H. Sun and H. Frei, *J. Phys. Chem. B*, 1997, **101**, 205.
856 H. Frei, *AIP Conf. Proc.*, 1998, **430**, 28.
857 S. Vasenkov and H. Frei, *J. Am. Chem. Soc.*, 1998, **120**, 4031.
858 S. Vasenkov and H. Frei, *J. Phys. Chem. A*, 2000, **104**, 4327.
859 Y. H. Yeom and H. Frei, *J. Phys. Chem. A*, 2002, **106**, 3350.
860 Y. H. Yeom and H. Frei, *J. Phys. Chem. B*, 2003, **107**, 6286.
861 F. Thibault-Starzyk, S. Chenevarin and C. Fernandez, *Stud. Surf. Sci. Catal.*, 2004, **154**, 1730.
862 L. K. Andersen and H. Frei, *J. Phys. Chem. B*, 2006, **110**, 22601.
863 J. Estephane, E. Groppo, J. G. Vitillo, A. Damin, D. Gianolio, C. Lamberti, S. Bordiga, E. A. Quadrelli, J. M. Basset, G. Kervern, L. Emsley, G. Pintacuda and A. Zecchina, *J. Phys. Chem. C*, 2010, **114**, 4451.
864 K. L. Tang Wong and H. H. Brintzinger, *J. Am. Chem. Soc.*, 1975, **97**, 5143.
865 H. H. Brintzinger, D. Fischer, R. Mulhaupt, B. Rieger and R. M. Waymouth, *Angew. Chem., Int. Ed. Engl.*, 1995, **34**, 1143.
866 J. Estephane, E. Groppo, A. Damin, J. G. Vitillo, D. Gianolio, C. Lamberti, S. Bordiga, C. Prestipino, S. Nikitenko, E. A. Quadrelli, M. Taoufik, J. M. Basset and A. Zecchina, *J. Phys. Chem. C*, 2009, **113**, 7305.
867 D. Gianolio, E. Groppo, J. Estephane, C. Prestipino, S. Nikitenko, A. Zecchina, S. Bordiga, M. Taoufik, E. A. Quadrelli, J. M. Basset and C. Lamberti, *J. Phys.: Conf. Ser.*, 2009, **190**, 012140.

868 K. A. E. O'Callaghan, S. J. Brown, J. A. Page, M. C. Baird, T. C. Richards and W. E. Geiger, *Organometallics*, 1991, **10**, 3119.
869 M. Y. Darensbourg, P. Jimenez, J. R. Sackett, J. M. Hanckel and R. L. Kump, *J. Am. Chem. Soc.*, 1982, **104**, 1521.
870 B. Longato, B. D. Martin, J. R. Norton and O. P. Anderson, *Inorg. Chem.*, 1985, **24**, 1389.
871 S. Bordiga, L. Regli, C. Lamberti, A. Zecchina, M. Bjorgen and K. P. Lillerud, *J. Phys. Chem. B*, 2005, **109**, 7724.
872 K. Hadjiivanov, J. Saussey, J. L. Freysz and J. C. Lavalley, *Catal. Lett.*, 1998, **52**, 103.
873 F. Haase and J. Sauer, *J. Am. Chem. Soc.*, 1995, **117**, 3780.
874 J. Kotrla, D. Nachtigallova, L. Kubelkova, L. Heeribout, C. Doremieux-Morin and J. Fraissard, *J. Phys. Chem. B*, 1998, **102**, 2454.
875 H. Schneider, S. Tschudin, M. Schneider, A. Wokaun and A. Baiker, *J. Catal.*, 1994, **147**, 5.
876 G. Busca, L. Lietti, G. Ramis and F. Berti, *Appl. Catal., B*, 1998, **18**, 1.
877 I. Nova, C. Ciardelli, E. Tronconi, D. Chatterjee and B. Bandl-Konrad, *AIChE J.*, 2006, **52**, 3222.
878 C. Ciardelli, I. Nova, E. Tronconi, D. Chatterjee, B. Bandl-Konrad, M. Weibel and B. Krutzsch, *Appl. Catal., B*, 2007, **70**, 80.
879 E. Tronconi, I. Nova, C. Ciardelli, D. Chatterjee and M. Weibel, *J. Catal.*, 2007, **245**, 1.
880 H. H. Phil, M. P. Reddy, P. A. Kumar, L. K. Ju and J. S. Hyo, *Appl. Catal., B*, 2008, **78**, 301.
881 N. W. Cant and I. O. Y. Liu, *Catal. Today*, 2000, **63**, 133.
882 Z. Sobalik, P. Sazama, J. Dedecek and B. Wichterlova, *Appl. Catal., A*, 2014, **474**, 178.
883 M. Schwidder, M. S. Kumar, K. Klementiev, M. M. Pohl, A. Bruckner and W. Grunert, *J. Catal.*, 2005, **231**, 314.
884 M. Schwidder, M. S. Kumar, U. Bentrup, J. Perez-Ramirez, A. Bruckner and W. Grunert, *Microporous Mesoporous Mater.*, 2008, **111**, 124.
885 A. Grossale, I. Nova and E. Tronconi, *Catal. Today*, 2008, **136**, 18.
886 A. Grossale, I. Nova and E. Tronconi, *J. Catal.*, 2009, **265**, 141.
887 I. Malpartida, O. Marie, P. Bazin, M. Daturi and X. Jeandel, *Appl. Catal., B*, 2012, **113**, 52.
888 L. Olsson, H. Sjovall and R. J. Blint, *Appl. Catal., B*, 2008, **81**, 203.
889 H. Sjovall, R. J. Blint and L. Olsson, *Appl. Catal., B*, 2009, **92**, 138.
890 L. M. Ren, L. F. Zhu, C. G. Yang, Y. M. Chen, Q. Sun, H. Y. Zhang, C. J. Li, F. Nawaz, X. J. Meng and F. S. Xiao, *Chem. Commun.*, 2011, **47**, 9789.
891 U. Deka, A. Juhin, E. A. Eilertsen, H. Emerich, M. A. Green, S. T. Korhonen, B. M. Weckhuysen and A. M. Beale, *J. Phys. Chem. C*, 2012, **116**, 4809.
892 J. H. Kwak, D. Tran, S. D. Burton, J. Szanyi, J. H. Lee and C. H. F. Peden, *J. Catal.*, 2012, **287**, 203.
893 L. Wang, W. Li, G. S. Qi and D. Weng, *J. Catal.*, 2012, **289**, 21.
894 U. Deka, I. Lezcano-Gonzalez, B. M. Weckhuysen and A. M. Beale, *ACS Catal.*, 2013, **3**, 413.
895 F. Gao, E. D. Walter, N. M. Washton, J. Szanyi and C. H. F. Peden, *ACS Catal.*, 2013, **3**, 2083.
896 P. N. R. Vennestrom, A. Katerinopoulou, R. R. Tiruvalam, A. Kustov, P. G. Moses, P. Concepcion and A. Corma, *ACS Catal.*, 2013, **3**, 2158.
897 P. N. R. Vennestrom, T. V. W. Janssens, A. Kustov, M. Grill, A. Puig-Molina, L. F. Lundegaard, R. R. Tiruvalam, P. Concepcion and A. Corma, *J. Catal.*, 2014, **309**, 477.
898 J. J. Xue, X. Q. Wang, G. S. Qi, J. Wang, M. Q. Shen and W. Li, *J. Catal.*, 2013, **297**, 56.
899 S. Shwan, M. Skoglundh, L. F. Lundegaard, R. R. Tiruvalam, T. V. W. Janssens, A. Carlsson and P. N. R. Vennestrom, *ACS Catal.*, 2015, **5**, 16.
900 R. Martinez-Franco, M. Moliner, J. R. Thogersen and A. Corma, *ChemCatChem*, 2013, **5**, 3316.
901 M. Moreno-Gonzalez, B. Hueso, M. Boronat, T. Blasco and A. Corma, *J. Phys. Chem. Lett.*, 2015, **6**, 1011.
902 F. Giordanino, *Towards a consistent NH3-SCR mechanism over Cu sites in zeolites: Cu-SSZ-13 as model and outperforming catalyst*, PhD in chemical and materials sciences, Department of chemistry, University of Turin, 2014.
903 I. Lezcano-Gonzalez, U. Deka, B. Arstad, A. Van Yperen-De Deyne, K. Hemelsoet, M. Waroquier, V. Van Speybroeck, B. M. Weckhuysen and A. M. Beale, *Phys. Chem. Chem. Phys.*, 2014, **16**, 1639.
904 M. Boudart and G. Djega-Mariadassou, *Kinetics of Heterogeneous Catalytic Reactions*, Princeton University Press, Princeton, New Jersey, USA, 1984.
905 G. Djega-Mariadassou and M. Boudart, *J. Catal.*, 2003, **216**, 89.
906 J. W. Ward, *J. Catal.*, 1968, **11**, 259.
907 J. F. Joly, N. Zanierszydlowski, S. Colin, F. Raatz, J. Saussey and J. C. Lavalley, *Catal. Today*, 1991, **9**, 31.
908 S. Jolly, J. Saussey, J. C. Lavalley, N. Zanier, E. Benazzi and J. F. Joly, *Ber. Bunsen-Ges.*, 1993, **97**, 313.
909 O. Marie, F. Thibault-Starzyk and P. Massiani, *J. Catal.*, 2005, **230**, 28.
910 R. Gounder and E. Iglesia, *J. Am. Chem. Soc.*, 2009, **131**, 1958.
911 J. F. Groust, G. Costentin, J. M. Krafft and P. Massiani, *Phys. Chem. Chem. Phys.*, 2010, **12**, 937.
912 H. Lauron-Pernot, *Catal. Rev.: Sci. Eng.*, 2006, **48**, 315.
913 M. Magureanu, N. B. Mandache, P. Eloy, E. M. Gaigneaux and V. I. Parvulescu, *Appl. Catal., B*, 2005, **61**, 12.
914 C. Subrahmanyam, A. Magureanu, A. Renken and L. Kiwi-Minsker, *Appl. Catal., B*, 2006, **65**, 150.
915 C. Subrahmanyam, A. Renken and L. Kiwi-Minsker, *Appl. Catal., B*, 2006, **65**, 157.
916 M. Magureanu, N. B. Mandache, J. C. Hu, R. Richards, M. Florea and V. I. Parvulescu, *Appl. Catal., B*, 2007, **76**, 275.
917 C. Subrahmanyarn, A. Renken and L. Kiwi-Minsker, *Plasma Chem. Plasma Process.*, 2007, **27**, 13.
918 A. E. Wallis, J. C. Whitehead and K. Zhang, *Appl. Catal., B*, 2007, **74**, 111.
919 A. E. Wallis, J. C. Whitehead and K. Zhang, *Catal. Lett.*, 2007, **113**, 29.

920 Y. Chao, C. T. Huang, H. M. Lee and M. B. Chang, *Int. J. Hydrogen Energy*, 2008, **33**, 664.
921 W. Chu, L. N. Wang, P. A. Chernavskii and A. Y. Khodakov, *Angew. Chem., Int. Ed.*, 2008, **47**, 5052.
922 M. Rivallan, I. Yordanov, S. Thomas, C. Lancelot, S. Mintova and F. Thibault-Starzyk, *ChemCatChem*, 2010, **2**, 1074.
923 H. B. Huang, D. Q. Ye, D. Y. C. Leung, F. D. Feng and X. J. Guan, *J. Mol. Catal. A: Chem.*, 2011, **336**, 87.
924 T. Liu, Q. Q. Yu, H. Wang, X. Y. Jiang and X. M. Zheng, *Chin. J. Catal.*, 2011, **32**, 1502.
925 T. Witvrouwen, S. Paulussen and B. Sels, *Plasma Processes Polym.*, 2012, **9**, 750.
926 A. Gomez-Ramirez, V. J. Rico, J. Cotrino, A. Gonzalez-Elipe and R. M. Lambert, *ACS Catal.*, 2014, **4**, 402.
927 K. Abedi, F. Ghorbani-Shahna, B. Jaleh, A. Bahrami, R. Yarahmadi, R. Haddadi and M. Gandomi, *J. Electrost.*, 2015, **73**, 80.
928 M. Zhang and H. Frei, *Catal. Lett.*, 2015, **145**, 420.
929 M. El-Roz, P. Bazin, M. Daturi and F. Thibault-Starzyk, *ACS Catal.*, 2013, **3**, 2790.
930 C. V. Raman, *Indian J. Phys.*, 1928, **2**, 387.
931 G. Landsberg and L. Mandelstam, *Naturwissenschaften*, 1928, **16**, 557.
932 S. J. Tinnemans, M. H. F. Kox, M. W. Sletering, T. A. X. Nijhuis, T. Visser and B. M. Weckhuysen, *Phys. Chem. Chem. Phys.*, 2006, **8**, 2413.
933 F. J. Keil, *Microporous Mesoporous Mater.*, 1999, **29**, 49.
934 A. Bruckner, *Catal. Rev.: Sci. Eng.*, 2003, **45**, 97.
935 C. Prestipino, L. Regli, J. G. Vitillo, F. Bonino, A. Damin, C. Lamberti, A. Zecchina, P. L. Solari, K. O. Kongshaug and S. Bordiga, *Chem. Mater.*, 2006, **18**, 1337.
936 E. Groppo, M. J. Uddin, S. Bordiga, A. Zecchina and C. Lamberti, *Angew. Chem., Int. Ed.*, 2008, **47**, 9269.
937 M. A. Newton, *Chem. Soc. Rev.*, 2008, **37**, 2644.
938 S. Nikitenko, A. M. Beale, A. M. J. van der Eerden, S. D. M. Jacques, O. Leynaud, M. G. O'Brien, D. Detollenaere, R. Kaptein, B. M. Weckhuysen and W. Bras, *J. Synchrotron Radiat.*, 2008, **15**, 632.
939 G. Agostini, R. Pellegrini, G. Leofanti, L. Bertinetti, S. Bertarione, E. Groppo, A. Zecchina and C. Lamberti, *J. Phys. Chem. C*, 2009, **113**, 10485.
940 M. A. Newton and W. van Beek, *Chem. Soc. Rev.*, 2010, **39**, 4845.
941 M. G. O'Brien, A. M. Beale and B. M. Weckhuysen, *Chem. Soc. Rev.*, 2010, **39**, 4767.
942 U. Bentrup, *Chem. Soc. Rev.*, 2010, **39**, 4718.
943 E. Borfecchia, S. Maurelli, D. Gianolio, E. Groppo, M. Chiesa, F. Bonino and C. Lamberti, *J. Phys. Chem. C*, 2012, **116**, 19839.
944 A. Kubacka, A. Iglesias-Juez, A. Martínez-Arias, M. Di Michiel, M. A. Newton and M. Fernández-García, *ChemCatChem*, 2012, **4**, 725.
945 M. A. Newton and M. Fernández-García, in *In-situ Characterization of Heterogeneous Catalysts*, ed. J. A. Rodriguez, J. C. Hanson and P. J. Chupas, John Wiley & Sons, 2013.
946 E. Borfecchia, D. Gianolio, G. Agostini, S. Bordiga and C. Lamberti, in *Metal Organic Frameworks as Heterogeneous Catalysts*, ed. F. X. Llabrés i Xamena and J. Gascón, The Royal Society of Chemistry, Cambridge, 2013, p. 143.
947 G. Agostini, C. Lamberti, R. Pellegrini, G. Leofanti, F. Giannici, A. Longo and E. Groppo, *ACS Catal.*, 2014, **4**, 187.
948 E. Groppo, G. Agostini, E. Borfecchia, L. Wei, F. Giannici, G. Portale, A. Longo and C. Lamberti, *J. Phys. Chem. C*, 2014, **118**, 8406.
949 (*a*) E. Groppo, E. Gallo, K. Seenivasan, K. A. Lomachenko, A. Sommazzi, S. Bordiga, P. Glatzel, R. van Silfhout, A. Kachatkou, W. Bras and C. Lamberti, *ChemCatChem*, 2015, **7**, 1432; (*b*) E. Groppo, K. Seenivasan, E. Gallo, A. Sommazzi, C. Lamberti and S. Bordiga, *ACS Catal.*, 2015, **5**, 5586.
950 C. Lamberti, E. Borfecchia, J. A. van Bokhoven and M. Fernández García, in *XAS and XES; Theory and Applications*, ed. J. A. van Bokhoven and C. Lamberti, Wiley, New York, 2015.
951 F. Bonino, A. Damin, S. Bordiga, M. Selva, P. Tundo and A. Zecchina, *Angew. Chem., Int. Ed.*, 2005, **44**, 4774.
952 L. Valenzano, B. Civalleri, S. Bordiga, M. H. Nilsen, S. Jakobsen, K.-P. Lillerud and C. Lamberti, *Chem. Mater.*, 2011, **23**, 1700.
953 L. Valenzano, J. G. Vitillo, S. Chavan, B. Civalleri, F. Bonino, S. Bordiga and C. Lamberti, *Catal. Today*, 2012, **182**, 67.
954 K. Seenivasan, E. Gallo, A. Piovano, J. G. Vitillo, A. Sommazzi, S. Bordiga, C. Lamberti, P. Glatzel and E. Groppo, *Dalton Trans.*, 2013, **42**, 12706.
955 A. L. Bugaev, A. A. Guda, K. A. Lomachenko, V. V. Srabionyan, L. A. Bugaev, A. V. Soldatov, C. Lamberti, V. P. Dmitriev and J. A. van Bokhoven, *J. Phys. Chem. C*, 2014, **118**, 10416.
956 S. Takeuchi and T. Tahara, *J. Chem. Phys.*, 2004, **120**, 4768.
957 N. Ulagappan and H. Frei, *J. Phys. Chem. A*, 2000, **104**, 7834.
958 W. Y. Lin, H. X. Han and H. Frei, *J. Phys. Chem. B*, 2004, **108**, 18269.
959 V. Bourdin, P. Grenier, F. Meunier and L. M. Sun, *AIChE J.*, 1996, **42**, 700.
960 J. Valyon, G. Onyestyak and L. V. C. Rees, *J. Phys. Chem. B*, 1998, **102**, 8994.
961 G. Onyestyak, J. Valyon and L. V. C. Rees, *Phys. Chem. Chem. Phys.*, 2000, **2**, 3077.
962 J. Valyon, G. Onyestyak and L. V. C. Rees, *Langmuir*, 2000, **16**, 1331.
963 S. Chenevarin and F. Thibault-Starzyk, *Angew. Chem., Int. Ed.*, 2004, **43**, 1155.
964 M. Rivallan, E. Seguin, S. Thomas, M. Lepage, N. Takagi, H. Hirata and F. Thibault-Starzyk, *Angew. Chem., Int. Ed.*, 2010, **49**, 785.